Computational multiscale modelling of grinding processes

von der Fakultät Maschinenbau
der Technischen Universität Dortmund
zur Erlangung des akademischen Grades

Doktor-Ingenieur (Dr.-Ing.)

genehmigte Dissertation
von

Dipl.-Ing. Raphael Holtermann
aus
Castrop-Rauxel

Referent:	Prof. Dr.-Ing. Andreas Menzel
Korreferenten:	Prof. Dr.-Ing. Dirk Biermann Prof. Dr.-Ing. Carsten Heinzel
Tag der Einreichung:	25.05.2016
Tag der mündlichen Prüfung:	25.10.2016

Bibliografische Information Der Deutschen Bibliothek
Die Deutsche Bibliothek verzeichnet diese Publikation in der Deutschen Nationalbibliografie; detaillierte bibliografische Daten sind im Internet über **http://dnb.ddb.de** abrufbar.

Bibliographic information published by Die Deutsche Bibliothek
Die Deutsche Bibliothek lists this publication in the Deutsche Nationalbibliografie; detailed bibliographic data is available in the Internet at **http://dnb.ddb.de**.

Schriftenreihe des Instituts für Mechanik

Herausgeber: Institut für Mechanik
Fakultät Maschinenbau
Technische Universität Dortmund
Leonhard-Euler-Str. 5
D-44227 Dortmund

Druck: Koffler DruckManagement GmbH

© by Raphael Holtermann 2016

This work is subject to copyright. All rights are reserved, whether the whole or part of the material is concerned, specifically the rights of translation, reprinting, reuse of illustrations, recitation, broadcasting, reproduction on microfilm or in any other way, and storage in data banks. Duplication of this publication or parts thereof is permitted in connection with reviews or scholarly analysis. Permission for use must always be obtained from the author.

Alle Rechte vorbehalten, auch das des auszugsweisen Nachdrucks, der auszugsweisen oder vollständigen Wiedergabe (Photographie, Mikroskopie), der Speicherung in Datenverarbeitungsanlagen und das der Übersetzung.

Als Manuskript gedruckt. Printed in Germany.

ISBN 978-3-921823-86-6

Für meinen Opa Werner

In science it often happens that scientists say, "You know that's a really good argument; my position is mistaken," and then they would actually change their minds and you never hear that old view from them again. They really do it. It doesn't happen as often as it should, because scientists are human and change is sometimes painful. But it happens every day. I cannot recall the last time something like that happened in politics or religion.

Carl Sagan

Acknowledgements

This thesis reflects my work from 2010 to 2016 during my time as a research assistant at the Institute of Mechanics of TU Dortmund University. What it does actually not reflect is my intensive personal evolution during this time—so I will keep this portion for myself and will provide the academic rest to the public. Hopefully, some day it will aid somebody making this world a tiny bit better.

I would at first like to thank Professor Andreas Menzel for giving me the opportunity to work in the pleasant atmosphere of our institute and to enable me to be a mechanics teacher for students of various levels. His impressive knowledge, perfectionism and his remarkable view for details, paired with outstanding fairness and permanent support was a great guidance for me to become the scientist I am today. I also thank Professor Dirk Biermann for agreeing to be the co-referee of this work, for the intensive and fruitful professional cooperation and of course for playing lead guitar in our band *Need for Feed*, where we spent a lot of joyful hours rocking it together. Further thanks go to Professor Carsten Heinzel for serving as the third referee of this thesis and to Professor Andreas Brümmer for accepting the chairmanship of the examination committee.

Special thanks go to Sebastian Schumann for the immense cooperation we had during the six years we worked together on the topic of internal traverse grinding. I cannot count the endless night shifts we came through and the numerous arguments we had on various aspects of our collaboration, but in the end we always succeeded and created something perceptible.

Thank you so much, Dr. Richard Ostwald, for being the best office-mate I could think of for the five years we pretty much lived together. I deeply appreciate the infinite discussions we had as close friends, the music and moments we shared and the excellent conferences and business trips we experienced together. Muchas gracias y un fuerte abrazo a Dr. César Andrés Polindara, for being a great friend rather than a colleague, for always spreading the positive vibe and for the magnificent times we shared in the last years, either in Dortmund, Spain or whichever part of the world. Thank you, Comandante, for always having an open ear for me and for teaching me the Spanish that you don't learn in class!

I would like to express my deep gratitude to the entire team of the Institute of Mechanics for creating such a comfortable, intercultural, funny and friendly atmosphere at work and beyond. Thanks go to Tobias Asmanoglo for sharing his immense tensorial knowlegde and an office with me, to "Over-Engineer" Dr. Thorsten Bartel for our beneficial discussions and for sharing his facial expressions, to Alexander Bartels for always being able to tell an even dirtier joke, and to Rolf Berthelsen for his famous interpretation of ”just one drink”. Moreover, kind thanks to Karsten Buckmann, Dr. Guillermo Díaz Ortíz, Dinesh Kumar Dusthakar, especially for dragging us to India, Volker Fohrmeister, Dr. Krishnendu Haldar, Tim Heitbreder, Juniorprofessorin Sandra Klinge, Professor Jörn Mosler, Lars Rose, Robin Schulte, Leon Sprave and Christian Sievers. Further sincere thanks go to my former colleagues Dr. Till Clausmeyer, Dr. Ralf Denzer, Joshua Grodotzki, Dr. Christian Hortig, Dr. Tobias Kayser, Professor Björn Kiefer, Alexander Schowtjak, Dr. Maniprakash Subramanian, Professor Bob Svendsen and Dr. Tobias Waffenschmidt. Very special thanks definitely go to Kerstin Walter and Tina McDonagh for keeping that bunch of engineers and all of the institute together and running—for standing in for employees rights, for always offering an open ear for stressed-out and devastated PhD-students and for proofreading a hell lot of probably rather medium-interesting articles.

Some more very cordial thanks go to Joschi Derstappen for being the best flatmate of the world and a wonderful friend, to Janina Methorst for giving me the impulse to bring warm-heartedness to my life again, to Melanie Gräßer for the invaluable chats and coffee-breaks we had, and to Frank Turner for his music that got me back on my feet again for so many times.

Finally and most importantly, I gratefully thank my parents Gabi and Andreas, my sister Ramona and my dear Emilia for their endless patience, support and love that made me the man I am today and that helped me endure the times where things did not work out as expected—as it always happens in life, but especially in science.

Dortmund, December 2016 Raphael Holtermann

Abstract

This thesis deals with the modelling and simulation of high-performance grinding using electroplated cubic Boron Nitride (cBN) wheels. Special focus is set on the application to Internal Traverse Grinding which satisfies the manufacturing industry demands for a high rate of material removal along with a high surface quality while minimising the number of manufacturing processes invoked. To overcome the major problem of the abrasive process, namely a highly concentrated thermal load on the workpiece, a multi-scale simulation system that combines different modelling methods in a hybrid framework is presented. The latter consists of three main components. First, a kinematic simulation that models the grinding wheel surface based on experimentally determined measurements as well as subsequent numerical analysis is used to calculate the transient penetration history of every grain intersecting with the workpiece. Secondly, an h-adaptive, plane-strain finite element model incorporating elasto-plastic work hardening, thermal softening and ductile damage is used to simulate the proximity of one cBN grain during grinding and to capture the complex thermo-mechanical material response on a meso-scale. For the third component of the framework, the results from the preceding two simulation steps are—by incorporation of a special scale-bridging scheme—combined into a macro-scale thermo-mechanical load compound. This load is subsequently applied as boundary condition in a process model that captures the thermo-mechanical workpiece response on a macro-scale. Based on a subsequent process simulation that captures the workpiece response during grinding, compensation strategies are developed to improve the manufacturing accuracy of the investigated abrasive process by minimising the geometrical error of the finished workpieces.

Zusammenfassung

Die vorliegende Arbeit behandelt die Modellierung und Simulation von Hochleistungsschleifprozessen mit Schleifscheiben, welche mit kubischem Bornitrid (CBN) galvanisch belegt sind. Der Fokus liegt dabei auf der Simulation des Innenrundschälschleifens, welches als Schleifverfahren die Ansprüche der Fertigungsindustrie bezüglich hoher Materialabtragsrate bei gleichzeitig hoher Oberflächenqualität und einer Minimalanzahl von Arbeitsschritten erfüllt. Um dem zentralen Problem einer hohen thermischen Werkstückbelastung entgegenzuwirken, wird ein mehrskaliges Simulationssystem vorgestellt, welches verschiedene Modellierungsansätze in einem dreiteiligen Hybridmodell vereint. Die erste Teilkomponente ist eine Kinematiksimulation, welche basierend auf numerischen Analysen von experimentellen Messdaten den transienten Eingriffsverlauf jedes Schleifkorns mit dem Werkstück berechnet. Zweitens wird ein h-adaptives Finite-Elemente-Modell, welches elasto-plastische Verfestigung, thermische Entfestigung sowie duktile Schädigung des Werkstückmaterials abbildet, verwendet um die unmittelbare Umgebung eines CBN Korns auf der Meso-Ebene hinsichtlich ihrer komplexen thermo-mechanischen Reaktion zu simulieren. Um die Randbedingungen für die dritte Modellkomponente zu bestimmen, wird basierend auf den vorigen Simulationskomponenten ein spezieller Skalentransformationsansatz für die thermo-mechanischen Reaktionen vorgestellt, um diese Werkstücklasten von der Meso- auf die Makroskala zu transferieren. Mithilfe einer anschließenden Prozesssimulation wird das makroskopische Werkstückverhalten während des Schleifens nachgebildet und schließlich simulationsgestützte Kompensationsstrategien entwickelt, um thermisch bedingte Maßfehler des fertigen Bauteils zu minimieren.

Publications

The following peer-reviewed articles have been published with permission during the progress of the present thesis. All articles are listed in order of their publication date.

[37] R. Holtermann, S. Schumann, A. Menzel and D. Biermann. Modelling, simulation and experimental investigation of chip formation in internal traverse grinding. *Production Engineering*, 7(2-3):251–263, 2013.

[35] R. Holtermann, S. Schumann, A. Menzel and D. Biermann. A hybrid approach to the modelling and simulation of grinding processes, *Proceedings of 11th World Congress Computational Mechanics (WCCM XI)*, 1932–1937, 2014.

[85] S. Schumann, T. Siebrecht, P. Kersting, D. Biermann, R. Holtermann and A. Menzel. Determination of the thermal load distribution in internal traverse grinding using a geometric-kinematic simulation. *Procedia CIRP*, 31:322–327, 2015.

[38] R. Holtermann, A. Menzel, S. Schumann, D. Biermann, T. Siebrecht and P. Kersting. Modelling and simulation of internal traverse grinding: bridging meso- and macro-scale simulations. *Production Engineering* 9:451–463, 2015.

[39] R. Holtermann, S. Schumann, A. Zabel, D. Biermann and A. Menzel. Numerical determination of process values influencing the surface integrity in grinding. *Procedia CIRP* 45:39–42, 2016.

[16] D. Biermann, R. Holtermann, A. Menzel and S. Schumann. Modelling and simulation of thermal effects in internal traverse grinding of hardened bearing steel. *CIRP Annals – Manufacturing Technology*, 65(1):321–324, 2016.

For the articles listed, the author of this thesis has contributed essential parts of the theoretical outlines, the majority of the simulations presented and also carried out the main documentation of the above-mentioned works.

Beyond, the author of this thesis contributed to the following predominantly collaborative research articles in terms of planning and carrying out the adaptive finite element simulations, analysing and discussing the corresponding results and also writing relevant passages.

[15] D. Biermann, A. Menzel, T. Bartel, F. Höhne, R. Holtermann, R. Ostwald, B. Sieben, M. Tiffe and A. Zabel. Experimental and computational investigation of machining processes for functionally graded materials. *Procedia Engineering*, 19:22–27, 2011.

[36] R. Holtermann, S. Schumann, A. Menzel and D. Biermann. Ansätze zur Modellierung und Simulation des Innenrundschälschleifens. *diamond business*, 40(1):30–41, 2012.

[87] S. Schumann, E. Würz, D. Biermann, R. Holtermann and A. Menzel. Wärmeeintrag beim Hochleistungs-Innenrundschälschleifen beherrschen – Ermittlung der thermischen Werkstückbelastungen mittels FEM. *VDI-Z Integrierte Produktion*, 154(Spezial I):31–33, 2012.

[84] S. Schumann, R. Holtermann, D. Biermann and A. Menzel. Hochleistungs-Innenrundschälschleifen – Thermomechanische Betrachtung in Abhängigkeit vom radialen Gesamtaufmaß. *diamond business*, 45(2):36–43, 2013.

[86] S. Schumann, R. Holtermann, D. Biermann and A. Menzel. Lokale Betrachtung des Innenrundschälschleifens – Modellhafte Ermittlung der thermomechanischen Belastung in Abhängigkeit des Schruppzonenwinkels. *wt - Werkstattstechnik online*, 103(6):493–498, 2013.

[83] V. Schulze, E. Uhlmann, R. Mahnken, A. Menzel, D. Biermann, A. Zabel, P. Bollig, I. Ivanov, C. Cheng, R. Holtermann and T. Bartel. Evaluation of different approaches for modeling phase transformations in machining simulation. *Production Engineering*, 9:437–449, 2015.

[13] R. Berthelsen, H. Wilbuer, R. Holtermann and A. Menzel. Computational modelling of wear – application to structured surfaces of elastoplastic tools. *GAMM-Mitteilungen*, 39(2):210–228, 2016.

Contents

Notation ix

1 Introduction 1
- 1.1 Motivation and state of the art 1
  - 1.1.1 Internal Traverse Grinding 2
  - 1.1.2 Modelling and simulation of grinding 6
- 1.2 Objective of this work 16

2 Topography analysis 19
- 2.1 Measurement and preprocessing 19
- 2.2 Grain recognition and filtering 22
- 2.3 Approximation of the cutting edge 25
- 2.4 Results 26

3 Kinematic simulation 29
- 3.1 Implementation 29
- 3.2 Results 31
- 3.3 Local investigation of engagement conditions 35

4 Meso-scale single-grain model 39
- 4.1 Basics of continuum thermomechanics 39
- 4.2 Material modelling 45
- 4.3 Finite Element Implementation 47
- 4.4 Numerical examples and results 50
- 4.5 Parametric boundary value problem formulation 58
  - 4.5.1 Self-contact 60
- 4.6 Heat source definition and thermal results 62
- 4.7 Multiple grain engagement 67
  - 4.7.1 Multi-grain finite element setup 68
  - 4.7.2 Results 69
  - 4.7.3 Preliminary conclusion 71
- A.1 Material parameters 73
  - A.1.1 Isothermal material parameters 73
  - A.1.2 Material parameters of the parametric single grain model 74

B.1 SPP 1480 Benchmark 77
B.1.1 Model setup 77
B.1.2 Results 77

5 Bridging the meso and macro scale 81
5.1 Derivation of the scale-bridging strategy 81
5.2 Results and discussion 85
5.3 Bridging the process forces 88

6 Process model and compensation approaches 93
6.1 Experiments 96
6.1.1 Fundamental experimental results 97
6.2 Prototype Model 98
6.2.1 Influence of the clamping stress 106
6.2.2 Simulation of the clamping cover 114
6.3 Modelling of material removal 127
6.3.1 Element deletion 127
6.3.2 Modelling of material removal by solution mapping 128
6.3.3 Material removal by continuous solution mapping 131
6.3.4 Implementation details of the remeshing scheme 136
6.3.5 Numerical examples and results 141
6.4 Compensation strategies 144
6.4.1 Derivation of compensation approaches adapted to ITG 146
6.4.2 Definition of the residual norm 150
6.4.3 Results and discussion 151

7 Concluding remarks 157
7.1 Outlook 159
7.1.1 Three-dimensional single grain meso-scale model 159
7.1.2 Three-dimensional process model 160

Bibliography 161

Notation

The meaning of any variables used in this thesis is generally described in the corresponding sections. For the reader's convenience, we outline the general notation conventions and additionally display a list of symbols at the end of the present section. We use non-bold italic letters for scalars, bold-face italic letters for vectors as well as second-order tensors and bold-face sans-serif letters for fourth-order tensors. The $\bullet$ symbol is used as a general placeholder substituting a single symbol or even a complete mathematical expression.

Tensors Considering a three-dimensional Euclidean space that is represented by a set of orthonormal basis vectors $\{\boldsymbol{e}_i\}$ with $i = 1, 2, 3$, first, second and fourth order tensors are expressed as the sum of their coefficients $(\bullet)_i$, referring to Einstein's summation convention as

$$\begin{aligned}\boldsymbol{u} &= u_i\,\boldsymbol{e}_i\,,\\ \boldsymbol{T} &= T_{ij}\,\boldsymbol{e}_i\otimes\boldsymbol{e}_j\,,\\ \boldsymbol{\mathsf{C}} &= \mathsf{C}_{ijkl}\,\boldsymbol{e}_i\otimes\boldsymbol{e}_j\otimes\boldsymbol{e}_k\otimes\boldsymbol{e}_l\,.\end{aligned}$$

Inner tensor products Different inner products of tensors are represented by dots where the number of dots characterises the number of contractions, so that

$$\begin{aligned}\boldsymbol{a}\cdot\boldsymbol{b} &= a_i\,b_i\,,\\ \boldsymbol{A}\cdot\boldsymbol{b} &= A_{ij}\,b_j\,\boldsymbol{e}_i\,,\\ \boldsymbol{A}\cdot\boldsymbol{B} &= A_{ij}\,B_{jk}\,\boldsymbol{e}_i\otimes\boldsymbol{e}_k\,,\\ \boldsymbol{A}:\boldsymbol{B} &= A_{ij}\,B_{ij}\,,\\ \boldsymbol{\mathsf{A}}:\boldsymbol{B} &= \mathsf{A}_{ijkl}\,B_{kl}\,\boldsymbol{e}_i\otimes\boldsymbol{e}_j\,.\end{aligned}$$

Sets and regions Geometrical regions, which can as well be interpreted as sets of geometrical elements of any order, will be denoted with calligraphic capital letters. In this context, a region or body $\mathcal{B}$ can be rewritten as the sum or union of n subregions

$\Delta\mathcal{B}_i$ and can be approximated in terms of finite elements $\mathcal{E}_i$, which in turn represent a subregion again:

$$\mathcal{B} = \{\Delta\mathcal{B}_1,\, \Delta\mathcal{B}_2 \ldots \Delta\mathcal{B}_n\} = \bigcup_{i=1}^{n} \Delta\mathcal{B}_i \;\approx\; \mathcal{B}^{\boxplus} = \bigcup_{i=1}^{n} \mathcal{E}_i .$$

If not used in the context of a fraction for a partial derivative, the ∂ operator is in terms of regions used to refer to the boundary $\partial\mathcal{B}$ of a body $\mathcal{B}$. The symbol $\boxplus$ will be used throughout the present work to denote a finite element approximation.

Energy measures Scalar energy measures will be denoted with script style capital letters, such as the kinetic energy

$$\mathscr{K} = \frac{1}{2}\int_{\mathcal{B}} \dot{\boldsymbol{\varphi}} \cdot \dot{\boldsymbol{\varphi}} \varrho \,\mathrm{d}v$$

of a body $\mathcal{B}$ moving with the spatial velocity $\dot{\boldsymbol{\varphi}}$.

Configurations In the context of continuum mechanics, the formulations to describe the change in state a body is undergoing, are based on its initial or, opposing, its deformed state, and are commonly referred to as *Lagrange's formulation* if parametrised based on the reference configuration of a body and *Euler's description* if parametrised based on the spatial configuration[1] of a continuum, respectively. In the present context, we will use small letters to refer to quantities settled in a spatial, or deformed configuration, and capital letters to refer to quantities settled in an initial, or reference state. Therefore, a material point of a body $\mathcal{B}$ will transform from its initial position $\boldsymbol{X}$ to its spatial state $\boldsymbol{x}$ while being exposed to a change of time.

List of symbols An overview of the symbols used in this thesis is displayed on the following pages, organised in categories and beginning with general quantities that are used throughout every chapter. However, the categories used do not entirely reflect the chapters of this thesis but are chosen to cover the general topics used in the progress of this thesis. Furthermore, every category list is organised alphabetically, including both Latin and Greek characters. Prefixes to symbols such as Δ or ∂ will not be considered in the alphabetical ordering.

---

[1] Interestingly, Truesdell states in [96], that the Lagrange formulation was initially formulated by Euler, whereas the Euler description was introduced by D'Alembert.

General quantities

$\mathcal{B}$	body domain
$\mathcal{B}_0$	reference / initial body domain
$\partial\mathcal{B}$	boundary of a body $\mathcal{B}$
$\boldsymbol{e}_\bullet$	unit base vector for direction $\bullet$
i, j, k, l	counting indices
$\boldsymbol{I}$	second order unit tensor
$n_\bullet$	number of $\bullet$
$\boldsymbol{n}$	normal vector
Ω	domain
$\Omega_\bullet$	subdomain of with respect to $\bullet$
σ_{vM}	von Mises equivalent stress
t	time
$t_\bullet$	time step $\bullet$
Δt	time increment
ΔT	total simulation time
θ	temperature
θ_0	reference temperature
$\overline{\theta}_{\text{cl}}$	averaged coolant temperature
θ_k	temperature of node k
θ_{m}	melting temperature
θ_{S}	surface temperature
u	displacement magnitude
u_{std}	steady-state displacement magnitude
$\boldsymbol{u}$	displacement vector

Energy measures

$\mathscr{E}$	internal energy
$\mathscr{D}$	dissipation
$\mathscr{D}_{\text{mech}}$	mechanical dissipation
$\mathscr{D}_{\text{therm}}$	thermal dissipation
$\mathscr{K}$	kinetic energy
$\mathscr{P}_{\text{ext}}$	external mechanical power
$\mathscr{Q}$	thermal energy
$\mathscr{Q}_{\text{ext}}$	external thermal energy supply
$\mathscr{R}_{\text{ext}}$	rate input of entropy
$\mathscr{S}$	entropy
$\mathscr{W}$	work
ψ	Helmholtz free energy densitiy

Process kinematics quantities

$a_{\text{e,eff}}$	effective radial stock removal
$a_{\text{e,tot}}$	total radial stock removal
$a_{\text{ed,tot}}$	dressing stock removal
a_{f}	axial tool feed
$a_{\text{p,eff}}$	effective axial roughing zone engagement length
$d_{\text{s,eff}}$	effective grinding wheel outer diameter
d_{tool}	tool outer diameter
d_{wp}	(initial) workpiece diameter
γ_{s}	single grain rake angle
h^{s}_{cu}	single grain undeformed chip thickness
l_{ca}	axial contact zone length
l_{cc}	circumferential contact zone length
l_{fz}	axial length of finishing zone
l_{rz}	axial length of roughing zone
l_{wp}	(axial) workpiece length
Δl_{dex}	lateral dexel resolution
n_{s}	tool revolutions per unit time
n_{w}	workpiece revolutions per unit time
Q_{w}	material removal rate
Q'_{w}	specific material removal rate
Q^{s}_{w}	single grain material removal rate
r^{i}	inner radius
r^{i}_0	initial inner radius
$r^{\text{i}}_{\text{nom}}$	nominal inner radius
r_{tool}	tool effective outer radius
v_{fa}	tool axial feed velocity
v_{s}	tool circumferential velocity
v_{w}	workpiece circumferential velocity
$\boldsymbol{v}_{\text{fa}}$	tool axial feed velocity vector
$\boldsymbol{v}_{\text{s}}$	tool circumferential velocity vector
$\boldsymbol{v}_{\text{w}}$	workpiece circumferential velocity vector
$\Delta V^{\text{s}}_{\text{chip}}$	single grain chip volume
χ	tool roughing zone angle

Continuum thermomechanics

$\boldsymbol{b}$	body force vector
c	heat capacity / specific heat
$\boldsymbol{d}$	symmetric part of spatial velocity gradient
$\mathrm{d}a$	referential area element
$\mathrm{d}A$	spatial area element
$\mathrm{d}v$	spatial volume element
$\mathrm{d}V$	referential volume element
e	internal energy density
ε	total (logarithmic) strain
ε_{e}	elastic part of total strain
ε_{p}	plastic part of total strain
$\boldsymbol{E}$	Green-Lagrange strain tensor
$\boldsymbol{\mathcal{F}}$	general deformation measure
$\boldsymbol{F}$	deformation gradient
$\boldsymbol{F}_{\mathrm{e}}$	elastic part of deformation gradient
$\boldsymbol{F}_{\mathrm{p}}$	plastic part of deformation gradient
$\boldsymbol{\varphi}$	mapping operator / spatial position vector
$\dot{\boldsymbol{\varphi}}$	velocity
J	Jacobian determinant
$\boldsymbol{k}$	internal variable vector
$\boldsymbol{\kappa}$	internal variable driving force
λ	isotropic thermal conductivity
$\boldsymbol{\lambda}$	general thermal conductivity
m	mass
$\nabla_{\boldsymbol{X}}$	referential nabla operator
$\nabla_{\boldsymbol{x}}$	spatial nabla operator
$\boldsymbol{P}$	Piola stress tensor
q_m	mass specific heat energy
$\boldsymbol{q}$	spatial heat flux vector
$\boldsymbol{Q}$	referential heat flux vectors
r	heat source density
ϱ	mass density
ϱ_0	referential mass density
s	entropy density
$\boldsymbol{S}$	Piola-Kirchhoff stress tensor
$\boldsymbol{\mathcal{S}}$	general stress tensor
$\boldsymbol{\sigma}$	Cauchy stress tensor
$\boldsymbol{t}$	traction vector
$\boldsymbol{X}$	referential point position
$\boldsymbol{x}$	spatial point position

Finite element implementation

$\boldsymbol{a}$	vector of coefficients
α	single grain flank face angle
α_0	thermal expansion coefficient
d	damage internal variable
$\overline{d}$	saturated damage value
$\partial\mathcal{B}^{\mathrm{c}}$	boundary contact surface
$\boldsymbol{e}_{\vartheta}$	estimated error of variable ϑ
$\varepsilon_{\mathrm{p}}^{d}$	damage threshold plastic strain
$\dot{\varepsilon}_{\mathrm{p},0}$	reference strain rate
η	inelastic heat fraction
F_{n}	normal force magnitude
F_{t}	tangential force magnitude
$\boldsymbol{F}_{\mathrm{c}}$	cutting force vector
h	local element size
$\overline{h}$	refined local element size
h_{gr}	single grain total height
h_{wp}	single grain remaining workpiece height
l_{wf}	wear flat area length
λ_0	1st Lamé parameter
$\hat{\lambda}$	effective 1st Lamé parameter
λ^{wp}	thermal conductivity
$L_{\mathcal{E}}$	characteristic element length
μ_0	2nd Lamé parameter
$\hat{\mu}$	effective 2nd Lamé parameter
ν	Poisson's ratio
$\mathcal{N}_{\boldsymbol{x}}$	neighbourhood / element patch surrounding node $\boldsymbol{x}$
Ω^{ref}	reference volume / domain
p	polynomial degree
$\boldsymbol{p}$	vector of polynomial contributions
$P(\boldsymbol{x}, \boldsymbol{a})$	polynomial function
$\mathscr{P}_{\mathrm{therm}}$	thermal power
$\mathcal{P}_{\mathrm{meso}}$	meso-scale parameter tuple
$\mathcal{P}_{\mathrm{meso}}^{\mathrm{ext}}$	extended meso-scale parameter tuple
$\mathcal{Q}$	volume-specific heat
$\bar{\mathcal{Q}}$	normalised heat
$\overline{\mathscr{Q}}$	linearised heat energy

Finite element implementation (cont.)

$\mathscr{Q}^{\mathrm{FE}}$	heat energy in terms of finite element approximation
$\mathscr{Q}_{\mathrm{tot}}$	total heat energy
Δr	internal heat source increment
$\boldsymbol{\sigma}_{\mathrm{dev}}$	deviatoric part of Cauchy stress tensor
σ_{y}	yield stress
$\sigma_{\mathrm{y}}^{\mathrm{JC}}$	Johnson and Cook yield stress
τ	absolute shear stress
ϑ_d	damage saturation rate
$\boldsymbol{\vartheta}$	arbitrary field variable
$\widehat{\boldsymbol{\vartheta}}$	recovered value of ϑ
$\boldsymbol{x}_k^{\mathrm{GP}}$	integration point k
V_i	Volume of element i
$\dot{\xi}$	incremental contact surface slip
Δz_{ps}	plane strain thickness

Topography analysis quantities

η_{thr}	grain volume filter threshold
$E(\bullet)$	error function
$F(\bullet)$	roughness function
g	grain index
γ	grain rake angle
j	height level index
$\mathsf{P}_j^{\mathrm{ref}}$	reference plane
$\boldsymbol{v}_{\mathrm{s}}$	single grain velocity vector
V_g	volume of grain with index g
$\overline{V}_\Omega$	average volume of all grain in domain Ω
$\boldsymbol{x}$	data point position
$\bar{z}(\boldsymbol{x})$	interpolated data point vertical height
$\check{z}_j$	maximum grain count height value at height level j
z_j^{ref}	reference height value of height index j
$\hat{z}_g$	maximum height value of grain with index g

Scale-bridging quantities

$\boldsymbol{a}$	vector of coefficients a_i
A	area of Voronoi cell
$f(\bullet)$	frequency distribution of $\bullet$
$\overline{F}_\bullet^{\mathrm{bl}}$	bi-linear force regression approach for component $\bullet = \mathrm{n}, \mathrm{t}$
$\overline{F}_\bullet^{\mathrm{exp}}$	exponential force regression approach for component $\bullet = \mathrm{n}, \mathrm{t}$
$F_\bullet^{\mathrm{avg}}$	averaged force component magnitude for component $\bullet = \mathrm{n}, \mathrm{t}$
$\tilde{F}_\bullet$	computed macroscopic force magnitude for component $\bullet = \mathrm{n}, \mathrm{t}$
$\overline{r}^{\mathrm{bq}}$	bi-quadratic heat regression approach
$\overline{r}^{\mathrm{exp}}$	exponential heat regression approach
$\tilde{r}$	macroscopic heat power
$\langle \tilde{r} \rangle$	averaged macroscopic heat power
R^2_{bq}	squared error of bi-quadratic approach
R^2_{exp}	squared error of exponential approach
w_i	weight of Voronoi cell i
Δz_{ps}	plane strain thickness
$\Delta \bar{z}$	kinematic simulation grain engagement width

Process model

α_{cool}	heat transfer coefficient for cooling
$\mathcal{B}$	workpiece domain
$\mathcal{B}_n$	workpiece domain at time t_n
$\mathcal{B}_0$	reference workpiece domain
$\mathcal{B}^{\mathrm{fin}}$	final workpiece body domain
${}^{0}\mathcal{B}^{\mathrm{cool}}$	workpiece reference configuration of cooling model
$\mathcal{B}_0^{\mathrm{init}}$	initial workpiece body domain / reference configuration
${}^{\checkmark}\mathcal{B}_n^{\mathrm{init}}$	last converged state (spatial configuration) of initial workpiece model at time t_n
${}^{\checkmark}\mathcal{B}^{\bullet}_{n-1}$	converged state (spatial configuration) of workpiece prior to time t_n
${}^{0}\mathcal{B}_n^{\mathrm{abr}}$	reference configuration of abrasive workpiece model at time t_n
$\Delta\mathcal{B}$	removed workpiece domain
$\Delta\overline{\mathcal{B}}_n$	removed workpiece domain (area in axisymmetric case) at time t_n
$\Delta\overline{\mathcal{B}}_n^{\mathrm{nom}}$	nominal removed workpiece domain (area in axisymmetric case) at time t_n
$\partial\mathcal{B}$	workpiece boundary
$\partial\mathcal{B}^{\boldsymbol{q}}$	workpiece boundary loaded with heat flux
$\partial\mathcal{B}^{\boldsymbol{u}}$	workpiece boundary with prescribed displacement
$\partial\mathcal{B}^{\boldsymbol{u}}_{\mathrm{en}}$	workpiece boundary with prescribed displacement at tool entry side
$\partial\mathcal{B}^{\boldsymbol{u}}_{\mathrm{ex}}$	workpiece boundary with prescribed displacement at tool exit side
$\partial\mathcal{B}^{\mathcal{L}}$	workpiece inner load surface
$\partial{}^{0}\mathcal{B}_n^{\mathrm{abr}}$	workpiece boundary reference
$\partial{}^{\checkmark}\mathcal{B}_n^{\mathrm{abr}}$	boundary of converged state (spatial configuration) of abrasive workpiece model at time t_n
$\mathcal{C}$	general set of constraints
$\mathcal{D}$	Dirichlet boundary conditions
$\mathcal{D}^{\mathrm{cl}}$	Dirichlet boundary conditions representing clamping
$\mathcal{E}_k$	domain of finite element k
F_{tot}	total clamping force
F_{pre}	maximum bolt pre-load force
$\mathcal{F}_{\mathrm{env}}$	envelope function
$\mathcal{F}_{\mathrm{fin}}$	function to compute $\boldsymbol{x}^{\mathrm{fin}}$
$\mathcal{G}$	tool domain
$\partial\mathcal{G}$	tool domain boundary
$\boldsymbol{k}_k$	set of internal variables for element k
$\mathcal{L}$	thermo-mechanical load compound
μ_{con}	Coulomb friction coefficient
M	mesh mapping operator
$\mathcal{N}$	Neumann boundary conditions
q_0	heat flux magnitude
$\overline{q}$	axisymmetric heat flux magnitude
$\boldsymbol{q}_{\mathrm{conv}}$	convective heat flux vector
$\Delta r^{\bullet}$	radial error with respect to variable $\bullet$
$\Delta\overline{r}$	averaged measured radial error
$\overline{\sigma}^{\mathrm{cl}}$	averaged clamping pressure / stress magnitude
$\overline{\sigma}_z^{\mathrm{cov}}$	axial cover bolt stress magnitude
$\overline{\sigma}^{\mathrm{cl}}_{\mathrm{max}}$	maximum averaged clamping pressure / stress magnitude
$\hat{t}_{\mathrm{tc}\bullet}$	time of maximum temperature of thermocouple $\bullet$
Δt_{a}	axial contact zone passing time interval
Δt_{c}	circumferential contact zone passing time interval
$\mathcal{P}$	set of process parameters
$\hat{\mathcal{P}}$	modified set of process parameters
$\mathfrak{R}_{\Delta}$	general residual function
$\mathfrak{R}^2_{\Delta}$	L^2-based residual function

Process model (continued)

${}^{0}\boldsymbol{\sigma}_{k}^{\mathrm{wp}}$	initial stress tensor of workpiece element k
$\boldsymbol{\sigma}_{\mathrm{res}}$	residual stress tensor
$t_{\mathrm{max}}^{\mathrm{grd}}$	maximum grinding time
${}^{0}\theta_{k}^{\mathrm{wp}}$	initial temperature of workpiece element k
$\mathcal{T}$	tool trajectory
$\Delta\mathcal{T}$	tool trajectory correction
$\Delta\mathcal{T}^{\mathrm{exp}}$	experimental tool trajectory correction
$\Delta\mathcal{T}^{\mathrm{int}}$	integral tool trajectory correction
$\Delta\mathcal{T}^{\mathrm{inv}}$	inverted tool trajectory correction
u_r	radial displacement magnitude
u_r^{cl}	radial displacement magnitude of clamping cover contact surface
u_r^{max}	maximum radial displacement magnitude
u_z^{cl}	axial displacement magnitude of clamping cover contact surface
u_z^{cov}	axial displacement magnitude of clamping cover bolt surface
u_z^{max}	maximum axial displacement magnitude
$\boldsymbol{u}^{\mathrm{cl}}$	displacement representing clamping
$\boldsymbol{x}^{\mathrm{fin}}$	final spatial node placements
$\boldsymbol{x}^{\mathrm{nom}}$	nominal spatial node placements
$\boldsymbol{x}_k$	spatial placement of node k
$\boldsymbol{x}_{\mathrm{vr}}^{\mathcal{G}}$	tool singularity vertex placement
$\boldsymbol{X}_k$	reference placement of node k
$\mathsf{Y}_0^{\mathrm{cl}}$	initial yield stress of clamping cover material

1 Introduction

The present thesis is based on research that is carried out in the context of the German collaborative project framework *Priority Program SPP 1480*. To be precise, the Institute of Mechanics (IM) and the Institute of Machining Technology (ISF) in this framework process the sub-project entitled

Modelling and simulation of Internal Traverse Grinding – from
micro-thermo-mechanical mechanisms to process models

which constitutes a cooperative research on the corresponding topic, carried out at TU Dortmund University. Hence, there will be several references to work carried out by the ISF, as well as figures by courtesy of the same institute. According to the respective research focuses of both institutes involved, the ISF mainly contributes experimental outcome while the author of this thesis as a researcher of the IM predominantly is responsible for the development of modelling and simulation methods. In this context, the present thesis presents the advance of different simulation approaches and numerical methods to further develop the simulation of grinding processes. Since the underlying physics of grinding cover a broad range of scales, respective simulation methods on different scales, ranging from small to large, are invoked and presented in the respective order. The chapters of this thesis broadly represent the chronological evolution of the research carried out during the last five years—a detailed outline is given in Section 1.2 at the end of the present chapter.

1.1 Motivation and state of the art

Grinding processes typically constitute the final step of a production line in terms of finishing a functional—usually hardened or heat-treated—workpiece surface, hence requiring high precision at lowest desirable failure rates. Examples for these hard-finishing tasks are the internal finishing of a gear wheel bore or the internal manufacturing of bearing rings. Since improvement of the economic process efficiency is also demanded, high performance grinding processes with material removal rates similar to those of hard-turning are utilised to accomplish the above-mentioned task. High-performance grinding with electroplated wheels constitutes a very promising manufacturing process, which is potentially capable of combining both hard-turning and grinding in one single finishing process. Caused by permanently rising computational capabilities and corresponding expertise, the modelling and simulation of manufacturing processes nowadays incorporates a general requirement for the supporting evolution of the latter. This work therefore targets at progressing the current state of the art in the context of modelling and simulation of grinding processes and thermo-mechanical effects connected to this field of research.

1.1.1 Internal Traverse Grinding

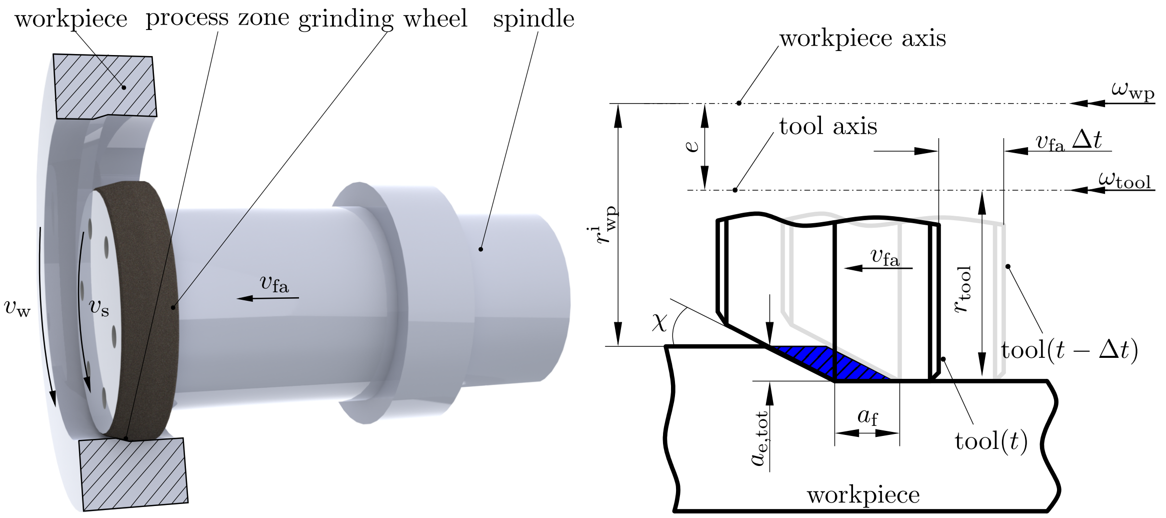
workpiece
process zone
grinding wheel
spindle
v_w
v_s
v_fa
workpiece axis
ω_wp
tool axis
$v_\mathrm{fa}\,\Delta t$
ω_tool
e
r^i_wp
v_fa
r_tool
χ
tool($t-\Delta t$)
$a_\mathrm{e,tot}$
a_f
tool(t)
workpiece

Figure 1.1: Process scheme of internal traverse grinding. Left: Macro-scale process kinematics. Right: Cross section of ITG process zone, showing workpiece and grinding wheel (tool) at times t (black stroke) and $t-\Delta t$ (light grey stroke). The blue hatched area represents the amount of material being removed during a workpiece revolution Δt. The stock removal $a_\mathrm{e,tot}$ is given by workpiece and tool radii r^i_wp and $r^\mathrm{i}_\mathrm{tool}$ in combination with the axes' eccentricity e. The tool angle is denoted by χ. Both workpiece and tool revolve with angular velocities ω_wp and ω_tool. The tool simultaneously moves axially with the axial feed velocity v_fa resulting in an axial feed $a_\mathrm{f} = v_\mathrm{fa}\,\Delta t$ per time step Δt or revolution, respectively. Adopted from [37].

Internal Traverse Grinding (ITG) with electroplated electroplated cubic Boron Nitride (cBN) wheels has proven to be capable of the demanding above-mentioned requirements in the context of internal hard-finishing. In fact, a surface roughness of $R_z = 2\,\mu\mathrm{m}$ at a material removal rate of $100\,\mathrm{mm}^3/\mathrm{s}$ is achievable, cf. [65, 66]. The key to this is a special grinding wheel geometry consisting of two separate zones, cf. Fig. 1.1. The roughing zone of the tool is conical and thus enables a high material removal rate, the finishing zone is cylindrical and optionally touch-dressed to finish the surface. In this way, a combined manufacturing process enabling both high material removal rate and superior surface integrity in just one stroke is designed.

One major drawback of ITG constitutes the high thermal load on the workpiece, causing geometrical errors of the finished part on the one hand, and unwanted phase transformations resulting in e.g. white layers on the workpiece surface, cf. [53] and Fig. 1.2 on the other hand.

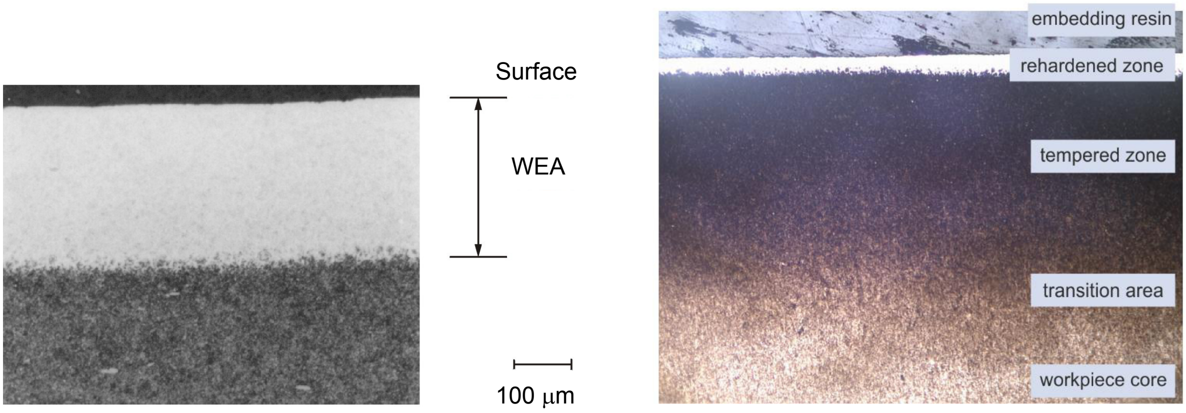

Figure 1.2: Left: White layer denoted as WEA on 100Cr6 taken from [53], where also chemical analyses of the white layer generated on 100Cr6 by grinding are discussed. Right: General influence zones of a ground workpiece, taken from [51]. The material depicted here is hardened and heat treated steel AISI 4140 (635 HV 0.3).

The fundamental kinematics of ITG with electroplated cBN grinding wheels are depicted in Fig. 1.1. The axes of tool and workpiece are arranged with a fixed eccentricity e, resulting in the radial stock removal $a_{\mathrm{e,tot}}$ of the process. During machining both tool and workpiece rotate with circumferential speeds v_{s} and v_{w} under the conditions $v_{\mathrm{w}} \ll v_{\mathrm{s}}$ and $\operatorname{sgn}(v_{\mathrm{s}}) = \operatorname{sgn}(v_{\mathrm{w}})$. The grinding wheel is moved axially with a constant feed rate v_{fa} through the workpiece, removing the desired amount of material in one single pass. With this information at hand, the following process parameter correlations follow. Given the circumferential velocities v_{s} and v_{w} as well as the radii $r^{\mathrm{i}}_{\mathrm{tool}}$ and $r^{\mathrm{i}}_{\mathrm{wp}}$ of the tool and the workpiece, respectively, the rotational velocity magnitudes follow as

$$n_{\mathrm{s}} = \frac{v_{\mathrm{s}}}{2\,\pi\,r_{\mathrm{tool}}} \qquad \text{and} \qquad \omega_{\mathrm{tool}} = \frac{v_{\mathrm{s}}}{r_{\mathrm{tool}}} \tag{1.1}$$

for the tool as well as

$$n_{\mathrm{w}} = \frac{v_{\mathrm{w}}}{2\,\pi\,r^{\mathrm{i}}_{\mathrm{wp}}} \qquad \text{and} \qquad \omega_{\mathrm{wp}} = \frac{v_{\mathrm{w}}}{r^{\mathrm{i}}_{\mathrm{wp}}} \tag{1.2}$$

for the workpiece, respectively. Taking furthermore the given axial feed a_{f} into account, the axial feed velocity simply takes the form

$$v_{\mathrm{fa}} = n_{\mathrm{w}}\,a_{\mathrm{f}}, \tag{1.3}$$

which establishes the relation between circumferential and axial motion.

The high material removal rate of ITG is enabled by using a single layer of electroplated cBN abrasives, characterised by a high grain protrusion up to approximately 50 % of the nominal grain diameter which in turn results in large chip space and thus enables a highly efficient chip formation process, compare [66]. Due to the process kinematics depicted in Fig. 1.1, ITG is characterised by a small tool-workpiece contact zone in comparison to other grinding processes, leading to small process forces but resulting in a highly concentrated thermal load on the workpiece and the above-mentioned problems, though. More detailed information about ITG, its inherent accuracy and tool wear behaviour as well as the comparison to alternative hard-machining processes can be found in [64–66] and references cited therein.

1.1.1.1 Fundamental experiments and results

To present a basic insight on the process-scale thermo-mechanical response of ITG, the present section outlines experimental findings resulting from a grinding wheel circumferential speed variation. In this regard, experiments are carried out using the experimental setup described in the following, while applying fixed process parameters shown in Tab. 1.1 and varied parameters depicted in Tab. 4.1. The basic experimental setup used

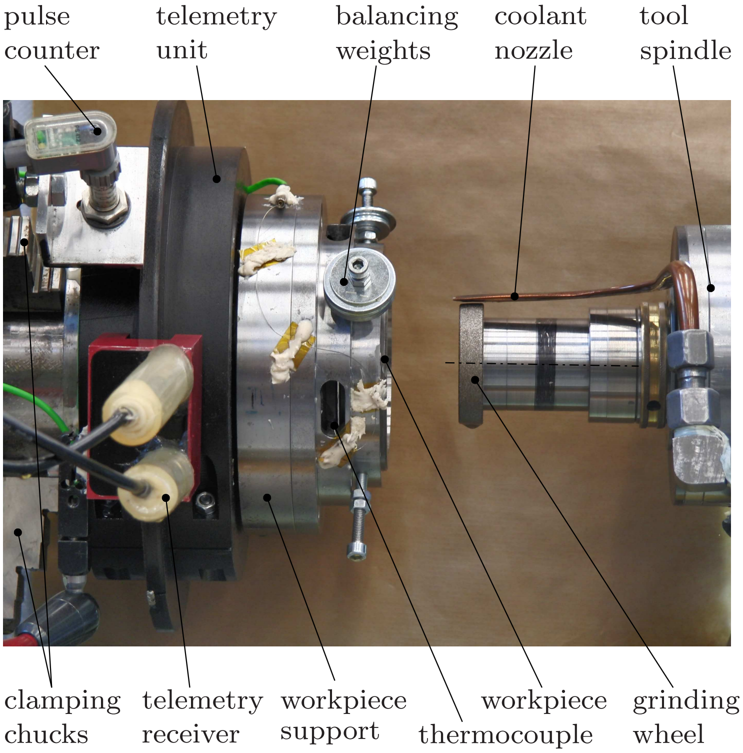
pulse counter
telemetry unit
balancing weights
coolant nozzle
tool spindle
clamping chucks
telemetry receiver
workpiece support
workpiece thermocouple
grinding wheel

Figure 1.3: Experimental setup taken from [37].

Table 1.1: Fixed process parameters for an exemplary experimental setup.

description	parameter	value	unit
workpiece circumferential velocity	v_{w}	2	m/s
axial tool feed	a_{f}	0.7	mm/rev
radial stock removal	$a_{\mathrm{e,tot}}$	0.1	mm
stock removal rate	Q_{w}	140.4	mm^3/s
roughing zone angle	χ	5	°
workpiece outer radius	r_{wp}	45	mm
workpiece inner radius	$r^{\mathrm{i}}_{\mathrm{wp}}$	32.5	mm
workpiece axial length	l_{wp}	20	mm
tool effective outer radius	r_{tool}	26.2	mm

in this context, excluding the grinding machine itself is depicted in Fig. 1.3, showing the workpiece attached to the clamping device on the left hand side. The figure also displays the tool spindle with mounted grinding wheel and coolant supply on the right hand side; for detailed information cf. [36]. Throughout the entire scope of this thesis, the workpiece consists of 100Cr6/AISI 52100 which is hardened to approximately 61–63 HRC. For the first fundamental investigations, the workpiece has a simple cylindrical shape with dimensions according to Tab. 1.1. The grinding wheel is, in this series of experiments, not touch dressed to exclude this influence from the examination of the thermal load on the workpiece. To record the temperature rise in the workpiece, one single thermocouple is soldered into an eroded hole of the workpiece in proximity (approximately 1 mm) to the surface being ground during the abrasive process. The thermocouple signal is transmitted to the stationary measurement equipment via a telemetry unit. The mechanical loads on the workpiece are captured by a force dynamometer platform onto which the tool spindle is mounted.

Figure 1.4 shows the experimental results for the variation of the grinding wheel circumferential velocity v_{s}. The process force components F_{t} and F_{n} decrease, whereas the temperature of the contact zone—calculated by the ISF via a heat conduction post-processing based on the temperature measurements, cf. [36, 84]—increases with rising grinding wheel circumferential velocity v_{s}. This tendency conveniently correlates with the following machining strategies.

In order to increase the efficiency of the process under consideration, the range of high performance grinding with cutting speeds exceeding 80 m/s is incorporated: With higher grinding wheel circumferential speed v_{s}—at constant material removal rate Q_w—the material removal is distributed among more grains and thus results in a decreasing chip thickness of one single grain being in contact with the workpiece material. A positive effect of this manufacturing strategy is that this decreasing chip thickness results in lower cutting forces and in turn smaller oscillation of the machine as well as in reduced tool wear, subsequently. Furthermore, the roughness of the resulting surface decreases, too

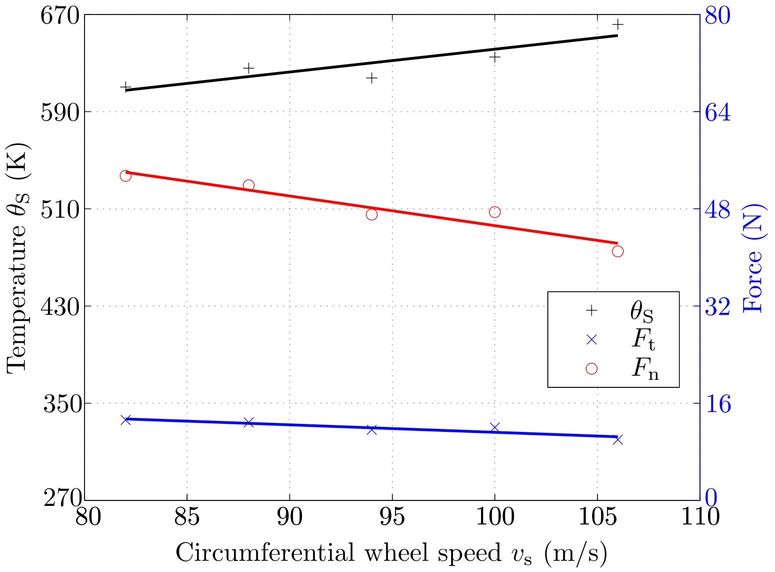

Figure 1.4: Postprocessed surface temperature θ_S and process forces in tangential and normal direction F_t and F_n resulting from the variation of the circumferential speed v_s of the grinding wheel. As forecasted, cutting forces develop contrary to the rising heat induction with increasing wheel speed. Data by courtesy of ISF, taken from [37].

[95]. The major disadvantage of this strategy though arises from the increasing area of frictional contact surfaces between cBN grains and workpiece material as well as the increasing amount of plastically deformed material. These two effects – friction and plastic dissipation – induce an increase in the overall heat generation of the grinding process, as stated in figure 1.4.

In the context of an introductory insight, this shall constitute a sufficient volume of quantitative experimental results. For further information on this topic, refer to the works of Schumann et al. [84, 85] and Holtermann et al. [37].

To furthermore give a brief insight on the meso-scale chip formation and the resulting surface states after applying ITG with altered process conditions according to Tab. 6.1, Figures 1.5, 1.6 and 1.7 can be referred to. These figures are based on a more complex workpiece geometry in combination with higher-performance process parameters. The altered geometries of workpiece, tool and clamping device are displayed in terms of drafts in Figures 1.8 to 1.10 and will later be of particular importance in the scope of compensation strategy development, see Chap. 6.

1.1.2 Modelling and simulation of grinding

Due to the stochastic nature of the process, the modelling and simulation of grinding is by far not as well-investigated—nor developed—as the simulation of machining processes with geometrically defined cutting edge, such as turning or milling. This is mainly caused by the complex material removal mechanism where numerous grains are

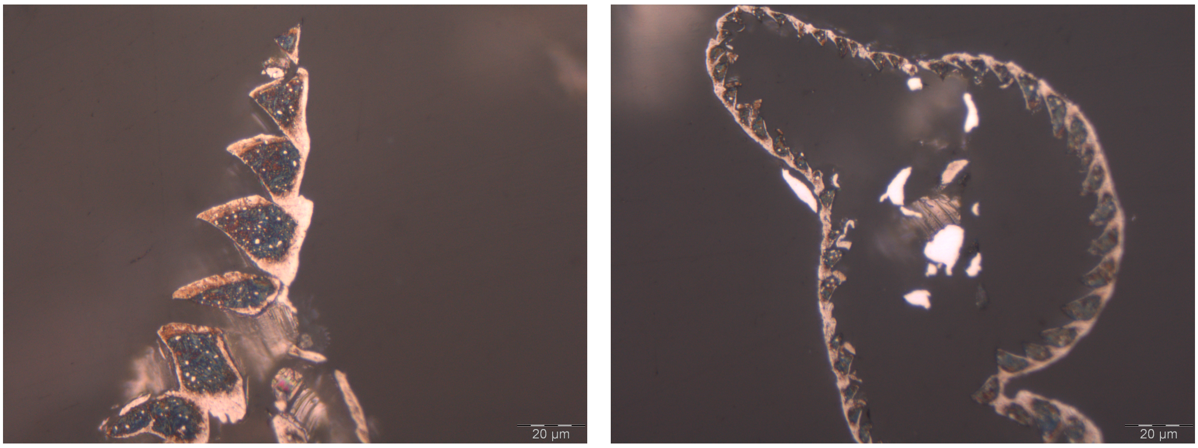

Figure 1.5: Microsections of ITG chips, cast in resin and subsequently etched. Courtesy of ISF.

engaging with the workpiece simultaneously, while, on top, transiently influencing each other. Moreover, the geometry of the abrasive grit is at first not certainly known and in addition very complex—most of the active cutting edges evince very large negative rake angles. Certainly, if we look at an electroplated grinding wheel on a sufficiently microscopic scale, see Fig. 1.11, we can examine a well-defined geometry—which on the other hand is only valid for this unique grinding wheel examined and therefore not usable in a general sense. This circumstance again proves the stochastic characteristics of grinding processes and the incredibly complex abrasive grit structure. Last, but not least, the complex grinding wheel topography complicates the modelling of a coolant liquid influence, which is usually applied in the regime of high-performance grinding. All these factors mentioned make grinding simulations a highly challenging task.

The current state of the art in modelling and simulation is comprehensively depicted in [5] and [6] in the context of machining processes in general, whereas in [28] and [19], the recent advances in modelling of grinding processes are focused on. Less recent grinding simulation approaches are assembled in [99].

As outlined by Brinksmeier et al. [19], cf. Fig. 1.12, the modelling and simulation of grinding processes can be categorised based on the scale, i.e. from macroscopic to microscopic, based on the modelling approach, such as empirical, physical or heuristic, respectively, or based on the field of application. Regarding the scale categorisation of the finite element analysis (denoted as FEA in the figure), this method is—at least in this classification—set to an intermediate position between macro- and micro-scale. However, the application on rather microscopic scales is commonly used and presented accordingly in [19].

Furthermore, Brinksmeier et al. [19, p. 675] state that “the microscopic simulation is the most detailed approach of the real grinding process to date”. However, the numerical cost increases with the chosen level of modelling detail, making e.g. molecular dynamics a very precise, but in practice not usable method for large scale simulations of grinding

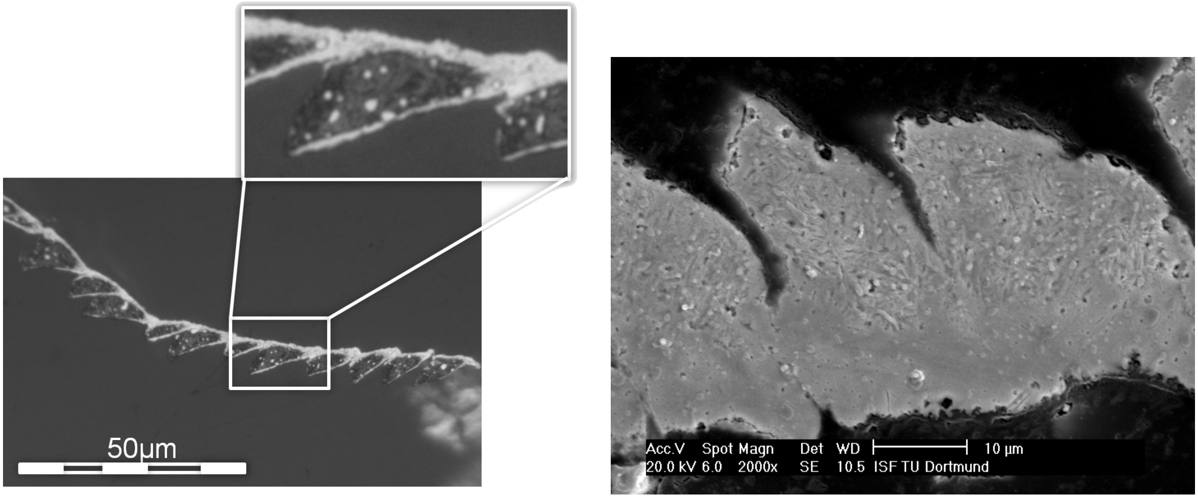
50µm
Acc.V Spot Magn Det WD 10 µm
20.0 kV 6.0 2000x SE 10.5 ISF TU Dortmund

Figure 1.6: Left: Etched and ground chip obtained from experiments carried out at the ISF. The white areas imply regions of austenite-martensite phase transformations, commonly referred to as white layers. Taken from [83] with kind permission. Right: SEM microsection of ITG chip, cast in resin and subsequently etched. Courtesy of ISF.

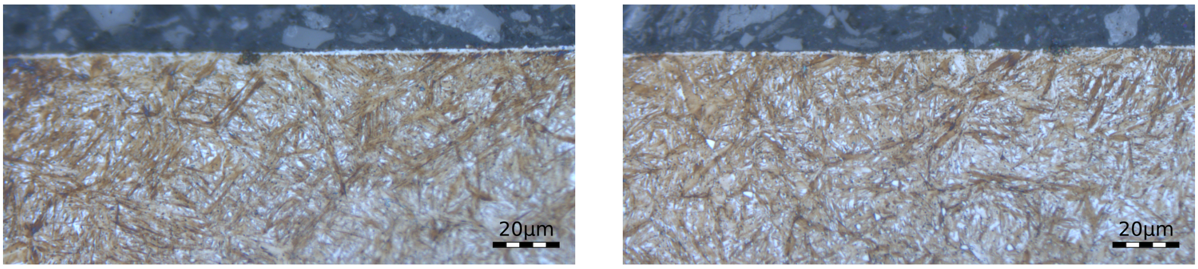

Figure 1.7: Etched workpiece cross-sections after grinding with process parameters shown in Tab. 6.1. The slight white layers on the surface indicate areas of a dominating re-transformed martensite phase, which however prove to measure at maximum 1 µm in thickness. Courtesy of ISF.

processes. Thus, a method has to be developed, which incorporates a sufficient level of detail while maintaining low computational cost. This can for example be achieved by making use of hybrid modelling approaches as concluded as a future necessity by Arrazola et al. [6, p. 19]. We will revive these statements in the objective of this work, see Sec. 1.2.

After this rather outlining presentation of modelling approaches in grinding, we will take a closer look at the concerning approaches referred to earlier. We will roughly orientate the order of the following items on an increasing scale ranging from micro- to macroscopic.

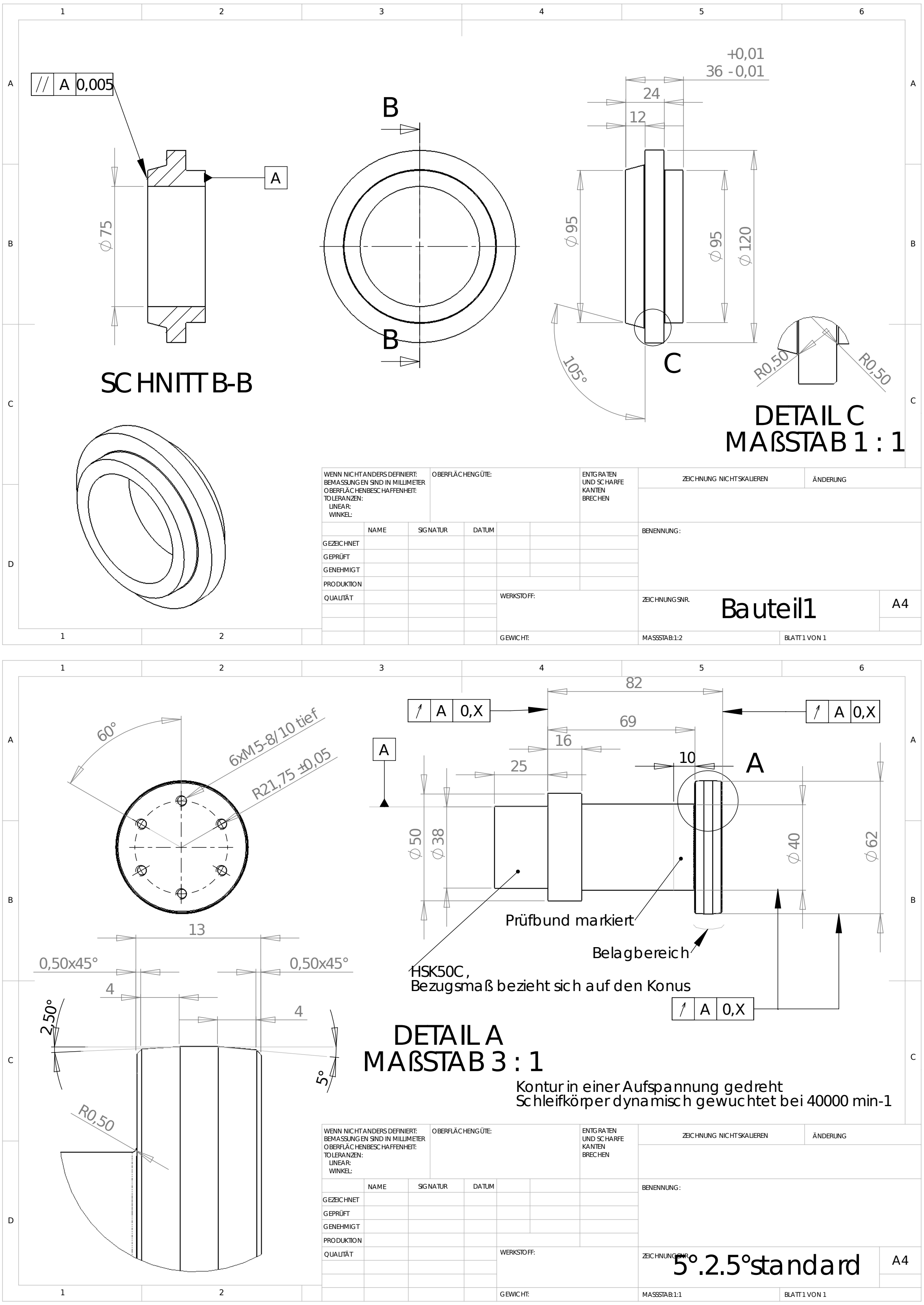
// A 0,005
A
B
B
SCHNITT B-B
⌀75
+0,01
36 -0,01
24
12
⌀95
⌀95
⌀120
105°
C
R0,50
R0,50
DETAIL C
MAßSTAB 1 : 1
WENN NICHT ANDERS DEFINIERT: BEMASSUNGEN SIND IN MILLIMETER OBERFLÄCHENBESCHAFFENHEIT: TOLERANZEN: LINEAR: WINKEL:
OBERFLÄCHENGÜTE:
ENTGRATEN UND SCHARFE KANTEN BRECHEN
ZEICHNUNG NICHT SKALIEREN
ÄNDERUNG
NAME
SIGNATUR
DATUM
BENENNUNG:
GEZEICHNET
GEPRÜFT
GENEHMIGT
PRODUKTION
QUALITÄT
WERKSTOFF:
ZEICHNUNGSNR.
Bauteil1
A4
GEWICHT:
MASSSTAB:1:2
BLATT 1 VON 1
60°
6xM5-8/10 tief
R21,75 ±0,05
A
↗ A 0,X
↗ A 0,X
82
69
16
25
10
A
⌀50
⌀38
⌀40
⌀62
Prüfbund markiert
Belagbereich
HSK50C,
Bezugsmaß bezieht sich auf den Konus
↗ A 0,X
13
0,50x45°
0,50x45°
4
4
2,50°
5°
R0,50
DETAIL A
MAßSTAB 3 : 1
Kontur in einer Aufspannung gedreht
Schleifkörper dynamisch gewuchtet bei 40000 min-1
5°.2.5°standard
A4
MASSSTAB:1:1
BLATT 1 VON 1
1
2
3
4
5
6
A
B
C
D

Figure 1.8: Drawings of the more complex workpiece (top) and tool (bottom) used in this thesis. Courtesy of ISF.

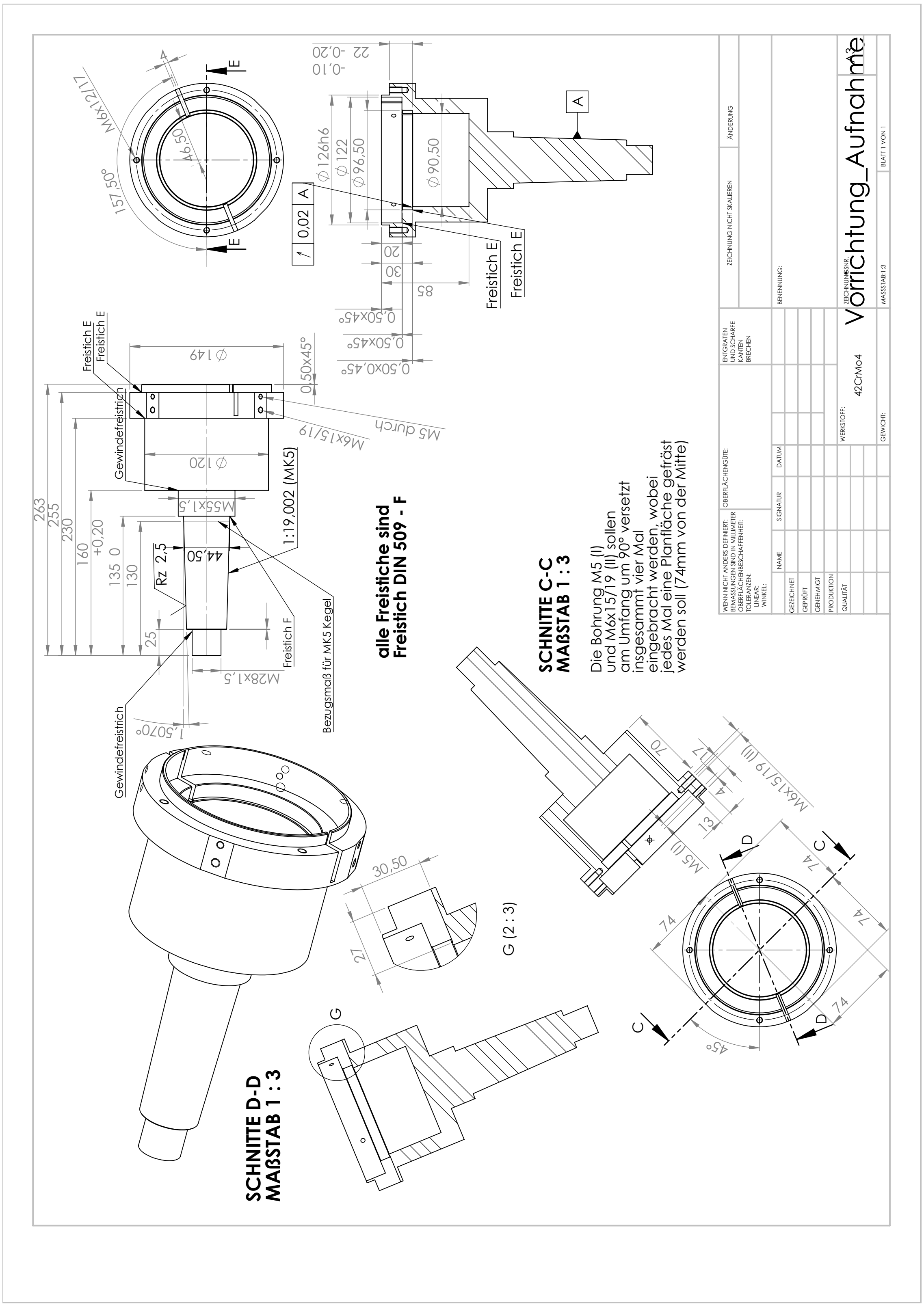
Vorrichtung_Aufnahme
42CrMo4
SCHNITTE C-C
MAßSTAB 1 : 3
SCHNITTE D-D
MAßSTAB 1 : 3
alle Freistiche sind
Freistich DIN 509 - F
Die Bohrung M5 (I)
und M6x15/19 (II) sollen
am Umfang um 90° versetzt
insgesammt vier Mal
eingebracht werden, wobei
jedes Mal eine Planfläche gefräst
werden soll (74mm von der Mitte)
G (2 : 3)
G
Freistich E
Freistich F
Gewindefreistrich
Bezugsmaß für MK5 Kegel
1:19,002 (MK5)
M55x1,5
M28x1,5
M6x15/19
M5 durch
M6x12/17
Rz 2,5
44,50
Ø 149
Ø 120
Ø 126h6
Ø 122
Ø 96,50
Ø 90,50
0,02 A
157,50°
A6,50
263
255
230
160
+0,20
135 0
130
25
1,5070°
0,50x45°
0,50x0,45°
22 -0,20 -0,10
20
30
85
70
17
4
13
30,50
27
74
45°
M5 (I)
M6x15/19 (II)
A
C
D
E

Figure 1.9: Drawing of the more complex clamping device that was used in conjunction with the work-piece depited in Fig. 1.8. Courtesy of ISF.

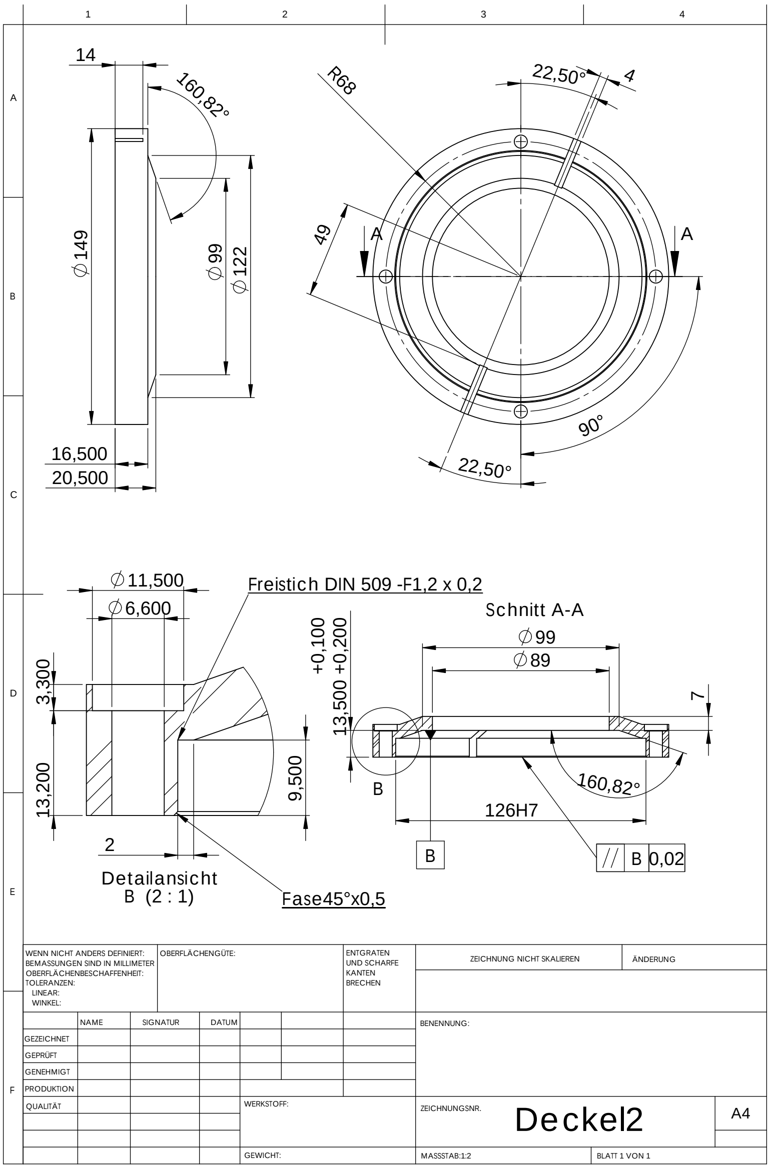
14
160,82°
∅149
∅99
∅122
16,500
20,500
R68
22,50°
4
49
A
A
90°
22,50°
∅11,500
∅6,600
Freistich DIN 509 -F1,2 x 0,2
3,300
13,200
9,500
2
Detailansicht
B (2 : 1)
Fase45°x0,5
+0,100
13,500 +0,200
Schnitt A-A
∅99
∅89
7
B
160,82°
126H7
B
// B 0,02
WENN NICHT ANDERS DEFINIERT: BEMASSUNGEN SIND IN MILLIMETER OBERFLÄCHENBESCHAFFENHEIT: TOLERANZEN: LINEAR: WINKEL:
OBERFLÄCHENGÜTE:
ENTGRATEN UND SCHARFE KANTEN BRECHEN
ZEICHNUNG NICHT SKALIEREN
ÄNDERUNG
NAME
SIGNATUR
DATUM
BENENNUNG:
GEZEICHNET
GEPRÜFT
GENEHMIGT
PRODUKTION
QUALITÄT
WERKSTOFF:
ZEICHNUNGSNR.
Deckel2
A4
GEWICHT:
MASSSTAB:1:2
BLATT 1 VON 1

Figure 1.10: Drawing of the clamping cover that corresponds to the clamping device depicted in the figure above. Courtesy of ISF.

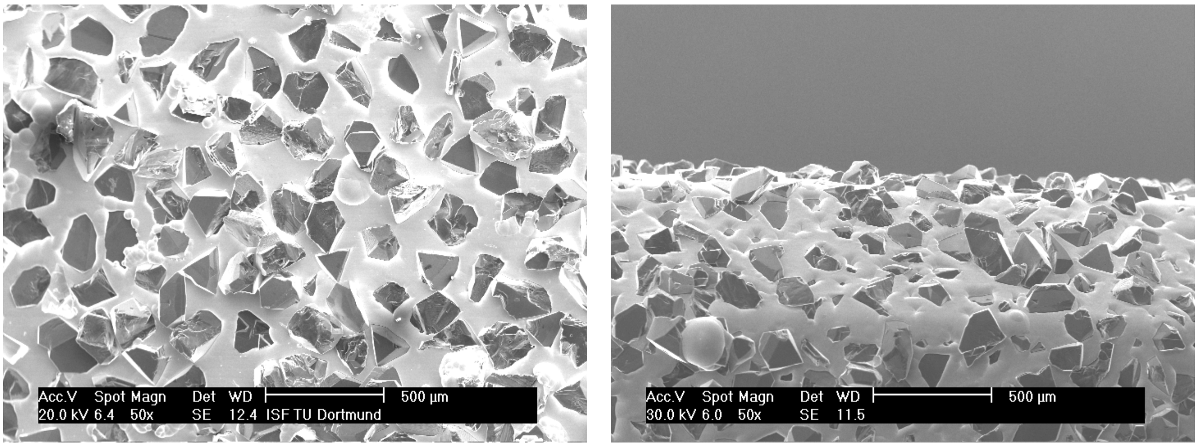
Acc.V Spot Magn Det WD 500 µm
20.0 kV 6.4 50x SE 12.4 ISF TU Dortmund
Acc.V Spot Magn Det WD 500 µm
30.0 kV 6.0 50x SE 11.5

Figure 1.11: SEM micrographs of a grinding wheel surface with single layer electroplated abrasive grit of grain size B181. Top view (left) and lateral perspective onto the edge of the wheel (right). Courtesy of ISF.

Molecular dynamics constitutes a very physical and highly detailed modelling approach of the process under consideration, as for example presented by Shimada et al. [88] or Brinksmeier and Rentsch [20]. Figure 1.13 depicts an exemplary simulation of this kind. Inter alia, this approach allows to capture the microstructure evolution of the workpiece material without having to use phenomenological assumptions, but on a very high computational cost. For this reason, it will not be considered as a modelling approach in the progress of this work.

Finite element analysis up to date constitutes a very commonly utilised method to simulate complex multi-physically coupled problems in a wide range of applications, cf. [5]. It therefore represents a promising method to model grinding processes on various scales, ranging from process-scale models focussing, e.g., on machine vibrations [25, 27] to micro-scale models simulating single grains interacting with the workpiece, cf. [3, 92]. Further recent examples on a smaller process scale simulate workpiece sections with finite elements and substitute the tool by moving heat sources or mechanical loads, see [81].

Lowering the scale towards the micro-scale again, Ljustina et al. [61] and Mohammed et al. [67], for example, apply a direct modelling of the workpiece microstructure evolution in terms of finite element machining simulations. One major concern that has to be dealt with when focusing on the cutting-edge–workpiece interaction in abrasive or machining processes is the generally occurring severe deformation of the finite element meshes. To account for this issue, mesh adaptivity methods have been established and successfully applied, cf. [40, 41]

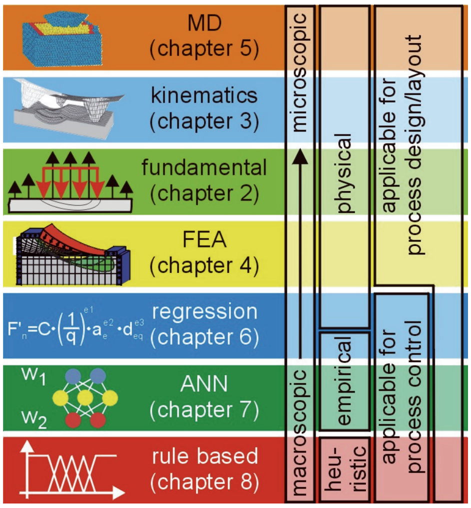
MD
(chapter 5)
kinematics
(chapter 3)
fundamental
(chapter 2)
FEA
(chapter 4)
$F'_n = C \cdot \left(\frac{1}{q}\right)^{e1} \cdot a_e^{e2} \cdot d_{eq}^{e3}$
regression
(chapter 6)
W1
W2
ANN
(chapter 7)
rule based
(chapter 8)
microscopic
macroscopic
physical
empirical
heu-
ristic
applicable for
process design/layout
applicable for
process control

Figure 1.12: Method classification with respect to modelling approaches applied to grinding according to Brinksmeier et al. [19]. Reprinted with kind permission.

Mesh-free methods constitute another promising methodology to overcome mesh-distortion and mesh-dependency in the context of machining processes. In this regard, Uhlmann et al. [100] present an application of the Finite Pointset Method in the regime of orthogonal cutting. Furthermore, Smoothed Particle Hydrodynamics can be used as another approach to this topic, see, e.g. [78].

Kinematic and geometric modelling and simulation approaches can be utilised to calculate a precise geometrical interaction between the grinding wheel and the workpiece in the time-domain. Kinematic simulations have been invoked to date by, e.g. Aurich and Kirsch [9]. The basic principle in this regime is a purely geometrical modelling approach that captures the kinematics of the process in high detail. The major drawback, however, is the missing thermal or mechanical response of the process simulated. In order to create a realistic grinding wheel model, the surface structure of the grinding wheel can be rebuilt by using measured statistical distributions based on topography characteristics such as grain size or protrusion heights [9, 44, 45, 75]. The shape of the grains are commonly modelled based on primitives, such as spheres [2, 55, 60], truncated cones [60], pyramids [23, 56, 60], or on a combination thereof [9, 75]. The grains generated are usually statistically allocated along the macro-scale shape of the tool with respect to a measured grains-per-area density of the grinding wheel under consideration. Another approach to rebuild the grinding wheel in kinematic simulations is the analytical approximation of the surface by a set of e.g. trigonometric functions, cf. [25, 79]. According to [49, 80], it is also possible to directly implement the measured topography in the kinematic simulation.

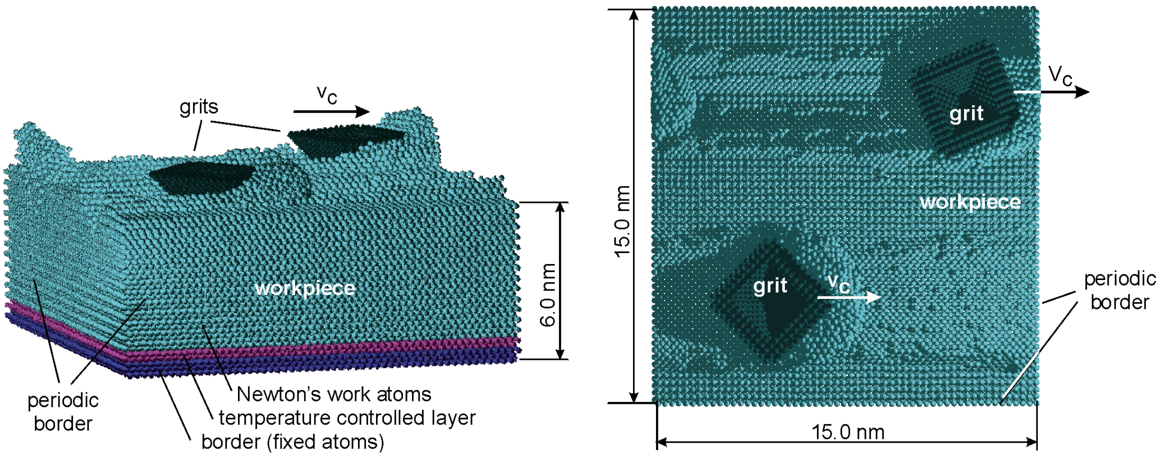

Figure 1.13: Molecular dynamics approach to grinding. Side view (left) and top view (right), taken from [19] and [20], respectively with kind permission.

To model the workpiece, solid,- wireframe-, or point-based discretisation methodologies are commonly applied, cf. [5]. Moreover, so-called voxel- or dexel-based methods [75] have been applied successfully to account for the numerical approximation of the material removed and to retrieve desired measures such as the resulting surface topography of the workpiece [9, 76, 90]. The key feature in this context is the spatial approximation of a volume by a combination of one-dimensional (dexels), or three-dimensional (voxels) sub-elements.

Analytical, empirical and regression methods constitute earlier concepts to model forces, heat induction, or energy partition measures in the context of grinding, see, e.g. [62, 63] and the very comprehensive keynote paper by Tönshoff et al. [99]. However, even up to date the development of these methods have by far not come to an end, cf. [1, 26]. An application of analytical-empirical simulation methods to gear grinding is presented in [54], where energy-based approaches are used to create analytical models to compute resulting cutting forces. To this extent, phenomenological macro-scale models are used to simulate the thermal loads on the workpiece according to the theory of Carslaw and Jaeger [42] or the elastic deflection between workpiece and grinding wheel [19], respectively.

However, the general drawback of these analytical and empirical models is their common phenomenologic character that causes a direct dependency on process parameters used to derive the referring relations. Hence, when applying a large change of the process parameters, a further calibration of the empirical model coefficients becomes necessary [6]. Another very recent example of regression modelling is presented by Rasim et al. [74], who investigate the influence of the meso-scale grain orientation on resulting chip formation. In anticipation of the scale-bridging scheme presented in Chapter 5 of this thesis, the investigation conducted in [74] basically constitutes a very valuable contribution the extension of our bridging scheme towards three-dimensional single grain finite element models. However, the results are unfortunately only included in empirical regression models that suffer from the above-mentioned drawbacks.

Agarwal and Rao [1] present another approach to the analytical modelling of grinding force and grinding power based on an undeformed chip thickness measure. Though in this case based on ceramic workpiece material, such approaches can in general be denominated as promising ”plug-ins” for kinematic simulations, as explained in the following.

Hybrid simulations make use of combining the above-mentioned approaches to benefit from advantages of the single methods. This methodology is successfully directly applied to manufacturing in terms of hybrid processes, cf. Lauwers et al. [58]. One popular hybrid approach to e.g. force modelling constitutes the ”plug-in” of empirical models—that connect an exemplary cutting force component to the volume of removed material—into a kinematic simulation, as presented by Kienzle [50]. Other more sophisticated approaches use finite element models that are combined with kinematic simulations to compute diverse process responses, cf. [5]. In [104], kinematic simulation approaches are combined with thermo-elastic finite element analysis methods to predict the resulting surface topography of the workpiece and the thermo-mechanical load profile acting on the latter. Further hybrid approaches calculate the transient process force history of the grinding process, see [9, 35, 89].

In conclusion, hybrid simulations represent a greatly promising range of approaches to the realistic and simultaneously computationally efficient simulation of grinding processes, which is supported by Arrazola et al. [6], as well.

Process-scale simulations and compensation approaches are the last modelling frameworks to be mentioned in terms of the current state of the art. These are used to take results of the above-mentioned solutions into account and minimise manufacturing errors of diverse kinds. Brinksmeier et al. [21] in this field, conducted a novel compensation approach based on so-called process signatures. Most approaches in this field make use of a vast range of optimisation methods, such as presented by Möhring et al. [68] and Ding et al. [27], who showed different approaches to the compensation of spatial and geometrical errors in terms of grinding processes. Ding et al. [27], in this context, especially focused on the compensation when finishing hypoid gears with a grinding process by at first defining a residual error measure that compares the nominal against the real shape resulting from the abrasive process. The minimisation of this indicator in terms of a non-linear least-square problem in conjunction with a trust-region algorithm is then used to generate more accurate process parameter variants.

Important in this regime is the simulation scale, which can easily take the entire machine into account—as for example presented by Baronin von Payrebrune [25] who included the compliance of the grinding machine into account when simulating the process-structure interaction inherent to tool grinding processes.

Up to this point, we can summarise that grinding simulation tasks commonly exhibit the following demanding challenges: Stochastic character and very complex wheel topography, highly coupled material response, such as thermo-mechanical coupling or fluid-structure interaction in terms of the coolant involved. Moreover, a very wide scale-range—material removal on a very microscopic scale, but process errors rather on the macro-scale—and a broad range of potential errors have to be overcome. The latter error range is due to the high precision regarding geometrical errors and surface smoothness, but also metallurgical errors on a small scale, extended by macro-scale vibrations being coupled to micro-scale geometry.

1.2 Objective of this work

This work focusses on the modelling and simulation of grinding processes with single-layer electroplated wheels—aiming at a maximum generality possible to account for a broad range of applications. Special focus is laid upon the application of these modelling approaches in the context of Internal Traverse Grinding, but is not restricted to this application. Different numerical topics such as surface analysis, material modelling, cutting simulation, process modelling and compensation strategies are touched and hopefully will be useful for future research. Due to the cooperative character of the project it is based on, the present work can benefit from first-hand experimental findings and a synergy of expertise supporting the targeted modelling and simulation development.

To accomplish the objective to develop a numerical method to simulate high-performance grinding up to a near-process scale and to develop compensation approaches that minimise the geometrical manufacturing errors resulting thereof, a hybrid simulation framework will be presented. Following again the scale order from micro- to macroscopic, the overall workflow of the simulation framework is designed as follows.

At first, the wheel topography will be analysed based on measurements carried out by the ISF. This component constitutes the basis for a subsequent kinematic simulation and is presented in Chapter 2.

Following up, a three-dimensional kinematic simulation is used to calculate the transient grain-to-workpiece interaction in high detail, but without any mechanical or thermal interaction, cf. Chapter 3. Resulting thereof, the kinematic engagement conditions for each grain on the grinding wheel surface can be calculated at every point of machining time. These engagement conditions mainly include the single grain undeformed chip thickness $h_{\mathrm{cu}}^{\mathrm{s}}$, the approximated rake face angle γ_{s} and the cutting velocity v_{s} which, as a compound, represent the input parameters for the meso-scale simulations.

The third component of the simulation framework is a parametric, thermo-mechanically coupled finite element model on a meso-scale which captures the proximity of a single cBN grain, presented in Chapter 4. Based on the frequency of the above-mentioned engagement conditions, several representative simulations are carried out to calculate the resulting thermo-mechanical load on the workpiece on the meso-scale. These loads are then homogenised and combined by a bridging approach with the objective to transfer the latter results back to the macro-scale. The referring procedure is demonstrated in the scope of Chapter 5 of the present thesis.

For the last component of the simulation framework—namely a finite element model on the macro-scale—the load compound from the preceding steps is applied as boundary condition in terms of a moving heat source in combination with a distributed mechanical surface load. Apart from this thermo-mechanical load compound, the exact tool and the workpiece geometries in combination with the macroscopic process parameters will be taken into account for the process model, since shape and size of the contact zone are strongly dependent on the latter parameters, cf. [84]. The clamping of the workpiece in terms of Dirichlet boundary conditions according to the real process condition completes the model setup. With the help of this process model, compensation strategies to efficiently minimise the geometrical error occurring during grinding, are developed and presented in Chapter 6.

2 Topography analysis

The topography of a grinding wheel can be distinguished into macro-topography and micro-topography. The latter describes the actual structure of the abrasive grit, whereas macro-topography comprises cavities, such as slots or segments in the grinding wheel body that can have a distinct influence on the cooling efficiency during grinding, cf. [51]. We will in the present case restrict our investigations to the micro-topography and will drop the micro-prefix for notational simplicity throughout the rest of this thesis.

To gather information about the geometrical grinding wheel surface properties such as grit protrusion, cutting edge distributions or chip space, a process to analyse the wheel topography is developed. The employment of digital image processing in the field of grinding wheel analysis has already been applied successfully, compare e.g. [94], where multiple photographs of the wheel surface are assembled numerically to reconstruct the three-dimensional topography of the functional surface.

2.1 Measurement and preprocessing

The analysis methods presented entirely base on measurements, that have been carried out by the ISF and kindly been provided. Due to a special light reflection characteristic, the cBN grains covering the grinding wheel cannot not be investigated directly with structured light microscopy. To overcome this major drawback, we make use of a casting compound to obtain a three-dimensional negative copy of the wheel surface. This molding of the grinding wheel surface is thereafter separated into several sections which are in turn measured by structured light microscopy, subsequently. In this context, sixty sections—each measuring approximately 1400 by 1900 pixels—per grinding wheel are normally taken into account. As output of the optical measurement, we receive a cloud of scattered data points $-z(\boldsymbol{x})$ on a non-regular grid $\boldsymbol{x}$ for each wheel section, representing the inverse wheel surface with a resolution of approximately 1 µm, enabling us to develop a high precision analysis of the wheel structure. The resulting raw data contour plot of an exemplary wheel section—however already inverted to its positive representation—is depicted in Fig. 2.1. As we can see, there are two main issues to overcome: At first, a definite zero level is not available, so the latter has to be determined.

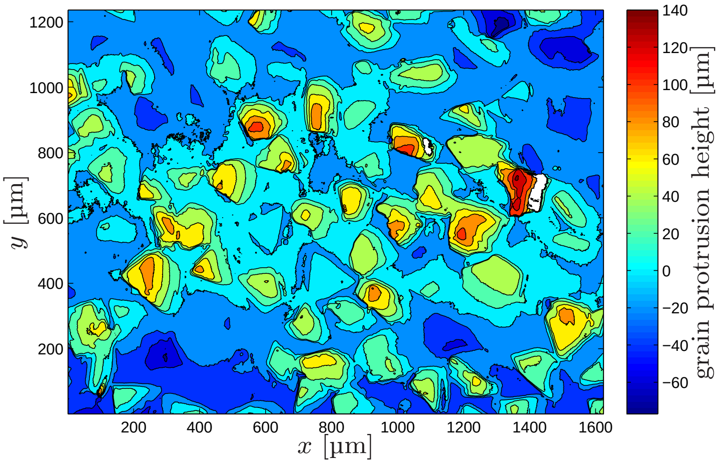

Figure 2.1: Raw data contour plot of a grinding wheel section. The white areas visible for example at ($x \approx 1500\,\mu$m, $y \approx 700\,\mu$m) imply failures in the data resulting from measurement errors and shaping errors in the casting compound, respectively. Taken from [37].

Secondly, as well resulting from the measurement method applied, there are erroneous areas occurring, which have to be accounted for, too.

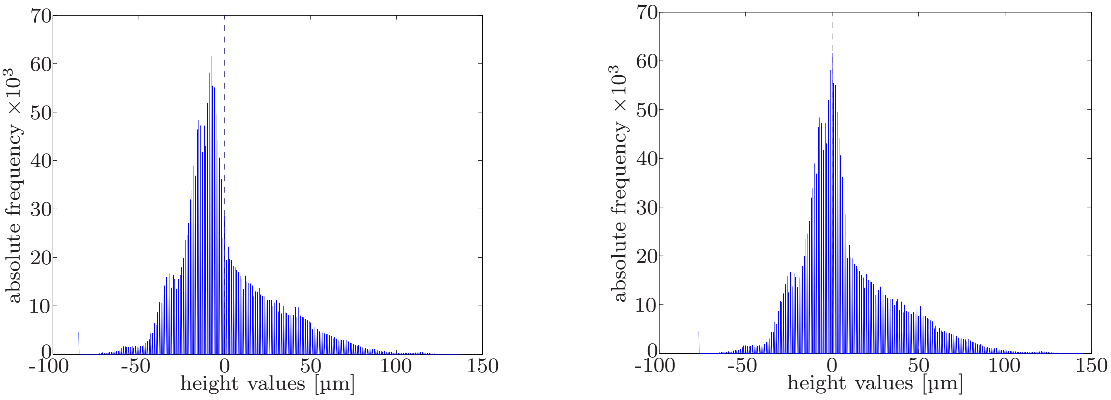

Figure 2.2: Histogram of the measurement data height values before zero level calibration (left) and after zero level calibration (right). The dashed line depicts the zero height frequency. Taken from [37].

The subsequent data processing starts with the determination of the zero level of each section. Therefore, we assume the altitude occurring most frequently to represent the zero level of the data set under consideration. Via a simple shift by the difference between zero and the most frequent height value of all data points, the calibration is finalised, see Figure 2.2.

Next, after substituting possible erroneous areas, see Fig. 2.1 by a cubic spline interpolate of the neighbouring regions, the data set is separated into positive and negative regions with respect to the latter zero level. This way, the positive set can be processed further to determine, e.g., cutting edge angle distributions, whereas the negative counterpart is used to investigate the number of grains broken out of the nickel bond after putting the wheel into operation for the first time. For simplicity, we will focus on the positive domain in the following.

To simplify the next step required, namely the recognition of individual grains, we make use of a cubic spline interpolation to smooth the noisy measurement data. This in turn enables the usage of gradient-based methods for the recognition of grains. In this context, a piecewise cubic spline $f(\boldsymbol{x})$ is established to minimise the weighted sum of the error function

$$E(f(\boldsymbol{x}_i)) = \sum_{i=1}^{n} w(\boldsymbol{x}_i)\,|z(\boldsymbol{x}_i) - f(\boldsymbol{x}_i)|^2 \tag{2.1}$$

and the roughness function

$$F(f(\boldsymbol{x}_i)) = \int_{\min(x)}^{\max(x)} \left|\frac{\partial^2 f(t)}{\partial t^2}\right|^2 \mathrm{d}t \tag{2.2}$$

at every position $\boldsymbol{x}_i$ of the domain under consideration to substitute the scattered data cloud. The parameter t represents the cumulating distance of the data points $\boldsymbol{x}_i$. The weight for the roughness term F is chosen to be small in a way that the interpolant $f(\boldsymbol{x}_i)$ has a high fidelity to its original sample points $z(\boldsymbol{x}_i)$, i.e. is close to the natural interpolated spline solution but is still sufficiently smooth. In the same context, the point data is interpolated onto a regular grid, to simplify subsequent gradient-based methods. The difference between measurement and smoothed data on a chosen subdomain is depicted in Figure 2.3, where the rough surface structure of the unprocessed data is clearly visible. The output of this interpolation procedure in terms of a complete wheel section is depicted in Fig. 2.4.

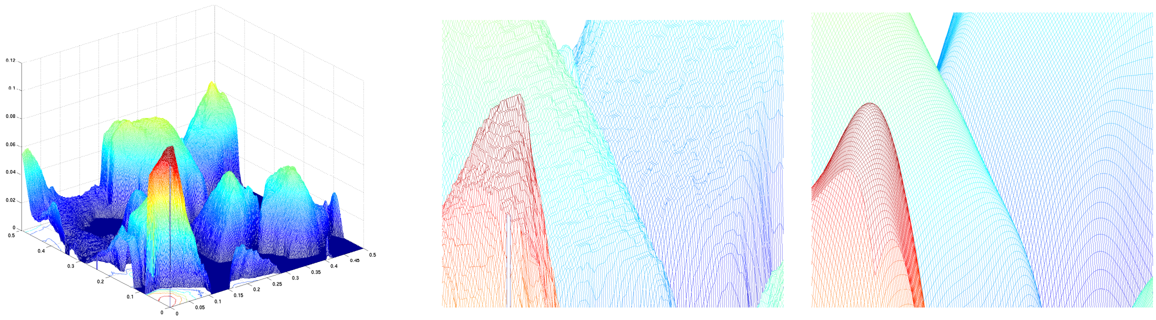

Figure 2.3: Unprocessed vs. smoothed three-dimensional data excerpt from the local extremum visible in the very left subfigure. The smoothing is necessary to enable gradient-based picture analysis methods for the following grain recognition procedure. Taken from [37].

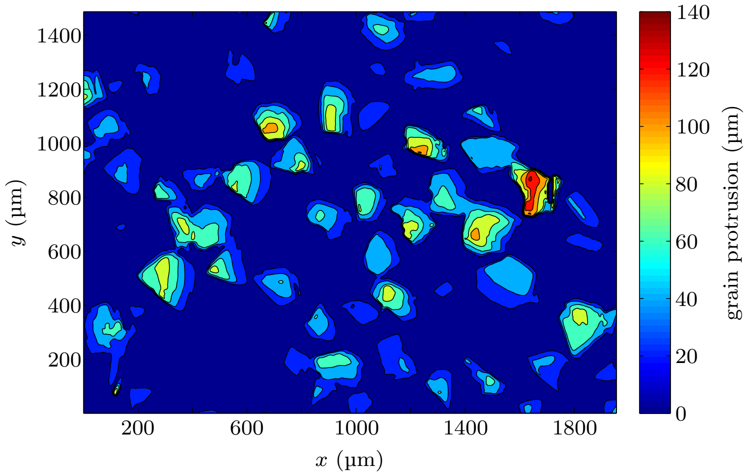

Figure 2.4: Resulting contour plot of the interpolated and smoothed data section shown in Fig. 2.1.

2.2 Grain recognition and filtering

After the smoothing procedure is finished, the grain recognition is the next step necessary towards an analysed wheel surface. Conceptually, we apply a simple procedure that subdivides the entire domain of a section into non-grain-containing and grain-containing subdomains, whereas the latter are stored in a set of data aggregates, each representing a single abrasive grit of the grinding wheel. Since in the present context, the data range close to each local maximum—representing the most protruding point of a cBN grain—is of higher interest than the grain base, we apply a lowering-plane approach to determine the single grain data aggregates. Figure 2.5 illustrates the concept of this method on a subdomain Ω of an exemplary wheel section.

Basically, one subsequently calculates a planar intersection of the interpolated data points $\bar{z}(\boldsymbol{x}) \in \Omega$ and a reference plane $\mathsf{P}_j^{\text{ref}} : z = z_j^{\text{ref}} \,\forall\, \boldsymbol{x} \in \Omega$ defined by a given height value z_j^{ref}. The latter is subsequently lowered from the absolute height value maximum $\hat{z}(\boldsymbol{x})$ of the corresponding domain to zero within n_{ref} steps. In each intersection at z_j^{ref}, we can now identify closed subdomains $\Omega_g \subset \Omega$ that have a non-zero height value as a grain g that has been cut by $\mathsf{P}_j^{\text{ref}}$. This closed-domain recognition procedure is implemented using the Matlab Image Processing Toolbox. Referring to Fig. 2.5, $n_{\text{ref}} = 6$ steps are applied to estimate the number of grains in the subdomain Ω. As can be observed, at a certain level close to $z = 0$, the number of grains detected tends to decrease again, which is due to a connection of the grain domains close to the zero level of the section subdomain Ω. This characteristic is utilised to determine a level $\check{z}_j$ of maximum grain count that is finally used to determine the number of grains of the investigated domain Ω. In the case depicted in Fig. 2.5, $j = 4$ holds and determines a grain amount of three. After the critical height $\check{z}_j$ has been determined, the corresponding intersection with the interpolated data $\bar{z}(\boldsymbol{x}) \in \Omega$ is defined as the grain base and one grain—represented

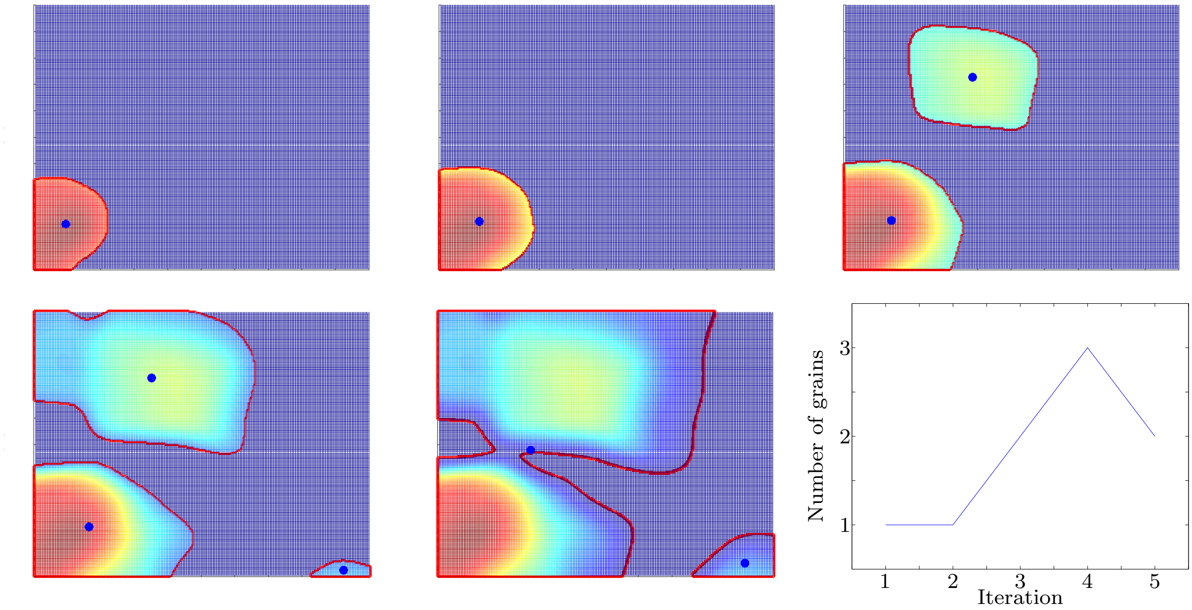

Figure 2.5: Basic principle of grain detection: The reference plain $\mathsf{P}_j^{\mathrm{ref}}$ is subsequently lowered from maximum height towards the zero level—depicted from top left to the bottom middle subfigure. The lower-right subfigure depicts the number of detected grain regions over the lowering iteration counter j. The blue dots denote the area-weighted centroid of a detected grain domain, not the local maximum determined by the minimisation scheme. The border of a grain domain is outlined with a red stroke.

as one data aggregate—is subsequently defined as the unity of all planar intersections $z \geq \check{z}_j$. After this procedure has succeeded, the local maximum position $\hat{\boldsymbol{x}}$ of each grain is determined by a steepest descent step, taking the area-weighted centroid—see blue dots in Fig. 2.5— as starting point. The volume V_g of each grain g can then straightforwardly be approximated as the integral over the grain domain from its base to its maximum height $\hat{z}_g$, i.e.

$$V_g = \int_{\check{z}_j}^{\hat{z}_g} \int_{\Omega_g} \mathrm{d}A \, \mathrm{d}z. \tag{2.3}$$

To prove the correctness of this method and to investigate the dependency on the number of intervals n_{ref}, the results of a corresponding study are depicted by Fig. 2.6. As observable, all variants deliver sufficiently comparable results, which is why $n_{\mathrm{ref}} = 10$ is chosen to be implemented due to computational efficiency.

After the recognition procedure is finished, a filtering of the grain data is applied to exclude grains with a sufficiently small volume. The respective threshold is defined in terms of a relative ratio

$$\eta_{\mathrm{thr}} = \frac{V_g}{\overline{V}_\Omega}, \tag{2.4}$$

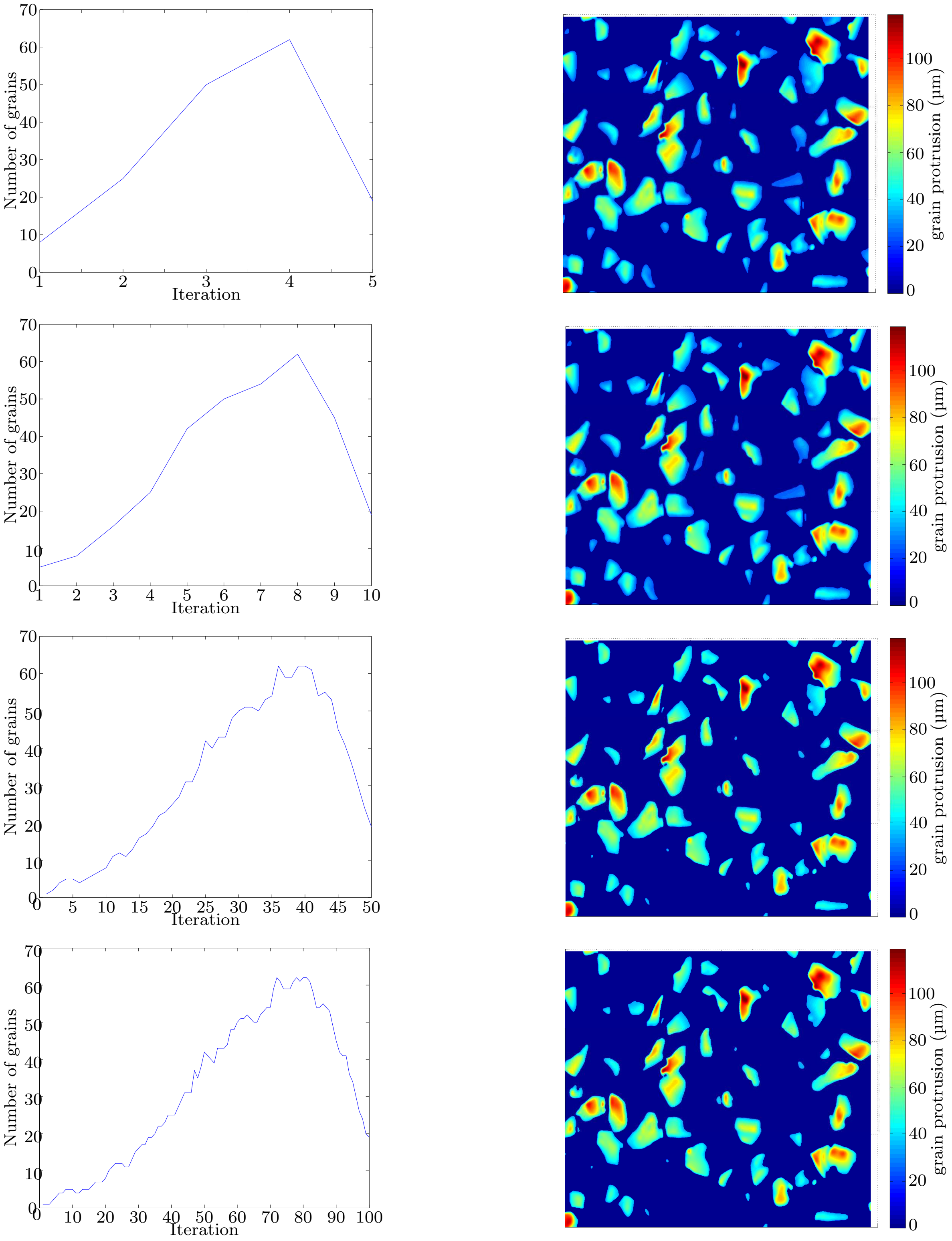

Figure 2.6: Influence of iteration steps: The left column shows the calculated number of grains against the current iteration step, the right hand side depicts the resulting grinding disc topography in µm grain protrusion.

related to the average volume $\overline{V}_\Omega$ of all grains g contained in a wheel section domain Ω. Figure 2.7 depicts the corresponding filter results for different thresholds Since even the most restrictive filter setting with $\eta_{\text{thr}} = 25\%$ still does not affect the broad spectrum of the kinematic cutting edges, we apply this threshold for future calculations.

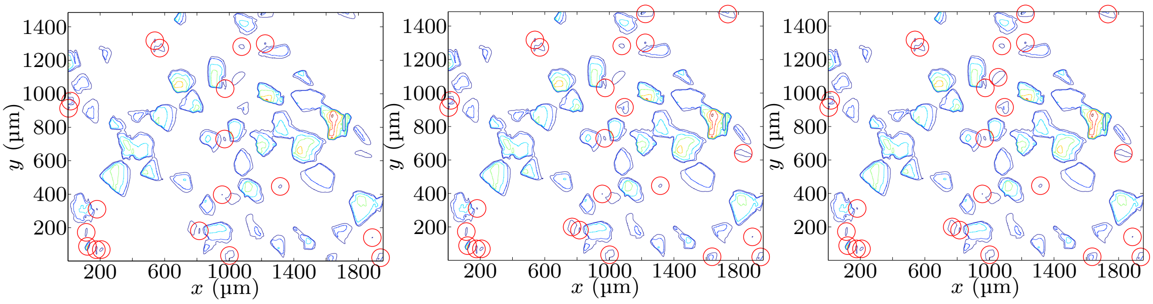

Figure 2.7: Different filter threshold values in comparison: $\eta_{\text{thr}} = 15\%$ (left), $\eta_{\text{thr}} = 20\%$ (middle) and $\eta_{\text{thr}} = 25\%$ volume filter (right). The red circled grains are marked as deleted.

2.3 Approximation of the cutting edge

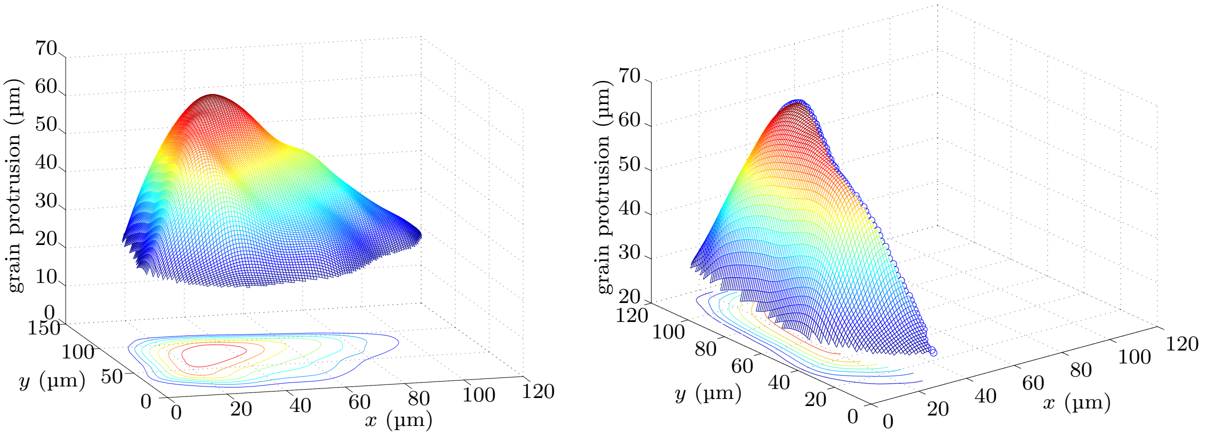

Figure 2.8: Determined grain (left) and points of this grain being potentially in contact with the workpiece material (right); in this case, approaching from the left in positive x direction.

The data aggregation presented in Sec. 2.2 allows us to analyse every grain separately in terms of height, volume, cross-sectional area, or rake face angles and cutting edge angles, respectively. To get an estimate of the latter rake angles, the flank of the grain having its normal vector oriented towards the direction of cut, i.e., $\boldsymbol{v}_{\text{s}}$, respectively, is approximated by a plane that is calculated by an orthogonal least square fit. In this context, a plane is used to represent the entire cutting surface of a grain, see Figure 2.9. This in turn allows us to calculate a distribution of cutting edge angles for the complete grinding wheel domain. The according computation is carried out in two steps: At first, every three-dimensional grain data aggregate is separated into the grain surface partition that is exposed to a workpiece material flow and the opposing side. That means, all surface elements $\mathrm{d}A_i$ of the grain that are characterised by a normal vector $\boldsymbol{n}_i$ having a positive contribution in the direction of the circumferential wheel velocity $\boldsymbol{v}_\mathrm{s}$, i.e. $\boldsymbol{n}_i \cdot \boldsymbol{v}_\mathrm{s} > 0$ are defined to be exposed to the workpiece material flow, compare Fig. 2.8. Second, this surface partition is linearly approximated as outlined above, yielding exemplary results as depicted in Figures 2.9 and 2.10. It has to be mentioned here, that this assumption can of course not in every case deliver good results—especially when the exposed grain surface partition is not sufficiently convex, the regression scheme tends to deliver lower quality approximations, as shown in Fig. 2.10, right. However, these cases only represent minor occurrences in comparison to well-posed approximations, so this scheme can be adopted for future utilisation.

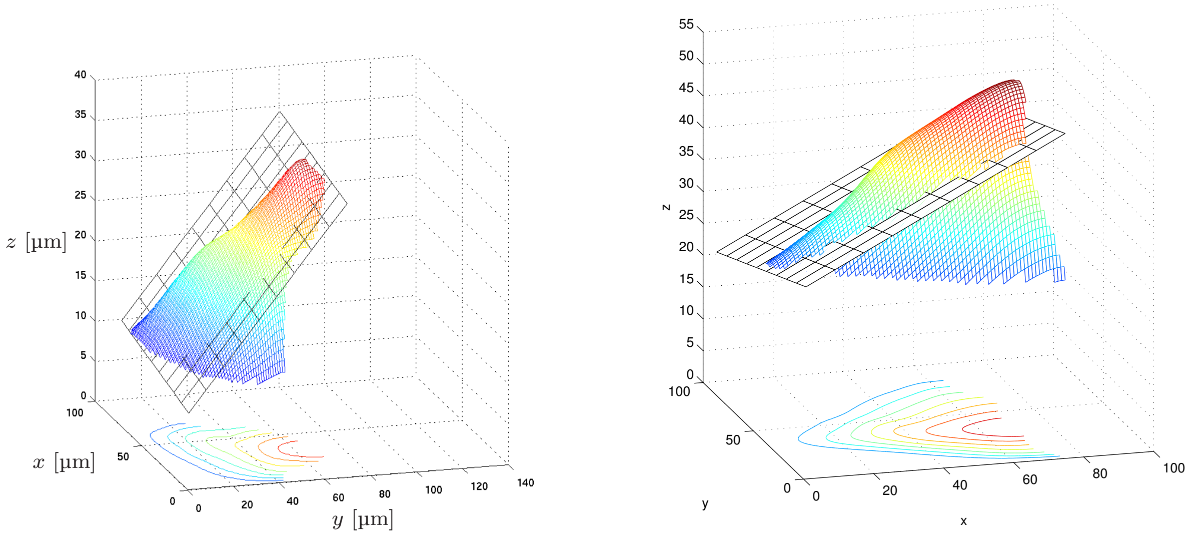

Figure 2.9: Examples for regression planes as an approximation of the grain flank that is in contact with the workpiece material. The lower part of the grains is not depicted due to the grain recognition procedure described in Sec. 2.2 and the corresponding cut-off.

2.4 Results

An illustration of the topography analysis output is depicted in Figures 2.11 and 2.12, where the same section that has been shown in Fig. 2.1 is drawn as contour plot and as a three-dimensional representation of the separated grain aggregates. The difference in field scale between Figures 2.1 and 2.11 results from the correction of measurement sample points: The grid on which the section data is recorded is not completely regular but possesses gaps in some areas. Before smoothing, a two-dimensional interpolation

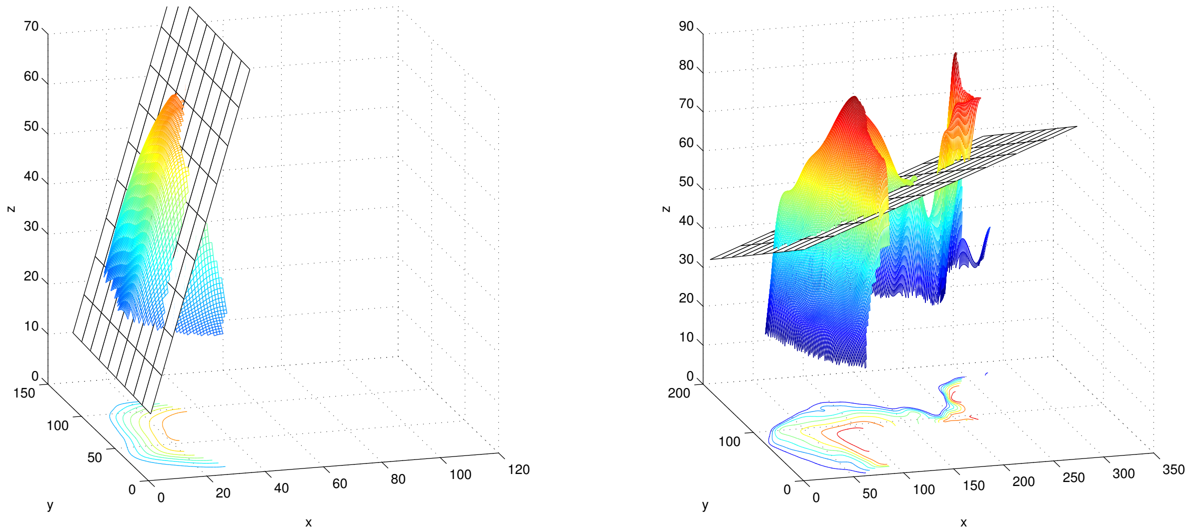

Figure 2.10: Exemplary grain showing a good fit when applying the reference plane approach (left) and counter example showing unsatisfactory regression plane fitting (right). This is likely, when flanks are not sufficiently convex or if the grains recognised are consisting of only weakly connected domains like on the right hand side.

is used as outlined above to map the section field onto a regular grid, resulting in a slightly finer resolution of the picture. Moreover, separate two- and three-dimensional grain geometries can be exported to FE-analyses later on, see Fig. 4.2 for use. Far more important are the results depicted in Figure 2.13, where the distributions of grain protrusion and approximated rake face angles are illustrated. Good agreement with a normal probability function around a centre of about 70 µm is shown by the grain protrusion distribution, although a slight skewness can be recognised. In other works, normal distributions were used to model grain sizes, cf. [104], the above-mentioned skewness of normally distributed grain protrusion heights was also observable in [9] as well as [45]. The rake angles depicted provide a strong asymmetrical distribution with the maximum probability at an angle of $\gamma \approx -65°$, which we fitted to a Γ-distribution. Other researchers also invoked Rayleigh or Weibull distributions in this context, cf. [32, 91].

Further results of the topography analysis include an approximate roughness profile prediction, the estimation of chip space as well as corresponding grain volume ratios and the wheel surface grain density. The latter measures will be used as in input parameter for the kinematic simulation presented in the next chapter of this thesis. Moreover, the number of grains broken out of the galvanic bond can be determined, and wear investigations can be performed, which enable the establishment of a wheel quality check with the analysis tool developed.

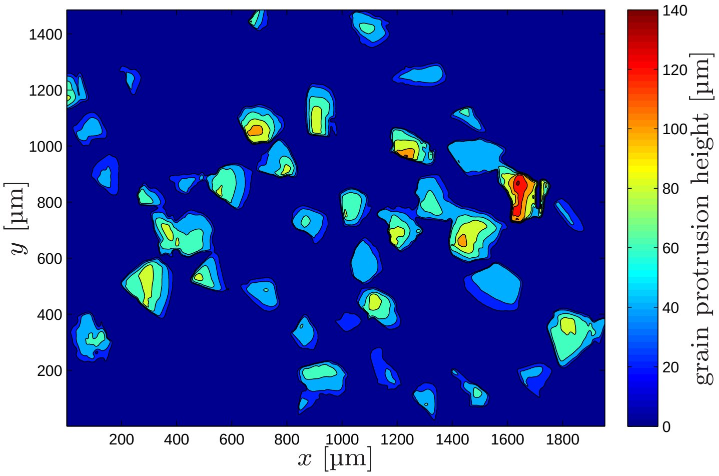

Figure 2.11: Contour plot of a grinding wheel section after finishing the grain recognition and subsequent filtering of grains with a volume smaller than the 25 % of the overall average volume.

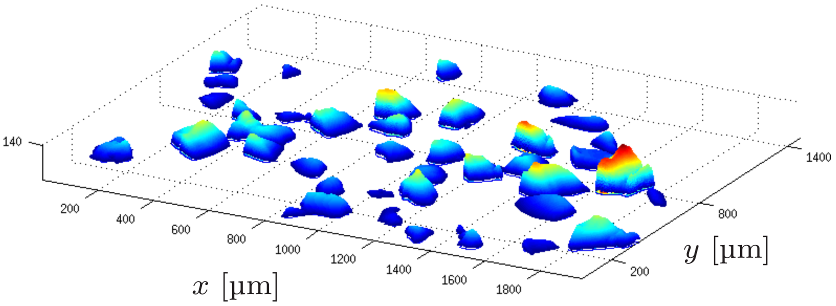

Figure 2.12: Topography analysis results: Overall grinding wheel surface after filtering and grain recognition.

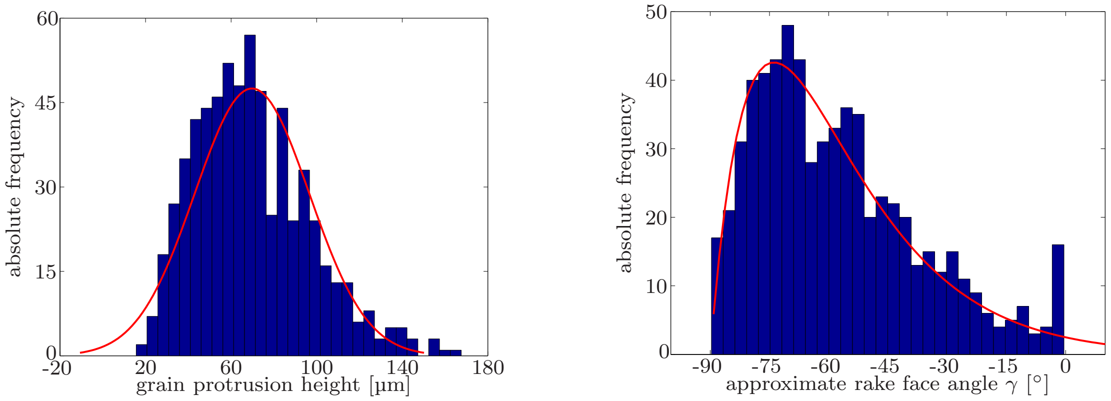

Figure 2.13: Topography analysis results. Left: Overall grinding wheel grain protrusion height, fitted with a normal distribution. Right: Overall grinding wheel cutting angle distribution, fitted with a Γ-probability density function due to its asymmetry. Since this function is only defined on the positive domain, the values have been shifted to the positive domain, fitted and then shifted back accordingly.

3 Kinematic simulation

The kinematic simulation which is used in the grinding simulation framework presented, is entirely developed by the ISF, which is why we will just briefly outline this framework component here. Moreover, precise investigations on different aspects of this simulation system are discussed in more detail in [29, 75, 85, 89, 90]. The present chapter at first gives an outline on the general implementation of the kinematic simulation, followed at first by an investigation of the global grain engagement conditions occurring when taking one complete tool pass during ITG into account. Secondly, a local investigation of the cutting mechanisms at a certain workpiece region is carried out, which builds the basis to a special examination in the subsequent Chapter 4.

3.1 Implementation

To gain detailed insight on the grain engagement conditions occurring in the context of high-performance grinding with electroplated wheels, a kinematic simulation is used which models the geometric interaction between the grinding wheel and the workpiece in high detail. According to the tool drawing provided in Fig. 1.8, the basic shape of the grinding wheel is modelled as a combination of a truncated cone—representing the conical roughing zone—and a cylinder, which reflects the cylindrical finishing zone, cf. Fig. 3.1.

To gather information on the grain size and shape distribution, approximately 1500 cBN grains have been measured with a light microscope, and a topography analysis of a ready-to-use grinding wheel is performed as described in the previous chapter. With this information at hand, the abrasive grit is modelled as follows. According to the ideal growth of cBN, [10], one single grain is defined as an intersection of a cube, an octahedron and a tetrahedron, see Fig. 3.2, left. By scaling these primitives according to two shape index values, a vast range of grain shapes can be obtained, yielding the morphology table as depicted in Fig. 3.2, right. By using a constructive solid geometry (CSG), cf. [30], representation of the above-mentioned grinding wheel body and the artificial cBN grains, the grinding wheel model is completed by stochastically rotating the grains and subsequently locating them along the circumferential area of the grinding wheel, cf. [75] and Fig. 3.4, left.

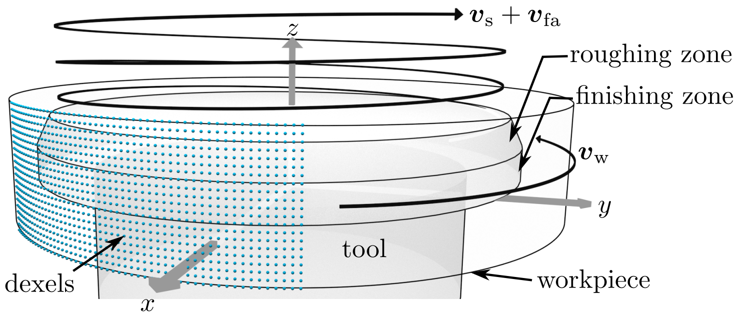
$\boldsymbol{v}_\mathrm{s} + \boldsymbol{v}_\mathrm{fa}$
z
roughing zone
finishing zone
$\boldsymbol{v}_\mathrm{w}$
y
tool
dexels
workpiece
x

Figure 3.1: Kinematic simulation scheme. The workpiece dexels are printed in light blue, while the grains on the tool or grinding wheel, respectively, are not depicted. The workpiece rotates with a constant circumferential velocity $\boldsymbol{v}_\mathrm{w}$, while the helical motion of a grain on the tool surface results from the superposition of the tool circumferential velocity $\boldsymbol{v}_\mathrm{s}$ and the axial feed velocity $\boldsymbol{v}_\mathrm{fa}$. Taken from [38].

To ensure a good surface quality of the machined workpiece in the real abrasive process, the finishing zone of the real grinding wheel is touch-dressed with a single grain diamond prior to application, cf. [65]. To model the numerical touch-dressing in the kinematic simulation, the grains generated in the finishing zone are flattened by calculating the intersection with a dressing cylinder, compare [34] and Fig. 3.7.

The radius of this dressing cylinder is chosen according to the total radial dressing stock removal $a_\mathrm{ed,tot} = 16\,\mu\mathrm{m}$, which was used during the experimental investigations carried out. This numerical dressing procedure results in grains that have a reduced identical protrusion height in the area of the finishing zone of the tool, whereas the grains in the roughing zone that are not intersected with the dressing cylinder, retain their original height and profile. In the undressed state, the distribution of the protrusion heights in the roughing and finishing zone is equal for a real and a modelled grinding wheel. In contrast, after dressing, the protrusion heights in the finishing zone are lower and equalised for both a real and a modelled grinding wheel.

The workpiece in contrast, is modelled by a radial dexel board. In order to reduce the calculation effort, only a circumferential section spanning about one quarter of the workpiece circumference is modelled, cf. Fig. 3.1. According to the real process kinematics, the tool moves axially along the z axis and with the axial feed velocity $\boldsymbol{v}_\mathrm{fa}$, superposed by the grinding wheel circumferential speed $\boldsymbol{v}_\mathrm{s}$, whereas the workpiece rotates with the workpiece circumferential speed $\boldsymbol{v}_\mathrm{w}$ in the same direction as the latter. The material removal is subsequently calculated by the intersection of the CSG grains with the dexel board, resulting in the set of transient values shown in Equation (3.1).

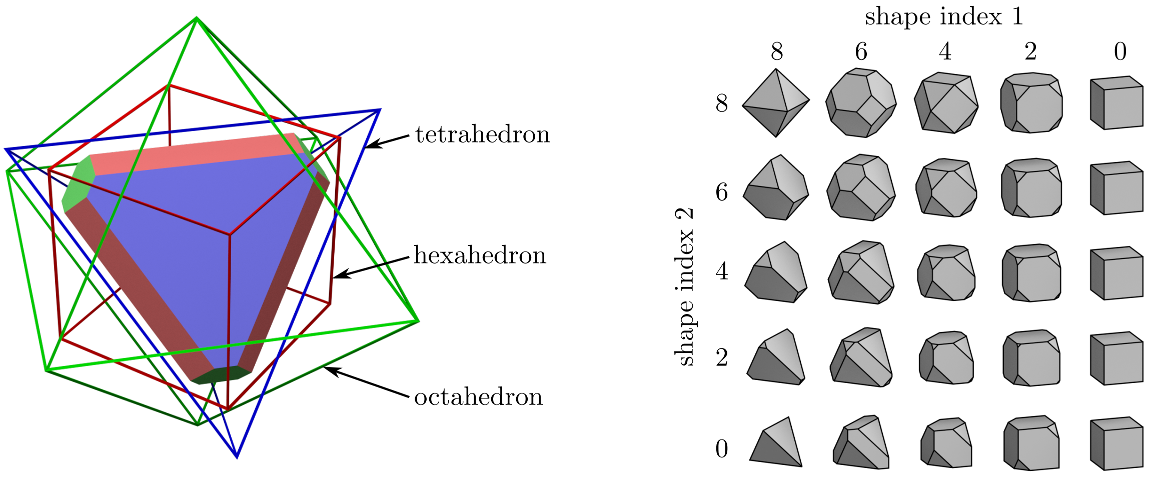

Figure 3.2: Left: Geometric primitives used for cBN grain generation. Right: Grain morphology used for the abrasive grit generation, according to [47]. Taken from [38].

3.2 Results

The output of the kinematic simulation is comprised of a highly accurate transient penetration history of every grain of the grinding wheel that intersects with the workpiece during a simulation time span ΔT, cf. Fig. 3.4, right. Due to the implemented discretisation in time and space, this engagement history is available at fixed time points $t_n \in \Delta T$ for a certain dexel resolution d_{res}. Therefore, we obtain a function set

$$\{h^{\mathrm{s}}_{\mathrm{cu}}(t_n),\, \gamma_{\mathrm{s}}(t_n),\, v_{\mathrm{s}}(t_n),\, Q^{\mathrm{s}}_{\mathrm{w}}(t_n)\}\ \forall\, t_n \in \Delta T \tag{3.1}$$

containing the single grain undeformed chip thickness $h^{\mathrm{s}}_{\mathrm{cu}}$, the approximated single grain rake angle γ_{s} and the single grain material removal rate

$$Q^{\mathrm{s}}_{\mathrm{w}} = \frac{\Delta V^{\mathrm{s}}_{\mathrm{chip}}}{\Delta t} \tag{3.2}$$

as a function of the discretised time t_n, respectively. At this stage and throughout this work, we will keep the absolute cutting speed constant at $\|\boldsymbol{v}_{\mathrm{s}}\| = v_{\mathrm{s}} = 120\,\mathrm{m/s}$. The calculation scheme of the approximated rake angle γ_{s} is depicted in Fig. 3.3. At first, all vertex points of the grain projection onto the plane that is normal to the grinding wheel axis and that contains the velocity vector $\boldsymbol{v}_{\mathrm{s}}$ are determined. Secondly, all of the latter vertex points that are in contact with the workpiece are then used to calculate a linear regression function which approximates the rake face and yields the approximated rake angle accordingly. Throughout the rest of this chapter, we will refer to this approximated rake angle when using the term rake angle.

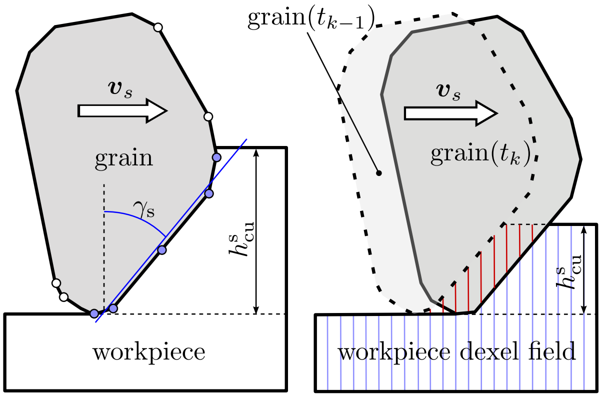

Figure 3.3: Rake angle approximation scheme (left) and material removal calculation (right) in the context of the kinematic simulation. Left: The projection of the three-dimensional grain onto the plane that is parallel to the grain cutting velocity vector $\boldsymbol{v}_\mathrm{s}$ is depicted in grey. Vertex points of the grain are printed as white dots while vertex points in contact with the workpiece are depicted as blue dots. The rake angle γ_s is approximated by the linear regression (blue line) through all vertex points that are in contact with the workpiece material. Right: The workpiece dexels are shown in light blue. The workpiece dexels that are intersected between subsequent time steps t_{k-1} and t_k are printed in red and constitute the removed workpiece material $\Delta V^\mathrm{s}_\mathrm{chip}(t_k)$. The grain engagement depth defines the current undeformed chip thickness h^s_cu as depicted.

Aiming at the meso-scale simulations, we first need to establish the representative points in a parameter space $\{h^\mathrm{s}_\mathrm{cu}, \gamma_\mathrm{s}\}$ to carry out the calculations of the meso-scale heat energy induced into the workpiece. Here, we take into account a two-dimensional histogram showing the absolute frequency of certain material removal conditions as a function of the meso-scale undeformed chip thickness h^s_cu and the rake angle γ_s. The according results are depicted in Fig. 3.5 for two exemplary sets of macro-scale process parameters A and B, namely on the left hand side a material removal rate of $Q^A_\mathrm{w} = 225\,\mathrm{mm}^3/\mathrm{s}$ resulting from a radial stock removal of $a^A_\mathrm{e,tot} = 0.15\,\mathrm{mm}$ in case A. On the right hand side, the material removal rate is $Q^B_\mathrm{w} = 75\,\mathrm{mm}^3/\mathrm{s}$ resulting from a total radial stock removal of $a^B_\mathrm{e,tot} = 0.05\,\mathrm{mm}$ in case B. Both experiments were carried out with the same grinding wheel and at a constant axial feed rate $a_\mathrm{f} = 0.75\,\mathrm{mm/rev}$ per revolution of the workpiece. The complete set of parameters for the macro-scale kinematic simulation is depicted in Tables 3.1 to 3.3. Note, that the exemplary comparison between the present experiments A and B is shown here only to give a brief overview on how the process parameters of ITG affect the results of the kinematic simulation.

When analysing the histogram plots in Fig. 3.5, it can be observed that the general shape of the engagement condition distribution is similar across both sets of parameters. Both plots show a tendency to cover a wide range of rake angles at low values of h^s_cu, whereas the range of rake angles in engagement thins out in a triangular shape with ascending undeformed chip thickness. Furthermore, it can be stated that there are indeed numerous penetrations at very large negative rake angles exceeding $-80°$ when the undeformed chip thickness is lowered below $10\,\mu\mathrm{m}$. When investigating the higher-

Table 3.1: Fixed process parameters of the kinematic simulation.

description	parameter	value	unit
workpiece circumferential velocity	v_w	2	m/s
grinding wheel circumferential velocity	v_s	120	m/s
workpiece axial length	l_wp	8	mm
roughing zone angle	χ	7.5	°
dressing stock removal	$a_\mathrm{ed,tot}$	16	µm
axial feed rate	a_f	0.75	mm/rev
tool outer diameter	d_tool	62.4	mm
tool roughing zone length	l_rz	2	mm
tool finishing zone length	l_fz	4	mm
lateral dexel resolution	Δl_dex	6.25	µm
time increment	Δt	$5.3 \cdot 10^{-8}$	s
simulation time	ΔT	9.81	ms
total number of grains	n_g	11476	

Table 3.2: Parameters of the kinematic simulation, experiment A.

description	parameter	value	unit
initial workpiece inner diameter	d^A_wp	80.855	mm
total radial stock removal	$a^A_\mathrm{e,tot}$	0.15	mm
macroscopic material removal rate	Q^A_w	225	mm^3/s

resolution version of the according plots below the coarse ones in the top row, a certain pattern of fine lines with higher frequency values can be observed. These lines are partially horizontal over a wide range of h^s_cu, resulting from the approximation scheme for the rake angle γ_s applied within the kinematic simulation, see Fig. 3.3: Due to the applied regression scheme that only uses the grain vertices in contact with the workpiece, different undeformed chip thicknesses h^s_cu may result in the same rake angle γ_s when the grain vertices are situated sufficiently far apart from each other. This explains the occurrence of the horizontal lines in Fig. 3.5. Most of these lines at some value of h^s_cu

Table 3.3: Parameters of the kinematic simulation, experiment B.

description	parameter	value	unit
initial workpiece inner diameter	d^B_wp	81.455	mm
total radial stock removal	$a^B_\mathrm{e,tot}$	0.05	mm
macroscopic material removal rate	Q^B_w	75	mm^3/s

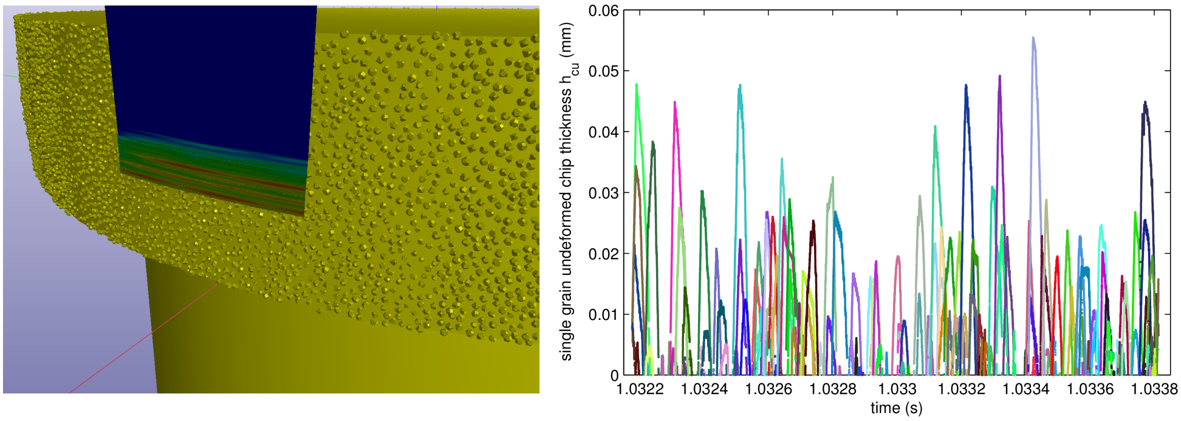

Figure 3.4: Kinematic simulation snapshot (left) and selected output (right). The yellow tool on the left is revolving around its upright axis and moving axially from bottom to top; the workpiece is reduced to a square section showing the single grain undeformed chip thickness $h_{\mathrm{cu}}^{\mathrm{s}}$ in terms of a blue-to-red colour coding. The plot on the right depicts the same measure for each grain in contact as a function of time. Here, each differently coloured stroke represents one cBN grain in contact. Taken from [35].

show an ascending behaviour, which coincides with the above-mentioned approximation scheme, that obviously results in lower absolute values of γ_{s} when taking into account a higher number of grain vertex points.

When comparing both sets of parameters, it can be observed that experiment A has a higher concentration of engagement situations in the lower left area, representing a higher absolute value of the rake angle in combination with a low undeformed chip thickness. Experiment B, on the other hand, shows a lower density in this area as well as a smaller range of parameters along with a lower amount of total intersections, which results from the lower rate of material removal $Q_{\mathrm{w}}^{\mathrm{s}}$ applied. Also note, that the range of $h_{\mathrm{cu}}^{\mathrm{s}}$ and γ_{s} differs between the experiments due to the process parameters applied. In the following, all analysis aspects will be carried out using experiment A as a reference due to the higher process performance present here. One very interesting result from the kinematic simulation is constituted by the number of grains being in contact simultaneously, which is depicted as a histogram in Fig. 3.6. Here, it can be clearly observed that at most only two to five grains intersect with the workpiece simultaneously which clearly governs the overall engagement conditions.

As a conclusion, we can now clearly state which parameter combinations of $h_{\mathrm{cu}}^{\mathrm{s}}$ and γ_{s} occur in which frequency and which parameter combinations barely occur, which in turn is helpful for the set-up of the meso-scale finite element simulations described in Chapter 4 of the present work.

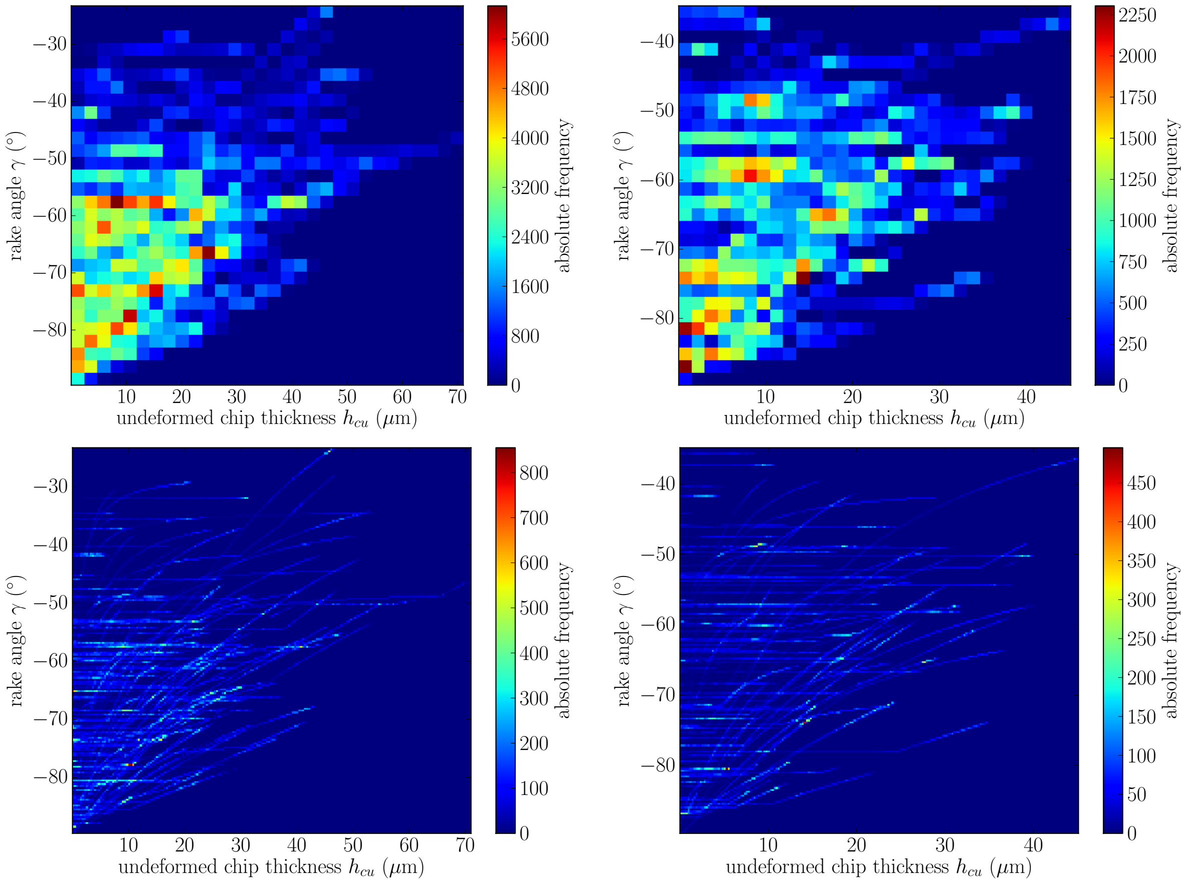

Figure 3.5: Results of the kinematic simulation. Histograms or absolute frequency distributions $f(h^{\mathrm{s}}_{\mathrm{cu}}, \gamma_{\mathrm{s}})$ with a square resolution of 30 bins per parameter (top row) and a resolution of 200 bins per parameter (bottom row). The left column depicts experiment A whereas the right column shows experiment B. Note, that the scales of the graphs differ in magnitude. Taken from [38].

3.3 Local investigation of engagement conditions

In the domain of grinding simulations, the question for how many grain engagements are necessary and in which order do they take place to finish the abrasive process with respect to a certain local area of the workpiece constitutes a highly interesting investigation. For this reason, and to be able to further investigate this issue with the help of a single-grain finite element model as presented in Chapter 4, the current section deals with this topic. The simulation parameters used in the present study are depicted in Table 3.4.

In order to determine the undeformed single grain chip thickness $h^{\mathrm{s}}_{\mathrm{cu}}$ in a defined section of the workpiece the chronological sequence of this value has to be estimated for a representative dexel over the entire process. In geometric-kinematic simulations, $h^{\mathrm{s}}_{\mathrm{cu}}$ can be estimated by the difference between the maximal dexel height before the cut and the minimum dexel height after the cut [90], cf. Fig. 3.7b. When a grain penetrates the

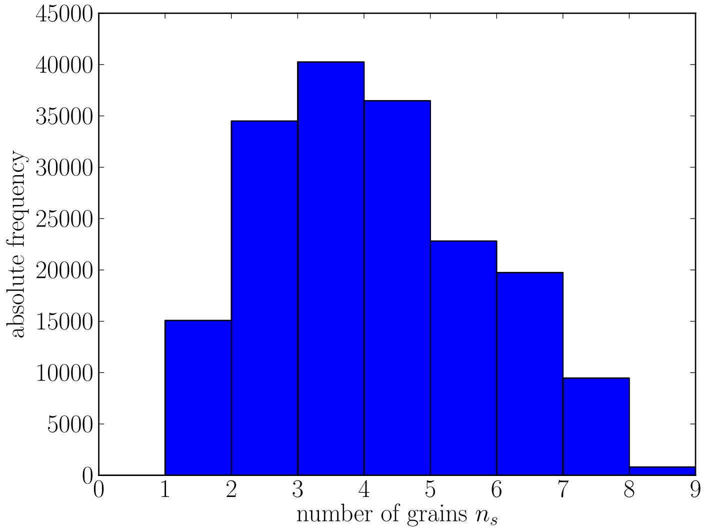

Figure 3.6: Absolute frequency of the number of grains being in contact with the workpiece simultaneously for experiment A. Taken from [38].

workpiece, this calculation is performed by dividing the contact area of the grain and the dexel grid in cutting slices according to the y-coordinate in the dexel grid (Fig. 3.7c). By using such a procedure, the local $h_{\mathrm{cu}}^{\mathrm{s}}$ can be calculated for every grain engagement, which is shown for an example grain in Fig. 3.8. Furthermore, the current stage of the workpiece topography and the grain cutting path can be affected by the $h_{\mathrm{cu}}^{\mathrm{s}}$ progress over the grain engagement at the representative dexel (Fig. 3.8a and b). For further considerations, the average $h_{\mathrm{cu}}^{\mathrm{s}}$ is estimated per grain engagement.

In Fig. 3.9, the chronological sequence of $h_{\mathrm{cu}}^{\mathrm{s}}$ for the representative dexel pointed out in Fig. 3.8 is depicted. The material removal at this certain position is plotted against workpiece revolutions (as in Fig. 3.7a), showing $h_{\mathrm{cu}}^{\mathrm{s}}$ of the currently engaging grain, which is represented by its unique colour. The major material removal takes place within the second revolution of the workpiece, which is due to the high material removal rate in the roughing zone of the tool. In the roughing zone region at workpiece revolution 2, it can be observed that the same grain cuts the exact same workpiece region twice, see Fig. 3.9, dark blue and dark green bars. As can be seen, the $h_{\mathrm{cu}}^{\mathrm{s}}$ decreases with increasing workpiece revolutions, which means that the position of the representative dexel comes in contact with the grains of the finishing zone, cf. Fig. 3.7. With respect to the position of the representative dexel, the entire material removal takes place conducting 13 grain engagements in total. The $h_{\mathrm{cu}}^{\mathrm{s}}$ sequence of grain engagements computed with respect to this representative dexel is subsequently transferred to the meso-scale FE-model as an input value.

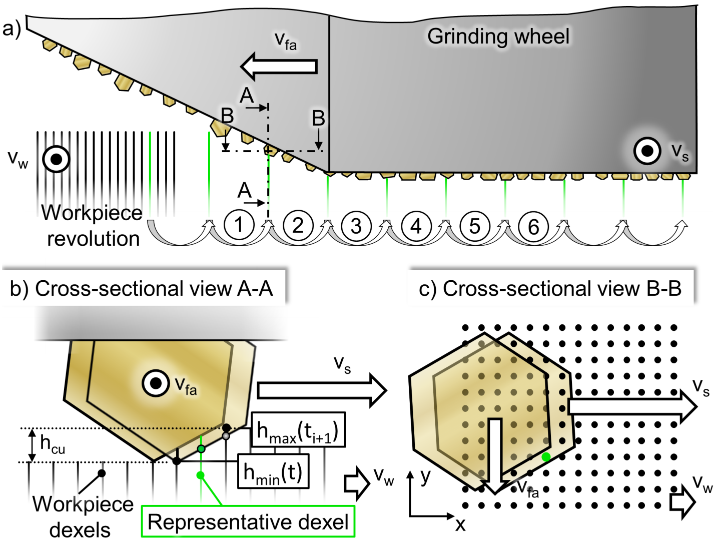
a)
v_fa
Grinding wheel
A
B
B
A
v_w
v_s
Workpiece revolution
1
2
3
4
5
6
b) Cross-sectional view A-A
c) Cross-sectional view B-B
v_s
v_fa
h_cu
h_max(t_i+1)
h_min(t)
v_w
Workpiece dexels
Representative dexel
y
x
v_s
v_fa
v_w

Figure 3.7: Structure and procedure for geometric-kinematic modelling of ITG: a) Cross-sectional view of the modelled grinding wheel and the CSG-grains: The workpiece dexel grid (black lines) and the representative dexel (green line) move with an axial feed per workpiece revolution a_f in axial direction and rotate with the workpiece circumferential velocity v_w. b) Cross-sectional view A-A: Estimation of h^s_cu. c) Cross-sectonial view B-B: Dexel grid definition according to the direction. Taken from [39].

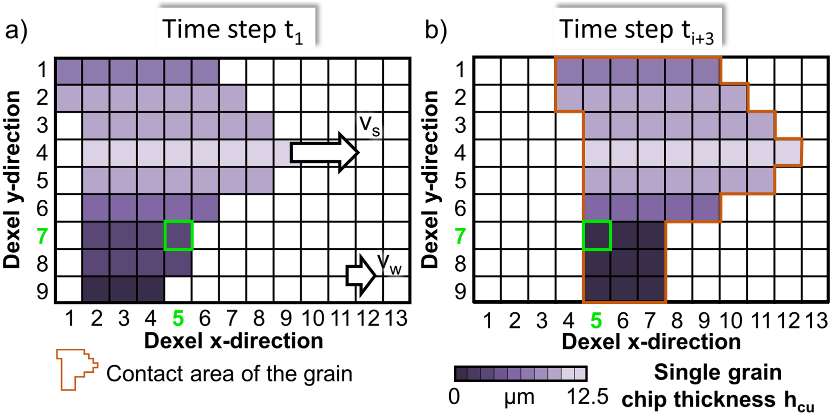

Figure 3.8: Locally calculated h^s_cu within the contact area between grain and dexel grid at two different time steps t_1 (a) and t_{i+3} (b). The green area denotes the representative dexel. Note the difference of the contact area shape between subfigures a) and b) due to the changing engagement conditions. Taken from [39].

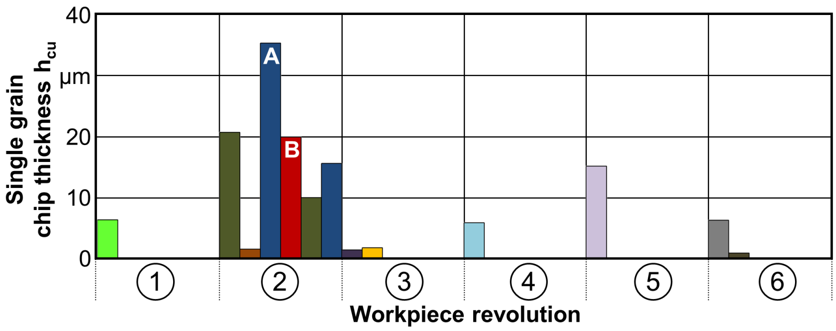

Figure 3.9: Chronological single grain chip thickness $h^{\mathrm{s}}_{\mathrm{cu}}$ resulting from the geometric-kinematic simulation of the representative dexel pointed out in Fig. 3.8. The circled numbers denote the revolution number of the tool, each color represents one unique grain. The blue bar emphasised with A corresponds to the first meso-scale simulation with $h^{\mathrm{s}}_{\mathrm{cu},1} = 35\,\mu\mathrm{m}$ applied, the red bar annotated with B corresponds to $h^{\mathrm{s}}_{\mathrm{cu},2} = 20\,\mu\mathrm{m}$. Taken from [39].

Table 3.4: Kinematic simulation parameters.

Description	Parameter/Type	Value	Unit
Grinding wheel abrasive	cBN, mesh size	B 181	
Roughing zone angle	χ	7.5	°
Axial length of roughing zone	l_{rz}	4	mm
Axial length of finishing zone	l_{fz}	4	mm
Total touch-dressing removal	$a_{\mathrm{ed,tot}}$	16	µm
Workpiece circumferential velocity	v_{w}	2	m/s
Grinding wheel circumferential velocity	v_{s}	120	m/s
Axial feed of tool	a_{f}	0.75	mm
Total radial stock removal	$a_{\mathrm{e,tot}}$	0.15	mm
Lateral dexel grid resolution	Δl_{dex}	6.25	µm

4 Meso-scale single-grain model

In this chapter, the key component to the computation of the thermo-mechanical response on a meso-scale—in the present context defined as the proximity of a single cBN grain—of the grinding simulation framework is presented. Due to the evolving character of the underlying project framework, the meso-scale simulation has been evolving accordingly. Hence, different stages of our experience of the respective topic will be reflected in the progress of the present chapter.

As common in the scope of computational mechanics, we will introduce the underlying thermo-mechanic foundations, see Sec. 4.1, followed by the material modelling, Sec. 4.2 and the subsequent implementation of the former aspects in terms of finite element setups, see Sec. 4.3 onwards. While the material model is mainly adopted from the literature, the finite element framework presented in this work is essentially extended compared to previous finite element approaches, as outlined in the following.

At first, a basic study based on a fixed grain geometry is presented, which investigates meso-scale simulation parameter variations that result from an analytic approach to estimate those parameters as a function of process-scale parameters, cf. Sec. 4.4. After getting a fundamental insight on respective results, the finite element model will be extended to an entirely parametric formulation, enabling the convenient and efficient automatic generation of single grain models, cf. Sec. 4.5, to carry out a bridging of the meso-scale response to the macro-scale, which will be presented in the subsequent chapter of this thesis. To finalise the current chapter, a study investigating the behaviour of sequential multi-grain engagement to a certain workpiece surface region will be presented, see Section 4.7.

4.1 Basics of continuum thermomechanics

To introduce the thermo-mechanical quantities, which are necessary for a comprehensive description of the physical processes targeted in this work, a brief outline on the former is presented here. We will, of course, not unravel all details concerning the continuum theory of materials—for further insight, the reader is referred to the works of Altenbach [4], Bonet [18], Liu [59], Parisch [70], Wriggers [105] or the classic literature such as Truesdell and Noll [97].

Let us first recall that the motion of every material point $\boldsymbol{x}$ as part of a deformed body $\mathcal{B}$ is described by a nonlinear mapping

$$\boldsymbol{x} = \boldsymbol{\varphi}(\boldsymbol{X}, t) \in \mathcal{B} \tag{4.1}$$

as a function of its reference position $\boldsymbol{X} \in \mathcal{B}_0$ and time t. The deformation gradient is defined as

$$\boldsymbol{F} = \nabla_{\boldsymbol{X}} \boldsymbol{\varphi}(\boldsymbol{X}, t) = \frac{\partial \boldsymbol{\varphi}}{\partial \boldsymbol{X}} = \frac{\partial \boldsymbol{x}}{\partial \boldsymbol{X}}, \tag{4.2}$$

which, in turn, can be used to derive any deformation measure that is commonly used in our field of research, cf. [70]. We will present the following formulation in mainly spatial configuration using the Lagrangian description and

$$\dot{\bullet} = \left.\frac{\mathrm{d}\bullet}{\mathrm{d}t}\right|_{\boldsymbol{X}} \tag{4.3}$$

denoting the material time derivative. The transformation of infinitesimal line elements $\mathrm{d}\boldsymbol{x}$, infinitesimal area elements $\mathrm{d}\boldsymbol{a} = \boldsymbol{n}\,\mathrm{d}a$ and infinitesimal volume elements $\mathrm{d}v$ can be summarised as

$$\mathrm{d}\boldsymbol{x} = \boldsymbol{F} \cdot \mathrm{d}\boldsymbol{X}, \qquad \mathrm{d}\boldsymbol{a} = \operatorname{cof}(\boldsymbol{F}) \cdot \mathrm{d}\boldsymbol{A} \qquad \text{and} \qquad \mathrm{d}v = \det(\boldsymbol{F})\,\mathrm{d}V \tag{4.4}$$

with

$$\det(\boldsymbol{F}) = J > 0 \qquad \text{and} \qquad \operatorname{cof}(\boldsymbol{F}) = \frac{\partial J}{\partial \boldsymbol{F}} = J\,\boldsymbol{F}^{-\mathrm{t}}. \tag{4.5}$$

A fundamental balance law in terms of a closed system—which does neither allow exchange of matter over its boundaries, nor mass production within the bulk material—is the conservation of mass

$$\frac{\mathrm{d}m}{\mathrm{d}t} = \frac{\mathrm{d}}{\mathrm{d}t}\int_{\mathcal{B}_0} \varrho_0\,\mathrm{d}V = \frac{\mathrm{d}}{\mathrm{d}t}\int_{\mathcal{B}} \varrho_0\,J^{-1}\,\mathrm{d}v = \frac{\mathrm{d}}{\mathrm{d}t}\int_{\mathcal{B}} \varrho\,\mathrm{d}v = 0 \tag{4.6}$$

which is assumed to hold in the present case. The balance of linear momentum in integral spatial form is

$$\frac{\mathrm{d}}{\mathrm{d}t}\int_{\mathcal{B}} \dot{\boldsymbol{\varphi}}\,\varrho\,\mathrm{d}v = \int_{\mathcal{B}} \boldsymbol{b}\,\varrho\,\mathrm{d}v + \int_{\partial\mathcal{B}} \boldsymbol{\sigma} \cdot \boldsymbol{n}\,\mathrm{d}a, \tag{4.7}$$

with the body force vector $\boldsymbol{b}$, the Cauchy stress tensor $\boldsymbol{\sigma}$ and $\boldsymbol{n}$ denoting the spatial outward normal unit vector on $\partial\mathcal{B}$. Here and in the following, use of basic transport theorems is made. Applying the Gauss-Cauchy divergence theorem to the last term in (4.7)

$$\int_{\partial\mathcal{B}} \boldsymbol{\sigma} \cdot \boldsymbol{n} \, \mathrm{d}a = \int_{\mathcal{B}} \nabla_{\boldsymbol{x}} \cdot \boldsymbol{\sigma} \, \mathrm{d}v \tag{4.8}$$

then enables the derivation of the local spatial form of the balance of linear momentum as

$$\ddot{\boldsymbol{\varphi}} \, \varrho = \nabla_{\boldsymbol{x}} \cdot \boldsymbol{\sigma} \; + \boldsymbol{b} \, \varrho. \tag{4.9}$$

Since we assume a standard mechanical continuum neglecting any body couples, the Cauchy stress tensor $\boldsymbol{\sigma}$ can be proven to be symmetric and thus, the balance of angular momentum is automatically fulfilled based on the above balance of linear momentum, cf. [59].

The first law of thermodynamics states, that the change in time of the overall energy of a body equals the sum of external powers acting on the former. The entire energy of a body is decomposed into the kinetic

$$\mathscr{K} = \frac{1}{2} \int_{\mathcal{B}} \dot{\boldsymbol{\varphi}} \cdot \dot{\boldsymbol{\varphi}} \, \varrho \, \mathrm{d}v \tag{4.10}$$

and internal energy

$$\mathscr{E} = \int_{\mathcal{B}} e \varrho \, \mathrm{d}v, \tag{4.11}$$

where e denotes the energy density. The external power acting on a body is split into the rate of mechanical

$$\mathscr{P}_{\mathrm{ext}} = \int_{\mathcal{B}} \dot{\boldsymbol{\varphi}} \cdot \boldsymbol{b} \varrho \, \mathrm{d}v + \int_{\partial\mathcal{B}} \dot{\boldsymbol{\varphi}} \cdot \boldsymbol{\sigma} \cdot \boldsymbol{n} \, \mathrm{d}a \tag{4.12}$$

and the thermal energy supply

$$\mathscr{Q}_{\mathrm{ext}} = \int_{\mathcal{B}} r \varrho \, \mathrm{d}v - \int_{\partial\mathcal{B}} \boldsymbol{q} \cdot \boldsymbol{n} \, \mathrm{d}a. \tag{4.13}$$

Here, $\boldsymbol{\sigma} \cdot \boldsymbol{n} = \boldsymbol{t}$ denote external tractions acting on the boundary $\partial\mathcal{B}$ of the body under consideration, r denotes a volume-specific heat source and $\boldsymbol{q}$ represents the heat flux tensor, according to the convention, that $\operatorname{sgn}(\boldsymbol{q}) > 0$ refers to energy that is transported into $\mathcal{B}$. With this at hand, the first law of thermodynamics takes the form

$$\dot{\mathscr{E}} + \dot{\mathscr{K}} = \mathscr{P}_{\text{ext}} + \mathscr{Q}_{\text{ext}} \tag{4.14}$$

$$\int_{\mathcal{B}} \dot{e}\varrho \, \mathrm{d}v + \int_{\mathcal{B}} \dot{\boldsymbol{\varphi}} \cdot \ddot{\boldsymbol{\varphi}} \varrho \, \mathrm{d}v = \int_{\mathcal{B}} \dot{\boldsymbol{\varphi}} \cdot \boldsymbol{b} \, \varrho \, \mathrm{d}v + \int_{\partial\mathcal{B}} \dot{\boldsymbol{\varphi}} \cdot \boldsymbol{\sigma} \cdot \boldsymbol{n} \, \mathrm{d}a + \int_{\mathcal{B}} r \varrho \, \mathrm{d}v - \int_{\partial\mathcal{B}} \boldsymbol{q} \cdot \boldsymbol{n} \, \mathrm{d}a \tag{4.15}$$

$$\int_{\mathcal{B}} [\dot{e} + \dot{\boldsymbol{\varphi}} \cdot \ddot{\boldsymbol{\varphi}}] \, \varrho \, \mathrm{d}v = \int_{\mathcal{B}} [\dot{\boldsymbol{\varphi}} \cdot \boldsymbol{b} + r] \, \varrho \, \mathrm{d}v + \int_{\partial\mathcal{B}} [\dot{\boldsymbol{\varphi}} \cdot \boldsymbol{\sigma} \cdot \boldsymbol{n} - \boldsymbol{q} \cdot \boldsymbol{n}] \, \mathrm{d}a. \tag{4.16}$$

Since we assume all of the above measures to be sufficiently smooth over the domain $\mathcal{B}$, the Gauss-Cauchy divergence theorem holds and we can, with (4.7) or (4.9), respectively, therefore derive the local form of the energy balance from (4.16) as

$$\varrho \, \dot{e} = \boldsymbol{\sigma} : \boldsymbol{d} - \nabla_{\boldsymbol{x}} \cdot \boldsymbol{q} + \varrho \, r, \tag{4.17}$$

where $\boldsymbol{d} = [\nabla_{\boldsymbol{x}} \dot{\boldsymbol{\varphi}}]^{\text{sym}}$ denotes the symmetric part of the spatial velocity gradient. Note, that relation (4.17) can as well be rewritten in different stress power expressions, depending on the referring stress and strain measures, or configurations used, respectively. Applying a pull-back operation to (4.17) yields the referential local form of energy balance as

$$\varrho_0 \, \dot{e} = \boldsymbol{P} : \dot{\boldsymbol{F}} - \nabla_{\boldsymbol{X}} \cdot \boldsymbol{Q} + \varrho_0 \, r, \tag{4.18}$$

as a function of the Piola stress tensor $\boldsymbol{P} = \boldsymbol{\sigma} \cdot \operatorname{cof}(\boldsymbol{F})$ instead of the Cauchy stress tensor $\boldsymbol{\sigma}$. Note, that the referential form of the spatial heat flux vector $\boldsymbol{q}$ transforms to

$$\boldsymbol{Q} = \boldsymbol{q} \cdot \operatorname{cof}(\boldsymbol{F}) = J \, \boldsymbol{F}^{-1} \cdot \boldsymbol{q} = J \boldsymbol{q} \cdot \boldsymbol{F}^{-\text{t}}. \tag{4.19}$$

In terms of the Piola-Kirchhoff stress tensor $\boldsymbol{S} = \boldsymbol{F}^{-1} \cdot \boldsymbol{P}$ and the Green-Lagrange strain tensor $\boldsymbol{E} = 1/2 \, \left[\boldsymbol{F}^{\text{t}} \cdot \boldsymbol{F} - \boldsymbol{I}\right]$, the above relation then takes the form

$$\varrho_0 \dot{e} = \boldsymbol{S} : \dot{\boldsymbol{E}} - \nabla_{\boldsymbol{X}} \cdot \boldsymbol{Q} + \varrho_0 \, r, \tag{4.20}$$

which concludes the exemplary summary of energy-conjugated stress and strain measures in the present context.

Introducing now the entropy

$$\mathscr{S} = \int_{\mathcal{B}} s \varrho \, \mathrm{d}v \tag{4.21}$$

and using the second law of thermodynamics, which states that the entropy production $\dot{\mathscr{S}}$ is never smaller than the rate input of entropy $\mathscr{R}_{\text{ext}}$ with respect to a body $\mathcal{B}$

$$\dot{\mathscr{S}} - \mathscr{R}_{\text{ext}} = \int_{\mathcal{B}} \varrho\, \dot{s} - \varrho\, r \,\mathrm{d}v \geq 0, \tag{4.22}$$

the Clausius-Duhem inequality in global form results as

$$\int_{\mathcal{B}} \varrho\, \dot{s} \,\mathrm{d}v \geq \int_{\mathcal{B}} \frac{\varrho\, r}{\theta} \,\mathrm{d}v - \int_{\partial\mathcal{B}} \frac{\boldsymbol{q} \cdot \boldsymbol{n}}{\theta} \,\mathrm{d}a. \tag{4.23}$$

Here it is considered, that $\mathscr{R}_{\text{ext}}$ is assumed to be proportional to the thermal energy supply $\mathscr{Q}_{\text{ext}}$. The proportionality factor in this context is the inverse of the absolute (Kelvin) temperature $\theta > 0$. Applying the divergence theorem, the local spatial form

$$\varrho\, \theta \dot{s} \geq \varrho\, r - \nabla_{\boldsymbol{x}} \cdot \boldsymbol{q} + \boldsymbol{q} \cdot \nabla_{\boldsymbol{x}} \ln(\theta) \tag{4.24}$$

follows and yields

$$\varrho\, \theta \dot{s} - \varrho\, r + \nabla_{\boldsymbol{x}} \cdot \boldsymbol{q} - \frac{\boldsymbol{q} \cdot \nabla_{\boldsymbol{x}} \theta}{\theta} \geq 0, \tag{4.25}$$

which can be split into two fundamental dissipation contributions $\mathscr{D}_{\bullet}$, namely at first a thermal contribution

$$\mathscr{D}_{\text{therm}} = -\frac{\boldsymbol{q} \cdot \nabla_{\boldsymbol{x}} \theta}{\theta} \tag{4.26}$$

that reflects the rise of entropy as a result of inner heat conduction, and secondly a mechanical part which—with consideration of (4.17)—takes the form

$$\mathscr{D}_{\text{mech}} = \varrho\, \theta \dot{s} - \varrho\, r + \nabla_{\boldsymbol{x}} \cdot \boldsymbol{q} = \boldsymbol{\sigma} : \boldsymbol{d} - \varrho\, [\dot{e} + \theta\, \dot{s}]\,. \tag{4.27}$$

The latter term corresponds to the inner entropy production resulting from arbitrary—in general and in nature—irreversible changes of state, which the continuum $\mathcal{B}$ is undergoing with passing time. Considering the Helmholtz free energy density ψ, which is connected via the Legendre transform to the internal energy e,

$$\psi = e - \theta\, s \qquad \Rightarrow \qquad \dot{\psi} = \dot{e} - \dot{\theta}\, s - \theta\, \dot{s} \tag{4.28}$$

we can rewrite the mechanical dissipation (4.27) in terms of the free energy as

$$\mathscr{D}_{\text{mech}} = \boldsymbol{\sigma} : \boldsymbol{d} - \varrho \left[\dot{\psi} - \dot{\theta}\, s\right]. \tag{4.29}$$

This represents the general framework to thermodynamically consistently deduct all necessary equations to entirely describe the response of a thermo-mechanical material.

Following Truesdell and Noll [97], who assume, that in (4.25), both dissipation contributions have to be fulfilled separately, hence

$$\mathscr{D}_{\text{mech}} \geq 0 \qquad \text{and} \qquad \mathscr{D}_{\text{therm}} \geq 0 \tag{4.30}$$

must hold, a complete set of constitutive equations can be deducted, or proven thermodynamically consistent, respectively. To fulfil the latter, there exist different approaches to formulate the dissipation mechanism in terms of constitutive modelling, cf. [4]. In computational mechanics, it is common to use the concept of internal variables, so we postulate the existence of an energy potential

$$\psi(\boldsymbol{\mathcal{F}}, \theta, \boldsymbol{k}) \tag{4.31}$$

as a function of a general deformation tensor $\boldsymbol{\mathcal{F}}$, the temperature field θ and, additionally, a set of internal variables $\boldsymbol{k}$. With (4.28), it follows

$$\dot{\psi} = \frac{\partial \psi}{\partial \boldsymbol{\mathcal{F}}} : \dot{\boldsymbol{\mathcal{F}}} + \frac{\partial \psi}{\partial \theta}\,\dot{\theta} + \frac{\partial \psi}{\partial \boldsymbol{k}} \circ \dot{\boldsymbol{k}} \tag{4.32}$$

for the change of energy in the system. The operator $\circ$ in this context denotes a general scalar contraction, that fits the tensor order of $\boldsymbol{k}$, e.g., in case of $\boldsymbol{k} = k_{ij}\,\boldsymbol{e}_i \otimes \boldsymbol{e}_j$, we substitute $\circ \leftarrow :$ with the double contraction. Constituting this relation into (4.29) and splitting the expressions into reversible and irreversible parts, the equations for a general stress tensor $\boldsymbol{\mathcal{S}}$, which is thermodynamically conjugated to $\boldsymbol{\mathcal{F}}$, and the mass specific entropy s result directly from the Helmholtz potential derivatives

$$\boldsymbol{\mathcal{S}} = \varrho\,\frac{\partial \psi}{\partial \boldsymbol{\mathcal{F}}} \qquad \text{and} \qquad s = -\frac{\partial \psi}{\partial \theta}. \tag{4.33}$$

The remaining irreversible part of the dissipation

$$\mathscr{D}^{\text{red}}_{\text{mech}} = -\varrho\,\frac{\partial \psi}{\partial \boldsymbol{k}} \circ \dot{\boldsymbol{k}} = \boldsymbol{\kappa} \circ \dot{\boldsymbol{k}} \geq 0 \tag{4.34}$$

finally delivers the thermodynamic conditions for the postulation of evolution equations of the internal variables $\boldsymbol{k}$ with respect to the energy-conjugated thermodynamic driving force $\boldsymbol{\kappa}$. We can subsequently formulate a material property, that relates the temperature of a continuum to the change of entropy with respect to temperature, or relates the change of mass specific heat energy q_m to the change of temperature, respectively, as

$$\frac{\partial q_m}{\partial \theta} = \frac{\partial q_m}{\partial s}\frac{\partial s}{\partial \theta} = \theta\,\frac{\partial s}{\partial \theta} = c, \tag{4.35}$$

and with (4.33), we can finally derive the heat capacity, or specific heat c, respectively of a material as

$$c = \theta \frac{\partial s}{\partial \theta} = -\theta \frac{\partial^2 \psi}{\partial \theta^2}. \tag{4.36}$$

As the final component of these thermodynamic considerations, let us remark that from (4.26), one can generally postulate the thermal conduction of the material under consideration to be modelled. Hence, the heat flux vector and the gradient of the temperature always enclose an obtuse angle, and heat is always transported from higher to lower temperatures—thus,

$$\boldsymbol{q} = -\boldsymbol{\lambda} \cdot \nabla_{\boldsymbol{x}} \theta \tag{4.37}$$

describes a sensible, linear anisotropic relation with the positive definite thermal conductivity $\boldsymbol{\lambda}$, also known as Fourier's law of heat conduction. For isotropically heat conducting materials, $\boldsymbol{\lambda} = \lambda \boldsymbol{I}$ holds and we retain the commonly known (spatially) isotropic form

$$\boldsymbol{q} = -\lambda \nabla_{\boldsymbol{x}} \theta. \tag{4.38}$$

4.2 Material modelling

We apply an isotropic thermo-elastic and thermo-viscoplastic material model that is fully thermo-mechanically coupled. We assume large plastic strains reflecting the typical behaviour of ferrous metal based materials in the regime of manufacturing processes. We make use of a multiplicative split of the deformation gradient

$$\boldsymbol{F} = \boldsymbol{F}_{\mathrm{e}} \cdot \boldsymbol{F}_{\mathrm{p}}, \tag{4.39}$$

so that related logarithmic strains additively decompose as

$$\boldsymbol{\varepsilon} = \boldsymbol{\varepsilon}_{\mathrm{e}} + \boldsymbol{\varepsilon}_{\mathrm{p}} \tag{4.40}$$

with, e.g., the elastic strains being defined as

$$\boldsymbol{\varepsilon}_{\mathrm{e}} = \frac{1}{2} \ln \left(\boldsymbol{F}_{\mathrm{e}} \cdot \boldsymbol{F}_{\mathrm{e}}^{\mathrm{t}} \right). \tag{4.41}$$

Assuming isotropic material behaviour, the Cauchy stress takes the representation

$$\boldsymbol{\sigma} = [\lambda_0 \, \mathrm{tr}\,(\boldsymbol{\varepsilon}_{\mathrm{e}}) - [\,3\,\lambda_0 + 2\,\mu_0\,]\,\alpha_0\,\theta\,]\;\boldsymbol{I} + 2\,\mu_0\,\boldsymbol{\varepsilon}_{\mathrm{e}}, \tag{4.42}$$

and the heat flux is, according to the isotropic version of Fourier's law, postulated as

$$\boldsymbol{q} = -\lambda \, \nabla_{\boldsymbol{x}} \, \theta, \tag{4.43}$$

respectively. Here, λ_0 and μ_0 denote the Lamé constants, α_0 is the thermal expansion coefficient, λ characterises the isotropic thermal conductivity, and θ represents the absolute temperature.

The constitutive model is restricted to an isotropic hardening behaviour, neglecting the Bauschinger-Effect of kinematic hardening. We make use of the well-established Johnson-Cook approach, cf. [48], in combination with an isotropic von Mises type associated flow rule for the evolution of the yield stress

$$\sigma_{\mathrm{y}}^{\mathrm{JC}} = \Big[[A + B\,[1 - \exp(-\varepsilon_{\mathrm{p}} N)]\Big] \left[1 + C\,\ln\left(1 + \frac{\dot{\varepsilon}_{\mathrm{p}}}{\dot{\varepsilon}_{\mathrm{p},0}}\right)\right] \left[1 - \left\langle \frac{\theta - \theta_0}{\theta_m - \theta_0} \right\rangle^{M}\right] \tag{4.44}$$

with $\langle \bullet \rangle$ denoting the McCauley operator defined as $\langle x \rangle \equiv \frac{1}{2}\,[x + |x|]$. Hence, the material model incorporates strain and strain rate dependent work hardening as well as thermal softening. The material parameters A, B, C, M, N, $\dot{\varepsilon}_{\mathrm{p},0}$ and θ_0 are taken from [43]. The full set of material parameters used in this section is depicted in Tab. A.2.

As common in high speed machining simulations, we introduce a local ductile damage variable d representing the local amount of micro-cracks and micro-voids. In the present framework, we restrict the damage—or more precisely softening influence—to a local approach that is evaluated solely at the material point level of the body under consideration. Though this technique inhibits the general drawback of mesh-dependency and is most elegantly solved by a non-local gradient-enhanced finite-element framework, cf. [40, 101, 102], we will incorporate adaptive remeshing to overcome this issue, see Sec. 4.3. The internal damage variable d evolves according to the saturation type equation

$$\dot{d} = \vartheta_d \, \left\langle \varepsilon_{\mathrm{p}} - \varepsilon_{\mathrm{p}}^{d} \right\rangle \, \left[\, \overline{d} - d \,\right] \, \dot{\varepsilon}_{\mathrm{p}} \tag{4.45}$$

with ϑ_d being the saturation rate, $\overline{d}$ denoting the saturation value and $\varepsilon_{\mathrm{p}}^{d}$ the critical accumulated plastic deformation activating the damage evolution. The accumulated plastic strain is given as

$$\varepsilon_{\mathrm{p}}(t) = \varepsilon_{\mathrm{p}}|_{t=0} + \int_0^t \sqrt{\frac{2}{3}\,\dot{\boldsymbol{\varepsilon}}_{\mathrm{p}} : \dot{\boldsymbol{\varepsilon}}_{\mathrm{p}}}\,\mathrm{d}t. \tag{4.46}$$

Following this ansatz, the yield stress then takes the form

$$\sigma_{\mathrm{y}} = [\,1 - d\,]\,\sigma_{\mathrm{y}}^{\mathrm{JC}}, \tag{4.47}$$

enabling the modelling of shear band evolution during the cutting process, which is discussed as this work proceeds.

Finally, the generation of heat in the model is based on plastic work on the one hand and frictional contact on the other. Thus, it is assumed that only a constant fraction η of the plastic work contributes to the local mass specific energy balance [93, 106], namely

$$\Delta r = \eta\, \boldsymbol{\sigma} : \dot{\boldsymbol{\varepsilon}}_{\mathrm{p}} \tag{4.48}$$

is added to the thermal energy balance. Furthermore, the influence of friction or surface traction, respectively, contributes to the local energy balance in terms of a rate of work

$$\int_{\partial\mathcal{B}^{\mathrm{c}}} \dot{\boldsymbol{\varphi}} \cdot \boldsymbol{t}\;\mathrm{da} = \int_{\partial\mathcal{B}^{\mathrm{c}}} \dot{\boldsymbol{\varphi}} \cdot \boldsymbol{\sigma} \cdot \boldsymbol{n}\;\mathrm{da} = \int_{\partial\mathcal{B}^{\mathrm{c}}} \tau\, \dot{\xi}\;\mathrm{da} \tag{4.49}$$

with $\partial\mathcal{B}^{\mathrm{c}}$ being the boundary contact surface, $\boldsymbol{v}$ and $\boldsymbol{t}$ denoting the spatial velocity field vector and the surface traction vector, respectively. The incremental slip between the two contact surfaces is represented by $\dot{\xi}$, the absolute shear stress value by τ.

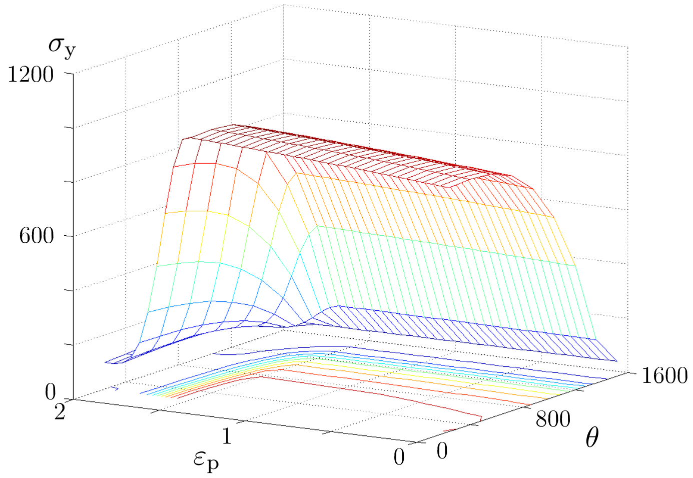

Figure 4.1: Exemplary yield surface representation as a function of temperature θ and plastic strain ε_p, illustrating the strain depending hardening and softening behaviour implemented.

4.3 Finite Element Implementation

To predict the amount of thermal energy per cBN grain being transported into the workpiece material during grinding, a two-dimensional plane strain FE model reflecting the proximity of one single grain on the meso-scale is considered. The basic setup

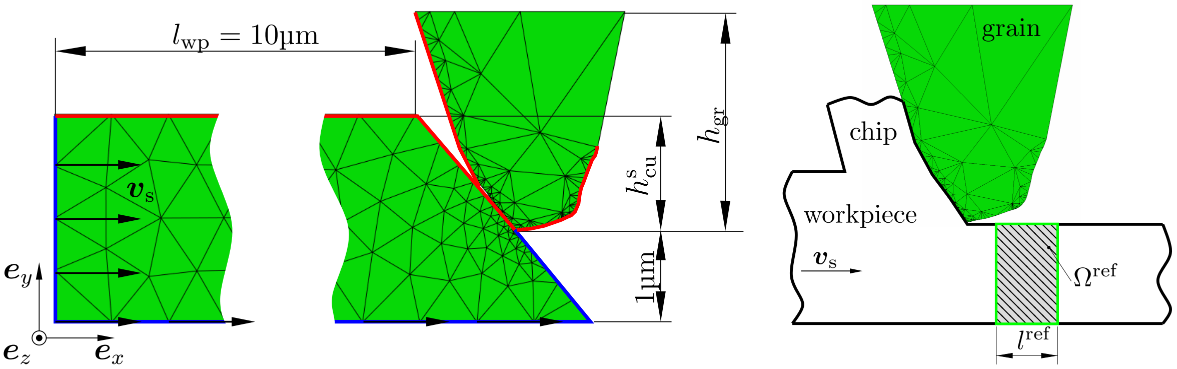

Figure 4.2: Meso-scale model setup displaying workpiece and grain with initial mesh and main dimensions at $t = 0$ (left) and reference volume Ω_{ref} for $t > 0$ (right). The grain is modelled as fixed rigid body, whereas on the blue region of the workpiece thermal ($\theta \equiv 300\,\mathrm{K}$) and mechanical ($\boldsymbol{v}_{\mathrm{s}}$) boundary conditions are applied. The red edges are defined as contact surfaces.

including the relevant dimensions and boundary conditions of the model is depicted in Figure 4.2. The grain is modelled as a rigid conductor, whereas the workpiece consists of the material discussed in the previous section. The workpiece is moved with a constant velocity of v_{s} in $\boldsymbol{e}_x$ direction, cf. blue edges in Fig. 4.2.

A grain geometry resulting from the topography analysis is used. The red edges in Figure 4.2 depict corresponding contact pairs. In addition to the contact between grain and workpiece, self contact of the latter surface is also enabled since the chip generated usually touches the free workpiece during the chip formation process. We use a Lagrangian formulation which is solved by an explicit time integration scheme using the commercial software Abaqus/Explicit.

The well-known main issues in the field of modelling high speed machining processes are large deflections at high strain rates with possible occurrence of local workpiece bulk separation. To overcome related algorithmic problems, widely employed methods are, e.g., a prescribed damageable / deleteable element layer or a remeshing algorithm to capture the structural response accordingly. Since the first method inherently induces a pre-defined deformation pattern regarding chip deformation, cf. [41], we employ an h-adaptive remeshing scheme developed in earlier work, cf. [40].

This enables us to overcome mesh dependency of the FE solution and allows the calculation of the onset and evolution of shear bands which in turn is essential for the predictive simulation of the resulting chip shape. Currently, besides a Zienkiewicz and Zhu error estimate, cf. [108], two additional, more physically motivated indicators are used to trigger local mesh refinement. These are firstly the equivalent plastic strain $\varepsilon_{\mathrm{p}}(t)$ and secondly it's rate, i.e. $\dot{\varepsilon}_{\mathrm{p}} = \mathrm{d}\varepsilon_{\mathrm{p}}(t)/\mathrm{d}t$. After a mesh refinement step, the nodal as well as the internal variables at the integration point level are mapped from one mesh to another using the superconvergent patch recovery technique proposed by Zienkiewicz and Zhu, cf. [107]. Coarsening of the element size is implemented by a spatial specification, i.e. as soon as the chip material exceeds the top of the grain, a gradually increasing element size is enforced.

In detail, the adaptivity method can be used in a very flexible manner, so the field variables on which the error estimation and mesh refinement is based, can be chosen freely from a sensible combination of variables. Let $\boldsymbol{\vartheta}(\boldsymbol{x})$ denote an arbitrary field variable of any dimension resulting from a finite element approximation of polynomial order p and a characteristic element size h in the neighbourhood $\mathcal{N}_{\boldsymbol{x}}$ of $\boldsymbol{x}$. The Zienkiewicz and Zhu (Z^2) error estimate $\boldsymbol{e}_\vartheta$ with respect to this variable is then defined as

$$\boldsymbol{e}_\vartheta = \widehat{\boldsymbol{\vartheta}} - \boldsymbol{\vartheta}, \tag{4.50}$$

where $\widehat{\boldsymbol{\vartheta}}$ denotes a more accurate solution of the finite element problem in terms of a Z^2 superconvergent node patch recovery [108]. The latter is computed by the determination of a polynomial function $P(\boldsymbol{x}, \boldsymbol{a}) = \boldsymbol{p} \cdot \boldsymbol{a}(\boldsymbol{x})$ of at least order $p + 1$, which approximates the field function $\boldsymbol{\vartheta}(\boldsymbol{x}) \in \mathcal{N}_{\boldsymbol{x}}$. In the present case of two-dimensional linear finite elements, $\boldsymbol{p} = [1, x_1, x_2, x_1^2, x_1\, x_2, x_2^2]$ represents the minimum approximation ansatz. The parameter vector $\boldsymbol{a}$ to entirely define P is determined by a least square fit that uses the values of $\boldsymbol{\vartheta}$ at the n integration points $\boldsymbol{x}_k^{\mathrm{GP}}$ of the element patch $\mathcal{N}_{\boldsymbol{x}}$ surrounding the nodal position $\boldsymbol{x}$. This yields the non-linear minimisation problem

$$\boldsymbol{a} = \operatorname{argmin} \left(\sum_{k=1}^{n} \left[\vartheta(\boldsymbol{x}_k^{\mathrm{GP}}) - P(\boldsymbol{x}_k^{\mathrm{GP}}, \boldsymbol{a}) \right]^2 \right) \tag{4.51}$$

to be solved for every component ϑ of $\boldsymbol{\vartheta} = \vartheta_i\, \boldsymbol{e}_i$. The recovered solution is finally computed via $\widehat{\boldsymbol{\vartheta}}(\boldsymbol{x}) = P_i(\boldsymbol{x}, \boldsymbol{a}) \boldsymbol{e}_i$. Knowing this error estimate $\boldsymbol{e}_\vartheta$ now at every node position of the workpiece body $\boldsymbol{x} \in \mathcal{B}$, the new local element size $\overline{h}$ is finally estimated by

$$\overline{h} = h \left[\frac{\|\boldsymbol{e}_{\boldsymbol{\vartheta}}\|}{\|\boldsymbol{e}_{\boldsymbol{\vartheta}}\|_{\max}} \right]^{-\frac{1}{p}}, \tag{4.52}$$

based on the assumption $\|\boldsymbol{e}_{\boldsymbol{\vartheta}}\| \sim h^p$, cf. [40], where $\|\boldsymbol{e}_{\boldsymbol{\vartheta}}\|_{\max}$ denotes the defined maximum error L^2 norm with respect to the variable $\boldsymbol{\vartheta}$. As already mentioned above, the definition of a local maximum error magnitude

$$\|\boldsymbol{e}_{\boldsymbol{\vartheta}}\|_{\mathcal{N}_{\boldsymbol{x}}} < \|\boldsymbol{e}_{\boldsymbol{\vartheta}}\|_{\max} \tag{4.53}$$

to define the local mesh refinement strategy can be extended in a flexible way to be suitable for a wide range of applications.

To illustrate a general tendency of the heat induced into the workpiece during the abrasive process under consideration, let us consider the volume-specific heat energy $\mathcal{Q}$ that is transported into the workpiece, or more precisely, the ground partition of the

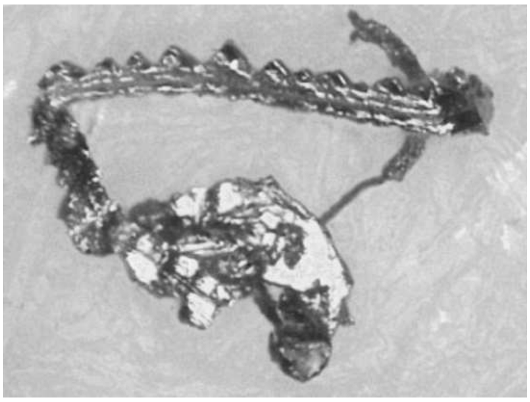

Figure 4.3: Micrograph of a serrated chip, produced by Internal Traverse Grinding. Taken from [37].

workpiece. Since in the present case, a complete separation of chip and workpiece is not implemented, we invoke a reference volume Ω_{ref} that reflects the latter workpiece part to formulate a corresponding heat measure, based on the thermodynamic balance laws presented earlier:

$$\mathcal{Q}(t) = \frac{\displaystyle\int_{\Omega_{\mathrm{ref}}} \varrho\, c\,[\theta(t) - \theta_0]\,\mathrm{d}v}{\displaystyle\int_{\Omega_{\mathrm{ref}}} \mathrm{d}v}, \tag{4.54}$$

The reference temperature θ_0 is set to $\theta_0 = 300\,\mathrm{K}$ here, c denotes the mass specific heat capacity of the workpiece material. Since we are at first only interested into a qualitative trend, this measure will be normalised to its maximum value for the subsequent postprocessing, i.e.

$$\bar{\mathcal{Q}}(t) = \frac{\mathcal{Q}(t)}{\max\left(\mathcal{Q}(t)\right)} \tag{4.55}$$

will be plotted in the following result graphs.

4.4 Numerical examples and results

The present section outlines first results of the thermo-mechanical load compound that is acting on the workpiece during the meso-scale simulation. Due to the kinematics of the process under consideration, the meso-scale process parameters, namely circumferential wheel speed v_{s} and equivalent chip thickness $h_{\mathrm{cu}}^{\mathrm{s}}$, depend on each other. The relation

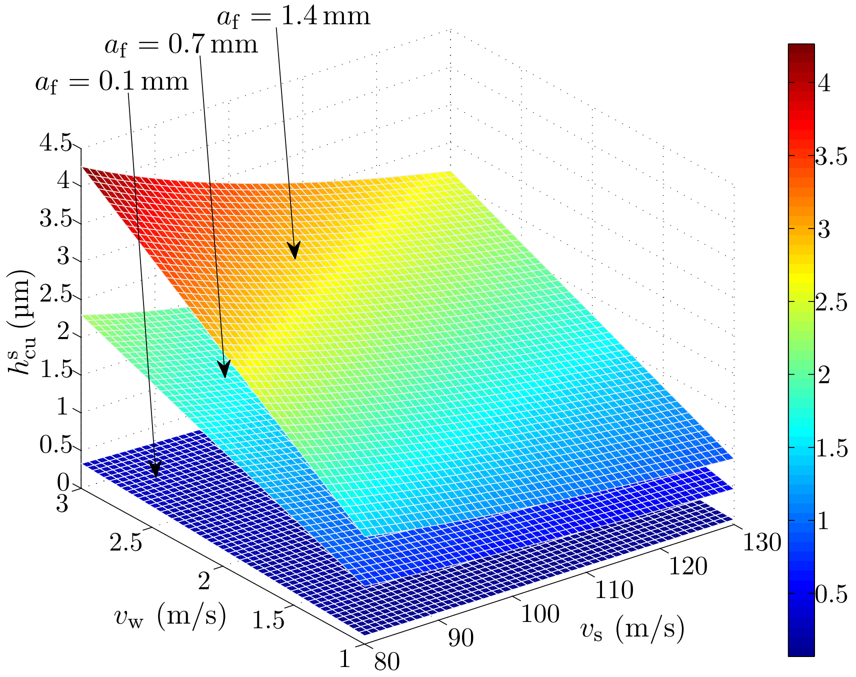

Figure 4.4: Functional dependency between macroscopic and mesoscopic process parameters. In the current case, an axial feed rate of $a_\mathrm{f} = 0.7$ mm/rev (middle plane) is used.

between these meso-scale and the macro-scale parameter magnitudes v_fa, v_s, v_w and $a_\mathrm{e,tot}$ result from the continuity equation, cf. e.g. [52, 66],

$$h^\mathrm{s}_\mathrm{cu} = \frac{Q'_\mathrm{w}}{v_\mathrm{s}} = a_\mathrm{f}\,\tan(\chi)\,\frac{v_\mathrm{w}}{v_\mathrm{s}} \tag{4.56}$$

which is visualised in Figure 4.4. In this context, Q'_w denotes the specific material removal rate [66]. To model a macroscopic variation of v_s, both meso-scale parameters have to be adjusted accordingly. For the present experimental study, the resulting sets of parameters are shown in Tab. 4.1. Besides the combined variation of v_s and h^s_cu, both of these parameters are varied separately while the other one is fixed, resulting in a total of three numerical test series, each consisting of five meso-scale simulations.

As mentioned above, the main purpose of the meso-scale simulations is to determine the thermal energy being transported into the workpiece material. What turns out to be really challenging in this context, is the correct transfer of the meso-scale thermal response to the macro-scale model in terms of thermodynamically consistent boundary conditions.

Table 4.1: Process parameters of the experiments #1 to #5 performed. The first line denotes the macroscopic circumferential wheel speed whereas the lower two lines represent the according meso-scale parameters.

parameter	unit	#1	#2	#3	#4	#5
v_s	m/s	82	88	94	100	106
h^s_cu	µm	1.5	1.4	1.3	1.2	1.1

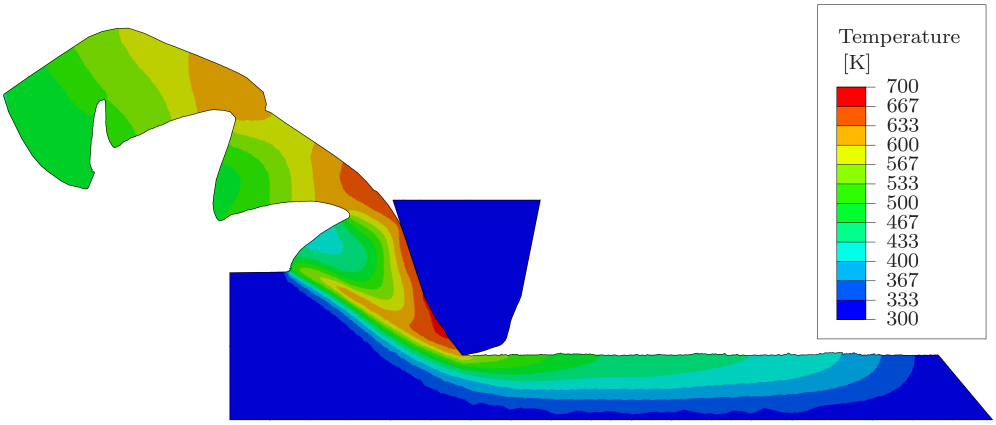

Figure 4.5: Temperature contour plot for undeformed chip thickness $h^\mathrm{s}_\mathrm{cu} = 1.3\,\mu\mathrm{m}$ at cutting speed $v_\mathrm{s} = 94$ m/s. The induced temperature rise resulting from plastic dissipation can nicely be observed in the primary shear zone. Taken from [37].

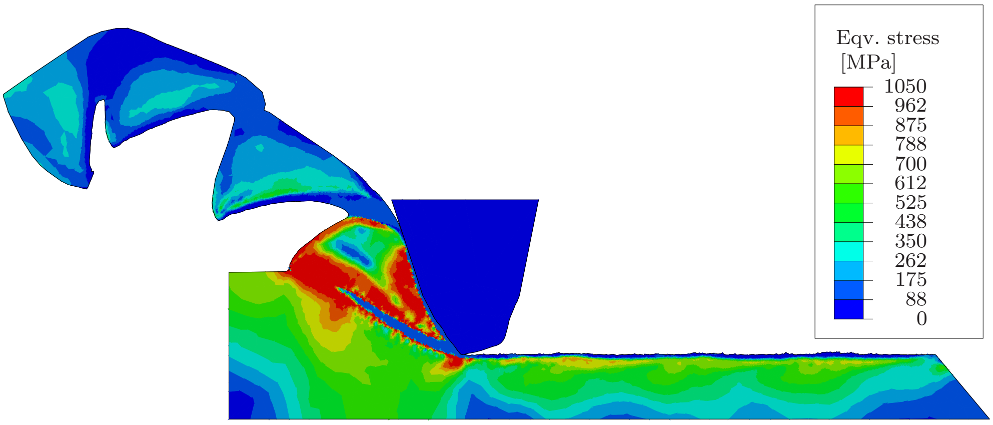

Figure 4.6: Equivalent stress contour plot for undeformed chip thickness $h^\mathrm{s}_\mathrm{cu} = 1.3\,\mu\mathrm{m}$ at cutting speed $v_\mathrm{s} = 94$ m/s. The softening effect of the material law can be seen in the onset of the shear band. Taken from [37].

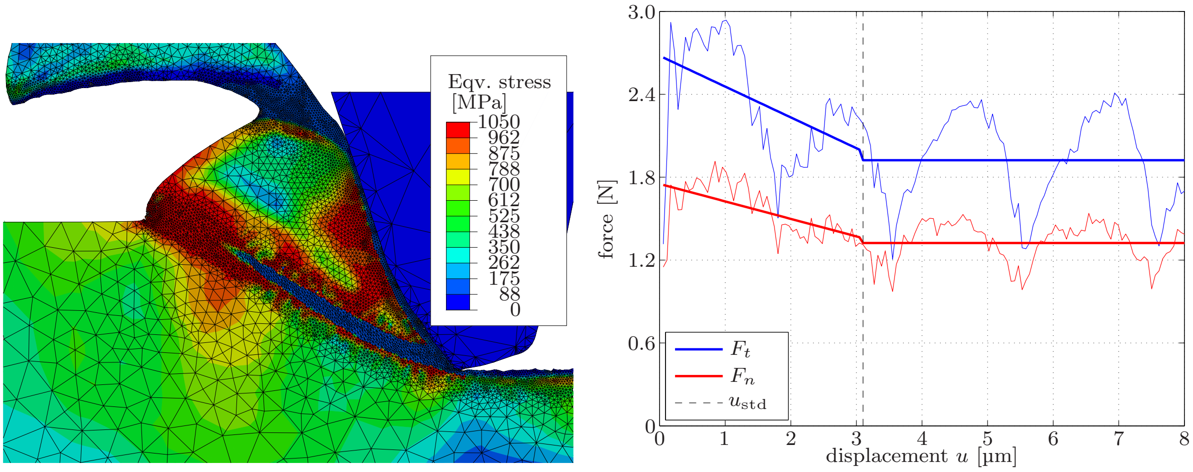

Figure 4.7: Mechanical results for undeformed chip thickness $h^{\mathrm{s}}_{\mathrm{cu}} = 1.3\,\mu\mathrm{m}$ at cutting speed $v_{\mathrm{s}} = 94\,\mathrm{m/s}$. Contour plot showing the von Mises equivalent stress and the adaptive mesh (left), and graph depicting the corresponding cutting force evolution (right). The vertical dashed line depicts the start of the steady state domain. Taken from [37].

The result of an exemplary meso-scale simulation is shown in Figures 4.5 and 4.6, depicting the temperature distribution and the resulting von Mises equivalent stress field

$$\sigma_{\mathrm{vM}} = \sqrt{\frac{3}{2}\boldsymbol{\sigma}_{\mathrm{dev}} : \boldsymbol{\sigma}_{\mathrm{dev}}} \tag{4.57}$$

for the entire model domain. Clearly visible is the serrated chip outline which is typically observed in high speed cutting processes, cf. [72] and Figure 4.3. Secondly, the temperature distribution nicely reflects the two major heat generating mechanisms in the model: The frictional influence causes high temperatures at the contact zone between chip and grain rake face, denoted as secondary shear zone, whereas the plastic work contribution can be nicely seen in the primary shear zone, i.e. in the connecting line between the cutting edge at the lower grain tip and the free workpiece surface. What can also be observed is that the major fraction of the heat generated is conducted into the chip and therefore transported away from the reference volume in the workpiece. The contour plot of the latter region therefore shows maximum temperatures of about 550 K.

The onset of a shear band can be seen in the corresponding stress plot, where a sharply separated domain of very low stress is observed in the primary shear zone, see Fig. 4.6. A closer look at the process zone with the mesh depicted, cf. Fig. 4.7, emphasises the mesh-independent shear band development: The adaptive remeshing algorithm causes the mesh in the primary shear zone to become very fine whilst the mesh in the unmachined workpiece regions remains rather coarse. Above the top of the grain, the above-mentioned mesh coarsening takes place. The right subfigure shows the development of the cutting force components: The blue curve depicts the tangential

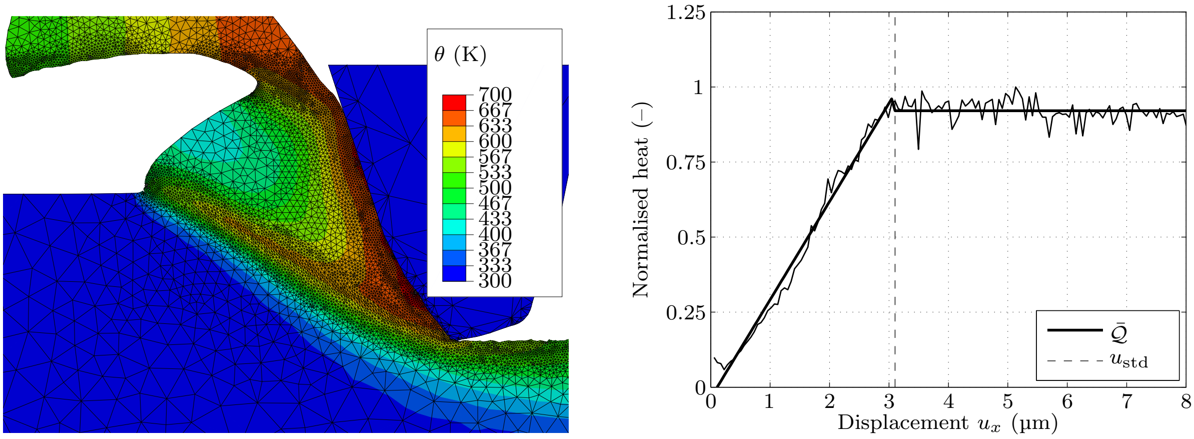

Figure 4.8: Thermal results for undeformed chip thickness $h^{\mathrm{s}}_{\mathrm{cu}} = 1.3$ µm at cutting speed $v_{\mathrm{s}} = 94$ m/s. The contour plot depicts the resulting temperature field (left) whereas the graph shows the time dependent heat generation (right). The vertical dashed line depicts the onset of the steady state domain. Taken from [37].

component, i.e. the reaction force in $\boldsymbol{e}_x$ direction, the red curve shows the normal component which corresponds to the reaction force in $\boldsymbol{e}_y$ direction of the meso-scale model, cf. Fig. 4.2. Both curves show an oscillating behaviour with approximately constant magnitude but evolving mean value as depicted by the straight lines in the graph.

The oscillation can be explained by the cyclic shear band evolution: The ascending slope in the graph shows the agglomeration of material which is accompanied by the generation of a shear band up to the local maximum of the force curve. Once the shear band has evolved completely, the remaining chip material above the shear band slips on the latter which corresponds to the descending slope of the cutting force curve. At the stage where the minimum force occurs, agglomeration of the workpiece material starts again and the cycle is “closed”.

The change in the mean value of the forces can be explained by the upcoming steady state behaviour of the simulation. At the beginning of the simulation, the process forces are high due to the mechanical boundary conditions of the model. After about one third of the overall horizontal displacement of the workpiece considered, the mean value of the process force remains constant which finally is the value that is transferred to the tendency charts, see Figs. 4.9 and 4.10.

A similar steady state behaviour is observable in the thermal response, cf. Figure 4.8. Here, the chart to the right depicts the evolution of the heat transported into the workpiece. From the beginning of the simulation, the heat generation rises approximately linearly up to the point of time where a steady state is reached –marked with the vertical dashed line in the graph– which reflects a constant mean value of heat generation. This mean value is the one used in the following tendency charts.

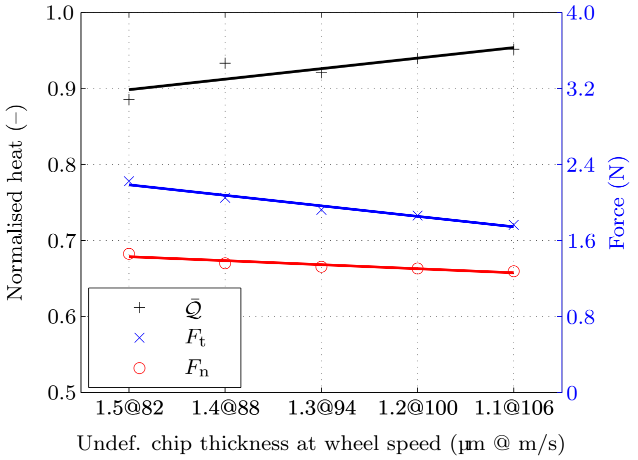

Figure 4.9: Finite element results of meso-scale full variation scheme, cf. Tab. 4.1. Taken from [37].

Figures 4.9 and 4.10 depict the tendency of the values under consideration, i.e., normalised heat $\bar{Q}$ as well as tangential and normal cutting force components $F_\mathrm{t} = \boldsymbol{F}_\mathrm{c} \cdot \boldsymbol{e}_x$ and $F_\mathrm{n} = \boldsymbol{F}_\mathrm{c} \cdot \boldsymbol{e}_y$ over the combined and the separated variation of the meso-scale process parameters h^s_cu and v_s, respectively.

In all three numerical experiments, the normal cutting force component F_n is significantly smaller than the tangential one F_t which is in contrast to the macroscopic behaviour typically observable in experiments, cf. [52], as in the present case, too, cf. Fig. 1.4. This phenomenon can be explained by two effects: Firstly, the meso-scale simulation is, up to this point, just two-dimensional under plane strain conditions. Hence, even for a small stock removal given, i.e., small undeformed chip thickness, the resulting tangential force component exceeds the normal one. In three-dimensional simulations though, the normal component rises at very shallow cuts due to the rather forming than cutting material deformation in the marginal zones of the cut which cannot be captured by two-dimensional models. Secondly, the aforementioned effect even increases when invoking a coupling of multiple grains which has not been implemented yet. Taking into account only one single grain, the force tendency recorded in the simulations seems reasonable, since in $\boldsymbol{e}_x$-direction a higher amount of plastic work has to be spent than in the normal direction to deform the material. Since, in the regime of high speed cutting processes, variations of the cutting speed result in nearly negligible cutting force responses, it is judicious that the current development of F_t increases by about 27 % from 1.7 N to 2.2 N when increasing h^s_cu by approximately 36 % from 1.1 to 1.5 µm, cf. Fig. 4.10.

Interestingly, the force curves in Figs. 4.9 and 4.10, right—illustrating the full and chip thickness variation, respectively—barely show any difference although the force curves in Fig. 4.10 are at least slightly ascending. In conclusion, the combined parameter variation seems to diminish the influence of the meso-scale cutting speed. Consequently, the cutting force trend for the combined parameter variation is predominantly driven

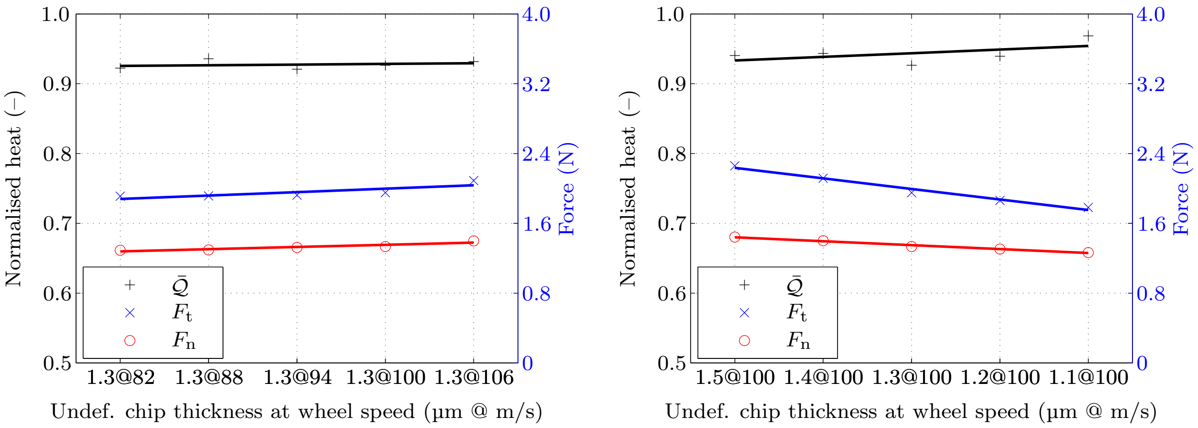

Figure 4.10: Left: Finite element results of meso-scale circumferential wheel speed variation at fixed undeformed chip thickness $h^{\mathrm{s}}_{\mathrm{cu}} = 1.3$ µm. Right: Undeformed chip thickness variation at a fixed circumferential wheel speed of $v_{\mathrm{s}} = 100$ m/s. Taken from [37].

by the change in the undeformed chip thickness $h^{\mathrm{s}}_{\mathrm{cu}}$. This again supports the above statement that a cutting speed variation in high speed machining causes only negligible force changes.

Considering the heat induction trend, the decrease of the chip thickness, cf. Fig. 4.10, results in an increase of the heat energy whereas with increasing cutting speed v_{s}, the heat value remains approximately constant. The combined variation of the meso-scale parameters which reflects the macroscopic wheel speed variation, causes a stronger rise in the heat generation, cf. Fig. 4.9, which nicely coincides with the experimental results shown in Fig. 1.4. However, due to the missing grain interaction not implemented yet, the rise of the resulting heat induction should be significantly lower in the mesoscopic single grain simulations because the equivalent amount of material, according to (4.56), is in the latter simulation removed by only one grain. Since on the other hand the macroscopic variation of the wheel speed v_{s} does not affect the material removal rate Q_{w}, the amount of material removed is distributed among more grains with smaller undeformed chip thickness and worse thermal efficiency, resulting in a steeper overall rise of induced heat which is shown in Fig. 1.4. Here, the surface temperature which is proportional to the absolute heat value, rises from about 80 % to 100 % of it's maximum, whereas in the meso-scale simulation, an increase from 90 % to the largest value is observed, supporting the above-mentioned statement.

To compare the outcome when carrying out the same meso-scale simulation with two arbitrary grain geometries resulting from the topography analysis, cf. Sec. 2.4, we can investigate Figures 4.11 and 4.12. Here, the cutting speed is kept constant at $v_{\mathrm{s}} = 94\,\mathrm{m/s}$ while maintaining an undeformed chip thickness of $h^{\mathrm{s}}_{\mathrm{cu}} = 0.65\,\mathrm{µm}$; the remaining simulation conditions are equal to the ones presented so far.

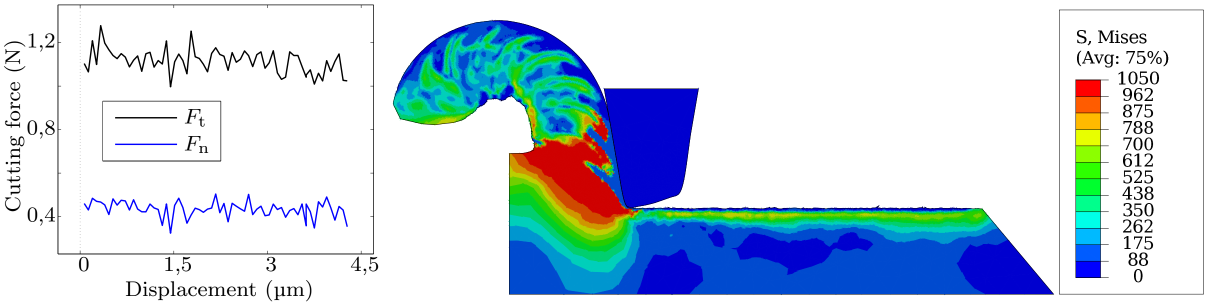

Figure 4.11: Meso-scale simulation results for a small magnitude rake angle $\hat{\gamma}_\mathrm{s} \approx -10°$: Force-displacement plot (left) and v. Mises equivalent stress (MPa), right. Taken from [36].

We can observe distinguishably different chip formation patterns, which in turn result in a corresponding evolution of cutting force components $F_\mathrm{t} = \boldsymbol{F}_\mathrm{c} \cdot \boldsymbol{e}_x$ and $F_\mathrm{n} = \boldsymbol{F}_\mathrm{c} \cdot \boldsymbol{e}_y$, referring to the coordinate system depicted in Fig. 4.2. As already stated in Chapter 2, rake angles are exclusively negative in the context of grinding and evince a maximum frequency for rake angles ranging in-between $-75° \leq \gamma_\mathrm{s} \leq -45°$, compare Fig. 2.13. Therefore, the two cases depicted with approximated rake angles of $\hat{\gamma}_\mathrm{s} \approx -10°$ and $\check{\gamma}_\mathrm{s} \approx -40°$ do not represent the most likely occurring engagement conditions.

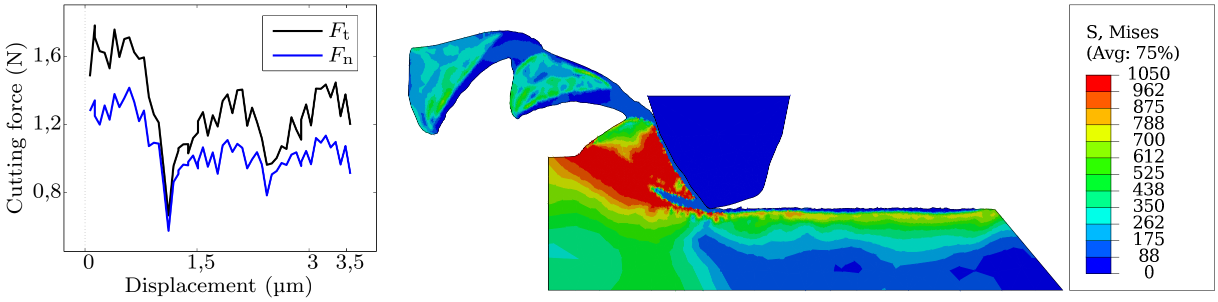

Figure 4.12: Meso-scale simulation results for a larger magnitude rake angle: Force-displacement plot (left) and v. Mises equivalent stress (MPa), right. Taken from [36].

However, the two opposing chip formation characteristics are more conveniently presentable in the present context. In the first case of $\hat{\gamma}_\mathrm{s}$, we can observe exactly the transition range between a flow chip and a serrated chip formation: The outline of the chip reflects a flow characteristic, however, based on the stress values depicted, we can clearly see periodically occurring strain localisation zones represented by low-stress areas. Hence, in these areas, the softening of the material has been active, although not in such extend, that actual shear banding is observable. The latter is, however, clearly visible in the simulation with $\check{\gamma}_\mathrm{s} \approx -40°$ applied: We can see, that the periodically occurring, deteriorated zones are far more evolved than in the first case, resulting in a clearly serrated chip, as also visible in Figures 1.5, 1.6 and 4.3. It comes as no surprise, that the tangential force component evolutions reflect the according chip formation state, but interestingly, the average value in both numerical experiments displayed is $F_\mathrm{t} \approx 1.2\,\mathrm{N}$ in the steady-state range. Opposing, the normal cutting force component evinces a close to constant value of $\hat{F}_\mathrm{t} \approx 0.4\,\mathrm{N}$ in the case of the steeper rake angle $\hat{\gamma}_\mathrm{s}$, but turns out to be more as twice as high, namely $\check{F}_\mathrm{t} \approx 0.9\,\mathrm{N}$ when cutting the material at an angle of $\check{\gamma}_\mathrm{s}$. In turn, this means, that the energy supply—with respect to the entire model presented—for $\check{\gamma}_\mathrm{s} \approx -40°$ is more that double as in the other case presented, which is supported by the equivalent stress fields observable. We can therefore conclude, that the meso-scale material removal becomes energy-wise more inefficient and thus, should generate a larger overall amount of heat in the model. However, it is yet to be investigated, if this energy difference will be observable in the remaining workpiece body in terms of higher temperatures, or if it will be conveyed to the chip and hence, will not have such a drastic impact on the workpiece.

4.5 Parametric boundary value problem formulation

In this section, the extension of the finite element simulation presented above towards a fully parametric single grain model is presented. The parametric design, in turn, enables an efficient automation of the simulation framework, which is important when aiming at an automatic bridging of the meso-scale thermo-mechanical results to be used as thermo-mechanical loads on the macro-scale. Therefore, the parametrisation of the underlying model constitutes the first step to accomplish this task. Regarding the grain shape, which is so far exported from the topography analysis, a drastic simplification of the cutting edge geometry needs to executed. As visible in Figures 4.11 and 4.12, and already briefly discussed in the above sections, the entire rake face of a grain can in the simplest fashion be approximated by a straight line. This constitutes an acceptable approximation, since it could be shown in the numerical experiments above, that the resulting friction between grain rake face and chip mainly affects the chip temperature and has a negligible influence

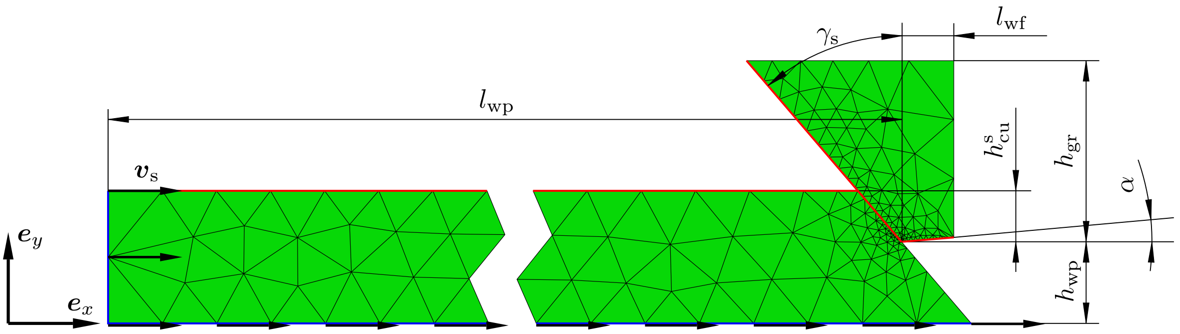

Figure 4.13: Boundary value problem for the parametric single grain model with simplified grain geometry. The red marked edges denote contact pairs, the blue marked edges represent the regions that are loaded with Dirichlet boundary conditions, such as the grinding wheel circumferential velocity $\boldsymbol{v}_\mathrm{s}$.

on the resulting workpiece heat induction, which we are interested in. Following this approach, we parametrise the rake face geometry for a plane strain assumption solely by the rake face angle γ_s. The next two major parameters to describe the single grain cutting conditions are the undeformed chip thickness h^s_cu and of course the cutting velocity magnitude v_s. This parameter tuple $\mathcal{P}_\mathrm{meso} = \{h^\mathrm{s}_\mathrm{cu}, \gamma_\mathrm{s}, v_\mathrm{s}\}$ will subsequently be used to evolve the fundamental theories. As widely known from experiments, the wear flat area of grains, comparable to the flank face in orthogonal cutting, basically constitutes a further parameter and will also be implemented in terms of the parametric model. In analogy to the orthogonal cutting model, we therefore introduce the flank, or relief angle α along with the flank face length, or wear flat area length l_wf, respectively. The extended parameter set is therefore denoted as $\mathcal{P}^\mathrm{ext}_\mathrm{meso} = \{h^\mathrm{s}_\mathrm{cu}, \gamma_\mathrm{s}, v_\mathrm{s}, \alpha, l_\mathrm{wf}\}$ The resulting general model is illustrated in Fig. 4.13.

All remaining geometric measures, i.e., lengths and angles, as well as all simulation parameters—such as overall simulation time, time incrementation and remeshing parameters—which are necessary to entirely define the underlying boundary value problem are subsequently defined as a functions of the above-mentioned parameters sets $\mathcal{P}^\bullet_\mathrm{meso}$.

Workpiece length The workpiece length l_wp is defined as 15 times the undeformed chip thickness and is extended by a dependency of the rake angle to elongate the workpiece for large magnitude rake angles, so

$$l_\mathrm{wp} = \left[15 + \frac{20}{\tan\left(\gamma_\mathrm{s} + \frac{\pi}{2}\right)}\right] h^\mathrm{s}_\mathrm{cu} \tag{4.58}$$

holds when γ_s is entered in radians.

Workpiece height The remaining workpiece height below the level of grain engagement is defined as

$$h_\mathrm{wp} = \left[2 + \frac{3}{2\,\tan\left(\gamma_\mathrm{s} + \frac{\pi}{2}\right)}\right] h^\mathrm{s}_\mathrm{cu} \tag{4.59}$$

to guarantee a sufficient amount of remaining workpiece material. Again, the rake angle γ_s needs to be defined in radians.

Grain heigth The grain height is defined as $h_\mathrm{gr} = 5\,h^\mathrm{s}_\mathrm{cu}$ to provide a sufficiently large rake face.

Total simulation time The overall simulation time obviously simply results from $\Delta T = l_\mathrm{wp}/v_\mathrm{s}$.

Number of remeshing steps The division of ΔT into $n_{\mathrm{rem}} = 150$ equidistant time intervals has been proven to yield a stable adaptive mesh evolution. Therefore, the simulation time between two remeshing procedures is set to $\Delta T_{\mathrm{rem}} = 1/n_{\mathrm{rem}}\, \Delta T$.

Time incrementation for the finite element solver To solve a corresponding boundary value problem with a constant mesh—and hence, a simulation time of ΔT_{rem}—automatic time incrementation with an element-wise stable time increment determination to compute Δt is used. This way, it is guaranteed, that the conditionally stable explicit time integration scheme used yields reliable results. In this manner,

$$\Delta t = \min \frac{L_{\mathcal{E}}}{\sqrt{\dfrac{\hat{\lambda} + 2\,\hat{\mu}}{\varrho_0}}} \tag{4.60}$$

is applied, where $L_{\mathcal{E}}$ denotes the characteristic element length of element $\mathcal{E}$, and $\hat{\lambda}$ and $\hat{\mu}$ denote effective Lamé parameters. The latter are determined by initially loading the finite element model with a prescribed displacement and calculate the corresponding response, cf. [93]. The reference mass density is denoted by ϱ_0, the square root represents the dilatational wave speed in the element $\mathcal{E}$.

The general structure of mechanical and thermal boundary conditions are equal to the ones presented in Sec. 4.3. However, the initial temperature of the workpiece body and the grain is assumed to be $\theta_0 = 400°\,\mathrm{C} \approx 670\,\mathrm{K}$, which reflects macroscopic steady-state process conditions determined in [86]. In contrast to the modelling approach presented above, we make the assumption that the grain comes in contact with a workpiece section evincing an initial temperature, however, pre-stressing or a initial hardening is assumed to be negligible.

Furthermore, the so far predominantly isothermal material parameters are extended to model the temperature-dependent material behaviour of the hardened 100Cr6 in more detail. In this context, especially the temperature-dependent heat capacity $c(\theta)$ will require special consideration as will be presented in Sec. 4.6. A major influence on the choice of material parameters is constituted by a benchmark study carried out in the context of the underlying project framework SPP1480—the corresponding details are printed in App. B.1. The complete set of material parameters is shown in Tables A.3 and A.4.

4.5.1 Self-contact

As can be observed in the results of Chapters 2 and 3, a majority of rake angles will exceed negative values of $\gamma_{\mathrm{s}} \leq -40°$, which in turn causes the chip generated in the numerical experiments to likely get in contact with the undeformed workpiece surface. Therefore, extensive self-contact is likely to occur during the single grain simulations, see Fig. 4.14. The commercial solver we use is generally able to resolve self contact,

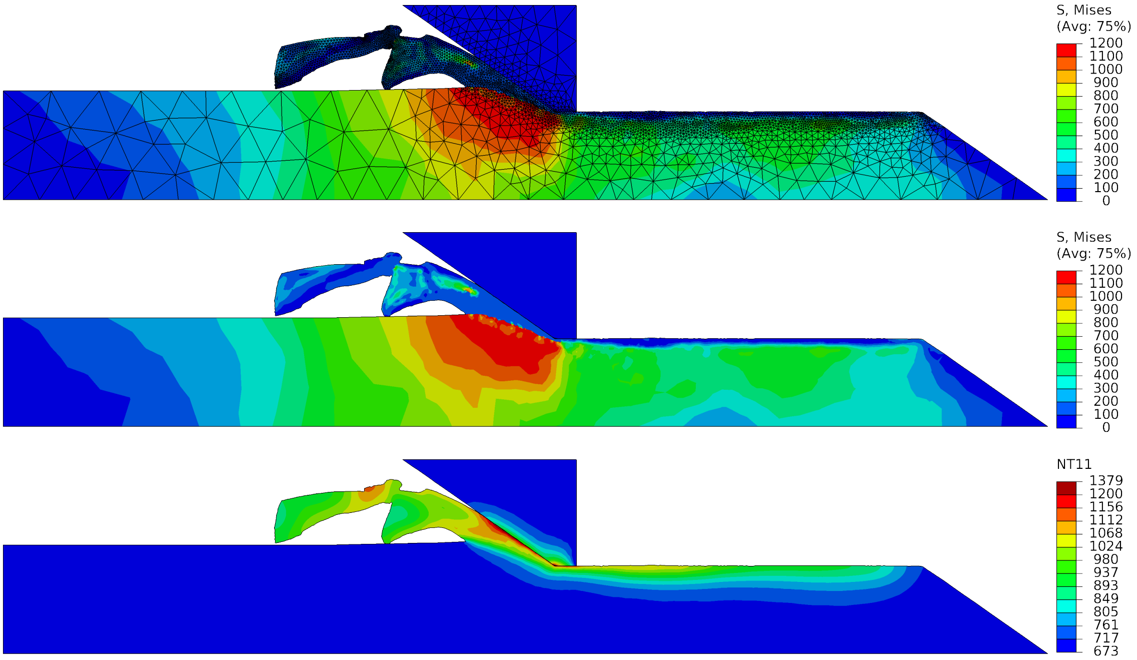

Figure 4.14: Exemplary simulation results for $\gamma_{\mathrm{s}} = -55^\circ$, $h^{\mathrm{s}}_{\mathrm{cu}} = 5\,\mu\mathrm{m}$, $v_{\mathrm{s}} = 120\,\mathrm{m/s}$. From top to bottom: Von Mises equivalent stress with mesh, equivalent stress without mesh and absolute temperature.

however, the remeshing framework invoked, cf. [40] is not. Since the penalty-based contact constraint enforcement algorithm invoked here allows a minimal penetration—due to a finite artificial stiffness that minimises the surface penetration—of the surfaces being in contact when solving the underlying boundary value problem, we generally cannot exclude this problem.

To overcome this issue, an extension to the adaptive remeshing scheme is implemented. What needs to be resolved in every remeshing step—more precisely, before every new mesh is generated—is the self-intersection of the workpiece boundary $\partial\mathcal{B}$. Restricting this problem at first to finite elements of linear order, this basically corresponds to the detection of self-intersections of a closed polygonal chain of line elements, that are bounding a simple polygon. Note, that convexity of bound polygon—in the present case the workpiece region $\mathcal{B}$—is by far not given, which complicates the problem. In contrast to Fig. 4.14, where the serrated chip touches the free workpiece surface twice, "spiralling" chips can cause a distinctively more complex problem, compare Fig. 4.15.

To solve this problem an iterative algorithm has been developed: Let us at first define the order of intersection by the number of nodes connecting two neighbouring line element. In every iteration, the order of self-intersection is determined first by simply computing the determinant of the system of linear equations solving for an intersection of a pair of segments. Secondly, the order of self-penetration is subsequently reduced

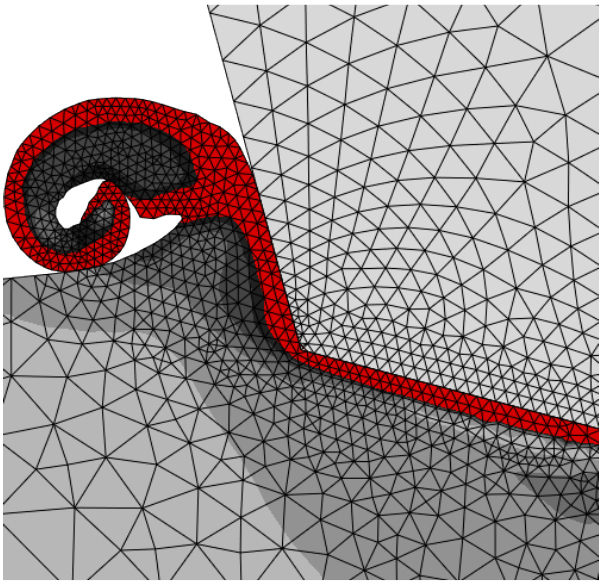

Figure 4.15: Exemplary complex self-intersecting "spiralling" chip formation. The red marked elements denote softened elements of high plastic equivalent strain, whereas the grey-to black scale represents moderate cumulative plastic straining.

by moving every node penetrating $\mathcal{B}$ negatively with respect to the normal vector of the nearest line element until the penetration vanishes. This procedure is repeatedly executed on $\partial\mathcal{B}$ until the subsequent self-intersection order check results to zero, i.e., until $\partial\mathcal{B}$ is ensured to constitute a simple polygon again. Figure 4.15 in this context shows the correctly working algorithm.

4.6 Heat source definition and thermal results

The parametric design allows the automatic creation of the model by just providing the three major parameters undeformed chip thickness $h_{\mathrm{cu}}^{\mathrm{s}}$, rake angle γ_{s} and the cutting velocity v_{s}, whereas the latter parameter is held constant throughout the rest of this work. In this context, the three major parameters are depicted in Fig. 4.16, where a contour plot of the resulting temperature field shows the basis for the following estimation of a heat source term to be transferred up to the macro-scale.

Since the main focus is on calculating the macroscopic thermal load on the workpiece, one first needs to define a thermal measure that is independent of the meso-scale model size and that represents the influence of all process parameters accordingly. Regarding the invariance against model size changes, the heat measure $\mathcal{Q}$, (4.54), presented in Sec. 4.3 does not meet this criterion, since the reference volume used scales proportional to the model size, or more precisely h_{wp}. Furthermore, an invariance against the reference temperature is desirable as well, since we are solely interested in the thermal energy

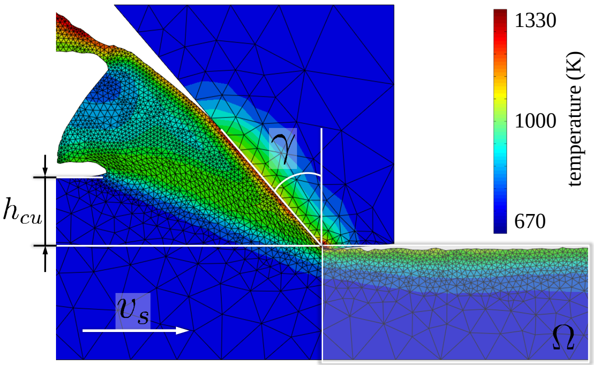

Figure 4.16: Meso-scale model temperature contour plot (left) showing the adaptively refined mesh as well as the reference volume Ω for the heat source determination. Taken from [38].

increment as a function of the major parameters. For this reason, a heat source term r is defined as a function of the three major parameters in terms of

$$r(h^{\mathrm{s}}_{\mathrm{cu}}, \gamma_{\mathrm{s}}, v_{\mathrm{s}}) =: \frac{\Delta\mathscr{Q}}{\Delta V_{\mathrm{chip}}}, \tag{4.61}$$

representing the amount of thermal energy $\Delta\mathscr{Q}$ induced into the workpiece with respect to the machined unit volume ΔV_{chip} of workpiece material. To calculate the heat energy $\mathscr{Q}$ induced in the machined workpiece bulk, we evaluate the volume integral

$$\mathscr{Q}(h^{\mathrm{s}}_{\mathrm{cu}}, \gamma_{\mathrm{s}}, v_{\mathrm{s}}, t) = \int_{\Omega} \varrho \int_{\theta_0}^{\theta} c(\theta)\,\mathrm{d}\theta\,\mathrm{d}v \tag{4.62}$$

in terms of a finite element discretisation

$$\mathscr{Q}^{\mathrm{FE}} = \sum_{i=1}^{n_e} \varrho_i\, V_i\, \frac{1}{2} \sum_{k=1}^{n_\theta} [\theta_{k+1} - \theta_k]\,[c(\theta_{k+1}) - c(\theta_k)] \tag{4.63}$$

for each time step over the remaining workpiece volume Ω according to Fig. 4.16. Here, $c(\theta)$ denotes the transient heat capacity depending on the temperature $\theta(t)$ and ϱ is the spatial mass density. The number of elements of volume V_i within the region Ω is represented by n_e, the number of sample points defining the discrete temperature dependency of the heat capacity $c(\theta_k)$ is denoted by n_θ. Since the undeformed chip thickness $h^{\mathrm{s}}_{\mathrm{cu}}$, the plane strain thickness Δz_{ps} of the meso-scale model as well as the cutting speed v_{s} remain constant over the meso-scale simulation time, the development of $\mathscr{Q}(t)$ is assumed to be approximately linear in time, which is proven in Fig. 4.17, where two exemplary evolutions of $\mathscr{Q}(t)$ for different meso-scale parameters are depicted.

In the graphs shown in Fig. 4.17, the red line represents the evolution of the heat energy $\mathscr{Q}$ according to (4.62) induced by the cutting process, and the blue line depicts

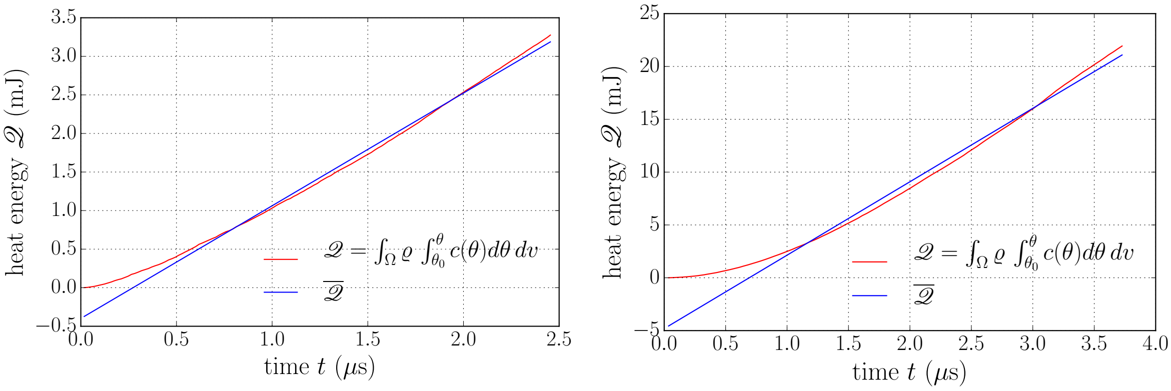

Figure 4.17: Heat energy $\mathscr{Q}$ vs. time t integrated over the remaining workpiece volume Ω (red stroke) and the corresponding linear regression $\overline{\mathscr{Q}}$ (blue stroke) for a undeformed chip thickness $h^{\mathrm{s}}_{\mathrm{cu}} = 10$ µm. The left graph depicts a rake angle of $\gamma_{\mathrm{s}} = -40°$, the simulation on the right hand side was run at $\gamma_{\mathrm{s}} = -68°$. Note, that the scales of the graphs differ in magnitude.

a linear regression function thereof that was calculated by least-square-minimisation, resulting in a function $\overline{\mathscr{Q}}$. As clearly observable, the error of the regression scheme in comparison to the original data is small and thus, the linear regression constitutes a highly efficient averaging scheme to approximate the induced thermal power $\mathscr{P}_{\mathrm{therm}}$ during the machining simulation. To now establish a functional dependency between $\mathscr{P}_{\mathrm{therm}}$ and r, we make use of the linear dependency between the above-mentioned meso-scale parameters and the machined chip volume

$$\Delta V_{\mathrm{chip}} = h^{\mathrm{s}}_{\mathrm{cu}} \, \Delta z_{\mathrm{ps}} \, \Delta x = h^{\mathrm{s}}_{\mathrm{cu}} \, \Delta z_{\mathrm{ps}} \, v_{\mathrm{s}} \, \Delta t \tag{4.64}$$

and insert this into the approximated thermal power induced into the workpiece

$$\mathscr{P}_{\mathrm{therm}} = \frac{\mathrm{d}\mathscr{Q}}{\mathrm{d}t} \approx \frac{\Delta \overline{\mathscr{Q}}}{\Delta t}, \tag{4.65}$$

finally yielding

$$r(h^{\mathrm{s}}_{\mathrm{cu}}, \gamma_{\mathrm{s}}, v_{\mathrm{s}}) = \frac{\Delta \overline{\mathscr{Q}}}{\Delta V_{\mathrm{chip}}} = \frac{\mathscr{P}_{\mathrm{therm}}}{h^{\mathrm{s}}_{\mathrm{cu}} \, \Delta z_{\mathrm{ps}} \, v_{\mathrm{s}}} \tag{4.66}$$

which constitutes the desired transferable heat measure. In the above equations, $\Delta x = v_{\mathrm{s}} \, \Delta t$ represents the displacement in direction of v_{s} during a time increment Δt whereas Δz_{ps} denotes the plane strain thickness of the two-dimensional finite element model.

The correct derivation of $r(h^{\mathrm{s}}_{\mathrm{cu}}, \gamma_{\mathrm{s}}, v_{\mathrm{s}})$ can moreover be supported when examining Figure 4.18, where different energy measure evolutions are depicted. Taking at first the

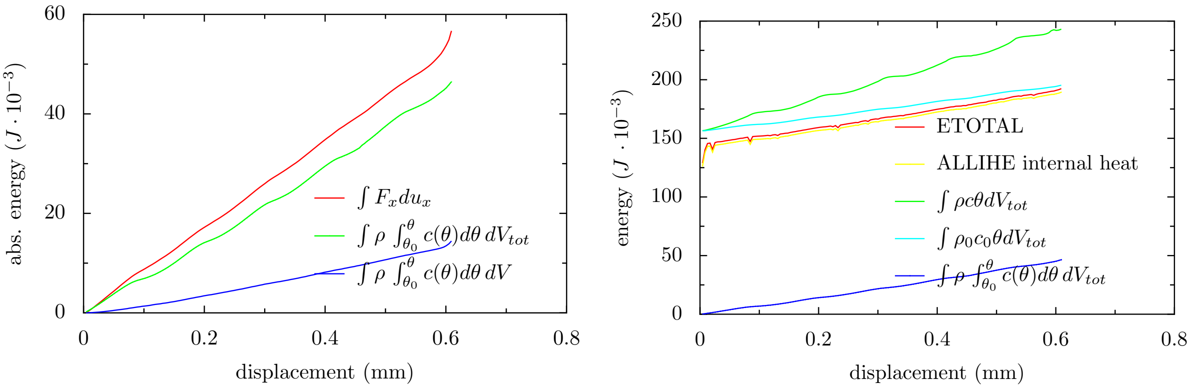

Figure 4.18: Different energies over displacement u_x, or time $t = u_x/v_\mathrm{s}$, respectively, for an undeformed chip thickness $h^\mathrm{s}_\mathrm{cu} = 30\,\mu\mathrm{m}$ and a rake angle of $\gamma_\mathrm{s} = -40°$. The curves annotated with ETOTAL and ALLIHE represent the Abaqus expressions for total energy and the internal heat energy of the model.

left hand side graph into account, the absolute mechanical energy supply, or external work supply, respectively,

$$\mathscr{W}(t) = \int\limits_0^{u_x(t)} F_x \, \mathrm{d}x \tag{4.67}$$

is represented by the red curve, which, in turn, represents an upper bound for the energy in the present system. The blue line represents the thermal energy $\mathscr{Q}(t)$ according to (4.62), and the green line depicts the same energy measure, but integrated with respect to the entire model domain $\mathcal{B}$ instead of just the remaining workpiece body Ω. Therefore, it reflects the total heat energy

$$\mathscr{Q}_\mathrm{tot}(t) = \int_\mathcal{B} \varrho \int_{\theta_0}^{\theta} c(\theta) \, \mathrm{d}\theta \, \mathrm{d}v. \tag{4.68}$$

The slight oscillating trend in all curves is caused by the serrated chip formation, the rise at the end of the curve result from the grain coming close to the boundary $\partial\mathcal{B}$ of the workpiece, where Dirichlet boundary conditions constrain the material motion and therefore cause this steep rise observable. The difference between $\mathscr{W}(t)$ and $\mathscr{Q}_\mathrm{tot}(t)$ is caused by the choice of η, cf. (4.48). Regarding the evolution of $\mathscr{Q}(t)$, we can state a significantly lower energy magnitude than the total energy contained $\mathcal{B}$ and can conclude a certain proportionality between $\mathscr{Q}(t)$ and $\mathscr{Q}_\mathrm{tot}(t)$. So by now, we have verified that the chosen energy measure $\mathscr{Q}(t)$ is sensibly bounded. With regard to the right hand side of Fig. 4.18, we can now prove the sensible choice of r and the invariance against θ_0. When we consider the yellow curve representing the total internal heat energy $\mathscr{E}(t)$ of the system—ALLIHE is the Abaqus expression for this measure—we can at first observe the same slope in both the yellow $\mathscr{E}(t)$ and the blue $\mathscr{Q}(t)$ curve. This proves, that $\mathscr{Q}(t)$ represents the correct magnitude of energy. The equidistant character of both curves lies in the fact, that $\mathscr{E}(t)$ refers to the absolute zero temperature $\theta = 0\,\mathrm{K}$ and therefore evinces an offset that is caused by the initial workpiece temperature $\theta_0 = 670\,\mathrm{K}$. However, due to the definition of $\mathscr{Q}(t)$, this influence is a priori excluded. Since r now only depends on an approximation of $\dot{\mathscr{E}}(t)$, or $\dot{\mathscr{Q}}(t)$, respectively, we have proven the correct definition of the above energy measures.

For a set of meso-scale parameters $\{h^{\mathrm{s}}_{\mathrm{cu}}, \gamma_{\mathrm{s}}\}^A$ that have been used in earlier investigations, cf. [37], and have been adopted to fit the parameter range in Fig. 3.5 for experiment A (left column of the figure), we can now plot the above heat source term $r(h^{\mathrm{s}}_{\mathrm{cu}}, \gamma_{\mathrm{s}})$ to visualise the functional dependency of these measures within the parameter range under consideration. The result is depicted in Figure 4.19, where a Delaunay triangulation [8] of $r(h^{\mathrm{s}}_{\mathrm{cu}}, \gamma_{\mathrm{s}})$ is visualised for eighteen parameter combinations each depicted by the blue dots in the figure, which we will refer to as heat source *sample points* in the progress of this work. Both subfigures show the same results, only the angle of view is altered to enable an easier comprehension of the function shape. As can be observed in Figure 4.19, the heat source term $r(h^{\mathrm{s}}_{\mathrm{cu}}, \gamma_{\mathrm{s}})$ strongly depends on the rake angle, showing a monotonously ascending trend with increasing absolute value of γ_{s}, whereas the undeformed chip thickness $h^{\mathrm{s}}_{\mathrm{cu}}$ only shows a weak impact on the heat source term. In the lower range of $\gamma_{\mathrm{s}} \in [-30°... - 40°]$, it can be observed that $\partial r / \partial h^{\mathrm{s}}_{\mathrm{cu}} \approx 0$ holds, hence there is very little dependency on the undeformed chip thickness. With increasing absolute values of γ_{s}, one can observe an approximately convex shape, showing a decrease of

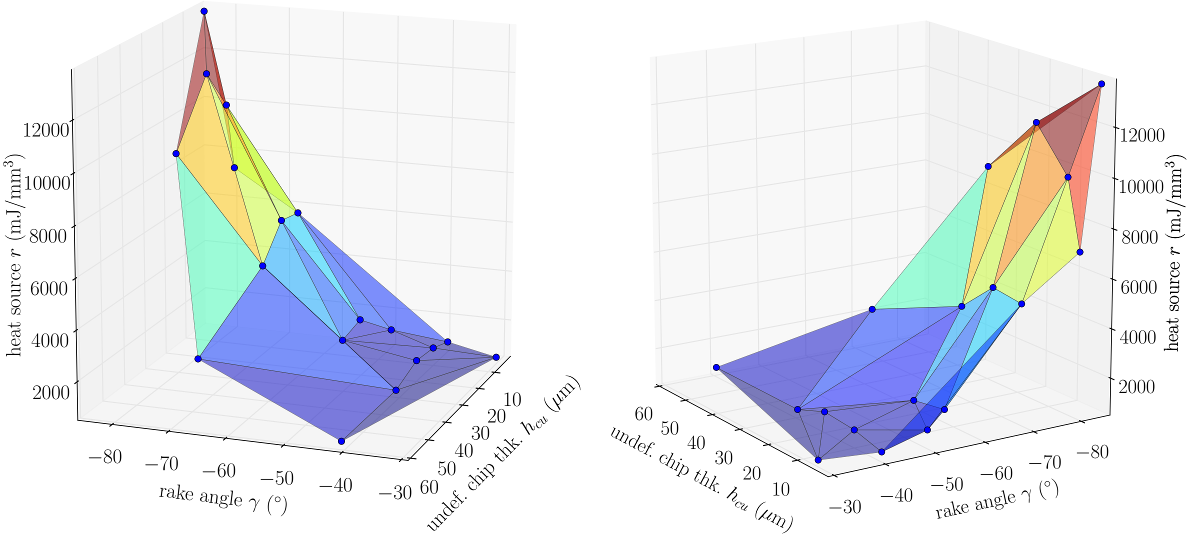

Figure 4.19: Delaunay triangulation of the heat source term r as a function of rake angle γ_{s} and undeformed chip thickness $h^{\mathrm{s}}_{\mathrm{cu}}$, resulting from the meso-scale simulations. Every vertex point (blue dots) of the triangulation constitutes one finite element simulation, resulting in the depicted surface. Both subfigures show the same data, only the angle of view is altered. Taken from [38].

r when increasing $h^{\mathrm{s}}_{\mathrm{cu}}$ at a constant rake angle of approximately $\gamma_{\mathrm{s}} = -60°$. This can be explained with the scaling of $\mathscr{P}_{\mathrm{therm}}$ with the inverse of $h^{\mathrm{s}}_{\mathrm{cu}}$, cf. Equation (4.66). Though it is difficult to derive a general dependency between the evolution of r with respect to γ_{s} and to explain the low influence of $h^{\mathrm{s}}_{\mathrm{cu}}$ in the present case, we can at least state that in the regime of high speed cutting of 100Cr6, an asymptotically descending trend of the specific cutting forces with increasing cutting speed was observed in orthogonal cutting experiments, cf. [71]. Since our meso-scale model basically represents such an orthogonal cutting experiment at very high cutting speeds, we can assume that the influence of $h^{\mathrm{s}}_{\mathrm{cu}}$ on the specific process force and the process efficiency may become negligible at a certain undeformed chip thickness. Postulating a defined dependency between the specific cutting force and the heat transferred into the workpiece would thus enable us to justify the weak dependency of $h^{\mathrm{s}}_{\mathrm{cu}}$ on the heat source r.

The strong dependency of r with respect to γ_{s}, however, can be explained with the increasing influence of the energy dissipation resulting from friction between tool and workpiece along with a decreasing chip formation trend when the rake angle is exceeding absolute values of about $|\gamma_{\mathrm{s}}| \geq 60°$. In this case, a comparatively large amount of plastically deformed material is accumulating in front of the cutting edge instead of being transported away from the primary shear zone by a properly formed chip. This is, in turn, resulting in a larger amount of heat energy stored inside of the workpiece and hence resulting in an increase of the heat source term r.

Concluding from this analysis, we can state that the dependency of r with respect to $r(h^{\mathrm{s}}_{\mathrm{cu}}, \gamma_{\mathrm{s}}; v_{\mathrm{s}})$ can be approximated by means of a polynomial or an exponential function, including a coupling between $h^{\mathrm{s}}_{\mathrm{cu}}$ and γ_{s} in terms of a linear coupling function, which will be discussed in detail in Chapter 5.

4.7 Multiple grain engagement

This section focuses on the influence of multiple grain engagements onto the surface layer using a two-dimensional chip formation simulation. In contrast to other machining processes, the material removal during grinding is constituted by multiple subsequent grit engagements. Hence, the surface integrity of the resulting surface is not only dependent on the last grain in contact, but on the entire engagement history of the material region under consideration. In the regime of process simulations, the modified initial conditions for a single grain simulation should be taken into account, if one aims at the prediction of surface integrity quantities. In order to estimate the chronological sequence of $h^{\mathrm{s}}_{\mathrm{cu}}$ for a defined section of the workpiece, the kinematic simulation presented in Chapter 3 is used.

4.7.1 Multi-grain finite element setup

To study the influence of multiple grain engagements at one fixed workpiece region, two cases are investigated. At constant cutting speed $v_\mathrm{s} = 120\,\mathrm{m/s}$ and at a constant rake angle of $\gamma_\mathrm{s} = -40°$, the same undeformed chip thickness sequence $h^\mathrm{s}_{\mathrm{cu},1} = h^\mathrm{s}_{\mathrm{cu},2} = 35\,\mathrm{\mu m}$ will be applied twice as a first case. As a second study, the latter parameter will be applied in a sequence according to Fig. 3.9, namely $h^\mathrm{s}_{\mathrm{cu},1} = 35\,\mathrm{\mu m} \rightarrow h^\mathrm{s}_{\mathrm{cu},2} = 20\,\mathrm{\mu m}$, restricted to the first two grain engagements at this stage. The corresponding boundary value problem is based on the one presented in the previous sections with the alteration depicted in Fig. 4.20. After one pass of the grain, the grain is shifted again to a new starting position that reflects the second undeformed chip thickness $h^\mathrm{s}_{\mathrm{cu},2}$. Furthermore, the chip resulting from the first engagement is at first coarsened and subsequently entirely constrained with Dirichlet boundary conditions to prevent further deformation. This is necessary, because the material softening in combination of the dynamic nature of the simulation causes the chip to severely distort during continuation of the second grain pass. In reality the chip would of course break and separate from the workpiece, however, the modelling of this process is not possible with the underlying remeshing algorithm invoked. Basically, Abaqus/Explicit supports such region separation, based on element deletion techniques, cf. [93], but the adaptive remeshing formulation of our framework yet is not capable of such extended modelling approaches. After the grain

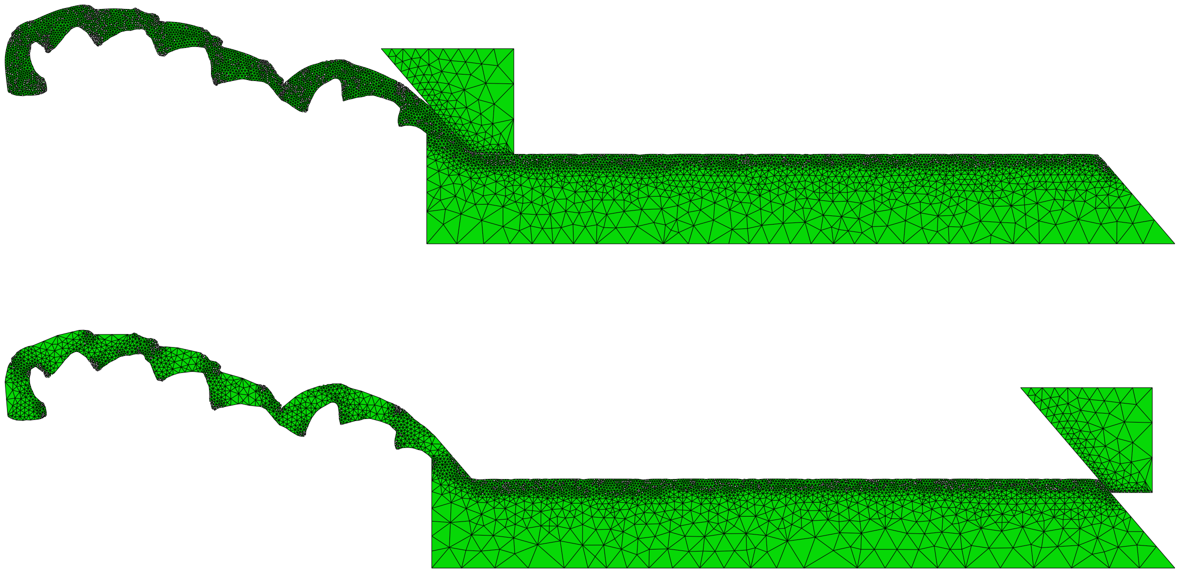

Figure 4.20: Concept of multi-grain analysis and referring model meshes. The top depicts the last step of the first grain pass, whereas the bottom picture shows the initial step of the second grain pass. Chip coarsening was applied to the first chip to minimise computational cost during the simulation of the second grain pass.

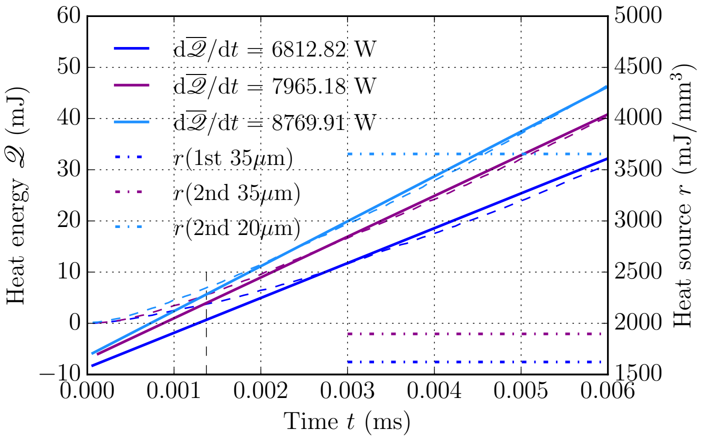

Figure 4.21: Absolute heat energy $\mathscr{Q}$ (dashed lines), according linear regression $\overline{\mathscr{Q}}$ (solid lines) and resulting heat source term r (dash-dotted line, right hand side y axis). The blue line represents the first grain engagement at $h^{\mathrm{s}}_{\mathrm{cu},1} = 35$ µm, the dark magenta line depicts the second engagement at the same $h^{\mathrm{s}}_{\mathrm{cu},2} = 35$ µm and the light blue line refers to the second engagement with $h^{\mathrm{s}}_{\mathrm{cu},2} = 20$ µm. Note, that for the linear regression, the first 15% of the simulation time (vertical dashed black line) were not considered to neglect the run-up effects of the chip formation process. Taken from [39].

shift, the mesh-to-mesh solution mapping algorithm is applied one extra time and the simulation is subsequently executed for the second grain engagement.

The wear flat area of the grain is chosen to be $l_{\mathrm{wf}} = 2\,h^{\mathrm{s}}_{\mathrm{cu},1}$ with a flank angle of $\alpha = 0°$. Remoter, the remaining workpiece thickness is, in contrast to (4.59) enlarged to enable a double grain pass according to

$$h_{\mathrm{wp}} = \left[3 + \frac{3}{2\,\tan(\gamma_{\mathrm{s}} + \frac{\pi}{2})}\right] h^{\mathrm{s}}_{\mathrm{cu}}. \tag{4.69}$$

4.7.2 Results

Figures 4.23 and 4.24 show the temperature and equivalent plastic strain contour plots for intermediate states of the second grain engagements for both $h^{\mathrm{s}}_{\mathrm{cu},2}$ applied in the meso-scale FE model. It can be stated that the chip structure differs strongly even at constant undeformed chip thickness $h^{\mathrm{s}}_{\mathrm{cu},1} = h^{\mathrm{s}}_{\mathrm{cu},2} = 35\,\mu\mathrm{m}$, which results from the pre-heating and the deterioration of the workpiece material due to the ductile damage implemented in the constitutive material model. Since the damage model used here strongly depends on the equivalent plastic strain, cf. [37], the green areas in Fig. 4.24 represent softened material. This in turn explains the flow chip formation occurring at $h^{\mathrm{s}}_{\mathrm{cu},2} = 20\,\mu\mathrm{m}$ and the reduced segmentation at $h^{\mathrm{s}}_{\mathrm{cu},2} = 35\,\mu\mathrm{m}$ in contrast to the strongly segmented chip of the first grain engagement.

In Fig. 4.21, the absolute heat induced into the remaining workpiece volume Ω after grain engagement $\mathscr{Q}(h^{\mathrm{s}}_{\mathrm{cu}}, \gamma_{\mathrm{s}}, v_{\mathrm{s}}, t)$ and the resulting heat source term $r(h^{\mathrm{s}}_{\mathrm{cu}}, \gamma_{\mathrm{s}}, v_{\mathrm{s}})$,

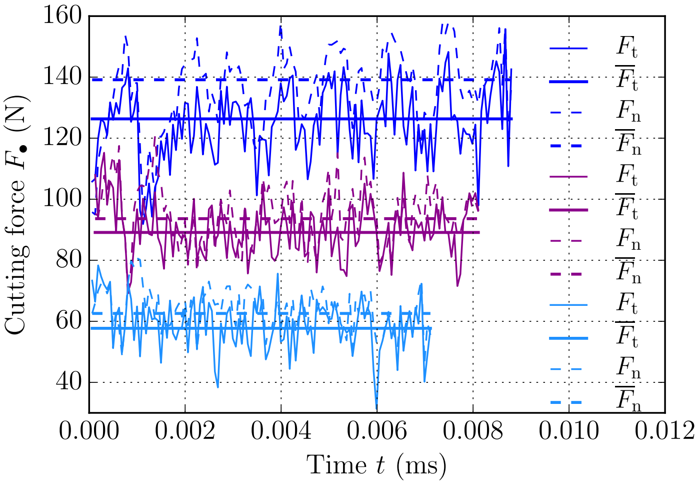

Figure 4.22: Force components and their mean values. The colour coding equals the one used in Fig. 4.21. Taken from [39].

see Eqns. 4.62 and 4.66, reflecting the heat energy induced into the workpiece per deformed chip volume are depicted—setting v_s =constant—for both sequences of grain engagement. Note, that the depicted $\mathscr{Q}$ reflects the integral energy rise over the entire remaining workpiece volume Ω, which explains why the second engagement graphs (light blue and magenta lines) show a steeper slope than the first grain. Concerning the heat source r, the large difference of the second engagement with lower h^s_{cu} in comparison to the other values results from the weighting with the inverse chip volume according to (4.66).

Interestingly, the lower second undeformed chip thickness (light blue line) results in a higher energy rise than $h^s_{cu,2} = 35$ µm, which is caused by the integral character of the measure $\mathscr{Q}$, compare Eq. (4.62). Since a lower amount of already heated material is

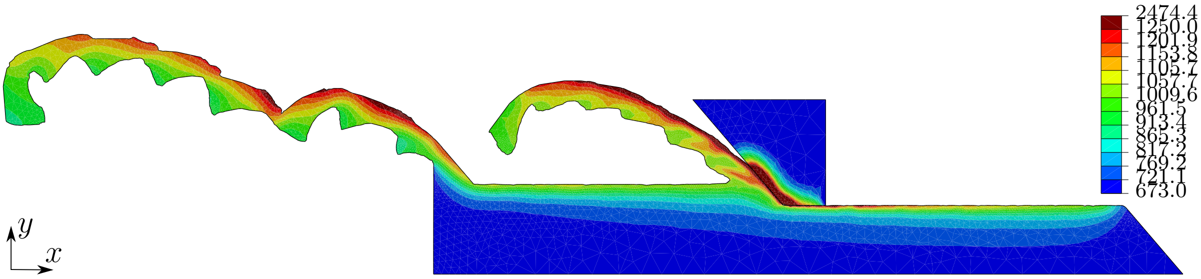

Figure 4.23: Temperature contour plot (unit K) when applying a second undeformed chip thickness of $h^s_{cu,2} = 35$ µm. Note, that the lines of higher temperature within the second grain depict the occurring shear bands during this high-speed grinding process. Taken from [39].

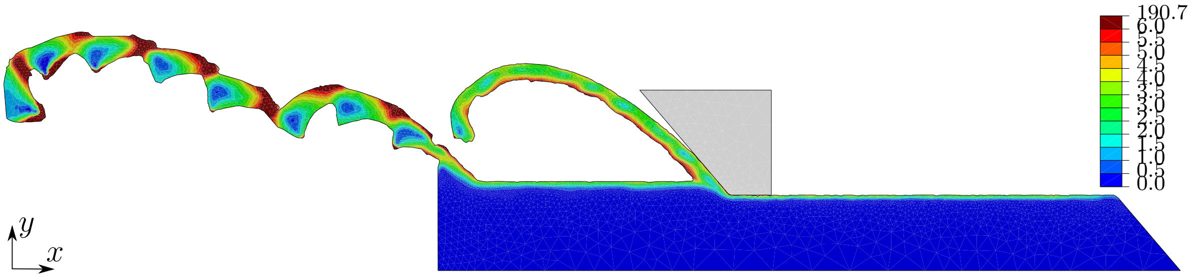

Figure 4.24: Equivalent plastic strain contour plot (no unit) when applying a second undeformed chip thickness $h^{\mathrm{s}}_{\mathrm{cu,2}} = 20$ µm. Since the tool is entirely constrained by Dirichlet boundary conditions, no deformation occurs for this body. Note, that the workpiece surface areas depicted in green refer to softened, or partly damaged material. Taken from [39].

deformed into the newly built-up chip, the heat remaining in the workpiece volume Ω is higher for $h^{\mathrm{s}}_{\mathrm{cu,2}} = 35$ µm.

The resulting cutting forces obtained from the simulations are shown in Fig. 4.22. It can be observed that the normal component F_{n} is generally higher than the tangential component F_{t}, which results from the constant rake angle γ_{s}. Due to the damage occurring, the difference between these components decreases from the first to the second grain engagement. The same cause can be taken into account when comparing the first engagement (blue lines) with the second one when applying the same $h^{\mathrm{s}}_{\mathrm{cu}}$ twice (magenta lines). Obviously, the second pass of the grain consumes approximately 35% less mechanical energy $\int F_t \, \mathrm{d}x$ than the first pass, although the integral induced thermal energy rate $\mathrm{d}\overline{\mathscr{Q}}/\mathrm{d}t$ increases by approximately 15%.

4.7.3 Preliminary conclusion

In the present section, a numerical case study invoking a hybrid simulation system was used to examine the grain engagement history at one fixed workpiece region in the regime of ITG. It could be shown that there is a strong fluctuation in engagement conditions, even in the same region, demanding further investigations to define a mathematical measure that covers e.g. typical sequences of $h^{\mathrm{s}}_{\mathrm{cu}}$ for the entire workpiece.

Numerical investigations on the meso-scale have shown a strong influence on the thermal effects resulting from the governing grinding process, causing a higher thermal load on the workpiece, especially when smaller undeformed chip thicknesses occur. Hence, a high impact on the surface integrity of the workpiece can be expected.

A.1 Material parameters

A.1.1 Isothermal material parameters

Table A.2: Isothermal material parameters for the finite element model presented in Sec. 4.3. The workpiece is made of 100Cr6 / AISI 52100 bearing steel hardened to 61–63 HRC, whereas the grain consists of monocrystalline cubic boron nitride (cBN). In this context, the abbreviation JC corresponds to Johnson-Cook and the referring parameters are taken from [43].

part instance	parameter	symbol	value
workpiece	Young's modulus	E^{wp}	208 GPa
	Poisson's ratio	ν^{wp}	0.28
	inelastic heat fraction	η	0.9
	mass density	ρ_0^{wp}	7810 $\mathrm{kg/m^3}$
	specific heat	c^{wp}	473.75 J/(kg K)
	thermal conductivity	λ^{wp}	52.5 W/(m K)
	thermal expansion coefficient	α_0^{wp}	$1.19 \cdot 10^{-5}$
	initial JC yield stress	A	774.78 MPa
	initial JC hardening modulus	B	134.46 MPa
	JC strain rate hardening parameter	C	0.0173
	JC thermal softening parameter	M	3.1710
	JC exponential hardening parameter	N	0.3710
	JC reference temperature	θ_0	300.0 K
	JC melting temperature	θ_m	1697.15 K
	JC reference strain rate	$\dot{\varepsilon}_{\mathrm{p},0}$	1.0
	damage saturation rate	ϑ_d	5.0
	damage threshold plastic strain	$\varepsilon_{\mathrm{p}}^{d}$	1.7
	saturated damage value	$\overline{d}$	0.9
cBN grain	mass density	ρ_0^{cBN}	4084 $\mathrm{kg/m^3}$
	specific heat	c^{cBN}	558 J/(kg K)
	thermal conductivity	λ^{cBN}	40 W/(m K)

A.1.2 Material parameters of the parametric single grain model

Table A.3: Isothermal material parameters for the materials used in the parametric finite element model, see Sec. 4.5. The workpiece consists of 100Cr6 / AISI 52100 bearing steel hardened to 61 HRC, the grain consists of monocrystalline cubic boron nitride (cBN). The Johnson-Cook parameters are taken from [73] and abbreviated with JC. The further parameters are adopted from [103] and [46].

part instance	parameter	symbol	value
workpiece	Young's modulus	E^{wp}	208 GPa
	Poisson's ratio	ν^{wp}	0.28
	inelastic heat fraction	η	0.9
	mass density	ρ_0^{wp}	7810 kg/m^3
	specific heat	c^{wp}	473.75 J/(kg K)
	thermal conductivity	λ^{wp}	52.5 W/(m K)
	thermal expansion coefficient	α_0^{wp}	$1.19 \cdot 10^{-5}$
	initial JC yield stress	A	688.17 MPa
	initial JC hardening modulus	B	150.82 MPa
	JC strain rate hardening parameter	C	0.04279
	JC thermal softening parameter	M	2.7786
	JC exponential hardening parameter	N	0.3362
	JC reference temperature	θ_0	300.0 K
	JC melting temperature	θ_m	1697.15 K
	JC reference strain rate	$\dot{\varepsilon}_{\mathrm{p},0}$	1.0
	damage saturation rate	ϑ_d	5.0
	damage threshold plastic strain	$\varepsilon_{\mathrm{p}}^{d}$	2.0
	saturated damage value	$\overline{d}$	0.9
cBN grain	mass density	ρ_0^{cBN}	4084 kg/m^3
	specific heat	c^{cBN}	558 J/(kg K)
	thermal conductivity	λ^{cBN}	40 W/(m K)

Table A.4: Temperature dependent material parameters for 100Cr6 / AISI 52100 bearing steel hardened to 61 HRC.

parameter	symbol	value	at temperature θ
Young's modulus	$\mathsf{E}^{\mathrm{wp}}(\theta)$	201.330 GPa	293.15 K
		178.580 GPa	473.15 K
		162.720 GPa	673.15 K
		103.420 GPa	873.15 K
		86.870 GPa	1073.15 K
		66.880 GPa	1273.15 K
Poisson's ratio	$\nu^{\mathrm{wp}}(\theta)$	0.277	293.15 K
		0.269	473.15 K
		0.255	673.15 K
		0.342	873.15 K
		0.396	1073.15 K
		0.490	1273.15 K
specific heat	$c^{\mathrm{wp}}(\theta)$	473.751 J/(kg K)	293.15 K
		487.836 J/(kg K)	373.15 K
		517.285 J/(kg K)	473.15 K
		530.089 J/(kg K)	523.15 K
		400.768 J/(kg K)	573.15 K
		572.343 J/(kg K)	623.15 K
		588.988 J/(kg K)	673.15 K
		651.728 J/(kg K)	773.15 K
		710.627 J/(kg K)	873.15 K
		773.367 J/(kg K)	973.15 K
		1588.988 J/(kg K)	1023.15 K
		626.120 J/(kg K)	1073.15 K

		550.576 J/(kg K)	1173.15 K
thermal conductivity	$\lambda^{\mathrm{wp}}(\theta)$	52.50 W/(m K)	293.15 K
		50.71 W/(m K)	373.15 K
		48.11 W/(m K)	473.15 K
		45.69 W/(m K)	573.15 K
		41.72 W/(m K)	673.15 K
		38.28 W/(m K)	773.15 K
		33.94 W/(m K)	873.15 K
		30.13 W/(m K)	973.15 K
		24.75 W/(m K)	1073.15 K
		32.90 W/(m K)	1273.15 K
		29.76 W/(m K)	1473.15 K
thermal expansion coefficient	$\alpha^{\mathrm{wp}}(\theta)$	$1.19 \cdot 10^{-5}$	293.15
		$1.25 \cdot 10^{-5}$	373.15 K
		$1.30 \cdot 10^{-5}$	473.15 K
		$1.36 \cdot 10^{-5}$	573.15 K
		$1.41 \cdot 10^{-5}$	673.15 K
		$1.45 \cdot 10^{-5}$	773.15 K
		$1.49 \cdot 10^{-5}$	873.15 K

B.1 SPP 1480 Benchmark

To demonstrate a further application of the meso-scale model developed, an orthogonal cutting benchmark test carried out in the context of the Priority Program SPP 1480 is briefly outlined here.

B.1.1 Model setup

The model is set up similarly to the meso-scale single grain model presented in Sec. 4.5, however with the parameters depicted in Fig. B.25. Two different material models for 100Cr6 (61-63 HRC) are compared in this context. First, the material model presented in Sec. 4.2 in combination with the material parameters shown in Sec. A.1.2. Secondly, the Abaqus Johnson-Cook implementation neglecting ductile damage is used in conjunction with the same set of material parameters.

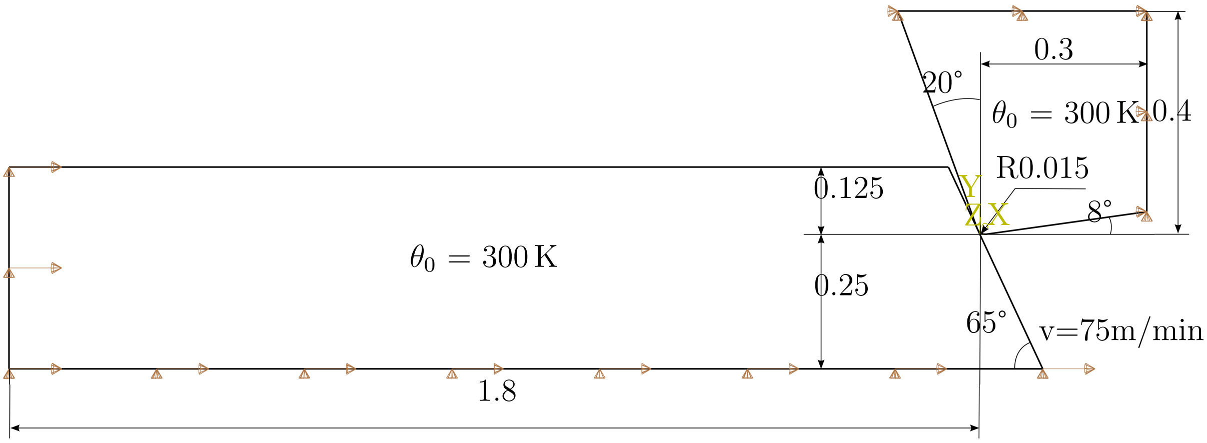

Figure B.25: Main model measures for the orthogonal cutting benchmark test. All dimensions are printed in mm.

B.1.2 Results

Figures B.26 to B.28 depict the thermo-mechanical results for the constitutive model including ductile damage, which becomes obvious from the serrated chip formation pattern. The corresponding evolutions of the cutting force components and the qualitative heat induction according to Sec. 4.4 or (4.54), respectively, are depicted in Fig. B.28.

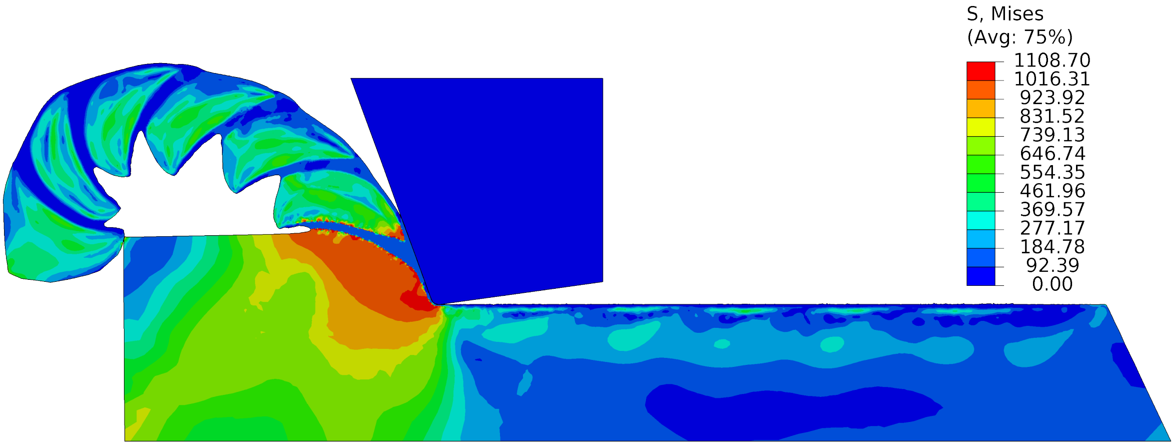

Figure B.26: Von Mises equivalent stress contour plot in MPa of the model incorporating ductile damage.

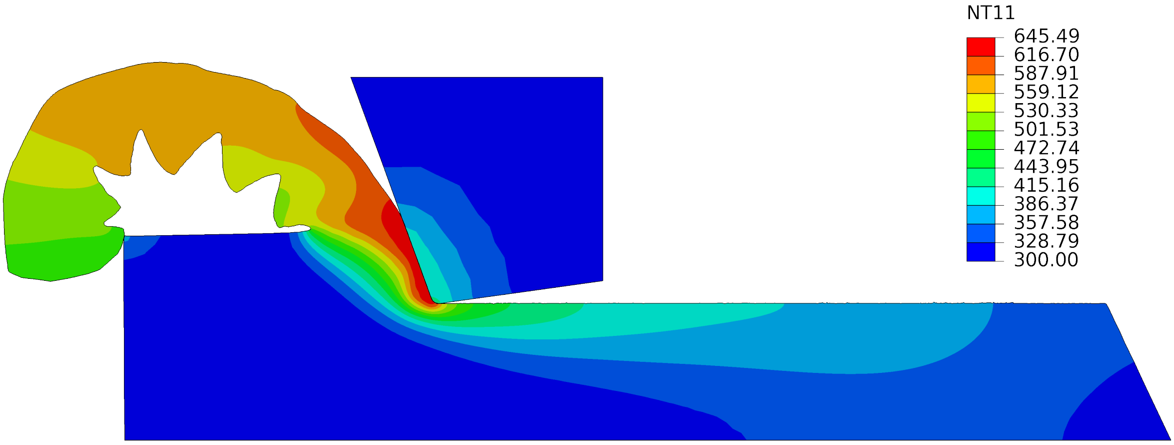

Figure B.27: Nodal temperature contour plot in K of the model incorporating ductile damage.

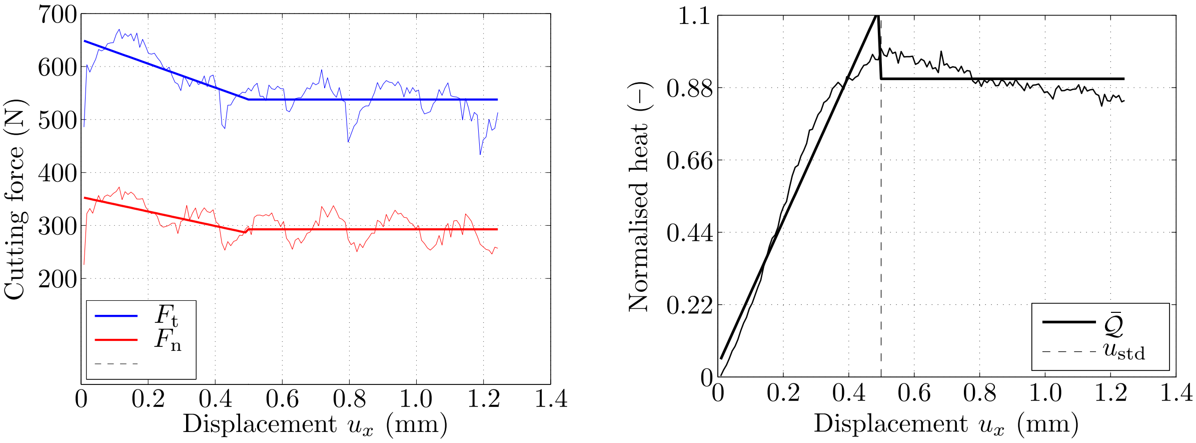

Figure B.28: Reaction force and normalised heat induction for the model including ductile damage.

In analogy to the resuls shown above, Figs. B.29 to B.31 illustrate the outcome of the simulations that invoke the Abaqus formulation of the underlying constitutive material routine, neglecting the damage driven softening.

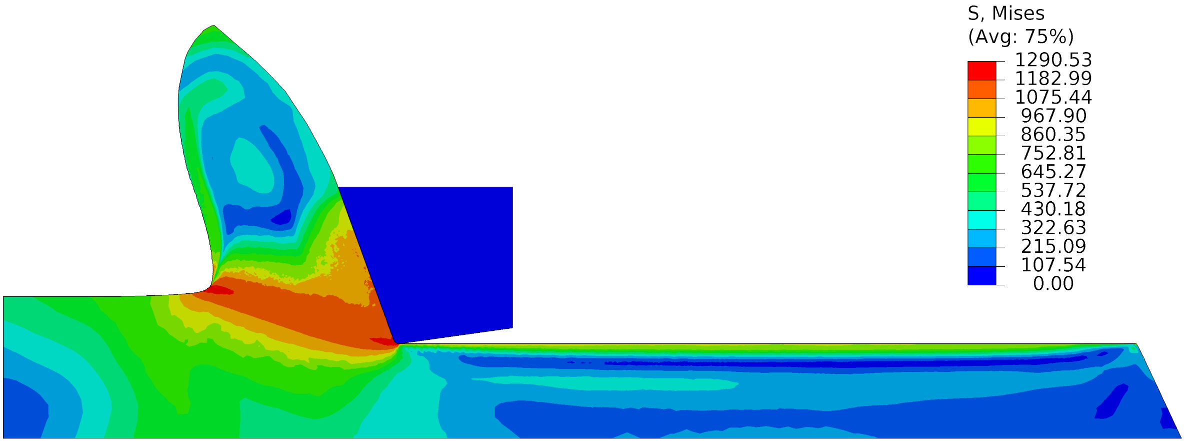
S, Mises
(Avg: 75%)
1290.53
1182.99
1075.44
967.90
860.35
752.81
645.27
537.72
430.18
322.63
215.09
107.54
0.00

Figure B.29: Von Mises equivalent stress contour plot in MPa of the model incorporating ductile damage.

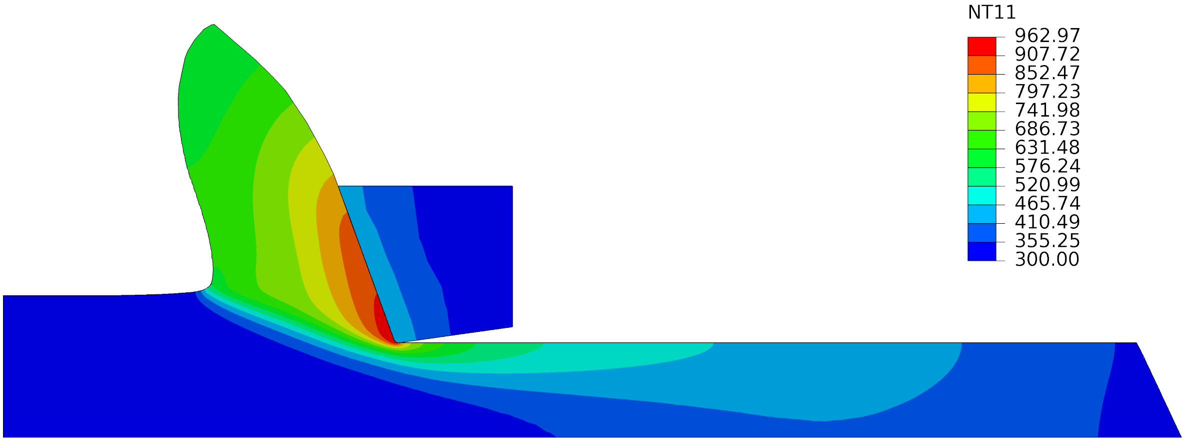
NT11
962.97
907.72
852.47
797.23
741.98
686.73
631.48
576.24
520.99
465.74
410.49
355.25
300.00

Figure B.30: Nodal temperature contour plot in K of the model incorporating ductile damage.

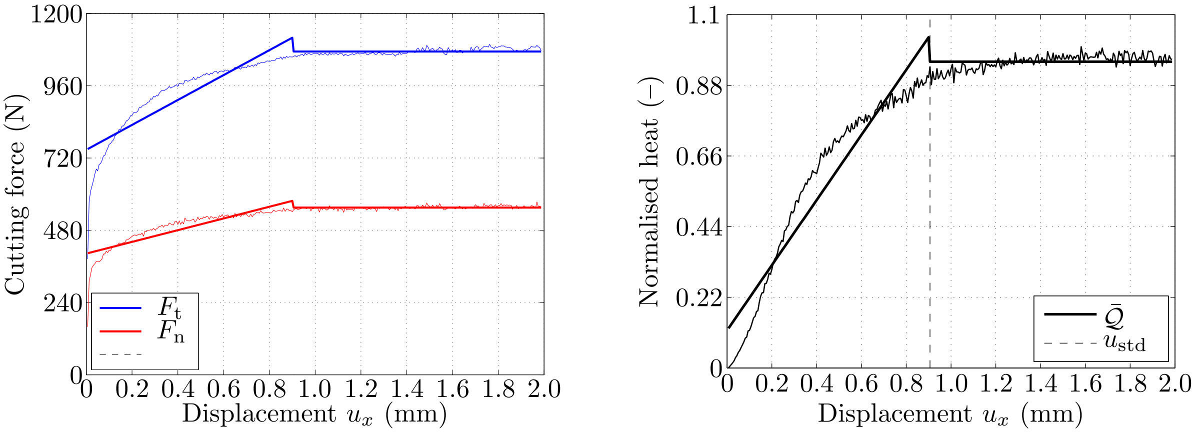

Figure B.31: Reaction force and normalised heat induction for the model neglecting ductile damage.

5 Bridging the meso and macro scale

In the present chapter, we will focus on the bridging approach between the meso- and the macro-scale of the grinding simulation framework. The methods developed are straightforwardly applicable to further physical measures beyond the thermo-mechanical responses presented here.

5.1 Derivation of the scale-bridging strategy

With a discrete functional dependency of the heat source term $r(h^{\mathrm{s}}_{\mathrm{cu}}, \gamma_{\mathrm{s}}; v_{\mathrm{s}}, l_{\mathrm{wf}}, \alpha)$, see (4.66), on the main meso-scale process parameters at hand, one approach to derive a respective continuous functional dependency is a direct use of the Delaunay triangulation of the sample points, cf. Fig. 4.19, which basically constitutes a C^0 continuous, two-dimensional piecewise linear interpolation of the heat source term r. However, there are two drawbacks in connection with this approach. First, this would necessitate a set of sample points that are definitely situated outside of the parameter range that is spanned by the kinematic simulation results. In practice, this is unfortunately not possible due to the numerical instabilities of the meso-scale finite element simulation we run into when trying to model rake angles with a magnitude larger than 85° or an $h^{\mathrm{s}}_{\mathrm{cu}}$ that heads towards zero. Secondly, we aim at the development of a computationally efficient simulation framework, which means that we target a minimum amount of sample points which in turn would drastically decrease the accuracy of the Delaunay interpolation.

For this reason, an approximation scheme to create a regression function to fit it through the set of sample points will be developed. To account for the frequency distribution $f(h^{\mathrm{s}}_{\mathrm{cu}}, \gamma_{\mathrm{s}})$ resulting from the kinematic simulation, a set of weighting factors w_i based on the engagement conditions will also be invoked.

Regarding the regression function design, we will compare two approaches: First, a bi-quadratic approach in $h^{\mathrm{s}}_{\mathrm{cu}}$ as well as γ_{s} invoking a linear coupling term will be investigated. Secondly, an exponential dependency on the rake angle will be combined with a quadratic approach for the undeformed chip thickness, since the dependency of r

on $h^{\mathrm{s}}_{\mathrm{cu}}$ is obviously weak in comparison with γ_{s}. Following this approach, we invoke the functions for the bi-quadratic

$$\overline{r}^{\mathrm{bq}}(h^{\mathrm{s}}_{\mathrm{cu}}, \gamma_{\mathrm{s}}) \approx a_0 + a_1\, h^{\mathrm{s}}_{\mathrm{cu}} + a_2\, \left[h^{\mathrm{s}}_{\mathrm{cu}}\right]^2 + a_3\, \gamma_{\mathrm{s}} + a_4\, \gamma_{\mathrm{s}}^2 + a_5\, h^{\mathrm{s}}_{\mathrm{cu}}\, \gamma_{\mathrm{s}} \tag{5.1}$$

and the exponential approach

$$\overline{r}^{\mathrm{exp}}(h^{\mathrm{s}}_{\mathrm{cu}}, \gamma_{\mathrm{s}}) \approx a_0 + a_1\, h^{\mathrm{s}}_{\mathrm{cu}} + a_2\, \left[h^{\mathrm{s}}_{\mathrm{cu}}\right]^2 + a_3\, \gamma_{\mathrm{s}} + a_4\, \exp(a_5\, [-\gamma_{\mathrm{s}} - a_6]) + a_7\, h^{\mathrm{s}}_{\mathrm{cu}}\, \gamma_{\mathrm{s}}, \tag{5.2}$$

respectively.

In addition, we will take into account the distribution information $f(h^{\mathrm{s}}_{\mathrm{cu}}, \gamma_{\mathrm{s}})$ from the kinematic simulation. To do so, we overlay this distribution with the heat source sample points and calculate a Voronoi tessellation [7] based on the latter in order to define influencing areas associated with each of the sample points. The application of a standard Voronoi tessellation yields the graph in Figure 5.1. Here, the sample points are plotted as white and blue points, whereas the resulting Voronoi cell edges are bound by ridges plotted as black strokes ending in the cell vertices represented as white points. The problem arising in connection with a standard Voronoi tessellation is that it usually contains infinite areas, depicted with dashed black lines in Fig. 5.1, which prohibit the calculation of the according areas.

To overcome this issue, we extend the tessellation algorithm to calculate the intersection of every ridge line crossing the boundaries of the kinematic simulation parameter range. We then reassemble the Voronoi cells to constitute *finite* polygons and to exactly coincide with the histogram boundaries, cf. Fig. 5.2.

With the finite Voronoi cells at hand, we can now calculate a normalised distribution of weighting factors for the set of sample points situated within the histogram area. This is accomplished by the evaluation of

$$w_i = \frac{\displaystyle\int_{\Omega_i} f_k \,\mathrm{d}A}{\displaystyle\int_{\Omega_{\mathrm{hist}}} f_k \,\mathrm{d}A}, \quad \text{such that} \quad \sum_{i=1}^{n_{\mathrm{v}}} w_i = 1, \tag{5.3}$$

for each of the n_{v} Voronoi cell regions Ω_i within the histogram area Ω_{hist}. Furthermore, f_k denotes the absolute frequency of a certain parameter combination $f_k(h^{\mathrm{s}}_{\mathrm{cu}}, \gamma_{\mathrm{s}}) \in \Omega_i$. In this context, the area of the Voronoi cells is calculated using Gauss' Area Formula for simple polygons

$$A = \frac{1}{2} \left| \sum_{i=1}^{n} x_i\, y_{i+1} - x_{i+1}\, y_i \right| = \frac{1}{2} \left| \det \begin{bmatrix} x_i & x_{i+1} \\ y_i & y_{i+1} \end{bmatrix} \right| \tag{5.4}$$

with $[x_i,\, y_i]^t$ representing the coordinates of vertex i belonging to the n vertices of the corresponding polygon. The resulting weighting factors are depicted in Figure 5.2 in terms of the white numbers within the cells. With these weights $w_i \in \{w_1, w_2, \ldots, w_{n_\mathrm{v}}\}$ at hand, we can now continue moving towards the calculation of the regression functions.

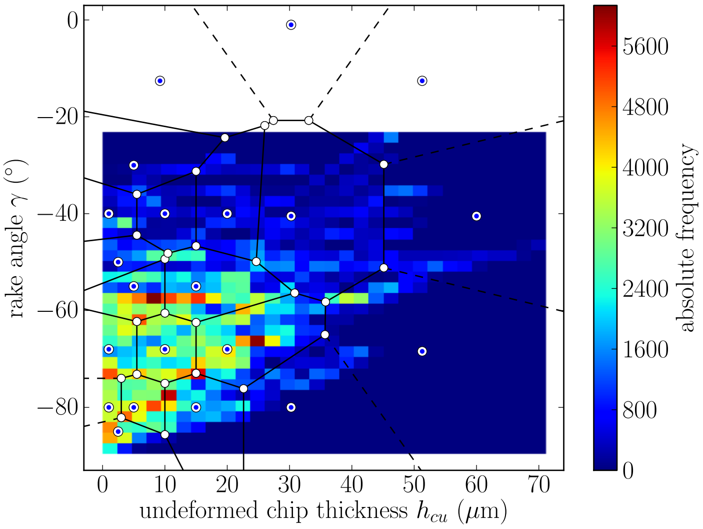

Figure 5.1: Absolute frequencies $f(h^\mathrm{s}_\mathrm{cu}, \gamma_\mathrm{s})$ with standard Voronoi tessellation overlay. The sample points are depicted as white-blue dots and constitute all sample points that have been calculated in the past project progress. Infinite Voronoi cells are bounded by dashed lines. Taken from [38].

To calculate the n_c coefficients a_j of $[a_1, a_2, \ldots, a_{n_\mathrm{c}}] = \boldsymbol{a}$ in Equations (5.1) and (5.2), we invoke a weighted non-linear least-square optimisation to fit the above-mentioned functions to the set of sample points from the meso-scale finite element simulations via

$$\boldsymbol{a} = \arg\min_{\boldsymbol{a}} \sum_{i=1}^{n_\mathrm{v}} w_i [r_i(h^\mathrm{s}_\mathrm{cu},\, \gamma_\mathrm{s}) - \overline{r}^\bullet_i(h^\mathrm{s}_\mathrm{cu},\, \gamma_\mathrm{s};\, \boldsymbol{a})]^2 \,, \tag{5.5}$$

where r_i denotes the heat source term resulting from the meso-scale simulation carried out at sample point i, and $\overline{r}^\bullet_i$ represents the above-mentioned regression functions, see Eqns. (5.1) and (5.2). The scalar n_v denotes the number of weights w_i, equalling the number of sample points or Voronoi cells Ω_i, respectively. As a result from this procedure we retrieve the coefficients depicted in Table 5.1 and the according function plots shown in Figures 5.3.

When comparing the resulting functions $\overline{r}^\bullet$ with each other, we can state that the exponential approach yields a fit that, especially in the area of large absolute rake angles and small depths of cut, covers the sample points by far better than the quadratic approach does. Furthermore, the quadratic approach shows a stronger dependency on h^s_cu in the region of $\gamma_\mathrm{s} \in [-30° \ldots -50°]$ and might therefore result in negative values for r, which reflects a non-physical behaviour. Taking into account the sums of squared

Table 5.1: Coefficients of the bi-quadratic (left column) and exponential (right column) regression function resulting from the regression analysis.

coefficient	bi-quadratic function	exponential function
a_0	5410.5271	-486.1174
a_1	145.5417	62.6139
a_2	-1.6062	-1.2414
a_3	297.1873	22.8165
a_4	4.2482	0.1280
a_5	1.1916	36.6064
a_6	-	-30.7391
a_7	-	-0.1809

errors for the unweighed regressions $R^2_{\mathrm{bq}} = 0.949$ and $R^2_{\mathrm{exp}} = 0.953$, respectively, the exponential approach also yields the better fit. Based on these arguments, we will continue all following investigations based on the exponential regression function $\overline{r}^{\mathrm{exp}}$.

To complete the above-mentioned coupling approach in terms of calculating a heat source term on the macro-scale, we evaluate the regression function $\overline{r}^{\mathrm{exp}}$ in the framework of the kinematic simulation. In detail, by superposing and averaging these results over a certain amount of tool revolutions, we finally retrieve a macroscopic thermo-mechanical load profile that can then be applied to a macro-scale process model as a boundary condition in terms of a moving load.

As stated above, at every time step t_i of the kinematic simulation, we evaluate the regression function

$$\tilde{r}(t_i) = \sum_{k=1}^{n_k} \left[\overline{r}^{\mathrm{exp}}(h^{\mathrm{s}}_{\mathrm{cu}}(t_k), \gamma_{\mathrm{s}}(t_k))\, Q^{\mathrm{s}}_{\mathrm{w}}(t_k)\right]_{t_k = t_i} \tag{5.6}$$

and superpose the grain-related heat source term $\overline{r}^{\mathrm{exp}}$ multiplied with the current single grain material removal rate $Q^{\mathrm{s}}_{\mathrm{w}}$ for all n_k grains that are in contact simultaneously with the workpiece at time t_k, resulting in a transient expression for the thermal power that is induced in the workpiece. By averaging this time-dependent thermal power over a certain time ΔT, or a number of time steps $n_{\Delta t}$, respectively, we retrieve

$$\langle \tilde{r} \rangle = \frac{1}{\Delta T} \sum_{i=1}^{n_{\Delta t}} \Delta t_i\, \tilde{r}(t_i) \quad \forall \quad t_i \in \Delta T \tag{5.7}$$

as the average thermal power induction that can subsequently be used in the macro-scale finite-element simulation currently under development.

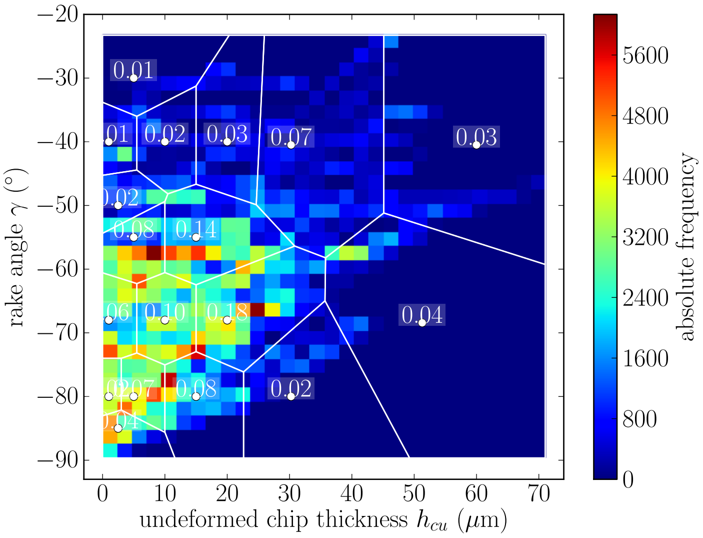

Figure 5.2: Absolute frequencies $f(h^{\mathrm{s}}_{\mathrm{cu}}, \gamma_{\mathrm{s}})$ of engagement conditions with finite Voronoi tessellation overlay. The numbers denote the according weights w_i of every cell belonging to the sample points plotted as white dots. Taken from [38].

5.2 Results and discussion

Following from the above calculation scheme, Figure 5.4 shows the according results. In the case depicted, an averaging over six revolutions of the grinding wheel after reaching a steady state is calculated, yielding $\langle \tilde{r}^A \rangle = 699.741\mathrm{W}$ as the overall thermal power induced. Steady state in the present case means, that a full engagement of the grinding wheel with the workpiece has been established. As can be seen, this thermal power evolution is periodical in t which meets the expectations, since the grains on the grinding wheel surface remain constant over time, and the machined workpiece surface will therefore be exposed to only small periodically repeating changes caused by the intersection with the grinding wheel. The evolution of the thermal power within one exemplary period is directly connected to the structure and the distribution of the modelled cBN grains on the grinding wheel and nicely reflects the according periodically reoccurring engagement conditions. As shown in Fig. 3.6, the number of grains being in contact simultaneously is surprisingly low, which can be observed in the thermal power evolution as well, namely in terms of values of $\tilde{r}$ that equal approximately zero, meaning, that there are no grains in contact at that time.

Comparing the simulated thermal power induced into the workpiece with experimental measurements and the according postprocessing presented in [84], we observe a measured thermal power of $\langle r^A_{\mathrm{meas}} \rangle = 679.262\mathrm{W}$, which depicts a relative error of only 2.9% in the case of experiment A.

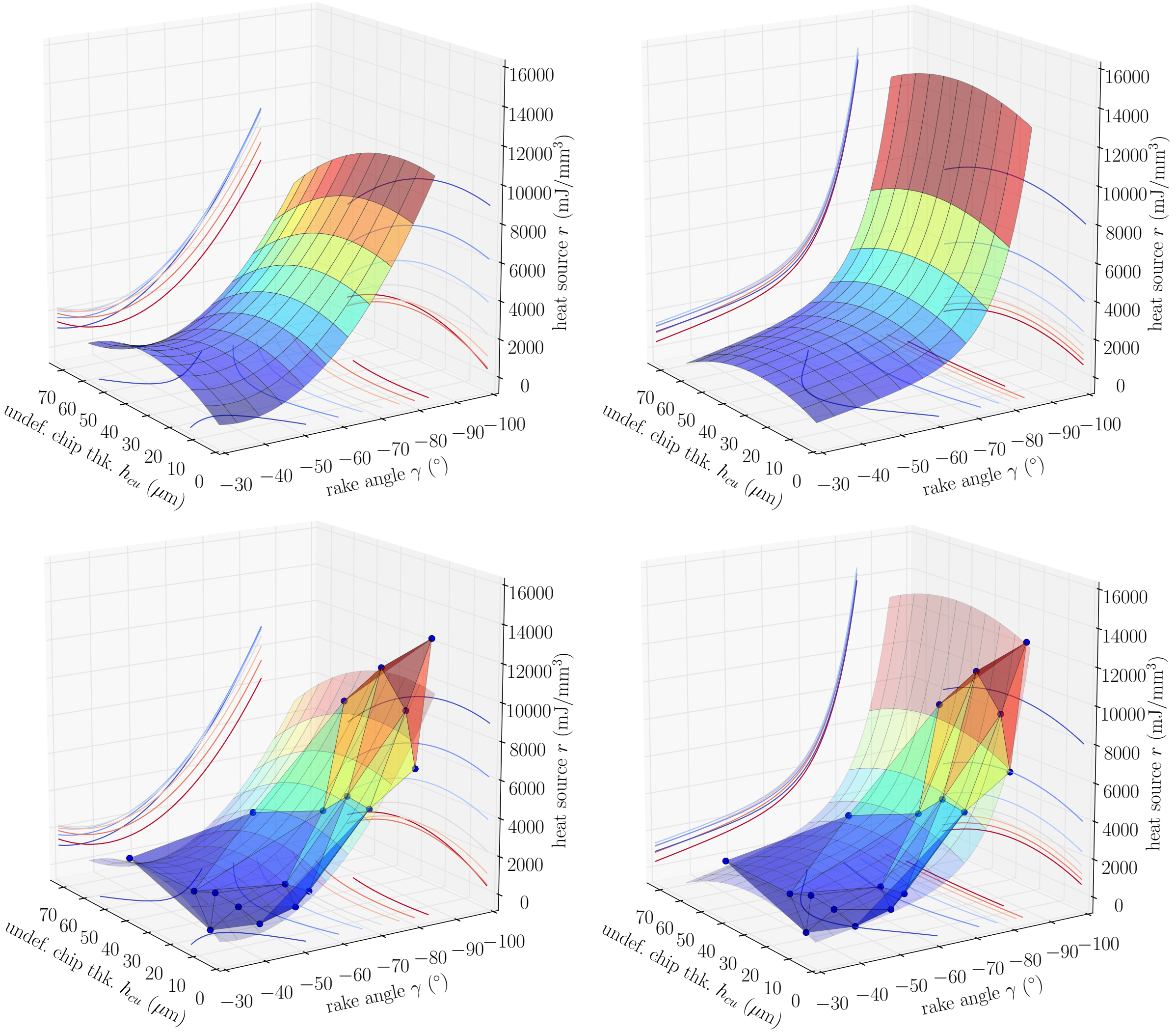

Figure 5.3: Bi-quadratic regression function $\overline{r}^{\mathrm{bq}}$ (left column) and exponential regression function $\overline{r}^{\mathrm{exp}}$ (right column), including a contour line projection onto each base plane. The top row shows only the regression functions, the bottom row in addition depicts the triangulated original data, compare Fig. 4.19. The squared error sums of the unweighed regressions are $R^2_{\mathrm{bq}} = 0.949$ and $R^2_{\mathrm{exp}} = 0.953$ for the bi-quadratic and the exponential fit, respectively. The original heat source sample points are plotted as blue dots along with the Delaunay triangulation of sample points to enable a comprehensive comparison between original data and approximation. Taken from [38].

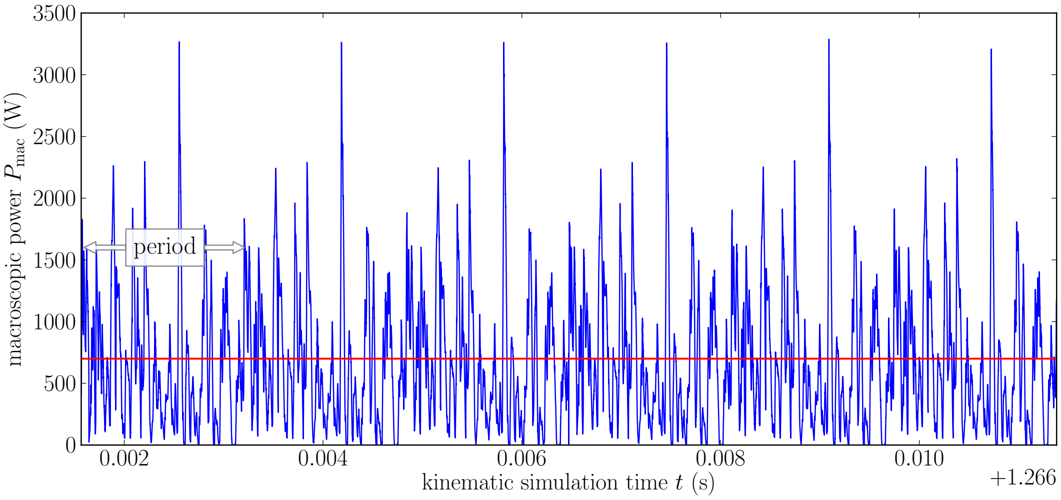

Figure 5.4: Overall estimated macroscopic thermal power $P_{\mathrm{mac}} \equiv \tilde{r}(t)$ over kinematic simulation time t for experiment A. The red line constitutes the average thermal power $\langle \tilde{r}^A \rangle = 699.741\mathrm{W}$ induced over the depicted time span $\Delta T_{\mathrm{kin}} = 0.00981\,\mathrm{s}$. The period, i.e. the duration of one exemplary grinding wheel revolution, is indicated by the white annotation box. Note, that the blue graph depicts a steady-state time interval, neglecting the initial 1.266 s of the process run-up time and also neglecting the time span until the grinding wheel has entirely passed through the workpiece. Taken from [38].

5.3 Bridging the process forces

In analogy to the heat bridging scheme presented, the force data is used to establish the mechanical contribution of the load compound that will be applied as a boundary condition in the process model. As before, the transient data resulting from the meso-scale single grain simulation is used for the development of the homogenisation scheme. Figure 5.5 depicts two exemplary force evolutions for the cutting force components F_t and F_n. Both graphs once again clearly show a typical oscillating behaviour resulting from the chip segmentation. The force evolution cannot fulfil the above-mentioned requirement for an invariance with respect to the meso-scale model size since the force components are directly dependent on the plane strain thickness Δz_ps. Therefore, all force graphs in the present section that are connected to meso-scale results depict specific cutting force components with respect to a unit plane strain thickness $\Delta z_\mathrm{ps} = 1\,\mathrm{mm}$. However, since a linear dependency is given, we will be able to use this property later on during the evaluation of the regression function (5.10). To determine a constant value which will be used as input parameter for the bridging scheme, the average force component values $F_\bullet^\mathrm{avg}(h_\mathrm{cu}^\mathrm{s}, \gamma_\mathrm{s})$ are chosen in the present case. The straight horizontal lines in Fig. 5.5 depict these quantities and prove this choice as sensible.

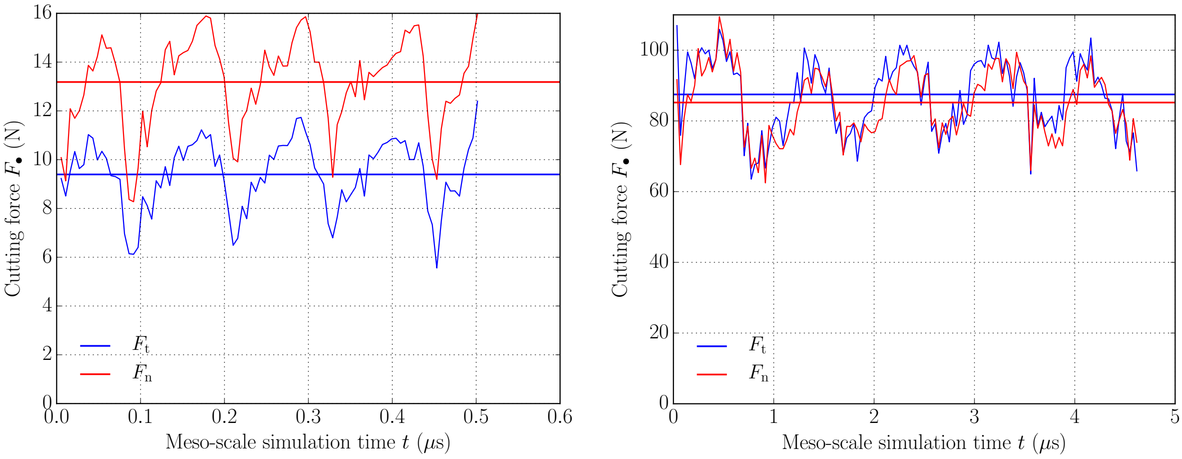

Figure 5.5: Exemplary meso-scale cutting force components $F_\bullet$ obtained from the single grain simulation. The horizontal lines denote the averaged values $F_\bullet^\mathrm{avg}(h_\mathrm{cu}^\mathrm{s}, \gamma_\mathrm{s})$ used for the bridging scheme. Left: $h_\mathrm{cu}^\mathrm{s} = 5.0$ µm, $\gamma_\mathrm{s} = -55°$; Right: $h_\mathrm{cu}^\mathrm{s} = 30.0$ µm, $\gamma_\mathrm{s} = -40°$.

The Delaunay triangulation of $F_\bullet^\mathrm{avg}(h_\mathrm{cu}^\mathrm{s}, \gamma_\mathrm{s})$ known at the sampling points—which are depicted in Fig. 5.2 for both force components—is illustrated in Fig. 5.6. The colour code in this context corresponds to the average slope of the triangular elements. As can be observed, the respective surfaces exhibit a completely different behaviour than observed with respect to the heat source term r, cf. Fig. 4.19. Especially an approximately linear

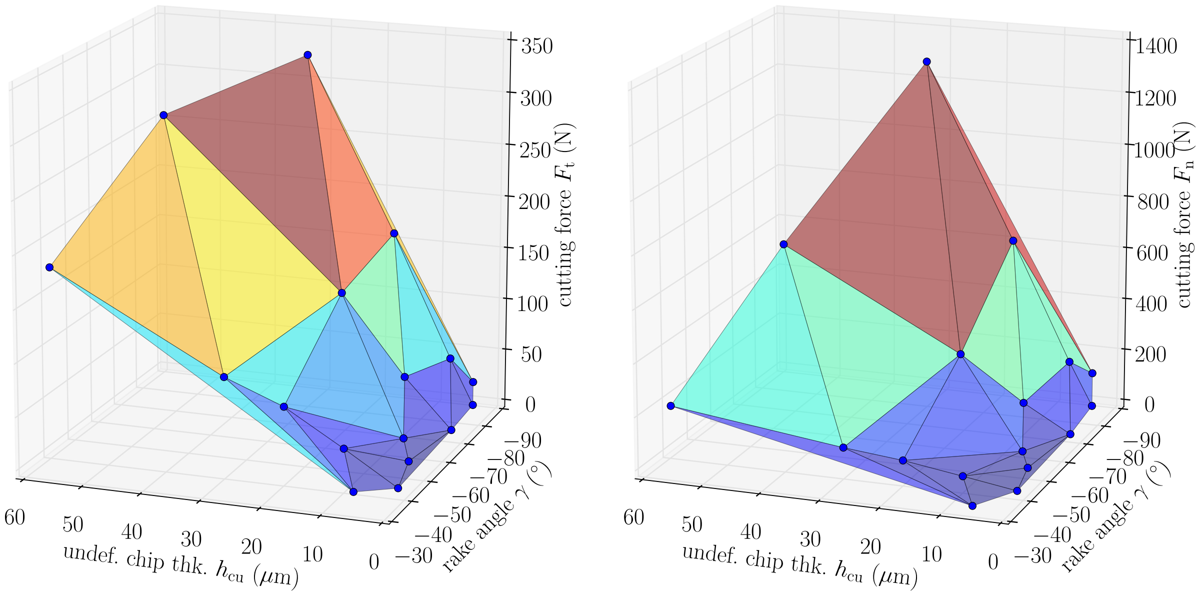

Figure 5.6: Delaunay triangulations of the averaged single grain cutting force components $F_\bullet$. Left: tangential component F_t; right: normal component F_n. The colour of the triangles corresponds to the average slope of the respective surface element.

dependence on the single grain undeformed chip thickness h^s_cu is obvious, whereas the graphs evince a stronger increase in force magnitude with respect to the rake angle γ_s. Therefore, two approaches to approximate the functional dependencies, will be taken into account. At first, a simple bilinear function

$$\overline{F}^{\,\mathrm{bl}}_\bullet(h^\mathrm{s}_\mathrm{cu}, \gamma_\mathrm{s}) \approx a_0 + a_1\, h^\mathrm{s}_\mathrm{cu} + a_2\, \gamma_\mathrm{s} + a_3\, h^\mathrm{s}_\mathrm{cu}\, \gamma_\mathrm{s} \tag{5.8}$$

will be invoked, as well as an exponential approach

$$\overline{F}^{\,\mathrm{exp}}_\bullet(h^\mathrm{s}_\mathrm{cu}, \gamma_\mathrm{s}) \approx a_0 + a_1\, h^\mathrm{s}_\mathrm{cu} + a_2\, \exp(a_3\, [-\gamma_\mathrm{s} - a_4]) + a_5\, \gamma_\mathrm{s} + a_6\, h^\mathrm{s}_\mathrm{cu}\, \gamma_\mathrm{s}, \tag{5.9}$$

which are both including a linear coupling of the parameters h^s_cu and γ_s. For the determination of the coefficients a_j of $[a_1, a_2, \dots, a_{n_\mathrm{c}}] = \boldsymbol{a}$ in the above equations, the same weighted non-linear least-square optimisation as presented in (5.5) is invoked, using the identical weights w_i as computed in the heat bridging scheme. The respective results of the optimisation procedure are depicted in Figs. 5.7 and 5.8. In analogy to the previous section, the approximated functions $\overline{F}^{\,\mathrm{bl}}_\bullet(h^\mathrm{s}_\mathrm{cu}, \gamma_\mathrm{s})$ and $\overline{F}^{\,\mathrm{exp}}_\bullet(h^\mathrm{s}_\mathrm{cu}, \gamma_\mathrm{s})$ are displayed as transparent surface, which is also projected to the three principal graph surfaces in terms of contour lines. The Delaunay triangulations of the corresponding quantities are also displayed for comparative reasons. As can be observed, the shape of both approximation approaches is comparably similar, especially with regard to the tangential force component. Considering the normal force component, only for $\gamma_\mathrm{s} \leq -60°$, a rel-

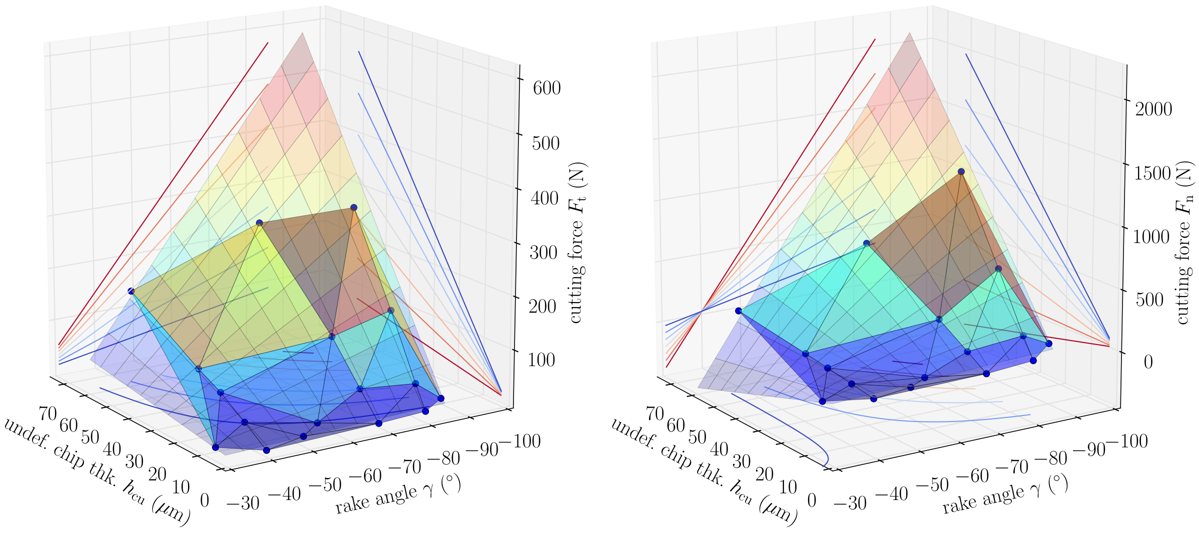

Figure 5.7: Results of the non-linear optimisation when invoking the bilinear approximation (5.8) with respect to the tangential force component (left) and the normal force component (right).

evant curvature of the contour lines is observable. The variation of the approximated data, which is a measure for the quality of the regression scheme is $R^2_\mathrm{bl} = 0.909$ and $R^2_\mathrm{exp} = 0.928$ for the tangential component as well as $R^2_\mathrm{bl} = 0.711$ and $R^2_\mathrm{exp} = 0.786$ for the normal component. We can therefore conclude, that—similar to the heat induction approximation—the exponential approach yields the better fit of the data, whereas the tangential force component approximation $\overline{F}^\mathrm{exp}_\mathrm{t}(h^\mathrm{s}_\mathrm{cu}, \gamma_\mathrm{s})$ evinces a distinctively better approximation than the normal component $\overline{F}^\mathrm{exp}_\mathrm{n}(h^\mathrm{s}_\mathrm{cu}, \gamma_\mathrm{s})$. As can furthermore be observed, both regression approaches exhibit negative function values, which represents an entirely unphysical behaviour, cf. Figs. 5.7 and 5.8. However, these negative values only occur in parameter scopes in terms of h^s_cu and γ_s, which are not relevant in the scope of the present range of engagement conditions, compare Fig. 3.5. Therefore, the exponential approximation will be used for the progress of this thesis.

To finally complete the bridging scheme, the evaluation in terms of the kinematic simulation to retrieve the macroscopic force evolution over time is done in analogy to the superposition presented in the scope of the heat bridging scheme and is defined as

$$\tilde{F}_\bullet(t_i) = \sum_{k=1}^{n_k} \left[\overline{F}^\mathrm{exp}_\bullet(h^\mathrm{s}_\mathrm{cu}(t_k), \gamma_\mathrm{s}(t_k))\, \Delta\bar{z}(t_k)\right]_{t_k=t_i}, \tag{5.10}$$

where $\Delta\bar{z}(t_k)$ denotes the kinematic simulation engagement width of the grain currently in contact at the kinematic simulation time t_k. With this at hand, the time-dependent macroscopic force evolution for both force components $\tilde{F}_\bullet(t_i)$ is completed and can—in analogy to the processing in the previous section—be evaluated in terms of the kinematic simulation and subsequently be used as mechanical boundary condition for the

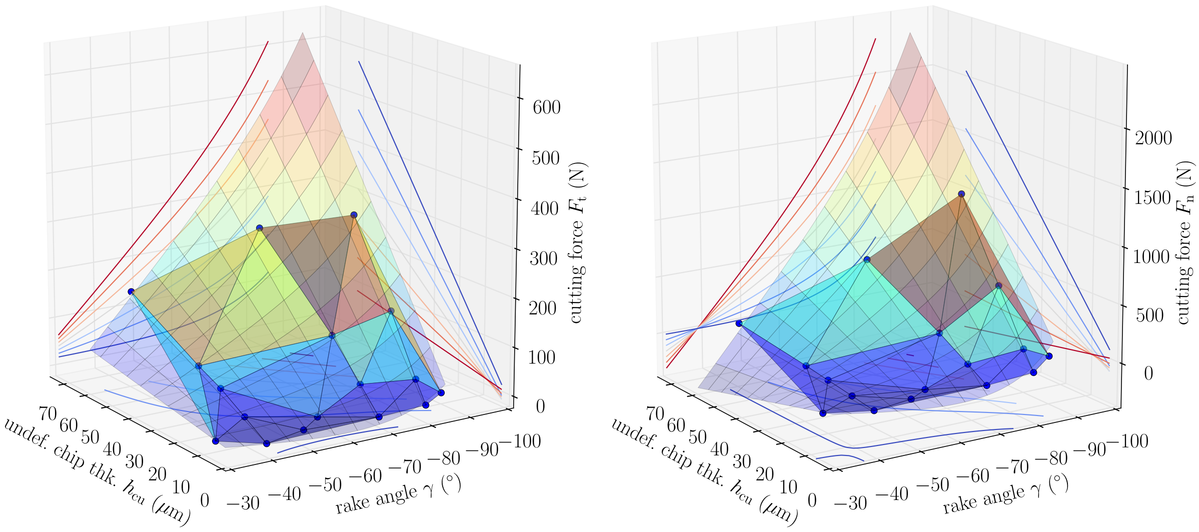

Figure 5.8: Results of the regression scheme when invoking the exponential approximation (5.9) with respect to the tangential force component (left) and the normal force component (right).

macro-scale process model. Figures 5.9 and 5.10 display the respective transient force component evolutions. In the present case, the comparison with measured data yields a larger deviation than presented in the previous section. Referring to the tangential force component, a computed value of $\langle \tilde{F}_\mathrm{t} \rangle = 11.53\,\mathrm{N}$ exceeds the respective measured value $\langle F_\mathrm{t}^\mathrm{meas} \rangle = 8.36\mathrm{N}$ by 37.8%. The normal force component results as $\langle \tilde{F}_\mathrm{n} \rangle = 37.43\,\mathrm{N}$, which represents a relative error of 11.5% in comparison to the measured value of $\langle F_\mathrm{n}^\mathrm{meas} \rangle = 44.94\,\mathrm{N}$. Surprisingly, this contradicts the regression quality presented in the previous paragraph of the present section.

The drawback of the methodology presented above is constituted in the choice of an approximation function, which needs to be designed to fit the underlying physical behaviour of the corresponding meso-scale quantity. The automation of this scope of the grinding framework presented will be referred to future research. To generalise the framework developed, a regression approach that can be based on Bézier curves, De Boor Splines (B-Splines) or Non-uniform rational B-Splines (NURBS), cf. e.g. [22], can be developed to accomplish the curve-fitting problem. A very promising approach is the application of a Clough-Tocher [24] interpolation scheme, which creates a piecewise cubic, C^1-smooth and curvature-minimizing approximation of the Delauney triangulation it is based on, see [69, 77]. This method does not require any more input than the sample points to compute an interpolant with the above-mentioned properties. To enable the usage of this solely interpolating approximation scheme, an extension to a smooth extrapolation is necessary—a very comprehensive survey on this topic with some exemplary applications is given in [17].

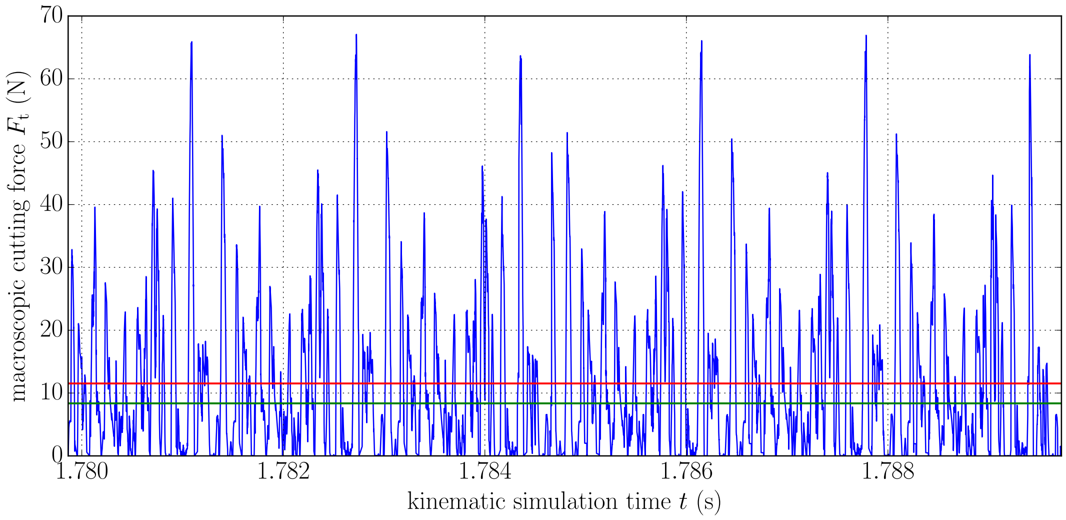

Figure 5.9: Macroscopic tangential force component $\tilde{F}_\mathrm{t}(t)$ over kinematic simulation time t. The red line constitutes the mean force $\langle \tilde{F}_\mathrm{t} \rangle = 11.53\,\mathrm{N}$ averaged over the depicted time span. The green line displays the referring measured value $\langle F_\mathrm{t}^\mathrm{meas} \rangle = 8.36\,\mathrm{N}$. Note, that the blue graph depicts a steady-state time interval, neglecting the process run-up time and also neglecting the time span until the grinding wheel has entirely passed through the workpiece.

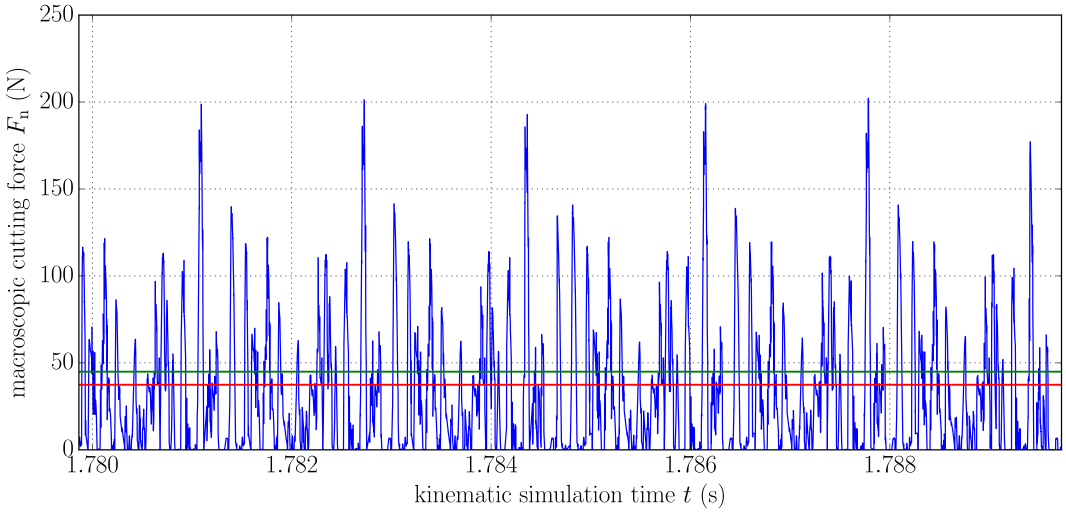

Figure 5.10: Macroscopic normal force component $\tilde{F}_\mathrm{n}(t)$ versus kinematic simulation time t. The red line constitutes the mean force $\langle \tilde{F}_\mathrm{n} \rangle = 37.43\,\mathrm{N}$ averaged over the depicted time span. The green line displays the referring measured average value $\langle F_\mathrm{n}^\mathrm{meas} \rangle = 44.94\,\mathrm{N}$.

6 Process model and compensation approaches

This chapter deals with the development of a macroscopic process model with the objective to capture the thermo-mechanical response of the workpiece during grinding, to compute thermally induced manufacturing errors and to develop compensation strategies to minimise the latter. Due to the process conditions, especially the compensation strategies are tailored to the ITG process and its inherent kinematics and therefore are not unconditionally transferable to grinding processes in general.

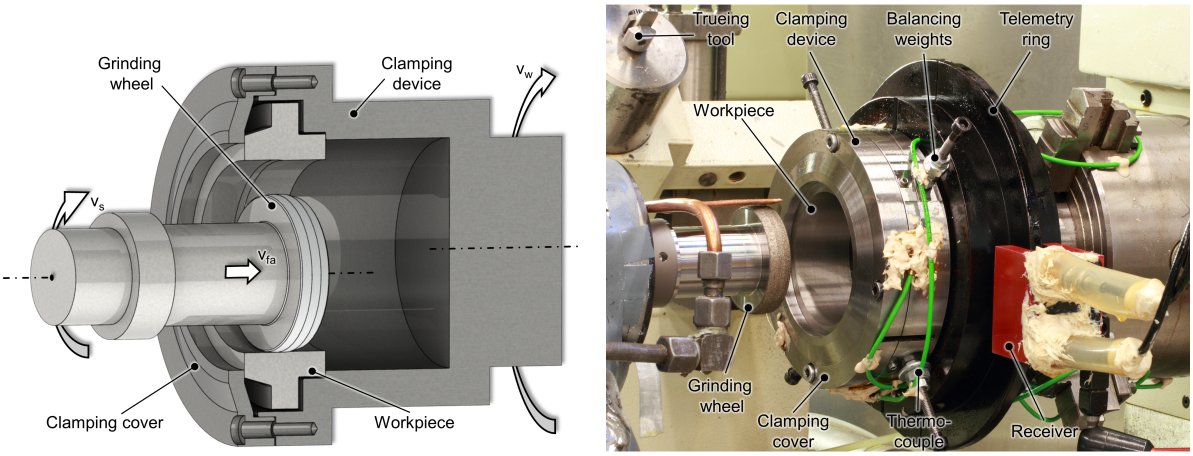
Grinding wheel
Clamping device
v_w
v_s
v_{fa}
Clamping cover
Workpiece
Trueing tool
Clamping device
Balancing weights
Telemetry ring
Workpiece
Grinding wheel
Clamping cover
Thermo-couple
Receiver

Figure 6.1: ITG process scheme (left) and experimental setup (right). Courtesy of ISF, taken from [16]

Let us first recall the process conditions and potentially occurring errors for the reader's convenience. As already briefly described in chapter 1, during ITG, the tool is moved axially through the workpiece along the tool axis, cf. Fig. 6.1, left. In a standard uncompensated process, the tool axis orientation remains parallel to the workpiece axis and does not change its initial spatial position. The resulting workpiece inner radius after grinding and cooling to initial temperature, however, turns out not to be constant along its axis but shows a typical geometrical deviation pattern as depicted in Fig. 6.3.

As a first hypothesis, the following possible reasons are taken into account and will be investigated throughout the present chapter. These aspects are summarised in order of the assumed impact on the geometrical workpiece errors.

Heat induction during grinding The heat generated from plastic dissipation and friction during the meso-scale chip generation causes thermal strains to deform the workpiece. As a result, the deformed configuration of the workpiece will be subject to material removal which is the most likely reason for geometrical errors.

Clamping mechanism To ensure a well-defined positioning of the workpiece during the abrasive process, the workpiece is actuated by adherence in the clamping device depicted in Figs. 6.1 as well as 1.9 and 1.10. Basically, four bolts M6 are used to tighten the clamping cover to the clamping device and as a result, apply an axial pretension on the workpiece. This tension will most likely result in an approximately constant deflection of the workpiece body which in turn may contribute to the overall geometrical error.

Compliance of the grinding machine Both workpiece and tool spindles of the grinding machine will undergo a certain elastic deformation as a result of the process forces. Moreover, the tool shaft on the one hand and the clamping device on the other hand are assumed to constitute a non-negligible part of the machine-based elasticity. Remoter, the guidance appliance of the grinding machine might evince a compliance as well.

Workpiece volumetric transformation strains Due to the concentrated heat induction that is characteristic for the ITG process, transformation induced strains may occur. Referring to Fig. 1.7, it can be observed that the occurring white layer, and thus the workpiece volume affected by transformation-induced volume changes in terms of Bain strains [11], is thinner than 1 µm. The maximum volumetric Bain strain observable in metal materials can be approximated by $\varepsilon_{\mathrm{B}} \leq 5\%$, cf. [14, 98]. In conclusion, this implies that the phase transformation influence on the geometric error is negligible and justifies a compensation strategy development solely based on the thermal expansion of the workpiece bulk due to heating effects.

Hydrodynamic influence of the coolant It has been shown by Heinzel [33], that the coolant liquid and its flow characteristics have an important influence on workpiece temperatures as well as on process forces and residual stresses in grinding processes. As depicted in Fig. 6.1, the clamping device housing constitutes a closed chamber that is continuously flushed with coolant liquid during the process. Observations of the ITG experiments showed that the coolant gushes out of the clamping device chamber shortly after the coolant pump is put into operation. Since the gap between tool and workpiece has the shape of a sickle, a reduced hydrodynamic lubrication effect might occur that causes a deflection of the tool shaft or the tool spindle. The assumption of a reduced lubrication is based on the fact that the abrasive layer of the tool is certainly not smooth enough to allow the application of a conventional hydrodynamic lubrication theory, cf. [31]. Experimental investigation of this issue would be possible by modifying the clamping device with radial discharge bores to prevent coolant impound and gush. This aspect, however, is not within the scope of this thesis.

Regarding the above assumptions, the first three items will be investigated in more detail during the present chapter.

For subsequent development of the process model—and hence, the compensation model—two requirements are crucial: First, the thermo-elastic behaviour of the material under consideration has to be captured reliably and in good agreement to experimental measurements. Secondly, the material removal in accordance to the process kinematics has to be modelled precisely. This is necessary to compute the final geometry of the workpiece cooled back to ambient temperature after applying the thermo-mechanical load compound that reflects the machining process. Due to the reversibility of elastic thermal expansion in metals (as a first approach, we do not assume plasticity or phase transformation effects to be observable), the modelling of material removal is necessary to compute a final configuration $\mathcal{B}^{\text{fin}}$ of the workpiece that is different from its reference configuration $\mathcal{B}^{\text{init}}$. Therefore, the fundamental concept depicted in Alg. 6.1 will be taken into account as a general development goal.

```
Data: workpiece reference configuration $\mathcal{B}^{\text{init}}$; set of process parameters $\mathcal{P}$
set time $t = 0$, initialise ${}^{0}\boldsymbol{\sigma}_k^{\text{wp}} = \mathbf{0}$ and ${}^{0}\theta_k^{\text{wp}} = \theta_0 \; \forall$ elements $\mathcal{E}_k \in \mathcal{B}^{\text{init}}$
for every time step $t_n \in [\,0,\, t_{\max}^{\text{grd}}\,]$ in the load cycle do
    remove material according to process kinematics
    apply thermo-mechanical load compound $\mathcal{L}$ on the newly generated surface
    for all elements $\mathcal{E}_k \in \mathcal{B}_n$ of the updated workpiece configuration at time $t_n$ do
        compute thermo-mechanical response $\boldsymbol{\sigma}_k$ and $\theta_k$
    end
end
remove thermal load and cool workpiece down to ambient temperature to retrieve the final geometry
return final workpiece geometry $\mathcal{B}^{\text{fin}}$, residual stresses $\boldsymbol{\sigma}_{\text{res}}$
```

Algorithm 6.1: Abstract algorithmic scheme for the first process model outline. Indices $\bullet_n$ denote time increments, whereas indices $\bullet_k$ refer to spatial discretisations. Therefore, all increments of discretised functions $\bullet(t_n)$ are denoted as $\bullet_n$.

6.1 Experiments

The development of a process model and corresponding compensation strategies heavily relies on experimental findings that need to be formulated in terms of a feasible model and the validation the latter. Therefore, a brief outline of the referring experiments and process conditions, accompanied with a condensed set of results is presented in the following.

Since the workpiece specimen are reused numerous times for the experimental measurements, the initial inner diameter before grinding r_i^0 increases permanently and the process parameters to maintain a constant circumferential tool velocity $v_\mathrm{c} = 120\,\mathrm{m/s}$ and a constant circumferential workpiece velocity $v_\mathrm{w} = 2\,\mathrm{m/s}$ have to be adjusted according to Chapter 1, Equations (1.1) to (1.3). Throughout the model development in the present chapter, we will keep the referring parameters constant at the values printed in Tab. 6.1, for a comprehensive comparability.

Beyond Equations (1.1) to (1.3), the other parameters necessary for the setup of the experiments as well as the process model are computed as follows. Here, we will use the attribute *nominal* for ideal measures, whereas *effective* will be used for parameters resulting from actual process conditions when incorporating e.g. thermal effects. The nominal axial length l_ca of the tool-workpiece contact zone or the load compound $\mathcal{L}$ to be modelled, respectively, is computed via

$$l_\mathrm{ca} = a_\mathrm{f} + a_\mathrm{p,eff} = a_\mathrm{f} + a_\mathrm{e,tot} \tan(\chi), \tag{6.1}$$

whereas the circumferential contact zone length is approximated by

$$l_\mathrm{cc} = \sqrt{a_\mathrm{e,eff}\, d_\mathrm{s,eff}}, \tag{6.2}$$

cf. [65]. The workpiece revolves with

$$n_\mathrm{w} = \frac{v_\mathrm{w}}{2\,\pi r^\mathrm{i}} \tag{6.3}$$

revolutions per unit time and the tool is moved axially with

$$a_\mathrm{f} = 0.5\,\mathrm{mm/rev}, \tag{6.4}$$

resulting in an axial feed velocity of

$$v_\mathrm{fa} = a_\mathrm{f}\, n_\mathrm{w}. \tag{6.5}$$

Based on the above equations, we can now determine the time span Δt_c necessary to pass the circumferential contact zone length l_cc via

$$\Delta t_\mathrm{c} = \frac{l_\mathrm{cc}}{v_\mathrm{w}}, \tag{6.6}$$

the time that is needed to move the tool axially by a_f as

$$\Delta t_\mathrm{a} = \frac{a_\mathrm{f}}{v_\mathrm{fa}} \tag{6.7}$$

and finally, the total process time representing the time interval that is needed to pass the sum of axial workpiece length and axial engaging tool length is

$$t^\mathrm{grd}_\mathrm{max} = \frac{l^\mathrm{wp} + a_\mathrm{p,eff} + l_\mathrm{fz}}{v_\mathrm{fa}}. \tag{6.8}$$

These equations constitute the complete set of process parameters necessary for the subsequent model development. The corresponding parameter values are summarised in Tab. 6.1.

6.1.1 Fundamental experimental results

The characteristic evolution of the workpiece temperature and the typical shape of the finished workpiece inner surface, which were both measured at the ISF, are depicted in Figs. 6.2 and 6.3, respectively. For the thermal measurements, workpieces equipped with thermocouples were ground using the above-derived process conditions. The thermocouple positions are depicted as coloured dots—corresponding to the line colours in Fig. 6.2—in the workpiece cross-section drawing in Fig. 6.3.

Considering the thermal loading characteristic depicted in Fig. 6.2, there are two main phases of temperatures rise, which will be explained referencing the first thermocouple tc1 (blue stroke) in Fig. 6.2: The preheating phase in the range $11.5\,\mathrm{s} \leq t \leq 32.8\,\mathrm{s}$ and the grinding phase during $32.8\,\mathrm{s} \leq t \leq 42.5\,\mathrm{s}$. During the preheating phase, the coolant pump of the grinding machine is switched on, but the abrasive process itself has not been started yet. As a result, the workpiece is heated by the warm ($\overline{\theta}_\mathrm{cl} = 309.85\mathrm{K}$) coolant liquid from ambient temperature of approximately $\theta_0 \approx 303.5\,\mathrm{K}$ to the preheating temperature $\theta^\mathrm{pre}_\mathrm{tc1} \approx 306\mathrm{K}$. Then, both workpiece and tool spindles are switched on and the rotating tool penetrates the rotating workpiece. During this grinding phase, the tool at first passes the conical section of the workpiece during $32.8\,\mathrm{s} \leq t \leq 35.7\,\mathrm{s}$ and thus causes the steeper temperature rise from $\theta^\mathrm{pre}_\mathrm{tc1}$ to $\theta^\mathrm{max}_\mathrm{tc1} \approx 311\mathrm{K}$. Due to the thermal conductance inertia of the workpiece material, the maximum temperature $\theta^\mathrm{max}_\mathrm{tc1}$ is reached after the tool has passed the respective thermocouple. This effect is observable for tc3, too, which causes $\hat{t}_\mathrm{tc3}$ to lie outside of the shaded grinding time span.

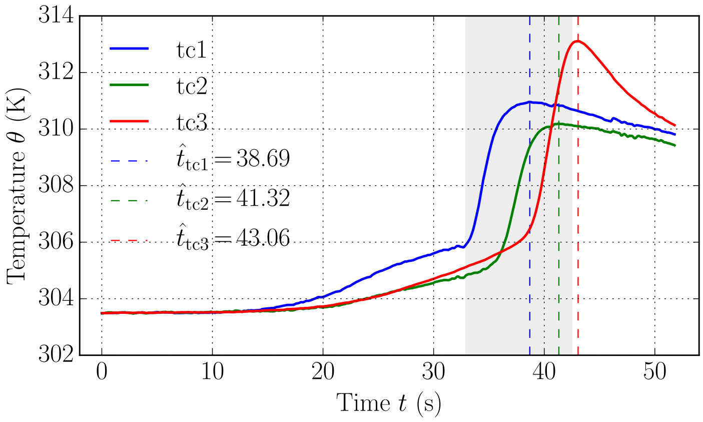

Figure 6.2: Measured temperatures from experiments carried out by ISF. The temperature sensors, i.e. the thermocouples are denoted by tc1 through tc3, in order of the axial feed motion of the tool. The shaded area represents the grinding time span t^{grd} between tool and workpiece, for which approximately $32.8\,\text{s} \leq t^{\text{grd}} \leq 42.5\,\text{s}$ holds—the graph displays the total time span of the experiment. The dashed lines depict the time points $\hat{t}_\bullet$ where the maximum temperatures at each thermocouple are reached.

In further experiments carried out at the ISF, workpieces were ground with equal process conditions to measure the resulting workpiece inner diameter in relation to the axial depth of the ground bore with a 3D coordinate measuring system, cf. [16]. The results of these six experiments are depicted in Fig. 6.3, showing the normalised radius difference Δr from the nominal inner radius $r^{\text{i}}_{\text{nom}}$ at all measurement points along with the standard deviation of the single measurements. Here, the typical error in radial direction is clearly observable: During the entry phase of the tool, $0 \leq z \leq 12\,\text{mm}$, the resulting radius is smaller than the nominal value, while for $z \geq 12\,\text{mm}$ axial protrusion, this trend inverts. This results in a too large inner radius of the workpiece for $12 \leq z \leq 30\,\text{mm}$. After this axial range, the radius once again tends to decrease and shows a peak value which can be assigned to the limited stiffness of the workpiece and grinding wheel spindles, cf. [16].

Remark To enable a more convenient graph reading comprehension and easier comparability between graphs and process model plots, the radial axes of the graphs within this chapter will be inverted.

6.2 Prototype Model

In order to gain a basic insight on the deformation behaviour of the cylindrical workpiece under consideration, cf. Fig. 1.8, and to adjust the load to experimental findings, a simple axisymmetric model is set up as depicted in Fig. 6.4. This model is capable of simulating the thermo-mechanical load on the workpiece according to the process kinematics and

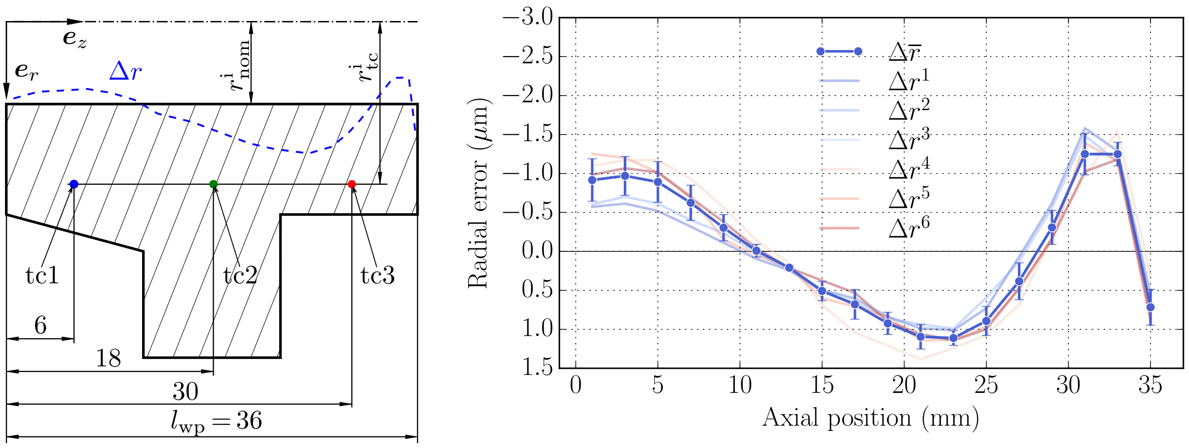

Figure 6.3: Workpiece main dimensions with thermocouple (tc•) positions (left) and measured radial error of the cooled workpiece after the abrasive process (right). The ordinate in the error plot is inverted to enable a convenient comparison with the workpiece drawings in this chapter, compare the dashed blue line in the workpiece drawing. The data rows $\Delta r^{\bullet}$ represent single measurements of six different workpieces that were ground and measured after cooling to ambient temperature. All data sets have been reduced to an average value denoted with $\Delta\overline{r}$ in combination with the standard deviation represented by the error bars. Hence, the horizontal black line at $\Delta r = 0 \mathrel{\widehat{=}} r^{\mathrm{i}}_{\mathrm{nom}}$ represents the nominal inner workpiece radius. Measurement data by courtesy of ISF.

clamping conditions occurring in the experiments. The pre-heating phase observable in Fig. 6.2 is not considered. Instead, the initial temperature of the workpiece will be set to $\theta^{\mathrm{wp}}_0 = 306$ K, so the simulation time of the prototype model will reflect the shaded area depicted in Fig. 6.2. The material model used in this simulation is taken from the meso-scale model presented in Chapter 4.

As shown in Fig. 6.4, the load compound $\mathcal{L}$ representing the tool enters the workpiece from the conical part at $z = 0$ and exits at the cylindrical part at maximum z-position. On the entry face, the clamping is applied from a diameter of $\varnothing 89\,\mathrm{mm}$ to the maximum outer diameter of the workpiece. On the exit face, the clamping starts at a diameter of $\varnothing 93\,\mathrm{mm}$. Both clamping surfaces are defined in conjunction with the clamping device assembly drafts in Figs. 1.9 and 1.10 and are depicted by $\partial\mathcal{B}^{\boldsymbol{u}}_{\mathrm{en}}$ and $\partial\mathcal{B}^{\boldsymbol{u}}_{\mathrm{ex}}$, respectively. As a first approach, the clamping is modelled by applying constant mechanical Dirichlet boundary conditions enforcing zero displacement at the cylindrical clamping faces $\partial\mathcal{B}^{\boldsymbol{u}}_{\bullet}$.

The load compound $\mathcal{L}$ is, at first, reduced to a heat flux $\boldsymbol{q}(t)$ that is moved along the inner surface with the axial feed velocity v_{fa}. This assumption is valid since the process forces are small, cf. [37, 66]. Two approaches to model the time-dependent thermal load will be compared: First, the heat source will be modelled in a quasi-rotating motion to capture the high temperature gradients occurring during the process and to enable better comparability to reference simulations that have been carried out at the ISF, see [85]. In this approach, the axisymmetric workpiece model is assumed to constitute a l_{cc} thick section of a full three-dimensional workpiece, comparable to a plane strain thickness.

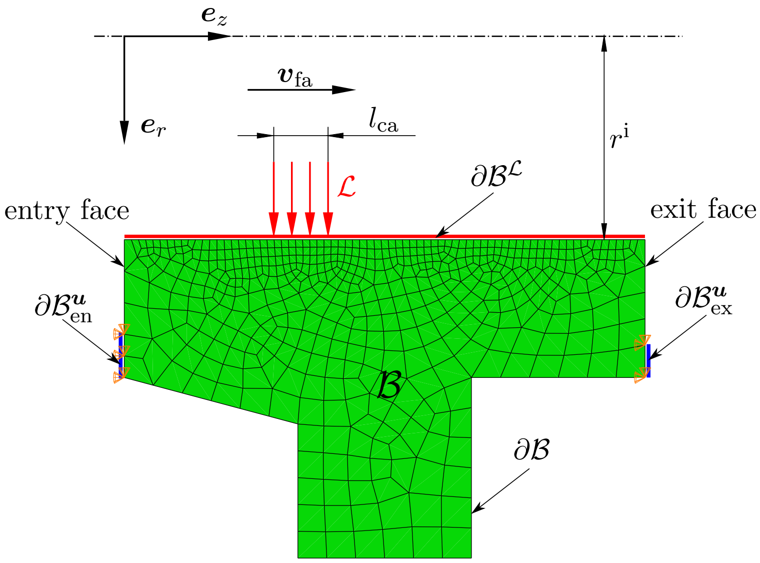

Figure 6.4: Reference configuration $\mathcal{B}$ of the axisymmetric workpiece model with an example initial mesh. The red-marked surface denotes the load surface $\partial\mathcal{B}^{\mathcal{L}}$, the blue marked surfaces represent the clamping surfaces $\partial\mathcal{B}^{\boldsymbol{u}}_{\text{en}}$ and $\partial\mathcal{B}^{\boldsymbol{u}}_{\text{ex}}$ at the workpiece entry and exit faces, respectively. The orange triangle symbols denote the mechanical Dirichlet boundary conditions applied in accordance with the clamping used in the experimental setup. The thermo-mechanical load compound $\mathcal{L}$ that represents the tool is depicted by the red line load. The axial feed motion of the tool is referenced by $\boldsymbol{v}_{\text{fa}}$, whereas the axial contact length of the tool engagement zone is denoted by l_{ca}.

With respect to this representation, the moving heat source representing the tool moves along a helix-shaped trajectory. As a result, the two-dimensional model is affected by the thermal load only during a short time Δt_{c} and is then subsequently load-free until the tool passes for the next time after one revolution of the workpiece. Secondly, a purely axisymmetric approach that moves a constant magnitude heat flux $\|\boldsymbol{q}(t)\| = q_0$ with constant velocity v_{fa} along the inner workpiece surface will be implemented. In both cases, the moving thermal Neumann load is implemented in terms of the Abaqus user subroutine interface, invoking the DFLUX routine, cf. [93]. Since the first approach is assumed to capture the transient thermo-mechanical response of the workpiece in higher detail, it will be invoked to calibrate the thermal load model according to the experimental findings.

To model the quasi-rotating movement of the tool relative to the workpiece, the heat flux $\boldsymbol{q}(t)$ is no longer kept constant but only active during the time span $\Delta t_{\text{c}} = l_{\text{cc}}/v_{\text{w}}$ that is needed to pass the approximated circumferential contact zone length l_{cc} with the circumferential workpiece velocity v_{w}, namely

$$\|\boldsymbol{q}(t)\| = \begin{cases} q_0 & \text{if} \quad t < n\,\Delta t_{\text{c}} \,|\, n \in \mathbb{N}^+ \\ 0 & \text{otherwise} \end{cases}. \tag{6.9}$$

With the calculations from the previous section and Eqns. (6.6) and (6.7) at hand, the usage of an axisymmetric modelling approach can be justified since

$$\frac{\Delta t_\mathrm{c}}{\Delta t_\mathrm{a}} = 0.0162 \ll 1.0 \tag{6.10}$$

is sufficiently small. Furthermore, it is now possible to estimate the lower bound for the number n_Δ of time increments Δt needed to resolve the circumferential motion of the tool "across" the cross-section of the workpiece in the regime of the quasi-rotating load compound. Assuming that the thermal load will be applied entirely within Δt, which represents a numerical singularity in $\boldsymbol{q}(t)$, and considering in addition the Nyquist-Shannon theorem,

$$n_\Delta \overset{!}{>} 2\,\frac{t^\mathrm{grd}_\mathrm{max}}{\Delta t_\mathrm{c}} \approx 9982 \tag{6.11}$$

holds. In conclusion, this necessitates approximately 10000 time increments to be solved for a proper discretisation of the present problem which, in turn, constitutes a drawback of this approach due to the numerical cost. For the temperature calibration, however, this disadvantage will be accepted.

The magnitude of the thermal load $\boldsymbol{q}(t)$ is determined based on the bridging scheme presented in the preceding Chapter 5, where an overall thermal power $\langle\tilde{r}\rangle \approx 700$ W was predicted. In addition, it is calibrated to match the temperature evolution that was measured in the experiments, cf. Fig. 6.2, ensuring a realistic prediction of the thermal workpiece deformation. A short excerpt of the calibration process concerning the temperature evolution at the nodes that represent the thermocouple positions in the workpiece is depicted in Fig. 6.5. To capture the experimental temperature evolutions, the modelling of the coolant liquid is necessary as well. Therefore, the grinding coolant is modelled as a second Neumann load $\boldsymbol{q}_\mathrm{conv}$ in addition to the heating $\boldsymbol{q}(t)$ caused by the abrasive process. As widely used in such type of simulations, cf. [84], this coolant is modelled as a convective Neumann load assuming a constant heat transfer coefficient $\alpha_\mathrm{cool} = 3000\,\mathrm{W/(mK)}$. Consequently, the effective heat flux acting on the referred surface is no longer constant, but depends on workpiece surface temperature and a sink temperature, which in the present case reflects the temperature of the coolant liquid used in the experiments. Measurements of the latter showed that the fluid can—as a good approximation—be assumed to retain a constant temperature of $\overline{\theta}_\mathrm{cl} = 309.85\,\mathrm{K}$. Two variants concerning the surface on which $\boldsymbol{q}_\mathrm{conv}$ acts are implemented, namely all exterior surfaces of the workpiece and only the inner circular surface of the workpiece. As can be deducted from Fig. 6.5, the second approach taking only the inner surface into account captures the experimental findings more precisely.

At this point, we can conclude that the application of a heat flux magnitude per unit area of $q = 80\,\mathrm{W/mm^2}$ along with the above-mentioned convectional cooling shows the best agreement with the thermal experimental results. The referring temperature field

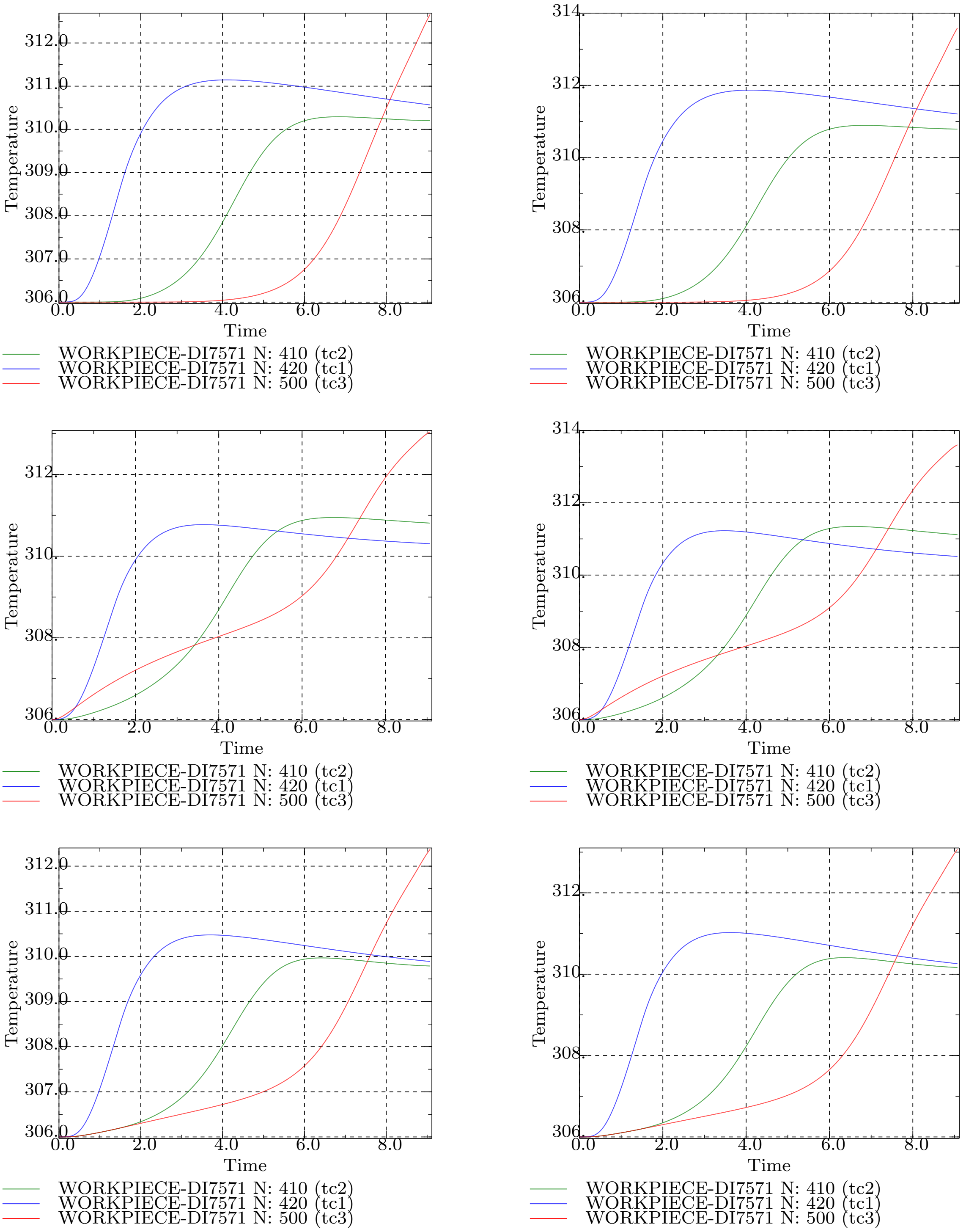

Figure 6.5: Simulated temperature evolution at the three thermocouple sensors tc1 through tc3. The left column depicts an applied heat flux magnitude per unit are of $q_1 = 70\,\mathrm{W/mm}^2$, for the right column, $q_1 = 80\,\mathrm{W/mm}^2$ was applied. The cooling convection is not applied in the top row, applied at the entire external surface $\partial\mathcal{B}$ in the middle row and only on $\partial\mathcal{B}^{\mathcal{L}}$ in the lower row.

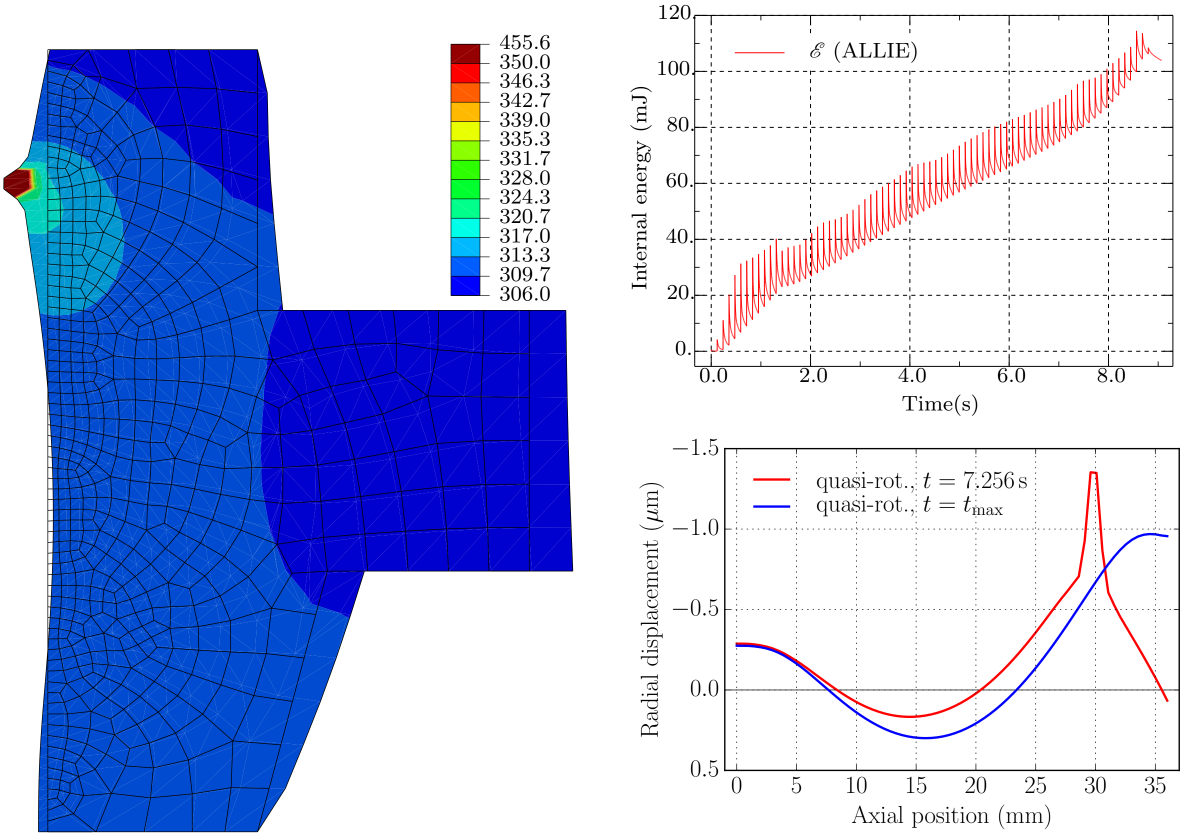

Figure 6.6: Temperature contour plot in Kelvin (left) at $t = 7.256\,\mathrm{s}$ and corresponding radial displacement and internal energy $\mathscr{E}$ (right) when applying a quasi-rotating thermal load. The mesh depicts the reference configuration, the displacement in radial direction is scaled by a factor of 1500. The point of time depicted represents the highest temperature rise and the largest displacement that occurred during the loading simulation. The variable ALLIE corresponds to the Abaqus expression for the internal energy.

as well as the deformation of the workpiece resulting from this thermal load is depicted in Fig. 6.6, representing the simulation at $t = 7.256\,\mathrm{s}$ where the maximum temperature rise at the contact zone is observed. As can be seen, the maximum displacement against the reference configuration reads $u_{\max} \approx 1.4\,\mu\mathrm{m}$ at $t = 7.256\,\mathrm{s}$ and less than $1\,\mu\mathrm{m}$ after the tool passed the workpiece. Interestingly, the shape of the workpiece—especially the voluminous middle section—causes a bending mode to occur, resulting in a too large diameter of the inner workpiece surface during loading. In addition, the evolution of the internal energy $\mathscr{E}(t)$ of the entire model is depicted, indicating a maximum value of about $105\,\mathrm{mJ}$. The numerous peaks represent the moments of time where the heat source is active, whereas the subsequent descents in internal energy denote the loss of thermal energy due to the cooling applied. As expected, the increase of internal energy is approximately linear with respect to time, because of the constant magnitudes of the thermal Neumann loads applied.

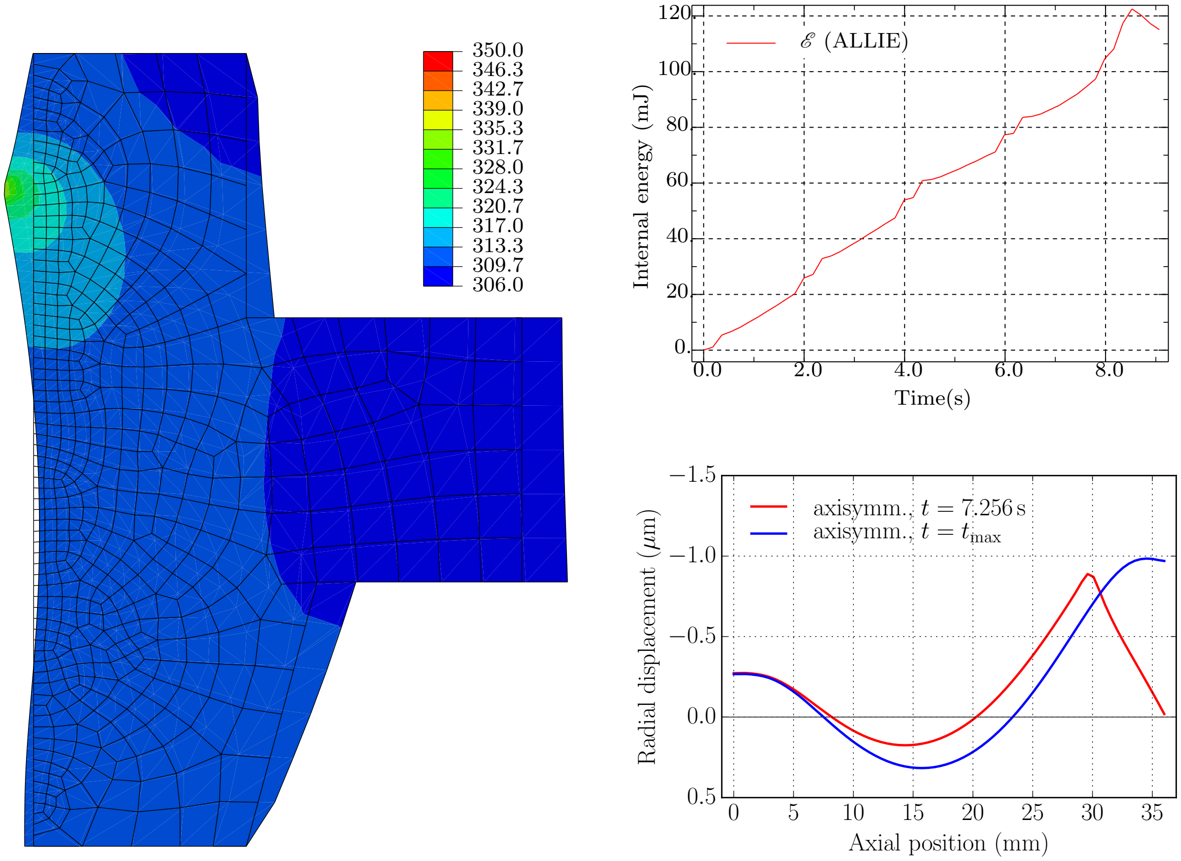

Figure 6.7: Temperature contour plot in Kelvin (left) at $t = 7.256$ s and corresponding radial displacement and internal energy (right) when applying a constant thermal load. The mesh depicts the reference configuration, the displacement in radial direction is scaled by a factor of 1500. The point of time depicted represents the highest temperature rise and the largest displacement that occurred during the loading simulation. The variable ALLIE corresponds to the Abaqus expression for the internal energy.

As addressed earlier, the computational cost of this type of modelling approach is comparably high[1], so it is required to simplify this model in view of the compensation strategies to be developed. Such a high computation time clearly prohibits the solution of the compensation problem by invoking an optimisation scheme, which represents a distinct method towards the minimisation of the addressed geometrical workpiece errors.

Since the transport of thermal energy is slow due to the limited thermal conductivity of the workpiece material, and since the ratio of circumferential and axial velocity of the moving heat source is sufficiently small, too, cf. Eq. (6.10), the fully axisymmetric approach to the application of a moving heat source is justified. The only compatibility condition among both modelling approaches that has to be fulfilled, is the establishment of the same amount of thermal energy $\int \mathscr{Q}_{\text{ext}}\,\mathrm{d}t$ that has to be transferred into the workpiece during the loading phase. Let $\bar{\bullet}$ denote the measures for the axisymmetric approach, the compatibility condition can in general be written as

---

[1] Total computation time was 19894 s ≈ 5h30’ using 8 Intel XEON CPUs with 2.8 GHz clock frequency in parallel in conjunction with 64GB RAM.

$$\int\limits_{t_0}^{t_{\max}^{\text{grd}}} \mathscr{Q}_{\text{ext}}\,\mathrm{d}t = \int\limits_{t_0}^{t_{\max}^{\text{grd}}} \bar{\mathscr{Q}}_{\text{ext}}\,\mathrm{d}t \tag{6.12}$$

$$\int\limits_{t_0}^{t_{\max}^{\text{grd}}} \int_{\partial\mathcal{B}^{\mathcal{L}}} q(t)\,\mathrm{d}A\,\mathrm{d}t = \int\limits_{t_0}^{t_{\max}^{\text{grd}}} \int_{\partial\mathcal{B}^{\mathcal{L}}} \bar{q}(t)\,\mathrm{d}\bar{A}\,\mathrm{d}t, \tag{6.13}$$

considering $\mathrm{d}A = l_{\text{ca}}\,l_{\text{cc}} = \text{constant}$, $\mathrm{d}\bar{A} = 2\,\pi\,r^{\text{i}}\,l_{\text{ca}} = \text{constant}$ along with $\bar{q}(t) = \text{constant}$ and Eqns. (6.9) to (6.7), the latter relation reduces to

$$\bar{q} = \frac{\Delta t_c}{\Delta t_a}\,q_0. \tag{6.14}$$

Here, $q(t)$ and $\bar{q}(t)$ denote the magnitudes of the heat flux per unit area applied in the quasi-rotating and the axisymmetric approach, respectively. Hence, the heat flux magnitude per unit area $q_0 = 80\,\text{W/mm}^2$ reduces to $\bar{q}(t) \approx 1.3\,\text{W/mm}^2$ for the axisymmetric modelling approach. The fact that this heat flux magnitude per unit area is constant in time and furthermore moves with a constant velocity magnitude of v_{fa} along $\partial\mathcal{B}^{\mathcal{L}}$ allows a drastic reduction of the time increment for the solution of the finite element boundary value problem.

The respective results of the finite element solution are displayed in Fig. 6.7, which enables a direct comparison to the results shown in Fig. 6.6. Basically, the only difference between both approaches is depicted by the peak temperature of the process zone, which differs by approximately 120K, and the conforming displacement, which shows a difference of about 0.5 µm. The temperature field of the remaining workpiece, as well as the referring displacement field show a very good agreement. The amount of internal energy induced into the workpiece also displays a consistent evolution and only differs by approximately 5 mJ referring to the absolute maximum value. Moreover, the progress of the thermocouple temperatures exhibits good agreement among both approaches, see Fig. 6.8, where the tc1 maximum is about 0.2 K lower and the tc2 maximum is about the same amount higher in the axisymmetric approach. With regard to the numerical cost however, the axisymmetric approach performs about 550 times faster, since the overall computation time for this model reads just 49.35 s even on one single CPU. In conclusion, the axisymmetric approach clearly outperforms the quasi-rotating model, which is why it will be used as a basis for the further development.

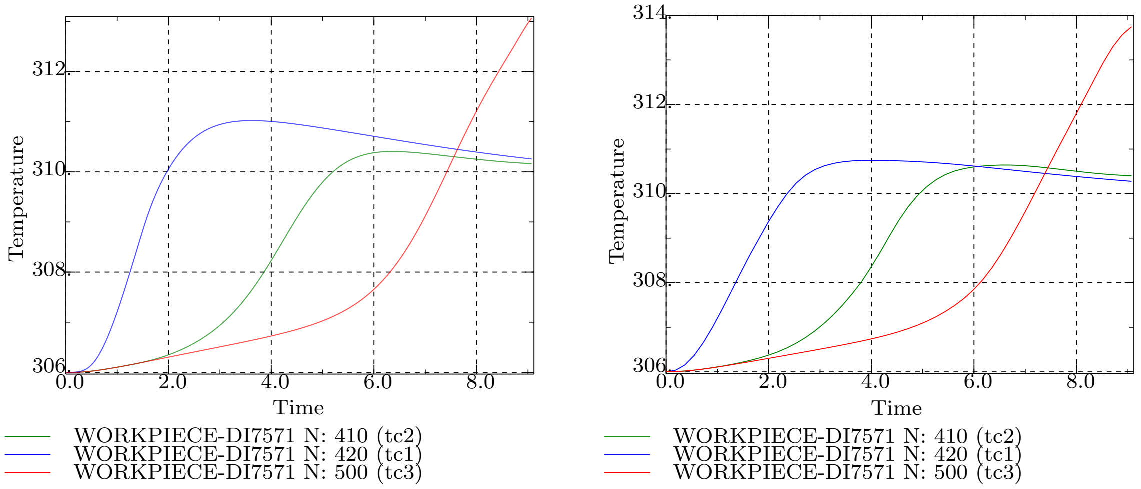

Figure 6.8: Comparison of the thermocouple temperature progress between quasi-rotating thermal load (left) and integral heating method (right).

6.2.1 Influence of the clamping stress

To determine the influence of the clamping stress, the above-mentioned axisymmetric prototype model is used with minor alterations. The Dirichlet boundary conditions $\boldsymbol{u}^{\mathrm{cl}}|_{\partial\mathcal{B}^{\boldsymbol{u}}_{\mathrm{ex}}}$ on the exit face remain, while the Dirichlet boundary conditions $\boldsymbol{u}^{\mathrm{cl}}|_{\partial\mathcal{B}^{\boldsymbol{u}}_{\mathrm{en}}}$ on the entry face are substituted by a Neumann load that is linearly increased to the maximum tension that can be applied with the clamping device used in the experiments, cf. Figures 1.9 and 1.10, respectively. Here, we assume the tension that can be transferred with the four bolts that tighten the clamping cover to be distributed homogeneously onto the annular clamping areas $\partial\mathcal{B}^{\boldsymbol{u}}_{\mathrm{en}}$ and $\partial\mathcal{B}^{\boldsymbol{u}}_{\mathrm{ex}}$ on each side of the workpiece.

According to Grote and Feldhusen [31], p. G169, the maximum pre-load or pre-stressing force F_{pre} that can be transmitted by each of the four M6 bolts of grade 8.8 when loading them up to 90% of the yield stress, mounted with a lightly lubricated surface ($\mu \approx 0.12$, cf. [31]) approximates to

$$F_{\mathrm{pre}} = 9.4\,\mathrm{kN}, \tag{6.15}$$

resulting in a total maximum force F_{tot} that reads

$$F_{\mathrm{tot}} = 4\,F_{\mathrm{pre}} = 37.6\,\mathrm{kN} = 37600\,\frac{\mathrm{t\,mm}}{\mathrm{s}^2}. \tag{6.16}$$

Hence, assuming an—at this stage—ideally stiff clamping lid, a maximum averaged clamping pressure $\overline{\sigma}^{\mathrm{cl}}_{\mathrm{max}}$ acting on the corresponding ring surface

$$\int_{\partial\mathcal{B}^{\boldsymbol{u}}_{\mathrm{en}}} \mathrm{d}A = A^{\mathrm{cl}}_{\mathrm{en}} \pi \left[\left[r^{\mathrm{a}}_{\mathrm{en}} \right]^2 - \left[r^{\mathrm{i}}_{\mathrm{nom}} \right]^2 \right] \qquad \approx 655.611\,\mathrm{mm}^2 \tag{6.17}$$

of the entry face, reading

$$\overline{\sigma}^{\mathrm{cl}}_{\mathrm{max}} = \frac{F_{\mathrm{tot}}}{A^{\mathrm{cl}}_{\mathrm{en}}} = \frac{37.6\,\mathrm{kN}}{655.611\,\mathrm{mm}^2} \qquad \approx 57.351\,\mathrm{MPa} \tag{6.18}$$

can be achieved with the clamping device used in the experiments. Since the clamping device cover is, of course, not ideally stiff in reality, this value represents an upper bound to the workpiece deformation that can occur.

To model the clamping mechanism, the radial degrees of freedom are fixed and the axial degrees of freedom of the nodes lying on the entry clamping surface are constrained to move equally by u_z in axial direction, i.e.

$$\boldsymbol{u}_k \cdot \boldsymbol{e}_r = 0 \;\wedge\; \boldsymbol{u}_k \cdot \boldsymbol{e}_z = u_z \;\forall\; \boldsymbol{x}_k \in \partial\mathcal{B}^{\boldsymbol{u}}_{\mathrm{en}}. \tag{6.19}$$

It is thus assumed that the surface $\partial\mathcal{B}^{\boldsymbol{u}}_{\mathrm{en}}$ does not rotate with respect to the circumferential axis $\boldsymbol{e}_\vartheta = \boldsymbol{e}_r \times \boldsymbol{e}_z$ of the model. The clamping stress $\overline{\sigma}^{\mathrm{cl}}(t)$ is distributed homogeneously on $\partial\mathcal{B}^{\boldsymbol{u}}_{\mathrm{en}}$ and is prescribed linearly increasing from zero to the abovementioned maximum value over ten time steps, cf. Fig. 6.9. As can be easily observed in this figure, the clamping mechanism in general has a clearly non-negligible influence on the deformation behaviour of the inner workpiece contour and thus will be accounted for in the progress of this chapter. In fact, the maximum deflection of the inner workpiece surface is larger than 1 µm, which equals approximately half of the overall radial error observable in the experiments.

To examine the influence of the clamping on the thermo-mechanical workpiece deformation behaviour during the thermal loading phase, two different modelling approaches will be compared: First, the clamping will be modelled as a pure Neumann boundary condition, maintaining a constant stress $\overline{\sigma}^{\mathrm{cl}}_{\mathrm{max}}$ on the clamping surface $\partial\mathcal{B}^{\boldsymbol{u}}_{\mathrm{en}}$ during thermal loading. This approach obviously neglects the compliance of the clamping cover and the bolts mounted, so during thermal loading, the axial workpiece expansion can be expected to antagonise the Neumann boundary conditions that represent the clamping. Therefore, this approach represents the weaker extremal case of the clamping situation.

Secondly, representing the opposing extremal situation in terms of an upper bound of the clamping cover compliance, a pure Dirichlet boundary condition will be taken into account to model the clamping cover. This boundary condition will be held constant at $u^{\mathrm{max}}_z = 4.068$ µm, cf. Fig. 6.9, during the subsequent thermal loading phase. The results in terms of the final displacement $\boldsymbol{u}_k$ and temperature fields θ_k at $t = t^{\mathrm{grd}}_{\mathrm{max}}$ are shown in Figures 6.10 and 6.11, respectively. It can be observed that the resulting temperature

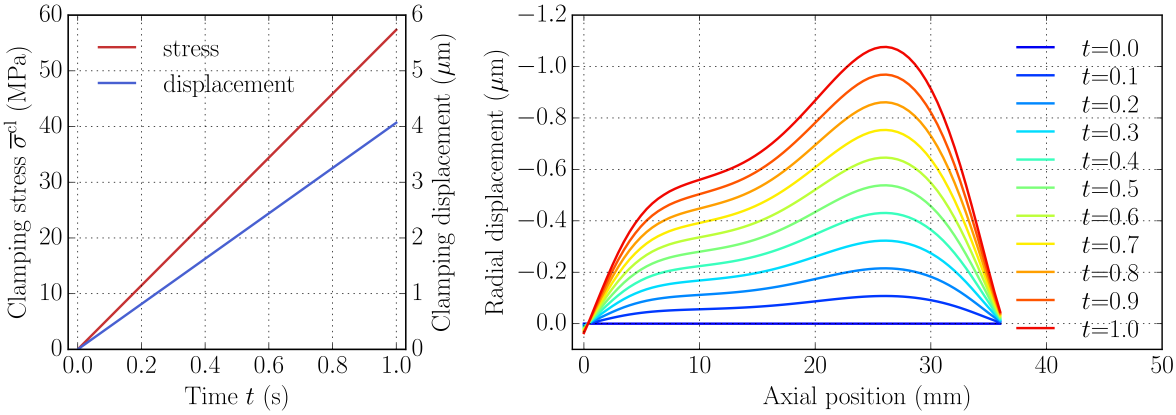

Figure 6.9: Results of the clamping stress test. Applied clamping stress and resulting axial displacement of the clamping area (left) and radial displacements of the load surface nodes as a function of time (right). The maximum axial clamping displacement when applying the maximum stress of $\overline{\sigma}^{\text{cl}} = 57.35\,\text{MPa}$ reads $u_z^{\max} = 4.068\,\mu\text{m}$.

field is expectedly equal among both simulations, whereas the displacement field differs drastically after the application of the thermal load. In the case of a Neumann-based clamping, the thermal expansion of the workpiece causes the clamping face $\partial\mathcal{B}^{\boldsymbol{u}}_{\text{en}}$ to move back towards the reference configuration, as nicely depicted in Fig. 6.12 as a series of spatial configuration temperature contour plots over time. Here, the transient evolution of the displacement and temperature fields is clearly observable as well. Moreover, the comparably slow thermal conductance is also displayed: Even at the end of the simulation time, the outermost segment of the workpiece still maintains the initial temperature θ_0.

When finally comparing the radial displacements of the load surface nodes $\boldsymbol{u}_k \cdot \boldsymbol{e}_r \,\forall\, \boldsymbol{x}_k \in \partial\mathcal{B}^{\mathcal{L}}$ depicted in Fig. 6.13, a very different behaviour for the two extremal cases can be observed. Therefore, we can confidently conclude that the compliance of the clamping cover definitely needs to be accounted for when aiming at a realistic simulation of the clamping mechanism. To do so, either an elastic substitute model representing the clamping cover and the bolts needs to be developed and applied, or the clamping cover needs to be modelled as a component of the process model as well. Since the geometry of the clamping cover crucially influences its structural elastic stiffness, a numerical model needs to be set up in any case to determine the according elastic behaviour. Due to this circumstance, the clamping cover will be included directly into the process model under development, which will be investigated in the subsequent section.

Table 6.1: Process parameters considered in this chapter.

process component	parameter	symbol	value
workpiece	initial inner radius	r_0^{i}	37.855 mm
	nominal inner radius	$r_{\mathrm{nom}}^{\mathrm{i}}$	37.955 mm
	axial inner surface length	l^{wp}	36.0 mm
	initial temperature (homogeneous)	θ_0^{wp}	306 K
	circumferential velocity	v_{w}	2 m/s
	revolutions per unit time	n_{w}	8.4087 1/s
	hardness (Rockwell)	hd^{wp}	61 – 63 HRC
	thermocouple inner radius	$r_{\mathrm{tc}}^{\mathrm{i}}$	44.5 mm
tool	roughing zone angle	χ	10.0°
	circumferential velocity	v_{s}	120 m/s
	axial length of roughing zone	l_{rz}	4 mm
	axial length of finishing zone	l_{fz}	4 mm
overall process	total grinding time	$t_{\mathrm{max}}^{\mathrm{grd}}$	9.6489 s
	average coolant temperature	$\overline{\theta}_{\mathrm{cl}}$	309.85 K
	total radial stock removal	$a_{\mathrm{e,tot}}$	0.1 mm
	axial feed	a_{f}	0.5 mm
	axial feed velocity	v_{fa}	4.204 mm/s
	engaging axial roughing zone length	$a_{\mathrm{p,eff}}$	0.5671 mm
	circumferential contact zone length	l_{cc}	3.8624 mm
	axial contact zone length	l_{ca}	1.0671 mm
	circumferential contact time	Δt_{c}	0.001931 s
	axial contact time	Δt_{a}	0.118925 s

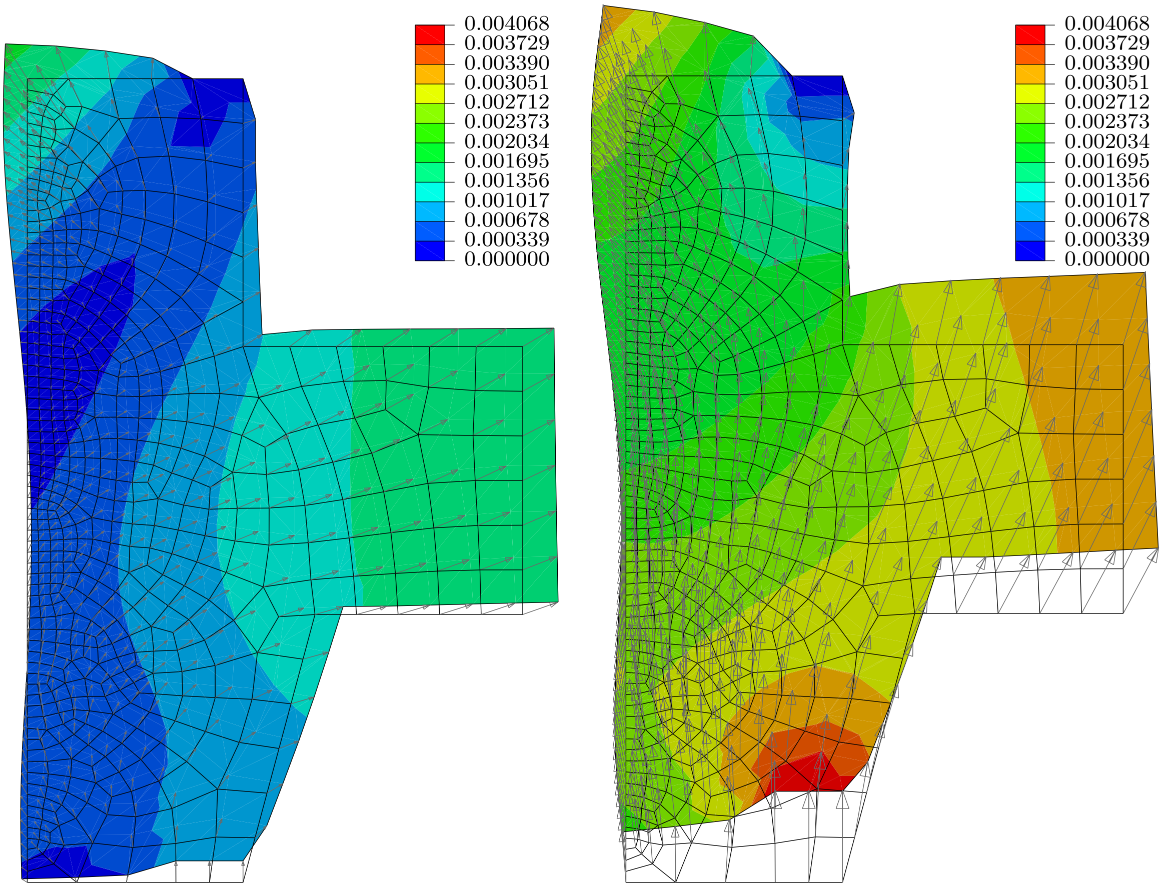

Figure 6.10: Displacement field comparison between Neumann (left) and Dirichlet (right) boundary conditions substituting the clamping cover. The contour plot displays the displacement magnitude $\|\boldsymbol{u}_k\|\,(t^{\mathrm{grd}}_{\mathrm{max}})$ in mm after applying an axisymmetric moving heat source with a constant heat flux magnitude per unit area of $q_0 = 1.3\,\mathrm{W/mm}^2$. The mesh represents the reference configuration $\boldsymbol{X}_k$, the arrows depict the displacement vectors $\boldsymbol{u}_k$ of each node k. Note, that the deformation scaling factor used here is 1000 in each spatial direction.

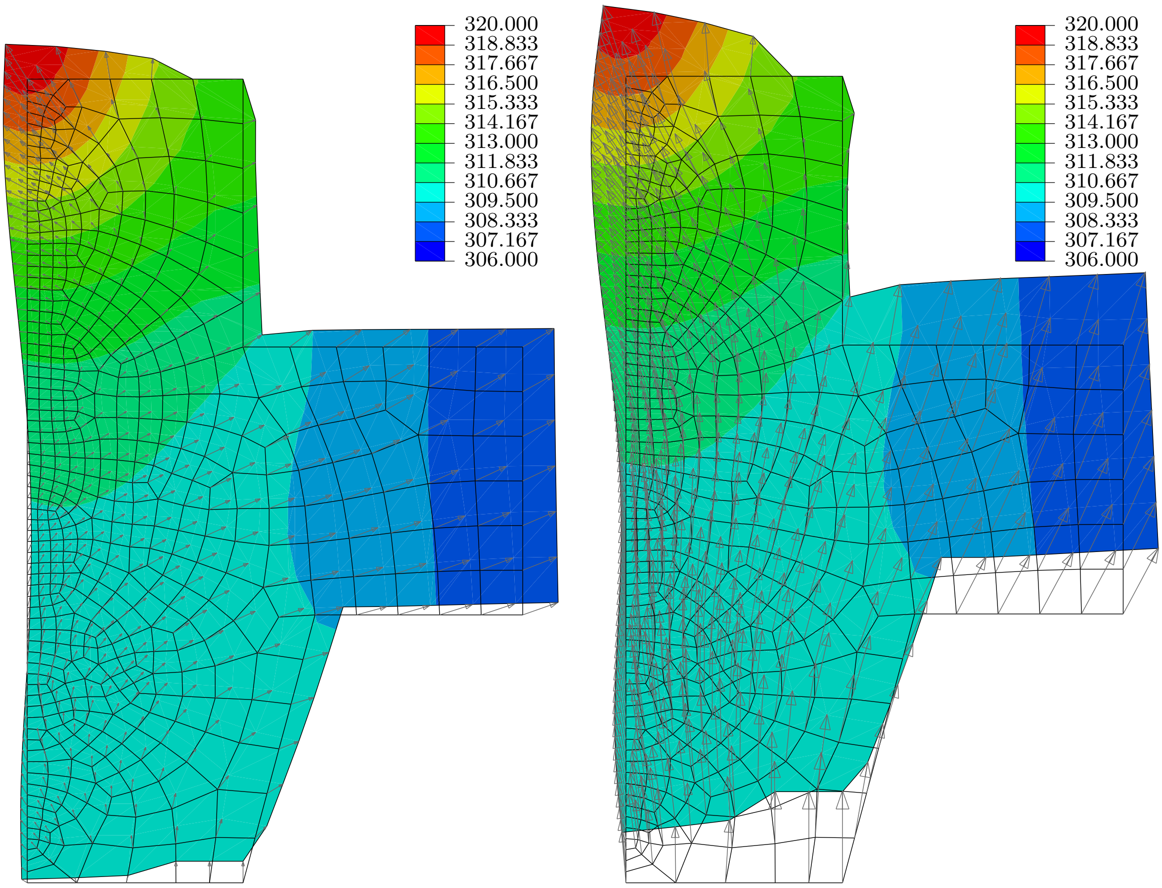
320.000
318.833
317.667
316.500
315.333
314.167
313.000
311.833
310.667
309.500
308.333
307.167
306.000
320.000
318.833
317.667
316.500
315.333
314.167
313.000
311.833
310.667
309.500
308.333
307.167
306.000

Figure 6.11: Temperature field (unit K) after applying a ring-type moving heat source with a heat flux magnitude per unit area of $q_0 = 1.3\,\mathrm{W/mm^2}$. Neumann-based (left) and Dirichlet-based (right) boundary conditions representing the clamping cover. Note, that the deformation scaling factor used here is 1000 in each direction.

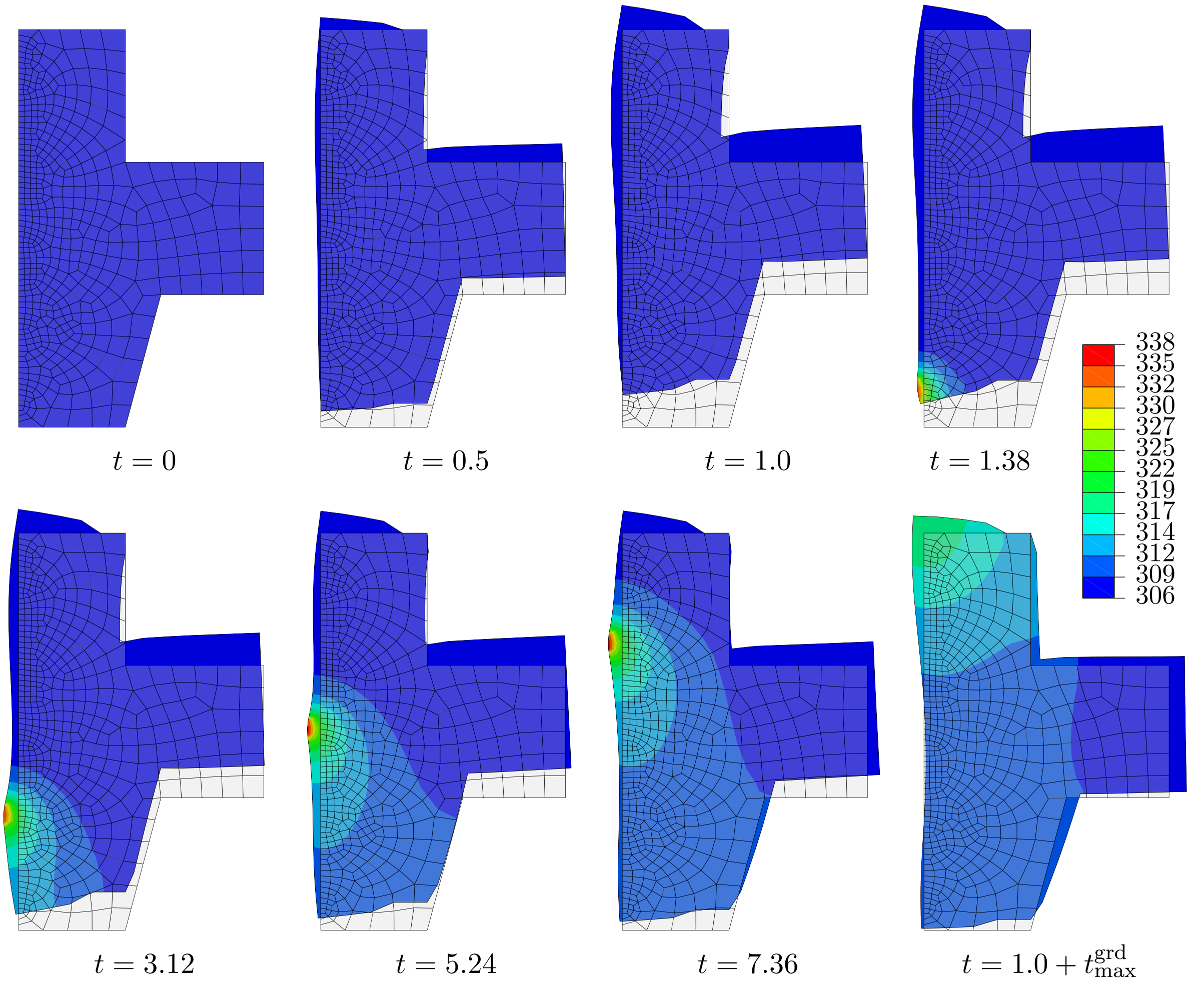

Figure 6.12: Progress of the workpiece loading simulation invoking the purely Neumann boundary condition approach to model the clamping cover. The contour plot represents the workpiece temperature (K). An isotropic displacement scaling factor of 1000 is applied. The mesh represents the reference configuration $\mathcal{B}_0$, the times are printed in seconds. For $0 \leq t \leq 1.0\,\mathrm{s}$, the clamping boundary conditions are applied, the thermal loading takes place for $t > 1\,\mathrm{s}$.

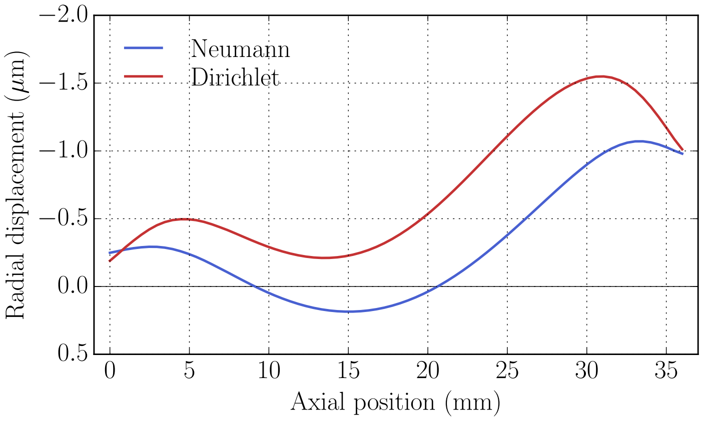

Figure 6.13: Comparison of the radial displacements $u_r(z)$ of the inner workpiece surface nodes $\boldsymbol{x}_k^\bullet \in \partial\mathcal{B}^\mathcal{L}$ between Neumann and Dirichlet boundary conditions representing the clamping cover. The graph depicts the deformed configurations after a complete pass of the tool when applying a heat flux magnitude per unit area of $q_0 = 1.3\,\mathrm{W/mm^2}$. Note, that the radial displacement is defined with respect to the cylinder coordinate system in Fig. 6.4, so a negative value denotes a displacement towards the workpiece axis.

6.2.2 Simulation of the clamping cover

To simulate the influence of the clamping cover and the resulting transient response of its combination with the workpiece, the model used up to this stage is extended to represent an assembly of the workpiece and the clamping cover. The referring boundary value problem is depicted in Fig. 6.14. As a first concept, the fixed Dirichlet boundary conditions at the workpiece exit face $\partial\mathcal{B}^{\boldsymbol{u}}_{\text{ex}}$ are retained, while the boundary condition on the entry face are replaced by a surface-based, impermeable (”hard”) contact condition between workpiece and clamping cover. The details of this contact condition are discussed later. As can be derived from the clamping device drawing, Fig. 1.9, only the clamping cover inner radial surface evinces a contact fitting with the clamping device. Apart from that, solely the bolt heads constitute a further geometric constraint to the clamping cover position. To represent these circumstances, only the inner radial surface of the cover will be applied a Dirichlet boundary condition to, retaining zero displacement in only the radial direction, compare the orange symbols in Fig. 6.14. All further surface and load definitions are equal to the properties of the prototype model depicted in Fig. 6.4, even if they are not printed in the subsequent figure.

As stated in the previous section, a maximum bolt load of $F_{\text{tot}} = 37.6\,\text{kN}$, see Eq. (6.16), is assumed to be applied by the four M6 bolts. To approximate this bold load in the extended prototype model, we assume this force to be applied onto a ring surface $A^{\text{cov}}_{\text{cl}}$ reflecting the contact area of the bolt head base. The axes of the bolts are evenly distributed on a circle with radius $r^{\text{bolt}} = 68\,\text{mm}$, cf. Fig. 1.10, the bolt head base has a radius $r^{\text{bolt}}_{\text{h}} = 5.0\,\text{mm}$, resulting in an area

$$A^{\text{cov}}_{\text{cl}} = \pi\left[\left[r^{\text{bolt}} + r^{\text{bolt}}_{\text{h}}\right]^2 - \left[r^{\text{bolt}} - r^{\text{bolt}}_{\text{h}}\right]^2\right] \qquad \approx 4272.566\,\text{mm}^2 \tag{6.20}$$

of the cover bold face, thus leading to a surface stress load of

$$\overline{\sigma}^{\text{cov}}_{\text{cl,max}} = \frac{F_{\text{tot}}}{A^{\text{cov}}_{\text{cl}}} = \frac{37.6\,\text{kN}}{4272.566\,\text{mm}^2} \qquad \approx 8.800\,\text{MPa}, \tag{6.21}$$

which will be applied in the corresponding simulations. To minimise the mesh influence, the mesh density was increased in the contact regions between workpiece and clamping cover. The contact condition in normal direction is enforced by Lagrange multipliers. For the tangential contact modelling, four cases are investigated: At first, a frictionless contact is implemented, allowing free relative movement of the contact surface nodes. Secondly, a frictional contact with a penalty constraint enforcement algorithm is implemented, assuming a constant Coulomb friction coefficient of $\mu_{\text{con}} = 0.1$. As a third approach, a rough contact is simulated, prohibiting any tangential relative motion of the nodes in contact. Finally, reflecting the fourth approach and the most restrictive case, a Dirichlet boundary condition is used to enforce zero radial displacement of the

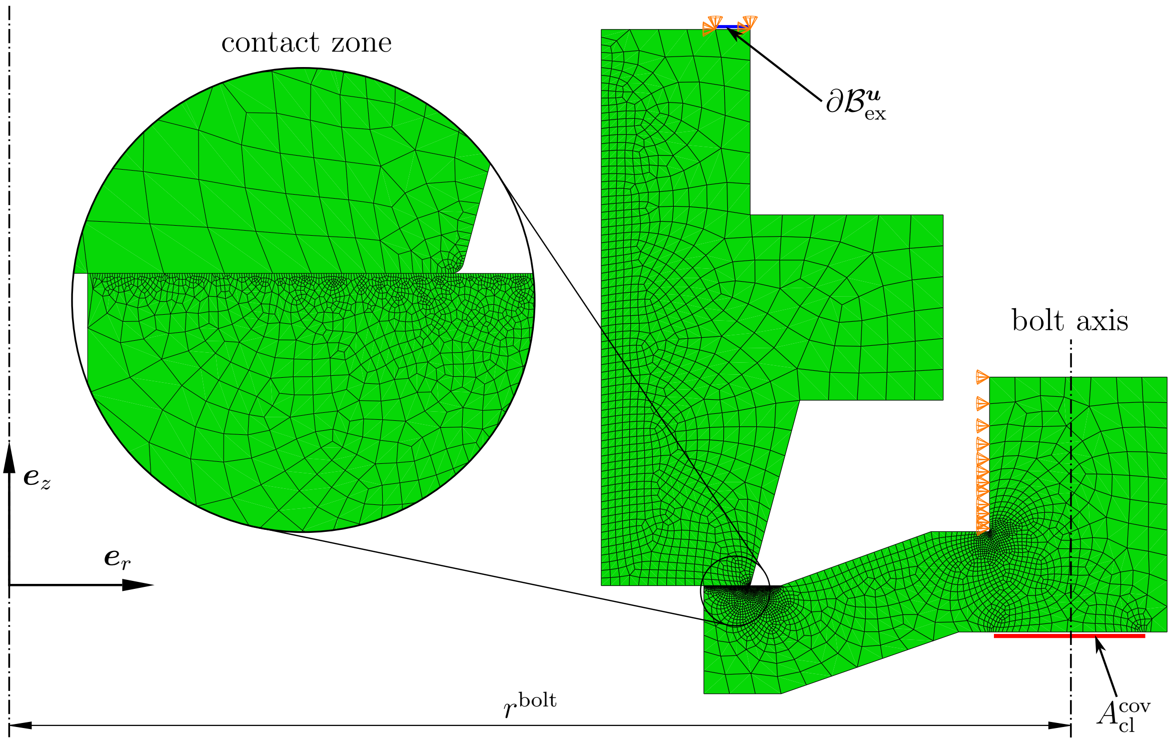
contact zone
$\partial\mathcal{B}^{\boldsymbol{u}}_{\text{ex}}$
bolt axis
$\boldsymbol{e}_z$
$\boldsymbol{e}_r$
r^{bolt}
$A^{\text{cov}}_{\text{cl}}$

Figure 6.14: Extended prototype model including the clamping cover. The orange symbols denote mechanical Dirichlet boundary conditions, the red marked surface represents the bolt load surface.

workpiece nodes within the contact zone. The material of the lid is 42CrMo4, which is modelled with a simple isotropic, thermo-elasto-plastic material model. The respective material parameters are displayed in Tab. 6.2.

The results of these four simulations are shown in Figures 6.15 through 6.18, respectively. The structure of these figures is equal: The left hand side depicts the linearly increasing bolt stress $\overline{\sigma}^{\text{cov}}_z$ that is applied onto the clamping cover and the resulting average axial displacement u^{cov}_z of the load surface as well as the average radial and axial displacement components u^{cl}_r and u^{cl}_z of the workpiece contact nodes $\boldsymbol{x}_k \in \partial\mathcal{B}^{\boldsymbol{u}}_{\text{en}}$ as a function of time. The right hand side shows the time-dependent radial displacements u_r of the workpiece inner surface nodes $\boldsymbol{x}_k \in \partial\mathcal{B}^{\mathcal{L}}$ for different time steps.

It can be observed that all variants constitutively exhibit very different deformation behaviours. Especially the three contact approaches that do not include a radial Dirichlet boundary condition show a positive radial displacement of the contact nodes, implying that the workpiece entrance face $\boldsymbol{X}_k | \, z = 0$ is widened up in radial direction, which fundamentally collides with all expectations. At this point, it is necessary to include measured reference to support the decision for one of the above-mentioned approaches. Therefore, experimental measurements have been carried out by the ISF to investigate

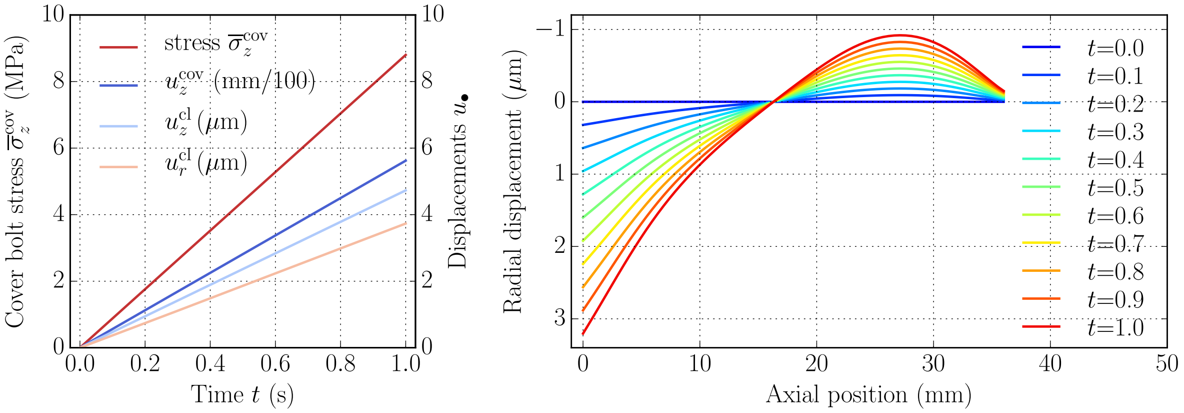

Figure 6.15: Results of the clamping stress test including the cover when applying a frictionless contact. Applied bolt stress, resulting displacements of both the workpiece clamping area and the lid bolt face as a function of time (left) and radial displacements of the thermal load surface nodes (right). The radial displacement of the workpiece clamping nodes is not constrained. The maximum axial workpiece clamping displacement when applying the maximum bolt stress of $\overline{\sigma}_z^{\mathrm{cov}} = 8.8\,\mathrm{MPa}$ reads $u_z^{\mathrm{cl}}(1.0) = 4.729\,\mu\mathrm{m}$, while the radial displacement of this region $\partial\mathcal{B}_{\mathrm{en}}^{\boldsymbol{u}}$ reads $u_r^{\mathrm{cl}} = 3.73\,\mu\mathrm{m}$.

the workpiece geometry before and after tightening the clamping cover bolts. The result in terms of the averaged radial difference Δr between those two states is depicted in Fig. 6.19. As can be seen in this figure, the workpiece indeed grows in diameter at both entry face and exit face with increasing bolt load, here depicted by the bolt torque. However, the maximum displacement of the inner workpiece surface at $z \approx 25\,\mathrm{mm}$, appears to remain constant at approximately $0.2\,\mu\mathrm{m}$ among all applied torques. Up to this point, this observation is quite surprising but was proven to be correct by several measurements conducted. Hence, the modelling approach that includes the Dirichlet boundary condition with respect to the contact can no longer be followed. Due to the observation of a too large radial deflection, the frictionless variant will also be excluded from further investigation. As can be deduced from the measurements in Fig. 6.19, the workpiece clamping faces on both the entry and the exit face apparently need to have a radial degree of freedom, the present simulation will be extended by a further contact constraint that shall replace the Dirichlet boundary condition on the workpiece exit face. Therefore, the rough contact formulation would no longer make any sense, either. In conclusion, the tangential contact will be implemented as the penalty variant enforcing $\mu_{\mathrm{con}} = 0.1$ for further investigation.

Figure 6.20 displays the referring model extension, where the clamping device is now modelled as an analytical rigid body[2] that is constrained for every spatial degree of freedom. In addition, the thus far sharp vertices at the clamping areas $\partial\mathcal{B}_\bullet^{\boldsymbol{u}}$ are rounded with a chamfer of 0.5 mm radius and the meshes are refined accordingly, see the magnified regions. The bolt load and materials are not varied from the previous stage of this model.

---

[2] This is the Abaqus term for an un-discretised body that is represented by some analytical equations.

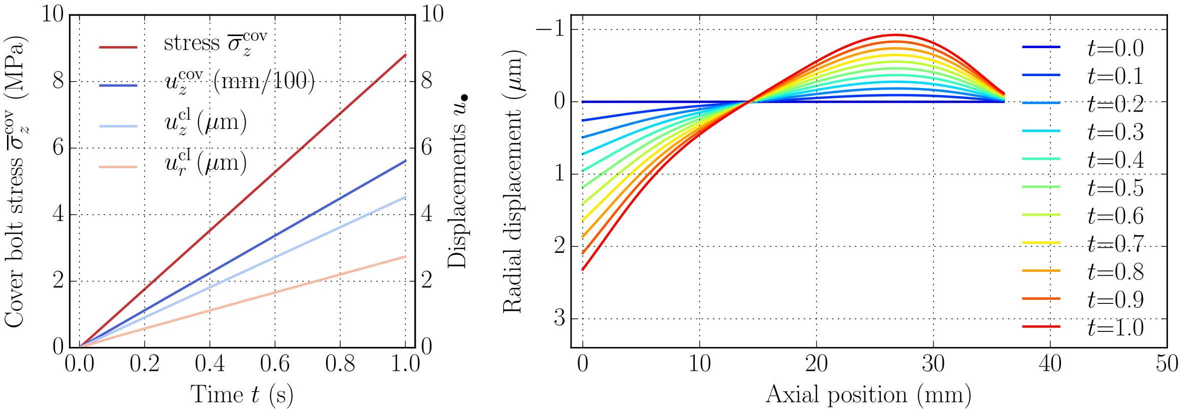

Figure 6.16: Results of the clamping stress test including the cover when allowing a free radial displacement of the workpiece clamping nodes in combination with a **penalty** tangential contact constraint enforcement, applying a friction coefficient of $\mu_{\mathrm{con}} = 0.1$. Applied bolt stress, resulting displacements of both the workpiece clamping area and the lid bolt face as a function of time (left) and radial displacements of the thermal load surface nodes (right). The maximum axial workpiece clamping displacement when applying the maximum bolt stress of $\overline{\sigma}_z^{\mathrm{cov}} = 8.8\,\mathrm{MPa}$ reads $u_z^{\mathrm{cl}}(1.0) = 5.611\,\mu\mathrm{m}$ while the radial displacement of this region $\partial\mathcal{B}_{\mathrm{en}}^{\boldsymbol{u}}$ is $u_r^{\mathrm{cl}} = 2.73\,\mu\mathrm{m}$.

Note, that the mechanical Dirichlet boundary conditions acting on the clamping cover are at first only applied on the inner radial cover surface as depicted by the orange boundary condition symbols. The respective results obtained are depicted in Fig. 6.22, where the displacements of the inner workpiece surface nodes near the entry and exit faces now reflect the measured data better. However, these displacements still exhibit too small values at the exit face while the displacement at the entry face still exceeds the measured displacement by a factor of approximately 2. Therefore, further adjustment to the model is necessary. As can be seen in Fig. 6.21, the surface $A_{\mathrm{cl}}^{\mathrm{cov}}$ of the clamping cover to which the bolt load is applied tends to rotate with respect to the circumferential axis $\boldsymbol{e}_\vartheta = \boldsymbol{e}_r \times \boldsymbol{e}_z$. In addition, the outer radial surface of the cover $A_{\mathrm{out}}^{\mathrm{cov}}$, cf. Fig. 6.22, shows a positive displacement in radial direction, too. As a result, the entire clamping cover moves outwards in radial direction, which seems to be the reason for the too large displacements of the workpiece inner surface nodes at the entry face.

To reduce these displacements, an additional Dirichlet boundary condition is applied to the outer radial surface of the clamping cover as depicted by the blue marked surface $A_{\mathrm{out}}^{\mathrm{cov}}$ in Fig. 6.20. The respective results are depicted in Figs. 6.24 and 6.23. Considering first the resulting workpiece load surface geometry $\boldsymbol{x}_k \in \partial\mathcal{B}^{\mathcal{L}}$, we can see in Fig. 6.24, that the inner surface displacements now show very good agreement with the measurements—the nodes at the entry and on the exit face, as well as the nodes evincing maximum displacement at $z \approx 24\,\mathrm{mm}$ nicely coincide with the experimental data. Referring to the whole-model stress and displacement contour plots depicted in Fig. 6.23, we can at first conclude that the clamping cover rotation of the region connected to the bolt clamping area $A_{\mathrm{cl}}^{\mathrm{cov}}$ is no longer observable as was intended. Furthermore, we can now investigate

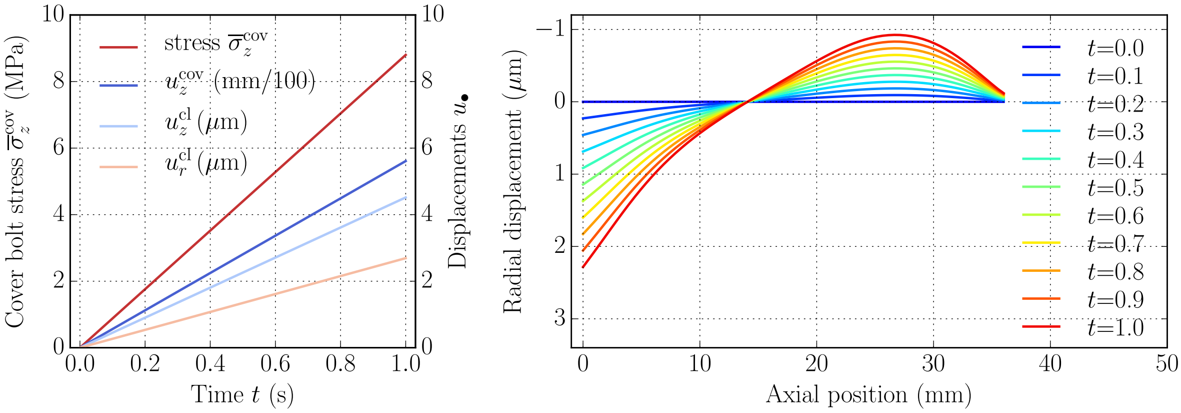

Figure 6.17: Results of the clamping stress test including the cover when allowing free radial displacement of the workpiece clamping nodes in combination with a **rough** tangential contact implementation. Applied bolt stress, resulting displacements of both the workpiece clamping area and the lid bolt face as a function of time (left) and radial displacements of the thermal load surface nodes (right). The maximum axial workpiece clamping displacement when applying the maximum bolt stress of $\overline{\sigma}_z^{\mathrm{cov}} = 8.8\,\mathrm{MPa}$ reads $u_z^{\mathrm{cl}}(1.0) = 4.516\,\mu\mathrm{m}$ while the radial displacement of this region $\partial\mathcal{B}_{\mathrm{en}}^{\boldsymbol{u}}$ reads $u_r^{\mathrm{cl}} = 2.692\,\mu\mathrm{m}$.

the stress response using the two different scales depicted for the same model: The left hand side plot depicting the more responsive scale $0 \leq \sigma_{\mathrm{vM}} \leq 250\,\mathrm{MPa}$ proves the correct assumption that the clamping cover constitutes the most compliant part of the model. The workpiece as the stiffer counterpart evinces only lower-scale equvivalent stresses. Furthermore, it needs to be proven that the clamping cover does not exceed the yield stress limit $\mathsf{Y}_0^{\mathrm{cl}}$ to enable a substitution of the clamping cover part excluding non-linear effects when simplifying the modelling approach in subsequent development stages. Here, we can see that there is basically no plasticity occurring, when investigating the right hand side of Fig. 6.23, where the stress scale was adjusted to $0 \leq \sigma_{\mathrm{vM}} \leq \mathsf{Y}_0^{\mathrm{cl}} = 500\,\mathrm{MPa}$. Although a maximum equivalent stress of $\sigma_{\mathrm{vM}} = 1136.77\,\mathrm{MPa}$ is indicated in the stress plot, this value occurrs in a practically non-visible area in the sharp inner corner of the clamping cover part and is therefore negligible.

In Figure 6.25, the radial displacements of the workpiece load surface $\partial\mathcal{B}^{\mathcal{L}}$ resulting from the different clamping modelling approaches presented in the present section are summarised for the reader's convenience. In addition, the resulting measured data is also plotted for comparative reasons. Here, it is clearly visible, that the last modelling approach presented shows the best approximation of the measurements, although the maximum deflection observable at $z \approx 25\,\mathrm{mm}$ differs from the measured curve by about half a micrometer.

After now having achieved the goal to model the clamping behaviour in good agreement to the experimental results, we need to investigate the thermo-mechanical response of the extended model when loading it with $\mathcal{L}(t)$. Therefore, the simulation including

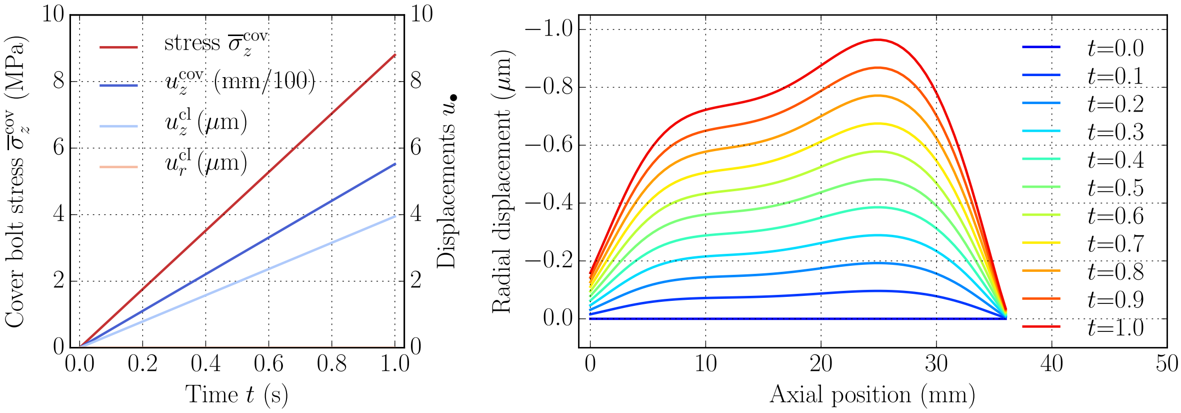

Figure 6.18: Results of the clamping stress test including the cover when enforcing zero radial displacement of the workpiece clamping nodes. Applied bolt stress, resulting displacements of both the workpiece clamping area and the lid bolt face as a function of time (left) and radial displacements of the thermal load surface nodes (right). The maximum axial workpiece clamping displacement when applying the maximum bolt stress of $\overline{\sigma}_z^{\mathrm{cov}} = 8.8\,\mathrm{MPa}$ reads $u_z^{\mathrm{cl}}(1.0) = 3.947\,\mu\mathrm{m}$.

the clamping cover is extended with a thermal loading step applying the adjusted $\mathcal{L}(t)$ presented in Section 6.2 after applying the clamping step.

The corresponding results in terms of an equivalent stress contour plot—once again in two scales comparing the reference and spatial configurations of the model—are displayed in Fig. 6.28. Again, it can be observed, that the von Mises equivalent stress exceeds the initial yield limit $\mathsf{Y}_0^{\mathrm{cl}}$ of 500 MPa only in a very small area in the proximity of the sharp transition between the clamping cover inner radial fitting face and the axial contact face of the clamping cover part. Since this vertex, however, was not modelled with a chamfer, the occurrence of plastic straining can be neglected in good approximation due to the geometric singularity present here. Therefore, the developed modelling approach proves to constitute a good approximation for the present process conditions. Let us now take a look on the transient radial displacement of the workpiece inner surface nodes $\boldsymbol{x}_k \in \partial\mathcal{B}^{\mathcal{L}}$ during the thermal loading phase. Obviously, the contact approach proven to be—in very good agreement—admissible for the clamping phase does not seem to be applicable for the subsequent thermal loading phase, which is easily observable in Fig. 6.26. Here, we can see from the graph on the right that the inner surface nodes entirely move outwards in radial direction during the heating phase. It is furthermore observable that the envelope of all radial displacement maxima does not exceed the radial displacements of the inner workpiece surface at $t = 1.0\,\mathrm{s}$. This would imply a resulting final workpiece inner surface profile after cooling that is too small (referring to the nominal value) over the entire axial range $0 \leq z \leq 36$ mm of the workpiece. This completely contradicts the measurements depicted in Fig. 6.19, where essentially the middle section $10 \leq z \leq 28$ mm shows too large radial values.

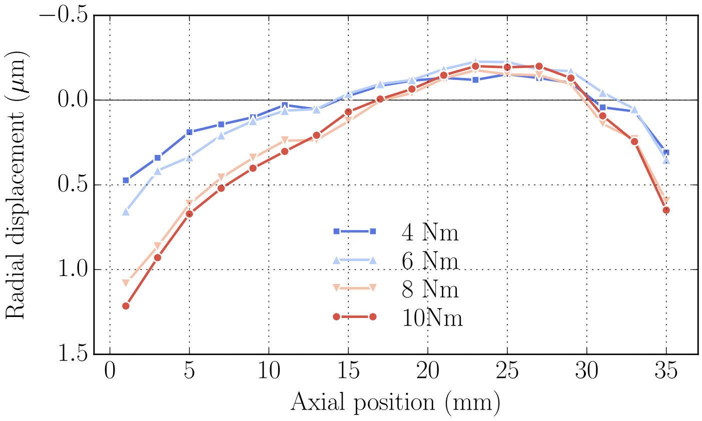

Figure 6.19: Measured inner workpiece surface radius difference between unloaded and clamped configuration depending on the torque applied to tighten the clamping cover bolts. Note, that 10 Nm is the maximum torque an M6 bolt of grade 8.8 can be tightened with. The line markers represent the axial positions, at which the actual measurements were conducted. Measurement data by courtesy of ISF.

As a first countermeasure, the tangential contact behaviour is updated to behave as a rough surface pairing, i.e. no more relative motion between the contact surfaces is admissible during the thermal loading phase. The respective results are depicted in Fig. 6.27. A second potential solution to this problem is the substitution of the contact areas by adapted non-constant Dirichlet boundary conditions. This appears reasonable because the deformation of the workpiece during the grinding process cannot be measured with the current experimental setup and, therefore, there is no experimental data available to verify any modelling assumptions. In addition, the computational cost as well as the model complexity would remain small which constitutes an advantage in view of the compensation strategies to be developed.

The application of a rough contact formulation during the thermal loading face apparently improves the displacement behaviour, as can be observed in Fig. 6.27. It can be seen, that the averaged axial displacement of the workpiece clamping nodes on the entry face decreases from 4.656 µm to 1.696 µm, whereas the radial displacement of this region evolves from 1.915 µm to 2.483 µm. As expected, the contact nodes at the workpiece exit face remain constant at 0.767 µm, due to the rigid body representing the clamping device. As a preliminary conclusion, we can deduce that modelling the clamping as transient Dirichlet boundary conditions appears to be the most reasonable approach with respect to the results presented so far. When applying the substitution of the contact pairs by transient Dirichlet boundary conditions, the above-mentioned values will be used to prescribe the spatial positions of the respective workpiece areas.

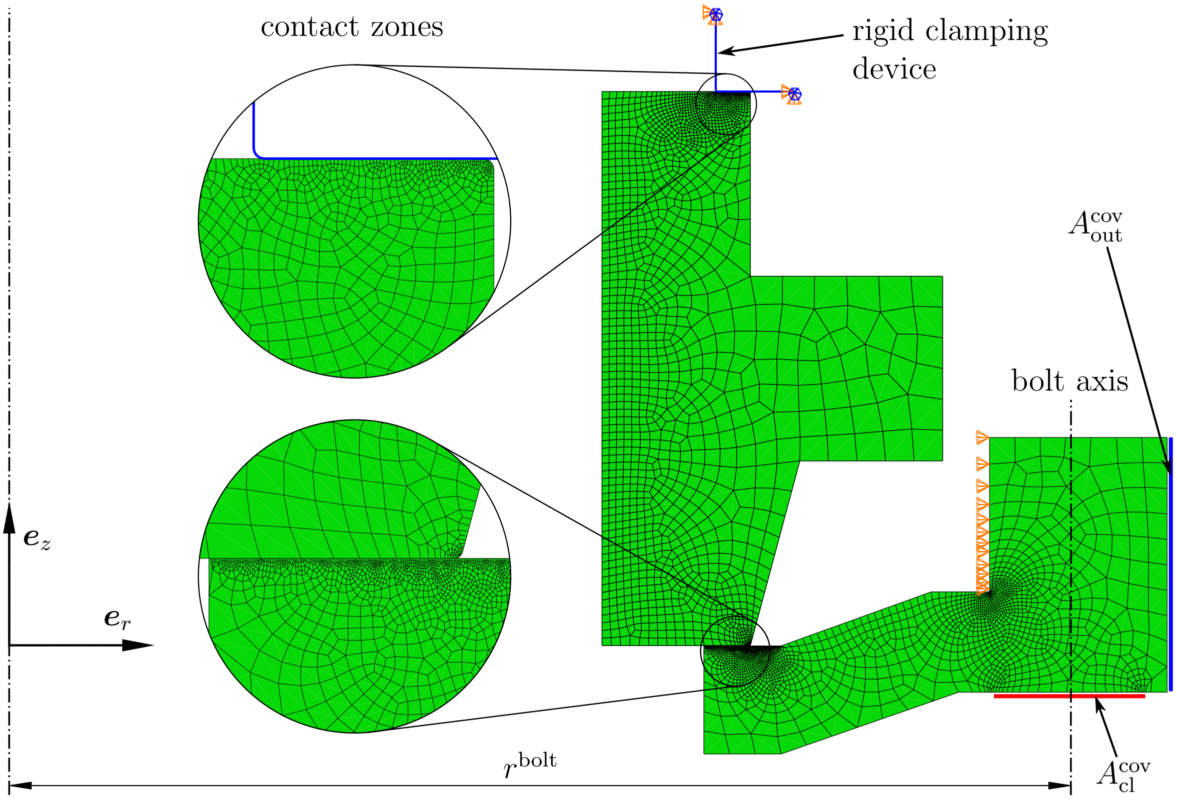
contact zones
rigid clamping device
$A^{\mathrm{cov}}_{\mathrm{out}}$
bolt axis
$\boldsymbol{e}_z$
$\boldsymbol{e}_r$
r^{bolt}
$A^{\mathrm{cov}}_{\mathrm{cl}}$

Figure 6.20: Workpiece model including the clamping cover and contact at both clamping faces $\partial\mathcal{B}^{\boldsymbol{u}}_{\mathrm{en}}$ and $\partial\mathcal{B}^{\boldsymbol{u}}_{\mathrm{ex}}$. The magnified regions depict the referring contact zones. The clamping device is assumed to be rigid and displayed as blue lines. The mechanical Dirichlet boundary conditions are represented by the orange symbols.

Table 6.2: Material parameters considered in this chapter.

process component	parameter	symbol	value
workpiece	— see Chapter 4 —		
clamping cover/device	Young's modulus	E^{cl}	210 GPa
	Poisson's ratio	ν^{cl}	0.28
	initial yield stress	$\mathsf{Y}^{\mathrm{cl}}_0$	500 MPa
	mass density	ρ^{cl}_0	7850 kg/m^3
	specific heat	c^{cl}	470 J/[kg K]
	thermal conductivity	λ^{cl}	50 W/[m K]

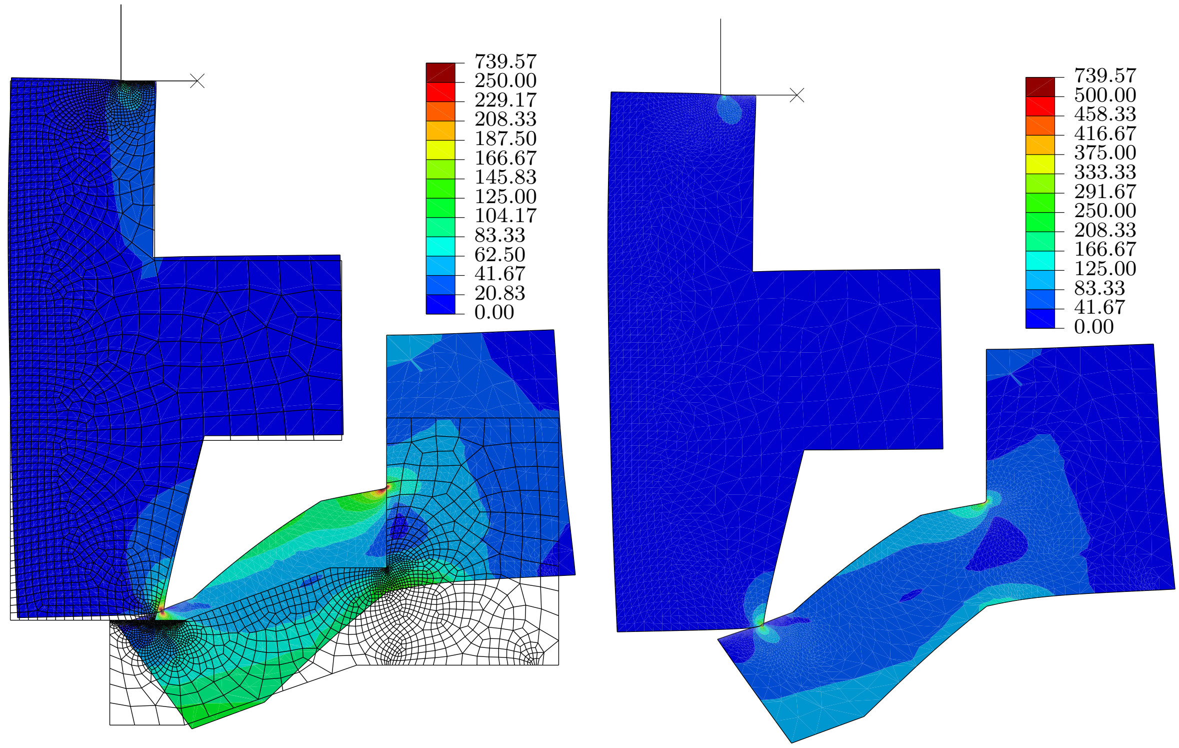
739.57
250.00
229.17
208.33
187.50
166.67
145.83
125.00
104.17
83.33
62.50
41.67
20.83
0.00
739.57
500.00
458.33
416.67
375.00
333.33
291.67
250.00
208.33
166.67
125.00
83.33
41.67
0.00

Figure 6.21: Workpiece model including the clamping cover and contact formulation for both clamping faces. The contour plot shows the von Mises equivalent stress [MPa] in two different scales after applying the clamping stress with a displacement scaling factor of 100 in axial and 200 in radial direction.

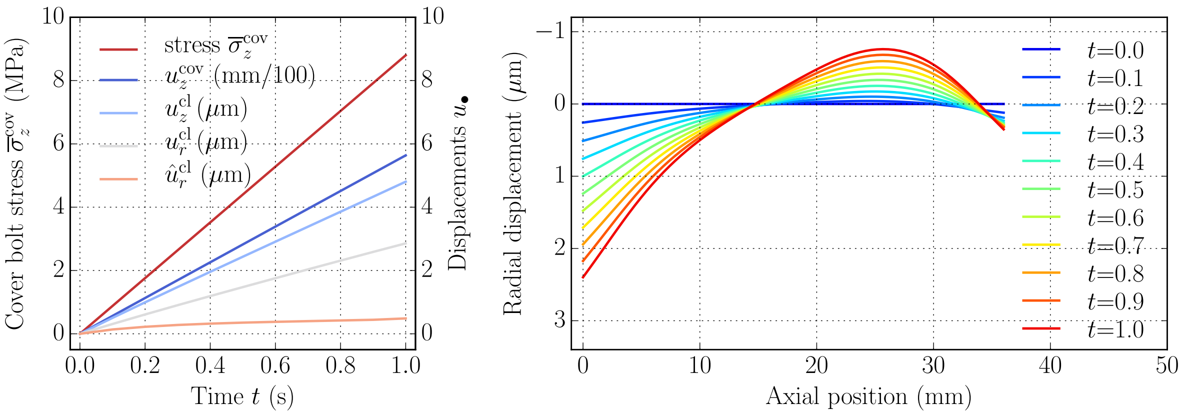

Figure 6.22: Results of the clamping stress test including the cover and contact at both workpiece clamping faces while applying Dirichlet boundary conditions only on the inner radial surface of the clamping cover. The radial displacement of the workpiece clamping nodes is free and only restricted by a **penalty** tangential contact constraint enforcement, implementing a friction coefficient of $\mu_{\text{con}} = 0.1$. The radial displacement of the workpiece clamping region at the exit face $\partial\mathcal{B}_{\text{ex}}^{\boldsymbol{u}}$ is denoted by $\hat{u}_r^{\text{cl}}$.

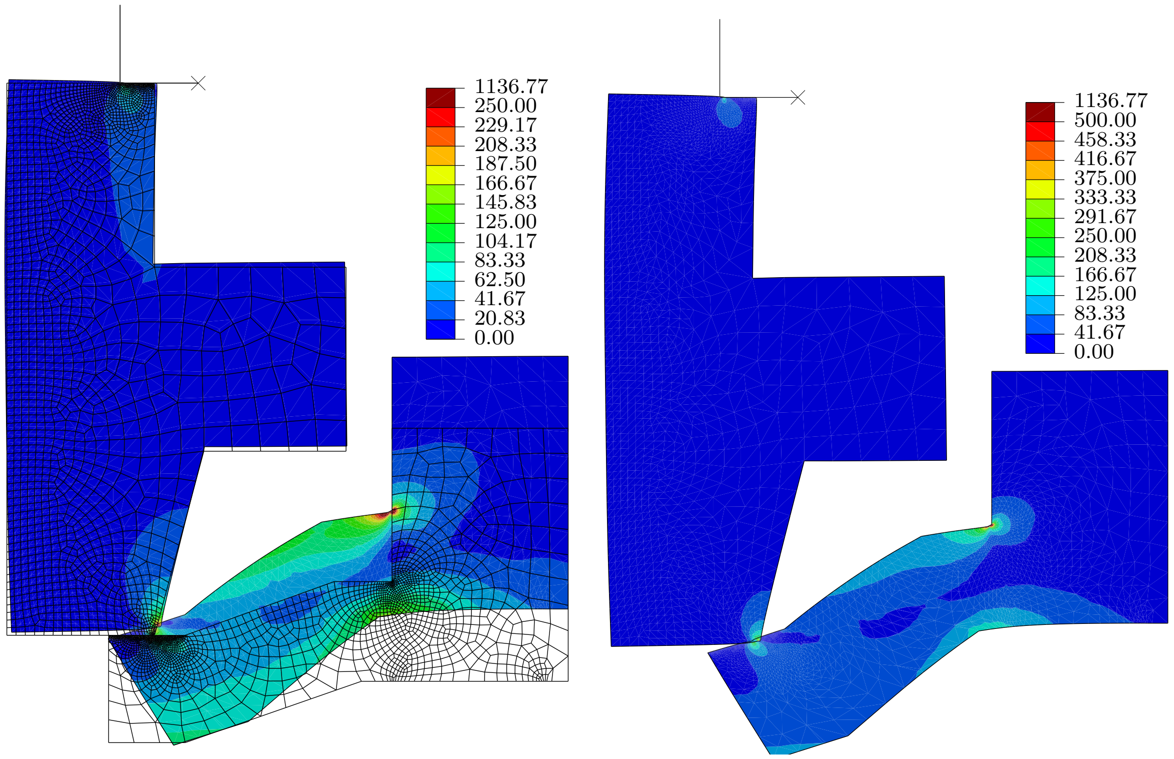

Figure 6.23: Workpiece model results including the clamping cover and contact formulation for both clamping faces. In addition, the outer radial clamping cover face is applied a Dirichlet boundary condition enforcing zero radial displacement. The contour plot shows the von Mises equivalent stress [MPa] in two different scales after applying the clamping stress with a displacement scaling factor of 100 in axial and 200 in radial direction. The mesh represents the reference configuration, whereas the contour plot shows the spatial configuration of the model.

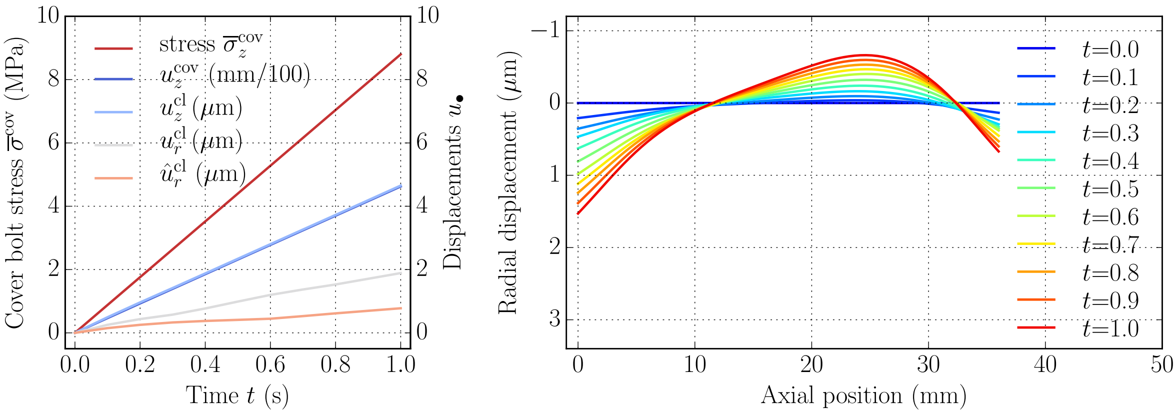

Figure 6.24: Results of the clamping stress test including the cover and contact at both workpiece clamping faces when enforcing zero displacement Dirichlet boundary conditions on both inner and outer radial clamping cover surfaces. The radial displacement of the workpiece clamping nodes is free and only restricted by a **penalty** tangential contact constraint enforcement, implementing a friction coefficient of $\mu_{\text{con}} = 0.1$. The radial displacement of the workpiece clamping region at the exit face $\partial\mathcal{B}^{\boldsymbol{u}}_{\text{ex}}$ is denoted by $\hat{u}^{\text{cl}}_r$.

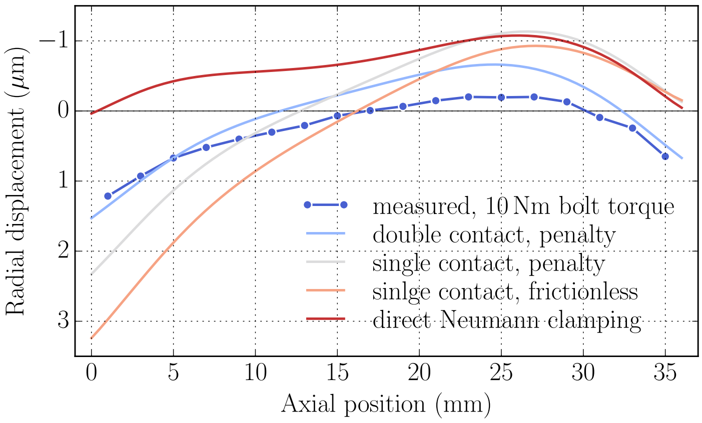

Figure 6.25: Comparison of the different clamping approaches implemented.

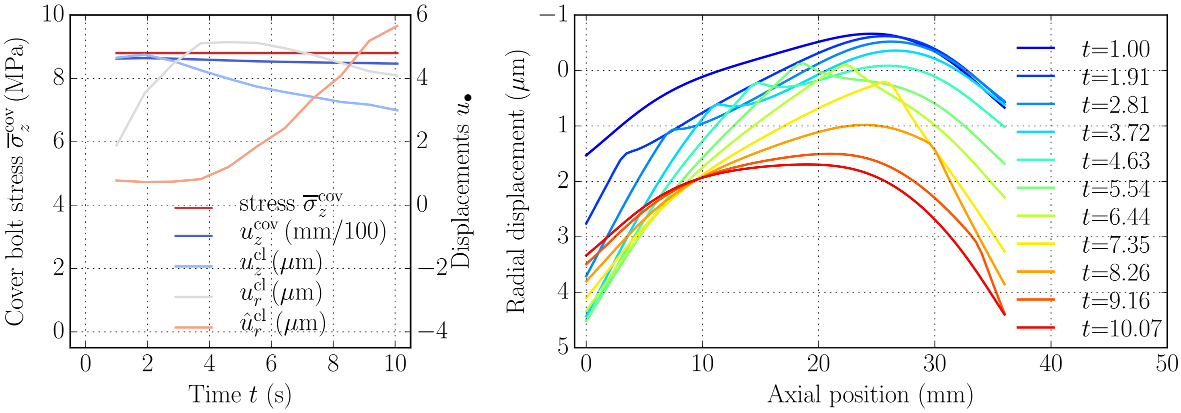

Figure 6.26: Workpiece inner surface and clamping face displacements during the thermal loading phase. This displays the follow-up simulation step referring to Fig. 6.24. The radial displacement of the workpiece clamping nodes is free and only restricted by a **penalty** tangential contact constraint enforcement, implementing a friction coefficient of $\mu_{\mathrm{con}} = 0.1$.

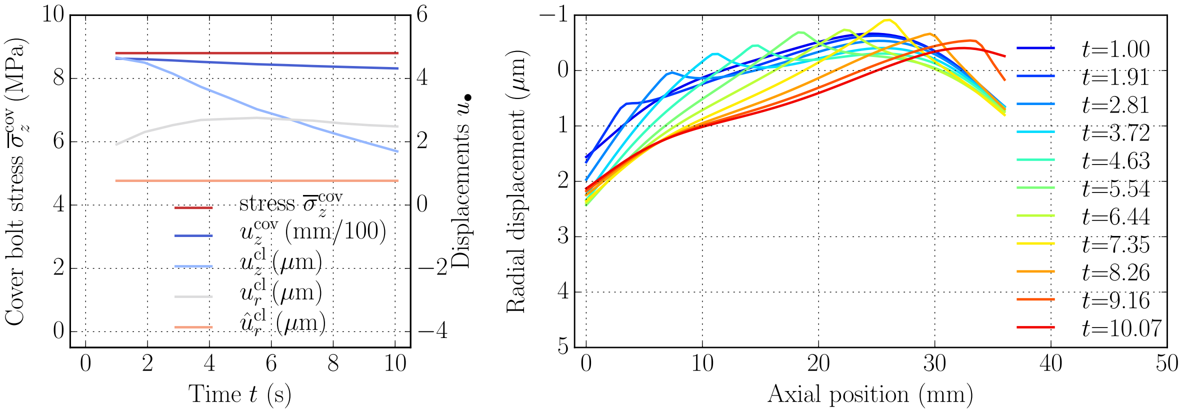

Figure 6.27: Results of the two-step clamping and loading simulation with **rough** contact conditions during the loading phase. The averaged axial displacement of the workpiece clamping nodes on the entry face decrease from 4.656 µm to 1.696 µm, whereas the radial displacement of this region evolves from 1.915 µm to 2.483 µm. As expected, the contact nodes at the workpiece exit face remain constant at 0.767 µm.

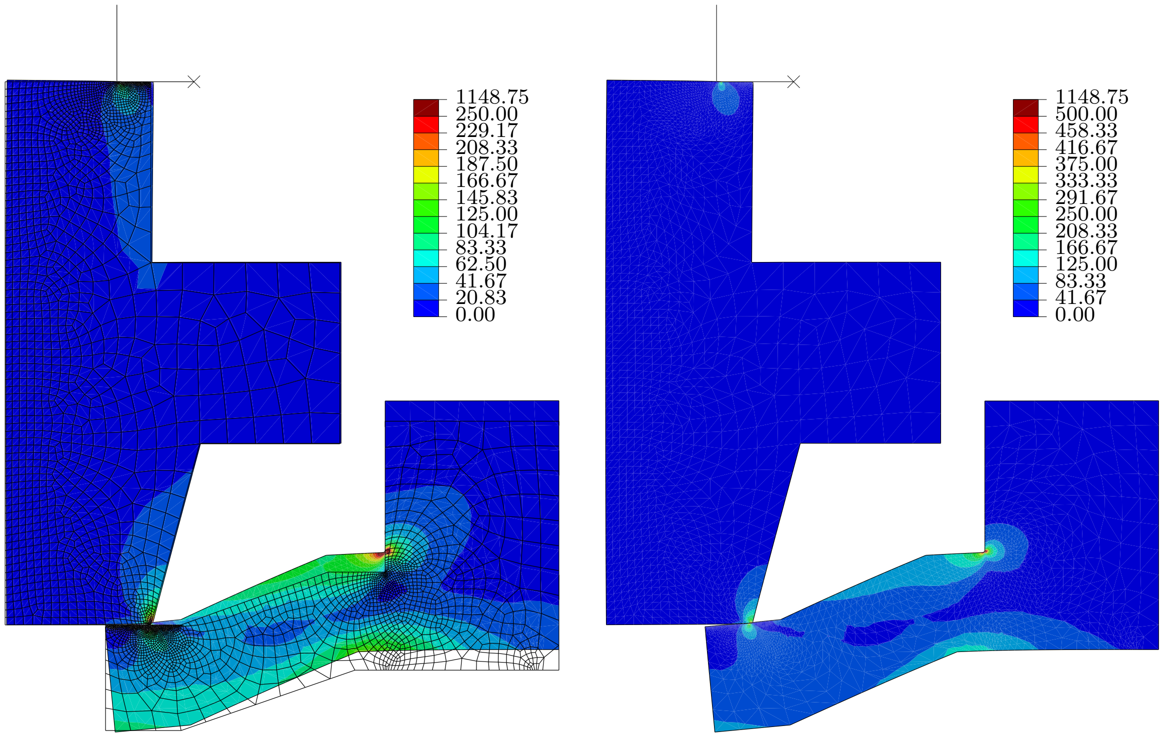

Figure 6.28: Workpiece model including the clamping cover and contact formulation for both clamping faces. In addition, the outer radial clamping cover face is applied a Dirichlet boundary condition enforcing zero radial displacement. The contour plot shows the von Mises equivalent stress [MPa] at $t = t_{\max}^{\mathrm{grd}}$ after the tool has passed entirely with an isotropic displacement scaling factor of 30.

6.3 Modelling of material removal

After creating a fundamental model that realistically captures the thermo-mechanical response during loading, the extension to a material removal approach is the next step towards a process model. As mentioned in the introduction, it is desirable to draw on the capabilities that Abaqus/Standard has already built in—at the current stage corresponding to version 6.14-2. The present section illustrates the different approaches under investigation.

6.3.1 Element deletion

In order to model the necessary material removal during the machining process, element deletion or deactivation, respectively, can be taken into account as a promising approach for this task. Abaqus fundamentally offers different approaches to deactivate elements. First, one has to distinguish between the possibilities that are offered by Abaqus/Standard and Abaqus/Explicit. Due to the explicit time integration scheme used in Abaqus/Explicit that does not rely on the computation of a tangent stiffness matrix, element deletion from a finite element mesh in its literal meaning is generally possible. This method can be triggered in different ways: One can either define a softening behaviour of the material, e.g. by the use of the input file keywords `*damage initiation` and `*damage evolution`, or define an internal variable that flags element deletion of an integration point. in Turn, this internal variable can be controlled by the use of a user subroutine such as VUMAT. An element is deleted as soon as all of its integration points are marked as deleted, cf. [93], Sec. *24.2.3 Damage evolution and element removal for ductile metals*. In addition, the `*section controls, element deletion=yes` keyword has to be set to enable the element removal for a certain section of the body under consideration. Abaqus/Standard on the other hand, is capable—since version 6.14-2, cf. [93], Sec. *Release Notes, 6.7 Element deletion controlled by state variables*—of handling element deactivation triggered by internal variables. The latter, in turn, can once again be controlled by user subroutines such as UMAT. However, deactivated elements are not truly detached from the mesh, but only are assigned a stiffness and heat conduction value numerically close to zero so as not to cause singularities in the system stiffness matrix.

However, there are two major drawbacks when targeting the concept of element-deletion-based material removal using Abaqus. First, the recognition of newly generated surfaces by exposing inner element faces or edges, respectively, after neighbouring elements have been deleted proves to be very cumbersome and partly even impossible with the built-in functions provided by Abaqus. This has also been confirmed by members of the 3DS company. The only method that rudimentary provides the above-mentioned demanded functionality, consists of a combination of element deletion that is triggered by a user defined internal variable controlled by a VUMAT in conjunction with the VUINTERACTION user subroutine when using Abaqus/Explicit only as a solver. The obligatory usage of the "general contact algorithm" which, in turn, is only available for three-dimensional models, cf. [93], constitutes an additional, and very extensive restriction to this method. Hence, this approach is cumbersome, since the invocation of VUINTERACTION requires the entire constitutive relations that represent the contact between two bodies to be implemented in a user subroutine. In addition, this approach is very susceptible to mesh-dependent results, and thus will not be developed any further. Secondly, as shown in Fig. 6.6, the maximum radial displacement magnitude caused by thermal expansion of the workpiece is approximately

$$u_r^{\max} \approx 1.4\,\mu\mathrm{m}. \tag{6.22}$$

This, in turn, requires the radial element edge length of the elements representing the workpiece contact zone to not exceed 1 µm to obtain a sufficiently exact resolution of the geometrical error caused by thermal straining. This leads to a very high computational cost when solving the according boundary value problem. Hence, another modelling approach towards the simulation of material removal needs to be developed, which will be described in the following sections.

6.3.2 Modelling of material removal by solution mapping

To overcome the issue of mesh-dependent material removal at high computational cost, we model the material removal with a mesh-to-mesh solution mapping approach, similar to the technique presented in Chapter 4. To do so, we split the finite element model into two separate boundary value problems. First, the initial workpiece is simulated by an axisymmetric cross-section model $\mathcal{B}^{\text{init}}$ which is constrained by Dirichlet boundary conditions $\mathcal{D}^{\text{cl}} = \boldsymbol{u}(t)\,|\,\partial\mathcal{B}_{\bullet}^{\boldsymbol{u}}$ representing the clamping. This workpiece model is thermally loaded by a transient Neumann boundary condition $\mathcal{L}(t)$ referring to the moving heat source substituting the tool—just as presented in the earlier sections of the present chapter, cf. Fig. 6.4. Secondly, the abrasive material removal is subsequently approximated by a second workpiece model $\mathcal{B}^{\text{abr}}$ that reflects the uncompensated machined workpiece when assuming ideal material removal, cf. Fig. 6.29. Via a mesh-mapping operator M, the last converged thermo-mechanical solution $\{\boldsymbol{\sigma}_k,\, \theta_k,\, \boldsymbol{k}_k\}\,\forall\,\mathcal{E}_k \in {}^{\checkmark}\mathcal{B}_n^{\text{init}}$ of the boundary value problem on $\mathcal{B}^{\text{init}}$ at time t_n is transferred to the updated discretised workpiece body ${}^{0}\mathcal{B}_n^{\text{abr}}$. Here, the index ${}^{\checkmark}\bullet$ denotes a converged state of the finite element model, the stress tensor of an element $\mathcal{E}_k$ is represented by $\boldsymbol{\sigma}_k$, the temperature field θ_k and internal variables $\boldsymbol{k}_k$ are defined accordingly. Note, that the spatial configuration $\boldsymbol{x}_k \in {}^{\checkmark}\mathcal{B}_n^{\text{init}}$ is undergoing some geometrical alterations in terms of the material removal and is subsequently used as reference configuration for the updated model $\boldsymbol{X}_k \in {}^{0}\mathcal{B}_n^{\text{abr}}$ at time t_n. Excluding the material removal, this method is commonly known as *updated Lagrangian formulation*, cf. e.g. [12, 105]. However, since we apply model alterations in

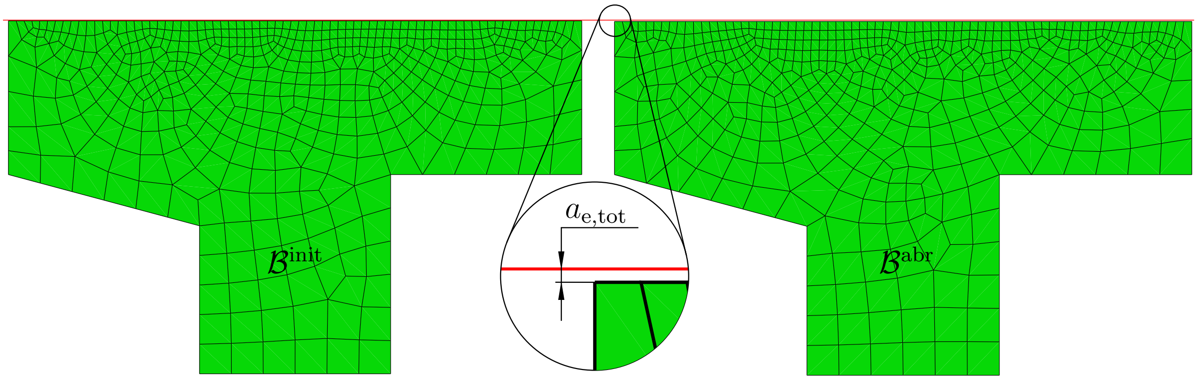

Figure 6.29: Modelling of material removal by mesh-to-mesh solution mapping. The model on the left hand side represents the loading phase of the unmachined workpiece with inner radius r_0^{i}, the part on the right hand side represents the machined workpiece geometry with inner radius $r_{\text{nom}}^{\text{i}} = r_0^{\text{i}} - a_{\text{e,tot}}$. Note the different meshes used in the models.

addition to the update of the reference configuration, we will refer to non-conservative updated Lagrangian formulation in the progress of this work.

After the solution mapping is complete, the second boundary value problem on $\mathcal{B}^{\text{abr}}$ with kept $\mathcal{D}^{\text{cl}}$ but altered Neumann load $\mathcal{L} = 0 \to \boldsymbol{q}^{\text{conv}}(t)\,|\,\partial\mathcal{B}^{\text{abr}}$ to be subsequently cooled to ambient temperature θ_0, will be solved. The result is the final workpiece configuration $\mathcal{B}^{\text{fin}}$ at ambient temperature reflecting the geometrical error caused by the ITG process. By using this approach, two advantages that can be benefited from. First, the material removal can now be modelled independently from the mesh, resulting in a significantly less complex—and therefore, computationally less costly—model that can easily reflect any changes in the workpiece geometry. Secondly, the loading phase is now decoupled from the cooling phase, enabling a more efficient application of an optimisation scheme which represents a powerful method to develop the compensation strategies targeted. At this stage, we could think of an optimisation loop that includes only the computationally cheaper abrasive/cooling model $\mathcal{B}^{\text{abr}}$ while the results of a more precise loading simulation reflecting $\mathcal{B}^{\text{init}}$ are already present and just need to be used as input parameter for the solution mapping M. This non-conservative updated Lagrangian approach is based on the following assumptions that need approval: At first, the inherent interpolation error by the mapping operator M that is—in the present case—provided by Abaqus, is sufficiently small to not induce errors in the stress or temperature field, which in turn would imply erroneous final geometries of the workpiece. Secondly, the material removal can be approximated as a one-step-procedure. Referring to Fig. 6.27 however, it can be observed that the transient displacement response of the inner workpiece surface $\boldsymbol{x}(t) \cdot \boldsymbol{e}_r \in \partial\mathcal{B}^{\mathcal{L}}$ opposes the latter assumption when using only the displacement information of the last converged loading simulation step ${}^{\surd}\mathcal{B}_n^{\text{init}}$. As one possible solution approach, the use of an envelope function $\mathcal{F}_{\text{env}}(\boldsymbol{x}, t)$ representing the union of tangential bounds in proximity of the local extremum of the inner workpiece surface can be proposed to approximate the excess of material removed due to thermal straining. To be precise,

$$\mathcal{F}_{\text{env}}(\boldsymbol{x}, t) = \bigcup_{t=0}^{t_{\max}^{\text{grd}}} r(\check{z}, t) \quad \forall\, \boldsymbol{x}(t) \cdot \boldsymbol{e}_r \in \partial\mathcal{B}^{\mathcal{L}} \quad \text{with} \tag{6.23}$$

$$\boldsymbol{x}(t) = r(t)\, \boldsymbol{e}_r + z(t)\, \boldsymbol{e}_z \tag{6.24}$$

denotes the union of local minima $\min(r(z,t)) = r(\check{z}, t)$ with respect to the given cylinder coordinate system over the time span $[0, t_{\max}^{\text{grd}}]$. The inner surface of the workpiece $\partial\mathcal{B}^{\mathcal{L}}$ at time t in this context is parametrised as a family of curves $r(z,t)$ for different times t. However, this envelope only represents a reasonable *geometrical* substitute, but an appropriate averaging scheme to define a physically correctly motivated union operator to induce thermal stresses over the abrasive time span appears very difficult to motivate. Due to this circumstance, we will use this approach to the modelling of material removal only to prove the first above-mentioned hypothesis related to a small interpolation error resulting from the mapping operation. For the transient material removal, a more sophisticated method will be developed in the progress of this thesis.

To test the behaviour of the mapping operator M offered by Abaqus, a simple numerical study is carried out: The workpiece is thermally loaded and then cooled to ambient temperature again, once with the mapping operator used, but $a_{\text{e,tot}} = 0$ applied, and once without any mapping scheme invoked. The results of these fundamental tests in terms of the remaining displacement fields are depicted in Figs. 6.30 and 6.31, respectively. As expected, the residual displacement fields differ, though, but all of them display a geometrical error that is significantly lower than the 1 µm magnitude of the smallest displacement detectable in the experiments. Referring to the applied mapping, it can be observed that the highest magnitudes of the remaining displacements are concentrated in the proximity of the clamping areas, which can be explained with the high gradients in the resulting stress field in these areas, cf. Fig. 6.23. Since the element edge length in this test is 0.5 mm only on the boundaries $\partial\mathcal{B}^{\mathcal{L}}$ and $\partial\mathcal{B}_{\bullet}^{\boldsymbol{u}}$ of the workpiece and the element size increases towards the core of the workpiece, the interpolation error caused by the mapping increases consequently. Considering the simulation without the mapping applied, the displacement error is at least one magnitude smaller than in the mapped solution, but exhibits a completely different spatial configuration. Referring to Fig. 6.31, all configurations as well as the respective displacements of the inner workpiece surface nodes are depicted for the simulation invoking the mapping operation. Interestingly, the sum of both displacement fields after loading and cooling equals exactly the difference between the remaining deformation of the load surface and the desired geometry, compare bottom right subfigure. We can therefore conclude that even with the temperature-dependent material parameters, the behaviour of the present system can be assumed to behave linearly elastic. As a conclusion, it can be stated that the interpolation error of the mesh-to-mesh solution mapping is negligible and can therefore be used for further development.

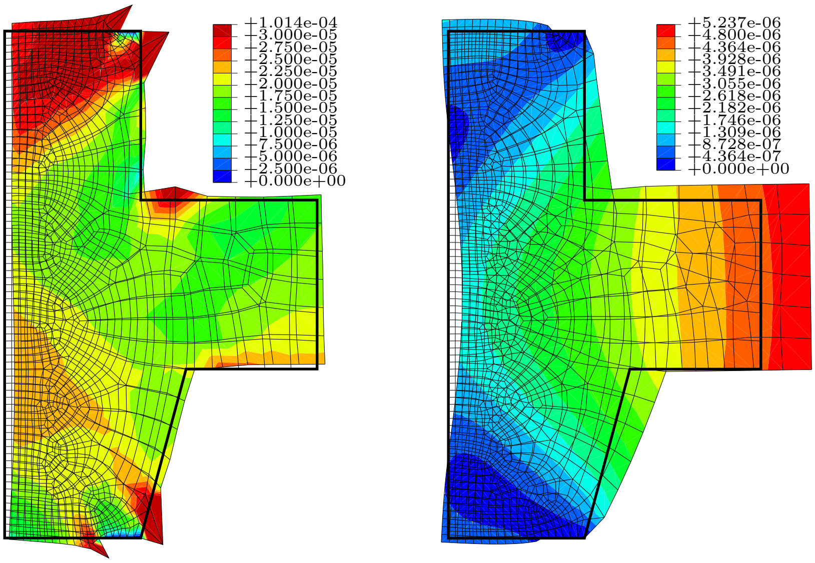

Figure 6.30: Comparison of the remaining displacement magnitude in mm when applying a thermal load $\mathcal{L}$ and cooling to reference temperature θ_0 without applying any clamping-induced deformation. Left: Mesh-to-mesh solution mapping M applied, right: Direct cooling. The bold black stroke represents the initial workpiece boundary.

6.3.3 Material removal by continuous solution mapping

To capture the transient geometrical error that occurs during the material removal of the abrasive process, it is necessary to refine the time discretisation concerning the time points in which material is actually removed. Referring to the approach presented in the previous section, the entire material removal was performed in one step, equalling a very coarse time discretisation. To overcome this issue, a time discretisation of the process towards a continuous remeshing is applied. We chose not to call it adaptive mapping, since the time points at which the interpolation takes place are prescribed by a certain function, namely are derived from the process kinematics. To be precise, material removal by remeshing takes place after one revolution of the workpiece or after an axial protrusion of a_f by the tool, respectively. However, as an optional sub-processing, mesh refinement based on discretisation error indicators such as the a posteriori Z^2 error estimate or physically motivated indicators—as used in the meso-scale model presented in Chapter 4—can easily be applied in the framework. For this reason, and to present a most general simulation outline, the adaptive mesh refinement will also be included as a feature in the presented framework. Moreover, the modelling framework presented

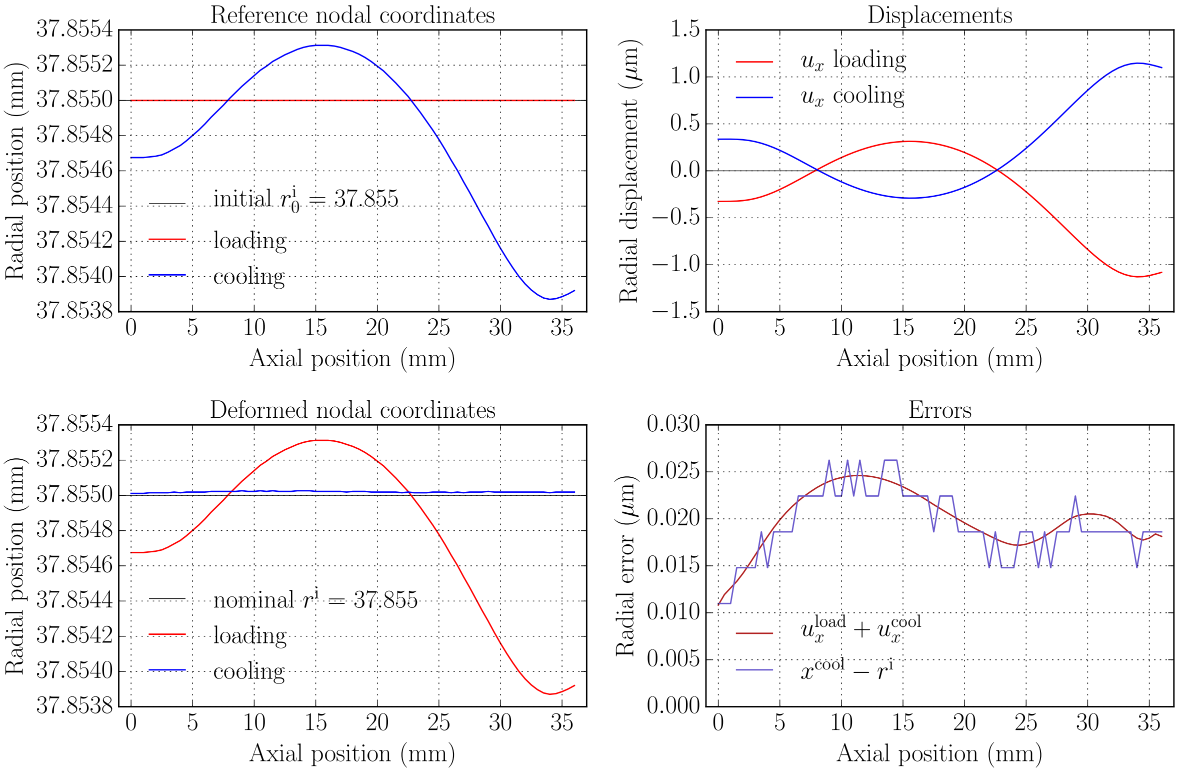

Figure 6.31: Results of the mapping algorithm test. Interestingly, the sum of both displacement fields after loading and cooling yields exactly the difference between the remaining deformation of the load surface and the desired geometry, compare bottom right subfigure. we can therefore conclude that even with the temperature-dependent material parameters, the behaviour of the present system can be assumed to behave linearly elastic. Furthermore, or most importantly, the interpolation error of the mesh-to-mesh solution mapping is negligible.

is applicable to two-dimensional, as well as three-dimensional problems without any restrictions.

The general simulation procedure is based on the one presented in the previous section, including some major improvements. Conceptually speaking, the above-mentioned load model $\mathcal{B}_0^{\mathrm{init}}$ is now split into a dedicated clamping phase and a subsequent abrasive phase where the solution mapping operation is now repeatedly executed. In this context, the tool is now included as analytical rigid part $\mathcal{G}$ in the model assembly. Since the abrasive procedure has been removed from the earlier $\mathcal{B}^{\mathrm{abr}}$, the final phase now exclusively represents a cooling procedure of the workpiece model. So, the process simulation is therefore subdivided into the following steps, which are represented by the models $\mathcal{B}^{\mathrm{init}}$, $\mathcal{B}^{\mathrm{abr}}$ and $\mathcal{B}^{\mathrm{cool}}$, respectively. The following description along with Fig. 6.32 defines the entire process model simulation outline.

Initial model $\mathcal{B}^{\mathrm{init}}$ Here, the initial workpiece geometry $\mathcal{B}^{\mathrm{init}}$ is defined, the initial clamping boundary conditions $\mathcal{D}_0^{\mathrm{cl}}$ are applied onto $\partial\mathcal{B}_{\bullet}^{\boldsymbol{u}}$ according to the findings

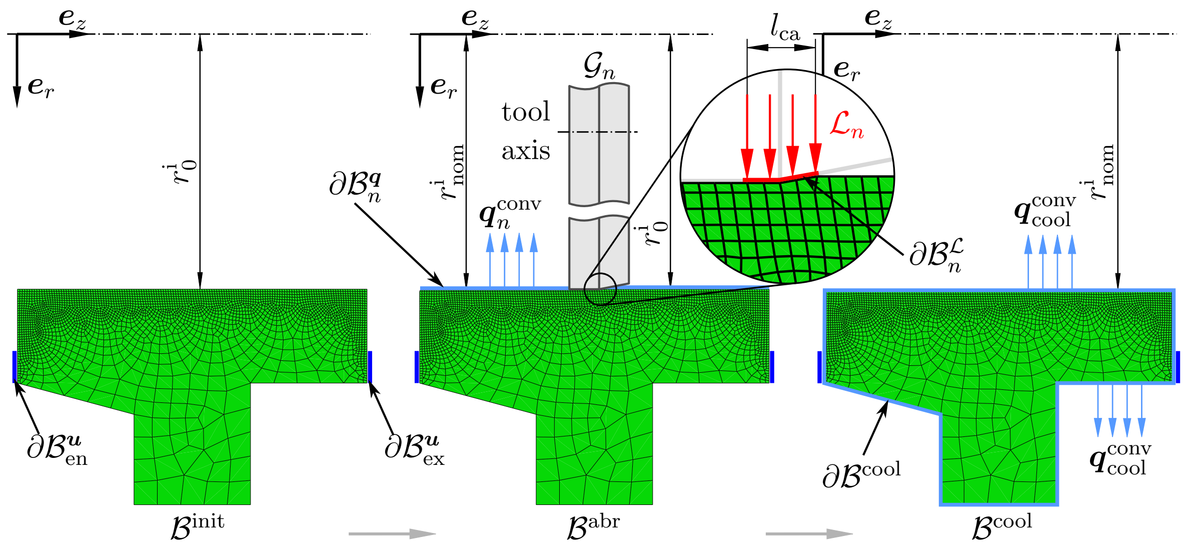
e_z
e_r
r_0^{i}
$\partial\mathcal{B}_{\mathrm{en}}^{\boldsymbol{u}}$
$\partial\mathcal{B}_{\mathrm{ex}}^{\boldsymbol{u}}$
$\mathcal{B}^{\mathrm{init}}$
e_z
e_r
$r_{\mathrm{nom}}^{\mathrm{i}}$
$\partial\mathcal{B}_n^{\boldsymbol{q}}$
$\boldsymbol{q}_n^{\mathrm{conv}}$
tool
axis
$\mathcal{G}_n$
r_0^{i}
l_{ca}
$\mathcal{L}_n$
$\partial\mathcal{B}_n^{\mathcal{L}}$
$\mathcal{B}^{\mathrm{abr}}$
e_z
e_r
$r_{\mathrm{nom}}^{\mathrm{i}}$
$\boldsymbol{q}_{\mathrm{cool}}^{\mathrm{conv}}$
$\partial\mathcal{B}^{\mathrm{cool}}$
$\boldsymbol{q}_{\mathrm{cool}}^{\mathrm{conv}}$
$\mathcal{B}^{\mathrm{cool}}$

initialisation and application of clamping

material removal and thermo-mechanical loading

cooling to reference temperature

Figure 6.32: Process model outline incorporating continuous mesh-to-mesh solution mapping and magnified process zone. The three models depicted will be invoked from left to right. The dark blue surfaces denote the clamping areas $\partial\mathcal{B}_{\bullet}^{\boldsymbol{u}}$ at which mechanical Dirichlet boundary conditions are applied, the light blue surfaces represent model boundaries at which convectional cooling takes place. The tool at time t_n is denoted by $\mathcal{G}_n$, the mesh density reflects the one used throughout the present section.

presented in Section 6.2.2, and the resulting boundary value problem is solved. This model therefore reflects the load model $\mathcal{B}_0^{\mathrm{init}}$ from the previous section, but excludes the thermal loading.

Abrasive model $\mathcal{B}^{\mathrm{abr}}$ This model reflects the stepwise looped material removal by intersecting the current configuration of the tool region $\mathcal{G}_n$ with the spatial configuration of the workpiece region $\mathcal{B}_{n-1}^{\mathrm{abr}}$ at given time points $t_n \in [t_1, t_{\mathrm{max}}^{\mathrm{load}}]$. The time incrementation is adjusted so that the axial tool protrusion per time step $\Delta t = t_n - t_{n-1} = 1/n_{\mathrm{w}}$ equals the axial feed a_{f}. Following the modelling assumptions in Sec. 6.3.3, the thermal load compound $\mathcal{L}_n$ is reduced to a transient heat flux $\boldsymbol{q}(t_n, \Delta\mathcal{B}_n)$ depending on the amount of material removed $\Delta\mathcal{B}_n$ at time t_n. The heat flux is assumed to be uniformly distributed along the effective axial engagement width of the grinding wheel l_{ca}, cf. Eq. (6.1) and Fig. 6.32. Simultaneously, the grinding coolant is modelled as a second convective Neumann load $\boldsymbol{q}^{\mathrm{conv}}$ acting on the entire inner workpiece surface $\partial\mathcal{B}_n^{\boldsymbol{q}}$ as described in Section 6.2. After the material removal, all variables from the last load step at t_{n-1} are interpolated to the new mesh, now acting as reference configuration with initial conditions of the current step t_n. So the above-mentioned non-conservative updated Langrangian formulation is kept. The material removal concept is described in more detail below.

Cooling model $\mathcal{B}^{\mathrm{cool}}$ After an entire pass of the tool through the workpiece, the clamping boundary conditions are set to the initial state $\mathcal{D}_0^{\mathrm{cl}}$ and a Neumann load in terms of a film cooling $\boldsymbol{q}_{\mathrm{cool}}^{\mathrm{conv}}$ acting on all exterior surfaces $\partial\mathcal{B}^{\mathrm{cool}}$ of the workpiece is applied to cool it to its initial temperature θ_0 to retrieve the final workpiece geometry that reflects the geometrical error resulting from the abrasive process.

The detailed outline of the program is defined in Algorithm 6.2. In this context, we will denote any reference configuration with ${}^{0}\bullet$ and every spatial configuration in terms of a converged solution of a boundary value problem with ${}^{\checkmark}\bullet$. Moreover, any set of Dirichlet boundary conditions will be denoted by $\mathcal{D}$, whereas Neumann loads will be represented by $\mathcal{N}$. Lower-right indices indicate countable measures or states, upper-right indices denote parts of an assembly to which the variable is assigned to and upper-left indices represent iterations of lower level, such as equilibrium iterations of a finite element analysis. Indices $\bullet_n$ denote time increments, whereas indices $\bullet_k$ refer to spatial discretisations. Therefore, all increments of time-discretised functions $\bullet(t_n)$ are denoted as $\bullet_n$.

Since the initial model $\mathcal{B}^{\mathrm{init}}$ reflects the model development described in Section 6.2.2, the abrasive model $\mathcal{B}^{\mathrm{abr}}$ will be focused on in the following.

As the core capabilities of the abrasive model are constituted by the material removal and the thermal loading resulting therefrom, we will focus on these two aspects. As described earlier, the tool $\mathcal{G}$ moves linearly in positive $\boldsymbol{e}_z$ direction along its axis as depicted in Fig. 6.32. To be precise, the tool $\mathcal{G}$ only undergoes a rigid body motion that is defined by a trajectory $\mathcal{T}(t)$, which in turn prescribes the tool axis position as a function of time. At this stage, let

$$\mathcal{T}(t) = \left[r_{\mathrm{nom}}^{\mathrm{i}} - r_{\mathrm{eff}}^{\mathcal{G}}\right] \boldsymbol{e}_r + v_{\mathrm{fa}}\, t\, \boldsymbol{e}_z \tag{6.25}$$

simply describe a parallel to the workpiece axis $\boldsymbol{e}_z$ which will be used to control the tool position. A more detailed discussion on the tool trajectory will be presented in the scope of compensation strategies, see Sec. 6.4.1. In Eq. (6.25), $r_{\mathrm{eff}}^{\mathcal{G}}$ denotes the effective tool radius which includes the abrasive layer of the tool and which is therefore defined by the most protruding grain situated on the tool body. Following the time incrementation defined in the above description, at t_n, the current tool position is denoted by $\mathcal{G}_n$.

At any time t_n, the material removal can be carried out by invoking the non-conservative updated Lagrangian formulation. So, to calculate the updated reference configuration $\boldsymbol{X}_k(t_n)$ for each workpiece node k, the spatial nodes $\boldsymbol{x}_k$ from the previous time step t_{n-1} that intersect with the tool region $\mathcal{G}_n$ are projected onto the tool boundary $\partial\mathcal{G}_n$, i.e.

$$\boldsymbol{X}_k(t_n) = \begin{cases} \boldsymbol{x}_k \overset{\boxplus}{\multimap} \partial\mathcal{G}_n & \text{if} \quad \boldsymbol{x}_k \in {}^{\checkmark}\mathcal{B}_{n-1} \cap \mathcal{G}_n \\ \boldsymbol{x}_k & \text{if} \quad \boldsymbol{x}_k \in {}^{\checkmark}\mathcal{B}_{n-1} \setminus \mathcal{G}_n \end{cases} \quad \forall\, t_n \in \left[t_1,\, t_{\max}^{\mathrm{grd}}\right]. \tag{6.26}$$

In this manner, the spatial configuration $\boldsymbol{x}_{n-1}$ resulting from the last converged equilibrium iteration of the previous load simulation is subsequently used as reference configuration $\boldsymbol{X}_n$ for the next load simulation. Here, the operator $\overset{\boxplus}{\multimap}$ shall denote a projection that is not strictly parallel to the surface normal of $\partial\mathcal{G}$, but additionally minimises the distance to any vertex of the tool surface or any intersection of both region boundaries $\partial\mathcal{G} \cap \partial\mathcal{B}$. This projection property assures a minimisation of the discretisation error when intersecting a discretised body $\mathcal{B}^{\boxplus}$ in terms of finite elements $\mathcal{E}_k$ with an analytical rigid body that contains singularities. Since the tool surface in the present case has been reduced to a cross-section that basically just consists of two straight lines, see Fig. 6.32, the vertex $\boldsymbol{x}_{\mathrm{vr}}^{\mathcal{G}}$ resulting from the intersection of these two lines represents a geometrical singularity. Thus, the projection $\overset{\boxplus}{\multimap}$ enforces a projected workpiece node $\boldsymbol{X}$ to exactly coincide with $\boldsymbol{x}_{\mathrm{vr}}^{\mathcal{G}}$. En plus, this enables the choice of arbitrary element sizes while ensuring an exact material removal and therefore improves the efficiency of the simulation. Though this method might appear trivial, it especially makes sense when extending the present framework to three-dimensional model definitions and when using C^0 smooth discretised tool geometries.

Although the nominal radial stock removal $a_{\mathrm{e,tot}}$ in the present implementation is small in comparison to the element edge length $l_{\mathcal{E}}$—currently, $l_{\mathcal{E}} = 0.25\,\mathrm{mm}\,\forall\,\mathcal{E}_k \in \partial\mathcal{B}^{\boldsymbol{q}}$ holds—it shall be noted here, that the projection operator presented above is applicable to arbitrary ratios p between stock removal and element edge lengths

$$p = \frac{a_{\mathrm{e,tot}}}{l_{\mathcal{E}}}. \tag{6.27}$$

In the case of $p \geq 1$, all elements that entirely lie within the intersection of tool and workpiece, namely

$$\mathcal{E}_k \subseteq [\mathcal{B} \cap \mathcal{G}] \tag{6.28}$$

have to be deleted from the current mesh, and the node adjustment procedure (6.26) will be subsequently applied to the neighbouring set of elements. Since the results from the previous finite element analysis will be interpolated to the new mesh any way, technically any mesh modification can be applied in-between two time steps. Regarding the interpolation error of course, new constraints to the mesh modification arise which have to be taken into account to prevent a cumulation of mapping errors.

Considering the thermal load that substitutes the engaging tool, a transient function $\boldsymbol{q}(t,\, \Delta\mathcal{B})$ has to be defined. However, the physical motivation of the heat flux magnitude is based on a dependency on the volume $\Delta\mathcal{B}$ of removed material—just as presented in terms of the heat source term r in Chapters 4 and 5 of the present work. Since $\Delta\mathcal{B}(t)$ implicitly depends on time, we can therefore solely define a thermal load $\boldsymbol{q}(\Delta\mathcal{B})$ that needs to be prescribed in the very general case. Regarding Eq. (6.25), however, we can set

$$\|\boldsymbol{q}(\Delta\mathcal{B})\| = \bar{q}(t) \tag{6.29}$$

in good approximation, just as established in Section 6.2, Eq. (6.14). Since the radial inner workpiece surface $\partial\mathcal{B}^{\boldsymbol{q}}$ permanently undergoes changes due to the material removal applied, the surface $\partial\mathcal{B}^{\mathcal{L}}$ needs to be redefined constantly according to the process conditions $\mathcal{P}$. Here, a distinct difference between the prototype model developed in Sec. 6.2 and the current process model needs to be emphasised: While, in the prototype model, the thermal load surface $\partial\mathcal{B}^{\mathcal{L}}$ is constant over time and spans the entire radial inner workpiece surface, now $\partial\mathcal{B}^{\mathcal{L}}$ is defined to be only as wide as the axial contact length l_{ca} and moving in accordance with the tool position $\mathcal{T}(t)$ in the process model. The entire inner radial surface of the workpiece is defined by $\partial\mathcal{B}^{\boldsymbol{q}}$ in the current setup. This difference is, on the one hand, crucial for the comprehension of Algorithm 6.2 and will also be of particular importance in the scope of the implementation presented in the next section. The redefinition of $\partial\mathcal{B}^{\mathcal{L}}$ in the context of the abrasive phase of the process model $\mathcal{B}^{\mathrm{abr}}$ results from the intersection of the current tool and workpiece configuration as

$$\partial\mathcal{B}^{\mathcal{L}}_n = \partial[\mathcal{B}^{\mathrm{abr}}_n \cap \mathcal{G}_n] \cap \mathcal{B}^{\mathrm{abr}}_n \tag{6.30}$$

With respect to the final phase of the process model in terms of $\mathcal{B}^{\mathrm{cool}}$, Algorithm 6.2, the above component description and the development in Sec. 6.2 completely define this submodel. At this stage, the general process model definition is completed. The following section elucidates implementation details of the program outline presented, especially focusing on features in conjunction with Abaqus. This is done in order to separate the general procedure, which can at this point be implemented by using arbitrary simulation codes, from the special implementation applied in the present work.

6.3.4 Implementation details of the remeshing scheme

This section briefly outlines important details with respect to the implementation of the previously developed general process model. With regard to the notation, `typewriter` expressions shall represent programme, subroutine or module names of the programming languages invoked. Some basic Python modules and commands will be referred to without special reference—for further details on the latter, refer to [93], Langtangen [57] and the references therein.

The process model developed in the last sections is implemented in Abaqus/Standard, using an implicit time integration scheme to solve the non-linear coupled problem.

To model the material removal, Python scripting is used to implement the remeshing, according to Algorithm 6.2. To enable a wider range of debugging facilities and to be able to use any Python module available, the usage of the Abaqus Python interpreter is by design reduced to a minimum. The reason for this concept lies in the fact, that the Abaqus Python distribution is cumbersome to extend with Python modules that are not included in the Abaqus software package. Therefore, the main programme is written in native Python, using the system Python distribution instead of the one that is shipped with Abaqus. However, to set up models within the Abaqus preprocessor, the use of some Abaqus Python modules is inevitable. Hence, three Python modules that are only callable from the Abaqus Python interpreter have been developed to create the initial, abrasive and cooling models $\mathcal{B}^{\text{init}}$, $\mathcal{B}^{\text{abr}}$ and $\mathcal{B}^{\text{cool}}$, respectively. To enable this functionality in standard Python, a wrapper programme `runCAE()` which runs the Abaqus/CAE Python interpreter with an `os.spawnv()` command has been implemented.

The communication between the system and the Abaqus Python modules is implemented in terms of data serialisation with the Python Pickle module, which basically writes or reads any Python object to or from a binary file on a persistent storage, cf. [57]. To improve the robustness of the programme, the model data storage is facilitated by exclusively using Abaqus data containers, such as model database `*.cae` and output database `*.odb` files. This features the advantage that the entire model definition of every simulation step is archived in a `*.cae` file and can easily be debugged or even modified conveniently without any further import processing. Even more importantly, every node or element set or any other more distinct model feature that is defined in the initial model $\mathcal{B}^{\text{init}}$, is transferred automatically to each time-dependent model state $\mathcal{B}_n^{\text{abr}}$ which guarantees a maximum robustness of the simulation. The key feature to this is the usage of the Abaqus import methods `mdb.ModelFromOdb()` and `mdb.model.PartFromOdb()`, cf. [93].

A comprehensive outline of the resulting programme structure is depicted in Fig. 6.33, where the connection between the main programme components along with the respective data containers is illustrated. The programme chart is fundamentally divided into three columns: The main routine constitutes the left column, whereas the right column contains all first-order subroutines. The centre column—as a connector between the outer ones—shows the files which are used for data exchange between the main programme and the subroutines. Beyond this, the figure is self-explanatory and should be read linearly from top to bottom, following the command lines printed in the main routine, keeping the algorithmic box 6.2 in mind. As can be seen, at every time step t_n, there is a corresponding model database as well as an output database that store the entire model definition along with every respective result, which enables a comprehensive insight into the process characteristics and represents an valuable scientific simulation tool. Moreover, the modular structure of the programme empowers a straightforward extension of the framework, since only the according model creation routines have to be exchanged or extended, respectively, whereas the fundamental programme persists.

To implement the time dependence of the Dirichlet boundary conditions $\mathcal{D}$ applied on the abrasive model

$$[\mathcal{D}(t) = \{\boldsymbol{u}_r^{\mathrm{en}}(t), \boldsymbol{u}_z^{\mathrm{en}}(t), \boldsymbol{u}_r^{\mathrm{ex}}(t)\}]_{\partial\mathcal{B}^{\boldsymbol{u}}_{\bullet}}\,, \tag{6.31}$$

in the context of a remeshing scheme, the permanent change between reference and spatial configuration of the model $\mathcal{B}^{\mathrm{abr}}$ needs to be taken into account. Therefore, every updated reference configuration at the beginning of a macroscopic time increment Δt_n will be constrained with a corresponding displacement increment $\Delta\mathcal{D}(t_n) = \Delta\mathcal{D}_n$. The application of $\mathcal{D}(t)$ thus also needs to be discretised in time, i.e.

$$\mathcal{D}(t) \approx \bigcup_{n=1}^{n_{\Delta t}} \Delta\mathcal{D}(t_n) = \bigcup_{n=1}^{n_{\Delta t}} \Delta\mathcal{D}_n, \tag{6.32}$$

which is carried out as a piecewise linear approximation of the continuous function $\mathcal{D}(t)$. Hence, it will be implemented as a Dirichlet boundary condition that linearly increases from zero to $\Delta\mathcal{D}_n$ for every remeshing step t_n of the abrasive model $\mathcal{B}_n^{\mathrm{abr}}$.

Finally, to be able to capture the thermocouple temperatures during the permanent remeshing to ensure a workpiece temperature evolution according to the experimental results, the corresponding nodes need to be identified in every time step of the simulation. Therefore, the nodes $\check{\boldsymbol{X}}_k$ closest to the thermocouple positions $\boldsymbol{X}_{\mathrm{tc1}}$ to $\boldsymbol{X}_{\mathrm{tc3}}$, cf. Fig. 6.3, are identified after the mesh creation of the abrasive model $\mathcal{B}_n^{\mathrm{abr}}$ at time t_n via

$$\check{\boldsymbol{X}}_k = \operatorname{argmin}\left([\boldsymbol{X}_{\mathrm{tc1}} - \boldsymbol{X}_k] \cdot [\boldsymbol{X}_{\mathrm{tc1}} - \boldsymbol{X}_k]\right) \tag{6.33}$$

which is implemented using the Python NumPy module which provides convenient high-level commands for numerical computations, especially in terms of efficient multidimensional array operations.

With all the above model definitions as well as the implementation at hand, we are now able to conduct some numerical experiments and examine the response of the developed process simulation, which will be presented in the subsequent section.

```
Data: initial workpiece geometry $\mathcal{B}^{\text{init}}$; set of process parameters $\mathcal{P}$; tool
      geometry $\mathcal{G}$; tool trajectory $\mathcal{T}(t)$; pre-calculated transient clamping
      function $\mathcal{D}^{\text{cl}}(t)$
set time $t = 0$, initialise ${}^0\boldsymbol{\sigma}_k^{\text{wp}} = \mathbf{0}$ and ${}^0\theta_k^{\text{wp}} = \theta_0 \,\forall$ elements $\mathcal{E}_k \in \mathcal{B}^{\text{init}}$
apply clamping boundary conditions $\mathcal{D}^{\text{cl}}(t_0)$, solve the boundary value problem
on $\mathcal{B}^{\text{init}}$ to retrieve the clamped spatial configuration ${}^{\checkmark}\mathcal{B}_0$, i.e.
for $\forall\, \mathcal{E}_k \in \mathcal{B}_0^{\text{init}}$ do
    compute thermo-mechanical response $\boldsymbol{\sigma}_k$ and $\theta_k$
end
for every time step $t_n \in \left[t_1,\, t_{\max}^{\text{grd}}\right]$ in the load cycle do
    update the tool configuration $\mathcal{G}_n$ according to $\mathcal{T}_n$
    ${}^0\mathcal{B}_n^{\text{abr}} \leftarrow {}^{\checkmark}\mathcal{B}_{n-1}^{\bullet} \setminus \mathcal{G}_n$, so remove material from workpiece, cf. Eq. (6.26).
    if refinement indicator $\neq 0$ then
        modify mesh, i.e. apply mesh refinement or other discretisation
        modifications to retrieve $\boldsymbol{X}_k \in {}^0\mathcal{B}_n^{\text{abr}}$
    end
    else
        adjust nodes $\boldsymbol{x}_k \in {}^{\checkmark}\mathcal{B}_{n-1}^{\text{abr}}$ to represent $\boldsymbol{X}_k \in {}^0\mathcal{B}_n^{\text{abr}}$, cf. Eq. (6.26).
    end
    apply mapping operator $\mathsf{M}\left({}^0\mathcal{B}_n^{\text{abr}} \leftarrow {}^{\checkmark}\mathcal{B}_{n-1}^{\text{abr}}\right)$
    identify load surface $\partial\mathcal{B}_n^{\mathcal{L}} = \partial[\mathcal{B}_n^{\text{abr}} \cap \mathcal{G}] \cap \mathcal{B}_n^{\text{abr}}$
    update boundary conditions and thermo-mechanical load compound
    $\mathcal{L}_n \leftarrow \left[\boldsymbol{q}\left({}^{\checkmark}\mathcal{B}_{n-1} \cap \mathcal{G}_n\right)\right]_{\partial\mathcal{B}_n^{\mathcal{L}}};\quad \mathcal{D} \leftarrow \mathcal{D}^{\text{cl}}(t)$ and solve the new boundary value
    problem
    for $\forall\, \mathcal{E}_k \in \mathcal{B}_n^{\text{abr}}$ do
        compute thermo-mechanical response $\boldsymbol{\sigma}_k$ and $\theta_k$
    end
end
apply mapping operator $\mathsf{M}\left({}^0\mathcal{B}^{\text{cool}} \leftarrow {}^{\checkmark}\mathcal{B}^{\text{abr}}\,\Big|_{t=t_{\max}^{\text{grd}}}\right)$
$\left[\mathcal{L} \leftarrow \{0\};\quad \mathcal{D}^{\text{cl}} \leftarrow {}^0\mathcal{D}_0^{\text{cl}};\quad \mathcal{N} \leftarrow \{\boldsymbol{q}^{\text{conv}}|_{\partial\mathcal{B}^{\text{cool}}}\}\right]_{\mathcal{B}^{\text{cool}}}$
for $\forall\, \mathcal{E}_k \in \mathcal{B}^{\text{cool}}$ do
    compute thermo-mechanical response $\boldsymbol{\sigma}_k$ and $\theta_k$
end
return final workpiece geometry $\mathcal{B}^{\text{fin}}$, residual stresses $\boldsymbol{\sigma}_{\text{res}}$
```

Algorithm 6.2: Modelling of material removal by continuous mesh-to-mesh solution mapping. Indices $\bullet_n$ denote time increments, whereas indices $\bullet_k$ refer to spatial discretisations. Therefore, all increments of discretised functions $\bullet(t_n)$ are denoted as $\bullet_n$.

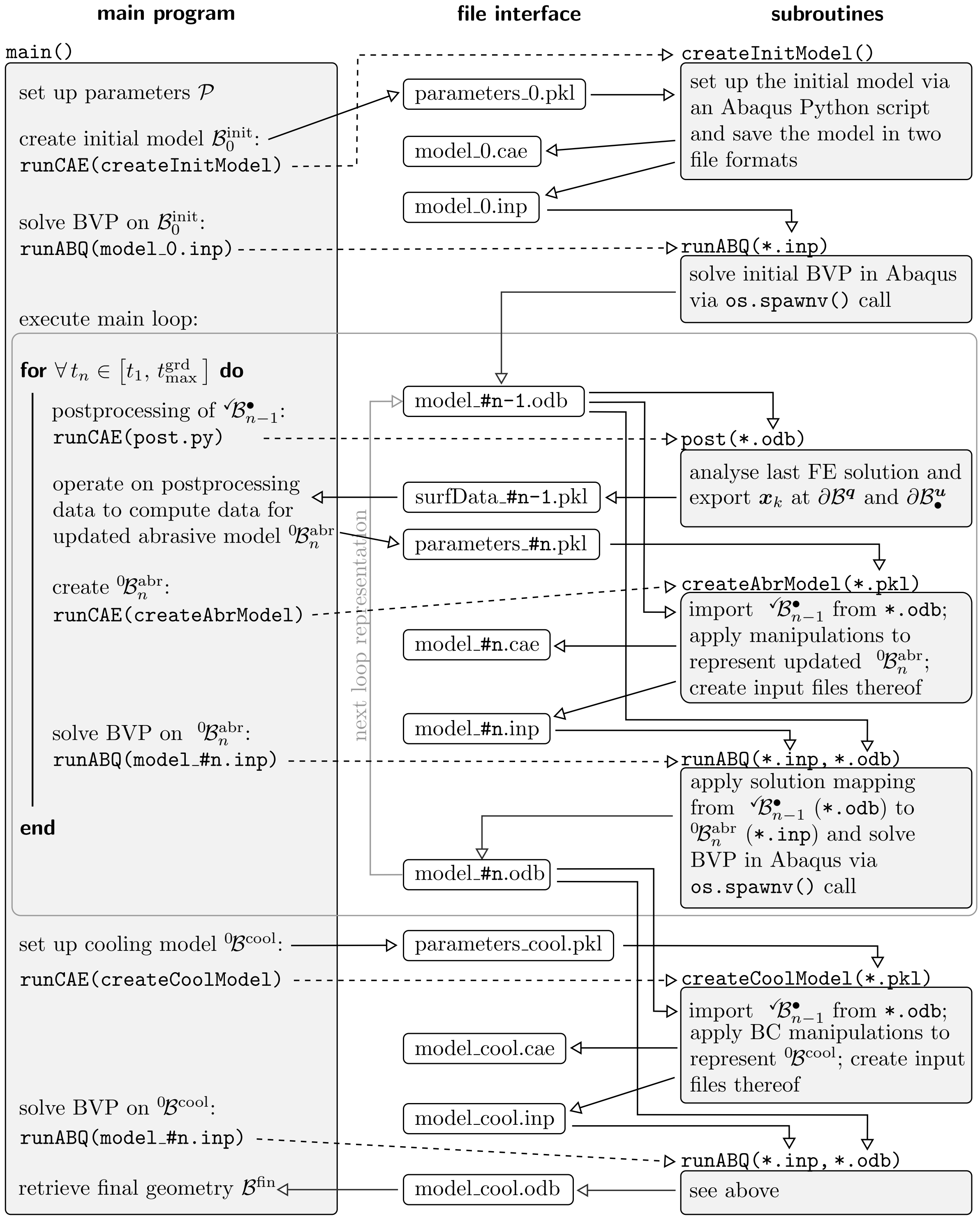
main program
file interface
subroutines
main()
set up parameters $\mathcal{P}$
create initial model $\mathcal{B}_0^{\text{init}}$:
runCAE(createInitModel)
solve BVP on $\mathcal{B}_0^{\text{init}}$:
runABQ(model_0.inp)
execute main loop:
for $\forall\, t_n \in [t_1,\, t_{\max}^{\text{grd}}]$ do
postprocessing of ${}^{\checkmark}\mathcal{B}^{\bullet}_{n-1}$:
runCAE(post.py)
operate on postprocessing data to compute data for updated abrasive model ${}^{0}\mathcal{B}_n^{\text{abr}}$
create ${}^{0}\mathcal{B}_n^{\text{abr}}$:
runCAE(createAbrModel)
solve BVP on ${}^{0}\mathcal{B}_n^{\text{abr}}$:
runABQ(model_#n.inp)
end
set up cooling model ${}^{0}\mathcal{B}^{\text{cool}}$:
runCAE(createCoolModel)
solve BVP on ${}^{0}\mathcal{B}^{\text{cool}}$:
runABQ(model_#n.inp)
retrieve final geometry $\mathcal{B}^{\text{fin}}$
parameters_0.pkl
model_0.cae
model_0.inp
model_#n-1.odb
surfData_#n-1.pkl
parameters_#n.pkl
model_#n.cae
model_#n.inp
model_#n.odb
next loop representation
parameters_cool.pkl
model_cool.cae
model_cool.inp
model_cool.odb
createInitModel()
set up the initial model via an Abaqus Python script and save the model in two file formats
runABQ(*.inp)
solve initial BVP in Abaqus via os.spawnv() call
post(*.odb)
analyse last FE solution and export $\boldsymbol{x}_k$ at $\partial\mathcal{B}^{\boldsymbol{q}}$ and $\partial\mathcal{B}^{\boldsymbol{u}}_{\bullet}$
createAbrModel(*.pkl)
import ${}^{\checkmark}\mathcal{B}^{\bullet}_{n-1}$ from *.odb; apply manipulations to represent updated ${}^{0}\mathcal{B}_n^{\text{abr}}$; create input files thereof
runABQ(*.inp, *.odb)
apply solution mapping from ${}^{\checkmark}\mathcal{B}^{\bullet}_{n-1}$ (*.odb) to ${}^{0}\mathcal{B}_n^{\text{abr}}$ (*.inp) and solve BVP in Abaqus via os.spawnv() call
createCoolModel(*.pkl)
import ${}^{\checkmark}\mathcal{B}^{\bullet}_{n-1}$ from *.odb; apply BC manipulations to represent ${}^{0}\mathcal{B}^{\text{cool}}$; create input files thereof
runABQ(*.inp, *.odb)
see above

Figure 6.33: Subroutine and data structure of the material removal simulation. Shaded boxes represent programmes and subroutines, unfilled boxes denote files. Dashed arrows depict subroutine calls, whereas solid arrows refer to reading or writing operations, respectively. `Typewriter expressions` represent function calls, subroutine or file names, whereas normal font denotes explanations. The thin grey frame represents the scope of the main abrasive loop.

6.3.5 Numerical examples and results

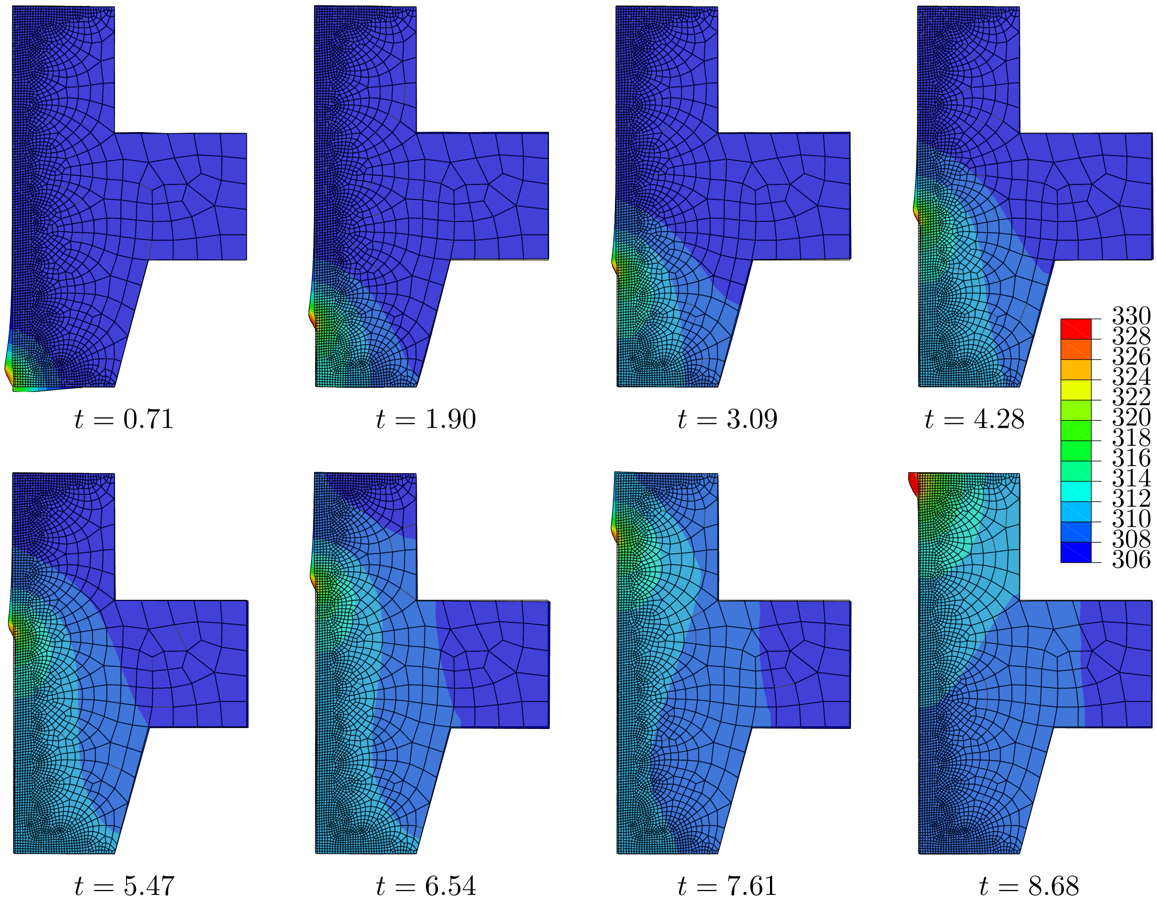

$t = 0.71$ $t = 1.90$ $t = 3.09$ $t = 4.28$

$t = 5.47$ $t = 6.54$ $t = 7.61$ $t = 8.68$

Figure 6.34: Results of the process simulation including material removal. The contour plot represents the temperature field θ_k (K) on the spatial configuration ${}^{\checkmark}\mathcal{B}_n^{\mathrm{abr}}$ at time t_n. The mesh represents the corresponding reference configuration ${}^{0}\mathcal{B}_n^{\mathrm{abr}}$, the times t are printed in seconds. An isotropic displacement scaling factor of 5000 is applied.

To prove the correctness of the process model developed, an entire process is simulated according to the process parameters $\mathcal{P}$ displayed in Tab. 6.1. The corresponding results are depicted in Figs. 6.34 and 6.35, respectively. The first shows the transient temperature and displacement response of the workpiece, whereas the latter figure shows a magnification of the process zone, which is not clearly observable in Fig. 6.34. The transient temperature evolution proves to be as expected and is comparable to the findings in Sec. 6.2 of the present chapter. Regarding the process zone magnification and the corresponding displacement field shown in Fig. 6.35, we can now gain insight on the cause for the geometrical error occurring in ITG. The tool boundary of the subsequent

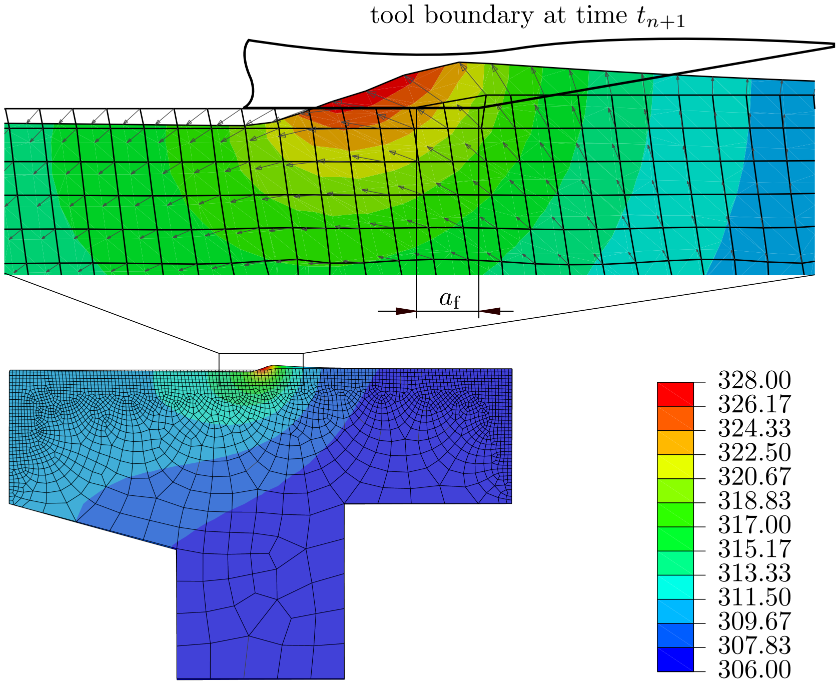

Figure 6.35: Temperature contour plot in Kelvin of one exemplary workpiece spatial configuration $\boldsymbol{x}_n$ at time t_n with magnified process zone. The displayed mesh represents the reference configuration $\boldsymbol{X}_n$, whereas the arrows represent the displacement vectors $\boldsymbol{u}_k$. An isotropic displacement scaling factor of 3000 is applied.

time step shown in the latter figure clearly intersects with more material than the nominal amount. So at this point, we can now proceed to some final model calibrations with respect to experimental findings.

Let us at first recall the experimental results to obtain an impression of the characteristic workpiece deformation pattern resulting from the abrasive process under investigation, cf. Fig. 6.3. To capture the behaviour shown therein, different numerical experiments are carried out with the following clamping approaches applied: First, a constant set of clamping boundary conditions $\overline{\mathcal{D}}$ used in an earlier development stage and published in [16] will be applied. Secondly, an adjusted set of initial clamping conditions $\widehat{\mathcal{D}}$ to optimally capture the measured initial clamping state, cf. Fig. 6.19, is used in conjunction with transient clamping during the abrasive phase. As a third approach, the previously developed transient clamping approach incorporating the parameters presented in Section 6.2.2, denoted by $\widetilde{\mathcal{D}}$ will be applied.

The results of this study are depicted in Fig. 6.40, where the left hand side displays the resulting radial inner workpiece surface node displacements. The graph on the right hand side shows the resulting error of the latter nodes with respect to the nominal inner radius after the workpiece has been ground and cooled to ambient temperature. Considering first the resulting simulated error in comparison to the measured radial

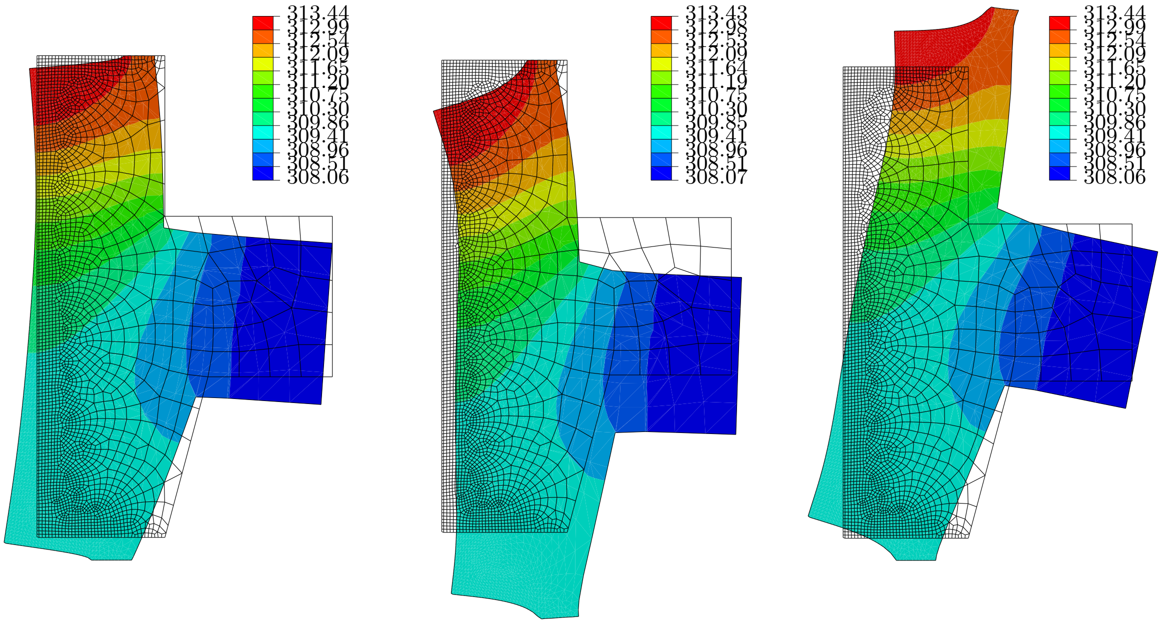

Figure 6.36: Temperature distribution at the beginning of the cooling phase after the mapped stress state was iterated to an equilibrium state. Different boundary conditions applied during the cooling of the workpiece after the abrasive process are depicted: Dirichlet on both entry and exit face (left), only on the exit face (middle) and only on the entry face (right). An isotropic displacement scaling of 1000 is applied to every variant.

error $\Delta\overline{r}$, an acceptable agreement—apart from the entry and exit effects observable in the blue measured line—can be asserted to all approaches presented. Especially the exit effect that causes a strong local minimum for $z \geq 30$mm, assumed to be caused by the limited stiffness of the grinding machine, is not captured due to the model assumptions mentioned in section 6.3.3. A similar effect is visible at the entry phase of the tool for $z \leq 10\,\text{mm}$, where predominantly the curvature of the measured curve deviates from the simulated one. However, in the steady state range $10\,\text{mm} \leq z \leq 30\,\text{mm}$ the qualitative tendency of the experiments can be captured well by the simulation.

When now comparing the quality of the resulting error predicted by the different approaches $\overline{\mathcal{D}}$, $\widehat{\mathcal{D}}$ and $\widetilde{\mathcal{D}}$, the transient clamping approach $\widetilde{\mathcal{D}}$ clearly exceeds the other two concepts: Especially in the range $5\,\text{mm} \leq z \leq 23\,\text{mm}$ the difference to the measured data is smaller than in $\overline{\mathcal{D}}$ and $\widehat{\mathcal{D}}$. Moreover, the measured magnitude of the local maximum deviation of approximately $1.1\,\mu\text{m}$ at $z \approx 22\,\text{mm}$ is captured in very good agreement, although the axial position $z \approx 27\,\text{mm}$ differs from the measured data. The simulated local maximum magnitudes of both $\overline{\mathcal{D}}$ and $\widehat{\mathcal{D}}$ show smaller values in comparison to $\widetilde{\mathcal{D}}$, what obviously correlates to the smaller axial clamping displacement applied in the initial model. This can be easily observed in the resulting clamping displacement graph on the left hand side of Fig. 6.40, where $\overline{\mathcal{D}}$ and $\widehat{\mathcal{D}}$ evince significantly smaller maximum values

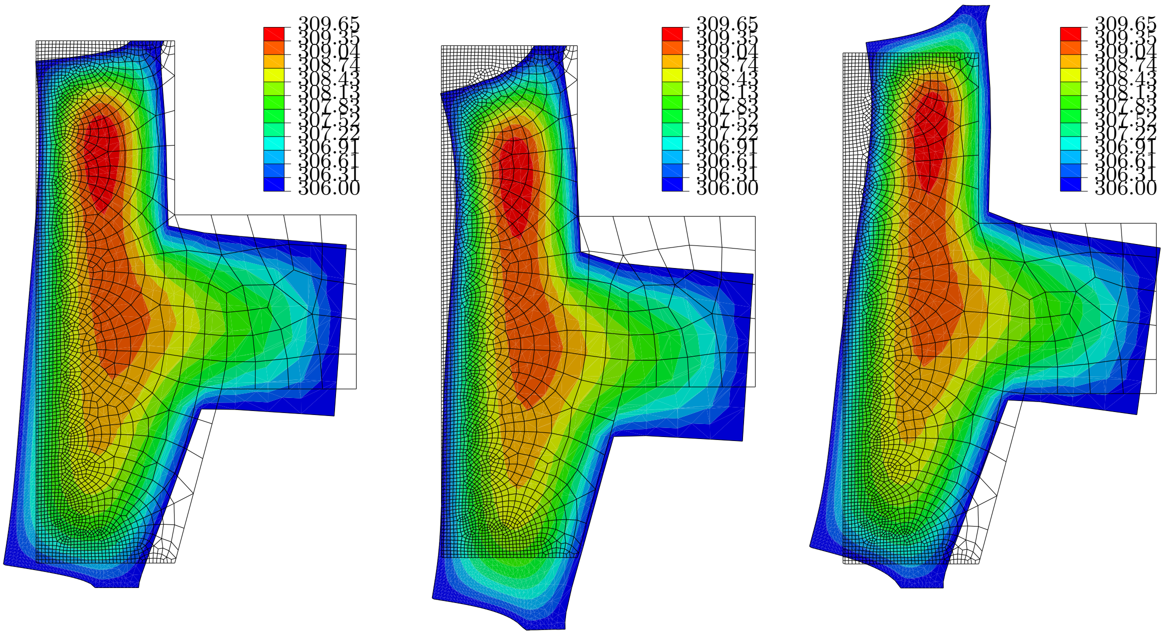

Figure 6.37: Temperature distribution after one fourth of the cooling phase has passed for the different boundary conditions applied during the cooling of the workpiece after the abrasive process. An isotropic displacement scaling of 1000 is applied here.

than $\widetilde{\mathcal{D}}$ at the overall, well captured axial position of the local extremum at $z \approx 25\,\mathrm{mm}$. Moreover, it is interesting to observe, that the optimally captured clamping displacement approach of $\widehat{\mathcal{D}}$ results in the worst approximation of the resulting workpiece inner surface profile. In summary, it can be concluded, that the transient clamping approach $\widetilde{\mathcal{D}}$ results in the best prediction of the final workpiece geometry, although it evinces the worst approximation of the initial clamping displacement. Based on this finding, this approach will be used as a basis for the following development of compensation strategies.

6.4 Compensation strategies

In a very general framework, the compensation of geometric errors in production processes can be summarised as the derivation of a manipulated set of process parameters $\hat{\mathcal{P}}$ aiming at the minimisation of the error $\boldsymbol{x}^{\mathrm{fin}} - \boldsymbol{x}^{\mathrm{nom}}$ between the resulting workpiece spatial shape $\boldsymbol{x}^{\mathrm{fin}}$ and the targeted nominal shape $\boldsymbol{x}^{\mathrm{nom}}$. The objectives of this task can certainly be extended to target certain material properties such as resulting hardness, residual stress states or phase composition of any kind. However, in the present context, only geometrical errors shall be aimed at. Though the introduction of this work outlined that especially the metallurgical composition of the ground workpieces may be affected by ITG, none of the experiments carried out showed a significant influence of

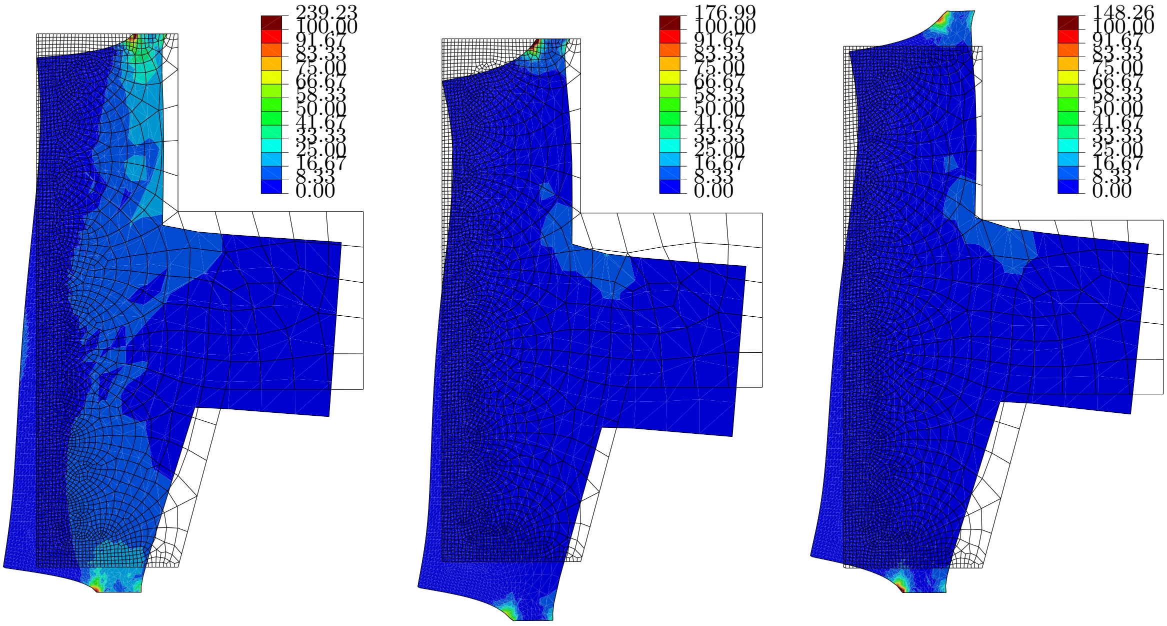
239.23
100.00
91.67
83.33
75.00
66.67
58.33
50.00
41.67
33.33
25.00
16.67
8.33
0.00
176.99
100.00
91.67
83.33
75.00
66.67
58.33
50.00
41.67
33.33
25.00
16.67
8.33
0.00
148.26
100.00
91.67
83.33
75.00
66.67
58.33
50.00
41.67
33.33
25.00
16.67
8.33
0.00

Figure 6.38: Remaining von Mises stress of the different boundary conditions applied during the cooling of the workpiece after the abrasive process. An isotropic displacement scaling of 1000 is applied here.

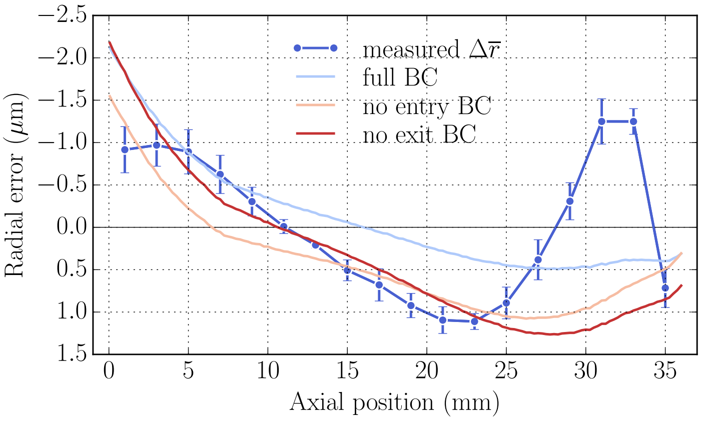

Figure 6.39: Comparison of the different boundary condition variants when cooling the workpiece after the abrasive phase. Measurement data by courtesy of ISF.

the expected phase transformations, cf. Fig. 1.7. This justifies the reduction of the present compensation problem to geometrical errors only. Moreover, those errors shall be reduced to exclusively reflect the diameter error of the resulting workpiece inner surface—other geometrical errors such as the ground bore roundness or parallelism will not be considered due to the restricted measurement data accessible. A compensation in the present experimental setup can furthermore only be carried out in terms of a

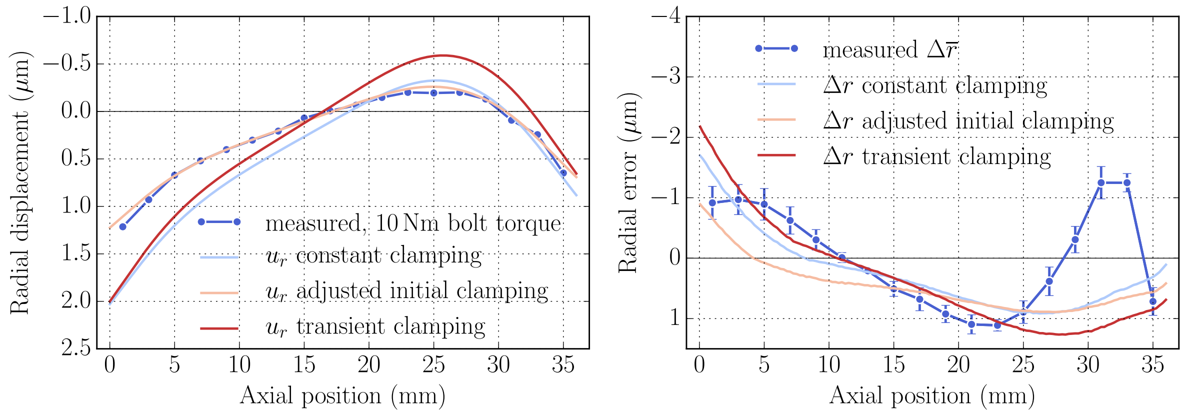

Figure 6.40: Results of the material removal simulation with different clamping approaches implemented in comparison to measured data from experiments. Radial displacement of the workpiece inner surface nodes after the clamping phase (left) and resulting radial error after cooling the ground workpiece to ambient temperature (right).

parallel shift of the tool protrusion axis $\boldsymbol{e}_y$ as a function of the axial tool position—the rotation of the tool axis currently does not constitute a degree of freedom in the context of the CNC (Computer Numerical Control) of the grinding machine used. Moreover, the macroscopic process parameters such as workpiece and tool speeds v_w and v_s or the axial feed velocity v_fa, respectively, shall at this stage of development also be kept constant.

From a mathematical point of view, the development of a compensation strategy can in general be condensed to a constrained optimisation problem

$$\hat{\mathcal{P}} = \arg\min_{\boldsymbol{\kappa}} \mathfrak{R}_\Delta(\boldsymbol{\kappa};\, \mathcal{P}) \,|\, \mathcal{C}, \quad \text{with} \tag{6.34}$$

$$\mathfrak{R}_\Delta = \hat{\mathfrak{R}}_\Delta(\boldsymbol{x}^\mathrm{fin}; \boldsymbol{x}^\mathrm{nom}) \quad \text{and} \tag{6.35}$$

$$\boldsymbol{x}^\mathrm{fin} = \mathcal{F}_\mathrm{fin}(\boldsymbol{\kappa};\, \mathcal{P}, \boldsymbol{x}^\mathrm{nom}), \tag{6.36}$$

where $\mathcal{F}_\mathrm{fin}$ denotes a highly non-linear function representing the process under consideration and where $\mathfrak{R}_\Delta$ represents a general formulation of a residual function, subject to a set of general constraints $\mathcal{C}$. For the set of free parameters $\boldsymbol{\kappa}$, usually representing a subset of all process parameters $\mathcal{P}$ available, i.e. $\boldsymbol{\kappa} \subseteq \mathcal{P}$, it thus holds $\hat{\mathcal{P}} = \boldsymbol{\kappa} \cup \mathcal{P}$.

6.4.1 Derivation of compensation approaches adapted to ITG

With the above mathematical basics and the aforementioned process restrictions at hand, we can reformulate (6.34) to reflect the present compensation task. As stated above, in the current experimental setup we are only able to vary the trajectory $\mathcal{T}$ of the tool during the axial pass through the workpiece, keeping all other process parameters constant. Hence,

$$\boldsymbol{\kappa} \equiv \mathcal{T}(t) \tag{6.37}$$

holds for the optimisation task. Referring to the cylindrical coordinate system used in the process model, an optimised trajectory

$$\hat{\mathcal{T}}(t) = \mathcal{T}(t) + \Delta_r \mathcal{T}(t) = \mathcal{T}(z) + \Delta_r \mathcal{T}(z) \tag{6.38}$$

needs to be derived. For the case of a non-compensated grinding process, $\mathcal{T}(t) = r^{\mathrm{i}}_{\mathrm{nom}} = r^{\mathrm{i}}_0 + a_{\mathrm{e,tot}}$ holds, representing a straight line at the targeted nominal inner radius $r^{\mathrm{i}}_{\mathrm{nom}}$ that is offset from the initial inner radius r^{i}_0 by the total radial stock removal $a_{\mathrm{e,tot}}$. In the following, the radial offset $\Delta_r \mathcal{T}(t)$ will be used to describe the trajectory of the tool.

Due to the axisymmetric finite element design of the process model representing f in accordance to (6.36), the residual function $\mathfrak{R}_\Delta$ can basically be formulated as the squared sum of the radial nodal errors

$$\mathfrak{R}_\Delta = \sum_{k=1}^{n_{\mathcal{E}}+1} \left[r_k - r^{\mathrm{i}}_{\mathrm{nom}} \right]^2 \tag{6.39}$$

along the inner workpiece surface discretised by $n_{\mathcal{E}}$ quadrilateral elements $\mathcal{E}$. This approach, however, is restricted to a discretisation of the workpiece inner surface that ensures the nodes $\boldsymbol{x}_k = r_k \, \boldsymbol{e}_r + z_k \, \boldsymbol{e}_z \in \partial \mathcal{B}^{\mathcal{L}}$ to remain constant in number. Since this condition will most likely be violated due to the remeshing applied, a more general residual norm will be invoked. The derivation is given in detail in Sec. 6.4.2; at this point, we will only use the resulting norm $\mathfrak{R}^2_\Delta$ given in Eq. (6.59).

With this, we have all necessary components at hand and hence, the following equations

$$\hat{\mathcal{T}}(t) = \arg\min_{\Delta\mathcal{T}} \mathfrak{R}^2_\Delta(\Delta\mathcal{T}(t);\, \mathcal{P}) \tag{6.40}$$

$$\mathfrak{R}^2_\Delta = \frac{\dfrac{1}{2} \displaystyle\sum_{k=1}^{n_k-1} \left[\sqrt{\left[\Delta r^{\mathrm{i}}_{k+1}\right]^2} - \sqrt{\left[\Delta r^{\mathrm{i}}_{k}\right]^2} \right] \left[z_{k+1} - z_k \right]}{\displaystyle\sum_{k=1}^{n_k-1} \left[z_{k+1} - z_k \right]} \tag{6.41}$$

$$f(\Delta\mathcal{T};\, \mathcal{P}, r^{\mathrm{i}}_{\mathrm{nom}}) \mathrel{\widehat{=}} \text{Algorithm 6.2} \tag{6.42}$$

describe the compensation task to be solved. Note, that $\Delta r^{\mathrm{i}}_k = r_k - r^{\mathrm{i}}_{\mathrm{nom}}$ refers to the radial error of a spatial node $\boldsymbol{x}_k$ and n_k represents the number of supporting points, or surface nodes $\boldsymbol{x}_k$, respectively—so for quadrilateral elements, $n_k = n_{\mathcal{E}} + 1$ holds.

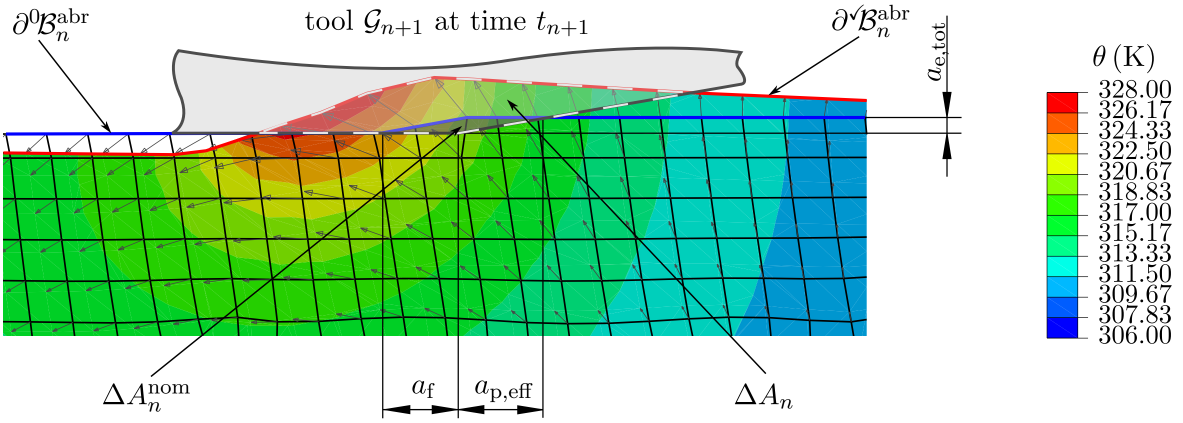
$\partial^0\mathcal{B}_n^{\text{abr}}$
tool $\mathcal{G}_{n+1}$ at time t_{n+1}
$\partial^{\checkmark}\mathcal{B}_n^{\text{abr}}$
$a_{\text{e,tot}}$
θ (K)
328.00
326.17
324.33
322.50
320.67
318.83
317.00
315.17
313.33
311.50
309.67
307.83
306.00
ΔA_n^{nom}
a_{f}
$a_{\text{p,eff}}$
ΔA_n

Figure 6.41: Effective and nominal amount of removed material in the process zone at time t_n. The displayed mesh represents the reference configuration $\boldsymbol{X}_n$, whereas the arrows represent the displacement vectors $\boldsymbol{u}_k$ pointing at the spatial configuration $\boldsymbol{x}_n$. The blue marked surface represents the reference model boundary $\partial^0\mathcal{B}_n^{\text{abr}}$, whereas the red line depicts the spatial boundary $\partial^{\checkmark}\mathcal{B}_n^{\text{abr}}$. The effective amount of material removed $\Delta\overline{\mathcal{B}}_n$ is emphasised by the light shaded area bounded by a grey dashed line, the nominal amount of ground material ΔA_n^{nom} is represented by the dark shaded area. An isotropic displacement scaling factor of 3000 is applied.

To calculate the compensated tool trajectory, the following compensation strategies will be taken into account:

Inversion of the resulting surface profile after cooling $\Delta\mathcal{T}^{\text{inv}}$ This approach is motivated by a basic experimental outcome, where a transient determination of the exact material removal discrepancies is not possible. It therefore uses the inverted resulting radial error after cooling as the tool trajectory correction, namely

$$\Delta_r\mathcal{T}^{\text{inv}}(t) = -\left[\boldsymbol{x}_k(t)\cdot\boldsymbol{e}_r - r^{\text{i}}_{\text{nom}}\right]\ \forall\ \boldsymbol{x}_k = r_k\boldsymbol{e}_r + z_k\boldsymbol{e}_z\ \in\partial\mathcal{B}^{\mathcal{L}} \tag{6.43}$$

$$= -\Delta_r r(t) \tag{6.44}$$

after cooling the workpiece back to ambient temperature, cf. Fig. 6.40, right. Note, that since $\dot{z}(t) = v_{\text{fa}}$ is known, and in the present case $\dot{v}_{\text{fa}} = 0$ holds, we can equivalently parametrise the trajectory function in space, which is more convenient with regard to the reading of the plots in this work. We furthermore drop the index r for notational simplicity and apply the time discretisation as presented in Eq. (6.52), and retrieve the incremental formulation

$$\Delta\mathcal{T}_n^{\text{inv}} = -\left[r_n(z) - r^{\text{i}}_{\text{nom}}\right] = -\Delta r_n. \tag{6.45}$$

This compensation approach is straightforward, easily applicable to experiments and is therefore applied in the present work. However, possible non-linear effects occurring during the process are assumed to be reversible which is a drawback of this method and will presumably not lead to very good results, especially, if plasticity or higher gradients in the temperature field occur. Recall the temperature-dependent material parameters implemented in this model, cf. Tab. A.3.

Compensation based on integral material removal $\Delta\mathcal{T}^{\text{int}}$ The second method is based on the target nominal amount of workpiece material $\Delta\mathcal{B}_n^{\text{nom}}$ removed at time step t_n, which can in general directly be determined from the set of material parameters $\mathcal{P}$ in combination with the tool geometry $\mathcal{G}$, cf. Fig. 1.1 and Equations (1.1) to (1.3). In the present axisymmetric context, the nominal removed material volume $\Delta\mathcal{B}_n^{\text{nom}}$ is represented by a trapezoidal area $\Delta\overline{\mathcal{B}}_n^{\text{nom}} = a_{\text{f}}\, a_{\text{e,tot}} = 0.05\,\text{mm}^2$, cf. the dark shaded area in Fig. 6.41. This nominal value represents the ideal amount of material removed during the process and can be compared with the effective amount of material removed that can be determined from the simulation, see the light shaded area bounded by the light grey dashed line in Fig. 6.41. This effective amount of material removed at time t_n

$$\Delta\overline{\mathcal{B}}_n = \mathcal{G}_{n+1} \cap {}^{\checkmark}\mathcal{B}_n^{\text{abr}} \tag{6.46}$$

can be expressed as the integral over all load surface nodes in spatial configuration at time t_n

$$\Delta\overline{\mathcal{B}}_n = \int_{\Delta z} [\,\boldsymbol{X}_{n+1} - \boldsymbol{x}_n\,] \cdot \boldsymbol{e}_r \,\mathrm{d}z \tag{6.47}$$

$$\forall\ \boldsymbol{x}_k = r_k\,\boldsymbol{e}_r + z_k\,\boldsymbol{e}_z\ \in \partial\mathcal{B}_n^{\mathcal{L}}\ \wedge\ \forall\ \boldsymbol{X}_{n+1} = R_k\,\boldsymbol{e}_r + Z_k\,\boldsymbol{e}_z\ \in \partial\mathcal{B}_{n+1}^{\mathcal{L}} \tag{6.48}$$

$$\Rightarrow \Delta\overline{\mathcal{B}}_n =: \int_{\Delta z} \left[\,\boldsymbol{X}_{n+1}^{\partial} - \boldsymbol{x}_n^{\partial}\right] \cdot \boldsymbol{e}_r \,\mathrm{d}z. \tag{6.49}$$

Here, the inner surface nodes $\boldsymbol{X}_{n+1}^{\partial} \in \partial\mathcal{B}_{n+1}^{\mathcal{L}}$ in the updated and modified reference configuration result from the intersection

$$\partial\mathcal{B}_{n+1}^{\mathcal{L}} = \partial\left[{}^{\checkmark}\mathcal{B}_n^{\text{abr}} \setminus \mathcal{G}_{n+1}\right] \cap \partial\mathcal{B}_n^{\mathcal{L}}, \tag{6.50}$$

which can be computed straightforwardly at t_n. Moreover, Δz denotes the spatial axial integration range that is used to determine the amount of material removed. In the present context, setting

$$\Delta z = \left[\partial\mathcal{G}_{n+1} \cap \left[\mathcal{G}_{n+1} \cap {}^{\checkmark}\mathcal{B}_n^{\text{abr}}\right]\right] \cdot \boldsymbol{e}_z, \tag{6.51}$$

cf. Fig. 6.41, represents a generally feasible and hence sensible choice and will therefore be applied throughout the rest of this work. It shall be remarked here, that the continuous tool correction function will be discretised in time in a stepwise constant manner, i.e.

$$\Delta_r\mathcal{T}(t) \approx \bigcup_{n=1}^{n_{\Delta t}} \Delta_r\mathcal{T}_n; \qquad \frac{\partial\left[\Delta_r\mathcal{T}_n\right]}{\partial t} = 0 \tag{6.52}$$

approximates $\Delta_r\mathcal{T}(t)$ in $n_{\Delta t}$ time increments, where all trajectory increments $\Delta_r\mathcal{T}_n$ are invariant in time. Taking now the following demand into account,

$$\Delta\overline{\mathcal{B}}_n \overset{!}{=} \Delta\overline{\mathcal{B}}_n^{\mathrm{nom}} \tag{6.53}$$

$$\Rightarrow a_{\mathrm{f}}\,\Delta_r\mathcal{T}_n = \left[\Delta\overline{\mathcal{B}}_n^{\mathrm{nom}} - \Delta\overline{\mathcal{B}}_n\right] = \left[a_{\mathrm{f}}\,a_{\mathrm{e,tot}} - \Delta\overline{\mathcal{B}}_n\right], \tag{6.54}$$

the compensated tool trajectory follows as

$$\Delta_r\mathcal{T}_n^{\mathrm{int}} = \frac{1}{a_{\mathrm{f}}}\left[\Delta\overline{\mathcal{B}}_n^{\mathrm{nom}} - \Delta\overline{\mathcal{B}}_n\right] \tag{6.55}$$

$$= \frac{1}{a_{\mathrm{f}}}\left[\Delta\overline{\mathcal{B}}_n^{\mathrm{nom}} - \int_{\Delta z}\left[\boldsymbol{X}_{n+1}^{\partial} - \boldsymbol{x}_n^{\partial}\right]\cdot\boldsymbol{e}_r\,\mathrm{d}z\right]\forall\,t_n \in \left[t_1,\,t_{\max}^{\mathrm{grd}}\right]. \tag{6.56}$$

This basically represents a discrete forward differential of the amount of material removed with respect to time.

6.4.2 Definition of the residual norm

To enable a comparability of the radial error resulting from the different compensation simulations as well as from the experimental data, an invariant residual norm needs to be defined. This means that the residuum must be independent from the number of supporting points, i.e. from the number of inner workpiece surface nodes in the case of a simulation or from the number of measurement points concerning experiments, respectively. Therefore, a standard squared error norm

$$\mathfrak{R}_\Delta = \sum_{k=1}^{n_k}\left[r_k^{\mathrm{i}} - r_{\mathrm{nom}}^{\mathrm{i}}\right]^2 = \left[\Delta r_k^{\mathrm{i}}\right]^2 = \left[\Delta r^{\mathrm{i}}(z)\right]^2 \tag{6.57}$$

is not admissible since it permits comparability only if the same amount of supporting points n_k is guaranteed among all sets of data to be compared. This is certainly not given in the present case. Moreover, the supporting points are not even equidistant any more in the case of the simulation. Following therefrom, a quadratic and integrally averaged residual, similar to an L^2 norm, will be taken into account as

$$\mathfrak{R}^2_\Delta = \frac{\int\limits_{z_{\min}}^{z_{\max}} \sqrt{\left[r^{\mathrm{i}}(z) - r^{\mathrm{i}}_{\mathrm{nom}}\right]^2}\,\mathrm{d}z}{\int\limits_{z_{\min}}^{z_{\max}} \mathrm{d}z} = \frac{\int\limits_{z_{\min}}^{z_{\max}} \sqrt{\left[\Delta r^{\mathrm{i}}(z)\right]^2}\,\mathrm{d}z}{\int\limits_{z_{\min}}^{z_{\max}} \mathrm{d}z} \tag{6.58}$$

$$\Rightarrow \mathfrak{R}^2_\Delta \overset{\boxplus}{=} \frac{\frac{1}{2}\sum\limits_{k=1}^{n_k-1} \left[\sqrt{\left[\Delta r^{\mathrm{i}}_{k+1}\right]^2} - \sqrt{\left[\Delta r^{\mathrm{i}}_{k}\right]^2}\right] \left[z_{k+1} - z_k\right]}{\sum\limits_{k=1}^{n_k-1} \left[z_{k+1} - z_k\right]}. \tag{6.59}$$

Note, that since we assume a piecewise linear approximation of the resulting surface increments between the supporting points, the trapezoidal integration rule displayed above exactly integrates the piecewise linear function, even in the L^2 space. The square root in the above terms is applied to scale the residuum $\mathfrak{R}^2_\Delta$ to the same unit as $\Delta r^{\mathrm{i}}(z)$ for the sake of convenience. As a result, the residual norm approximately reflects the averaged positive radial area per axial unit length along the entire axial data range and therefore entirely fulfils the above comparability conditions.

6.4.3 Results and discussion

In Figures 6.43 and 6.44, the tool trajectories $\Delta\mathcal{T}^\bullet$ deducted from the above-mentioned compensation approaches are depicted with the resulting radial errors $\Delta r^\bullet$ when applying the tool trajectories in simulations as well as in experiments. However, these results are at first restricted to constant Dirichlet boundary conditions representing the clamping. Moreover, spring-back effects will be at first also be neglected, so the investigation conditions are equal to the ones applied in [16]. Since the application of compensation strategies to transient clamping boundary conditions in combination with spring-back effects needs some extra discussion, these topics are investigated at the end of this section in more detail.

Considering first the simulative compensation approaches, both the inverted and the integral strategies deliver similar correction trajectories $\Delta\mathcal{T}^{\mathrm{inv}}$ and $\Delta\mathcal{T}^{\mathrm{inv}}$, cf. Fig. 6.42, left. The respective results when applying these trajectories to the process simulation can be seen in the right hand side plot of Fig. 6.44 when comparing the non-compensated line Δr with the compensated curves Δr^{inv} and Δr^{int}. It is possible to reduce the radial error varying from approximately 3 µm to -1.5 µm to a range below 0.5 µm, which proves the successful deviation reduction of both methods. The jumps observable in the red curves correspond to the integral nature of the computation of $\Delta\mathcal{T}^{\mathrm{int}}$: Since this integral

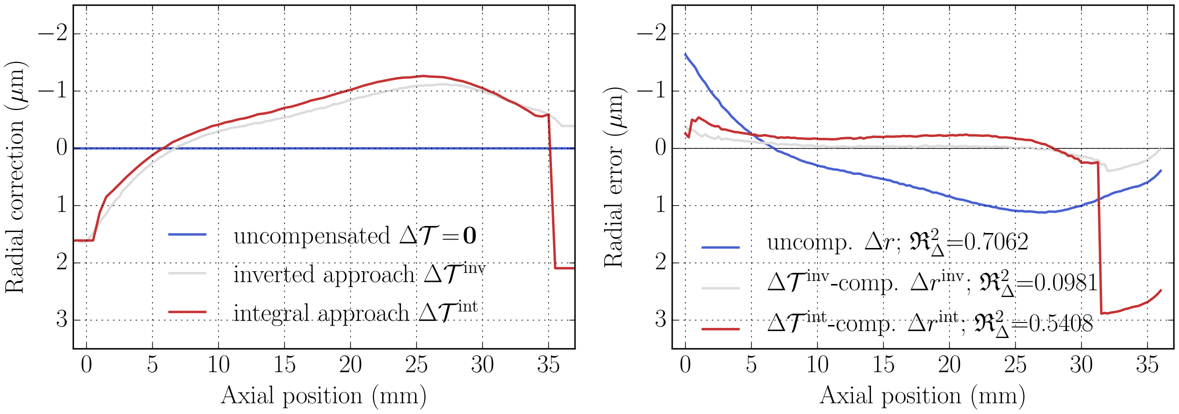

Figure 6.42: Results of the simulated compensation when applying constant Dirichlet boundary conditions representing the clamping.

in Eq. (6.56) is evaluated only in the range of the roughing zone of the tool, it delivers too strong correction values $\Delta\mathcal{T}^{\mathrm{int}}$ for $z \geq 35\,\mathrm{mm}$ when the roughing zone of the tool is no longer in contact with the workpiece. The according response is clearly observable in the resulting error plot and the corresponding residuum $\mathfrak{R}^2_\Delta(\Delta r^{\mathrm{int}}) = 0.5408\,\mu\mathrm{m}$, which represents a relatively large value. Interestingly, the inverted compensation approach performs significantly better although the tool trajectory $\Delta\mathcal{T}^{\mathrm{inv}}$ is offset only approximately $0.1\,\mu\mathrm{m}$ from $\Delta\mathcal{T}^{\mathrm{int}}$. In the axial range $10 \leq z \leq 27\,\mathrm{mm}$, barely any radial deviation Δr^{inv} is observable—en plus, the radial error close to the workpiece exit face is visible though, but by far not as extensively as in the red error line, causing the residual $\mathfrak{R}^2_\Delta(\Delta r^{\mathrm{inv}}) = 0.0981\,\mu\mathrm{m}$ to show a drastically better value than the integral approach. So up to this point, we can conclude that—against earlier expectations—the inverted compensation approach $\Delta\mathcal{T}^{\mathrm{inv}}$ outperforms the integral strategy $\Delta\mathcal{T}^{\mathrm{int}}$ with respect to the application investigated. To further improve the quality of the integral approach, the inherent outliers in $\Delta\mathcal{T}^{\mathrm{int}}(z)$ for $z \geq 35\,\mathrm{mm}$ will be removed by simply substituting all subsequent correction values with the last undistorted value, i.e.

$$\Delta\mathcal{T}^{\mathrm{int}}(z)\big|_{z>l^{\mathrm{wp}}-l_{\mathrm{ca}}} \equiv \Delta\mathcal{T}^{\mathrm{inv}}(l^{\mathrm{wp}} - l_{\mathrm{ca}}). \tag{6.60}$$

This alteration will be employed when applying the compensation strategies to the extended model including transient clamping and springback.

To prove the general correctness of the deducted simulations and trajectories, an experiment was carried out twice: Once in the standard way without any compensation applied ($\Delta\mathcal{T} = \mathbf{0}$) and once applying the corrected trajectory $\Delta\mathcal{T}^{\mathrm{exp}}$ derived from an intermediated, piecewise linear approximation of the afore-developed simulated compensation trajectories $\Delta\mathcal{T}^{\mathrm{inv}}$ and $\Delta\mathcal{T}^{\mathrm{int}}$. All trajectories are depicted in the left hand side plot of Fig. 6.43. The piecewise linear approximation is due to the restrictions of the CNC of the axial feed of the grinding machine used in the experiments. The corre-

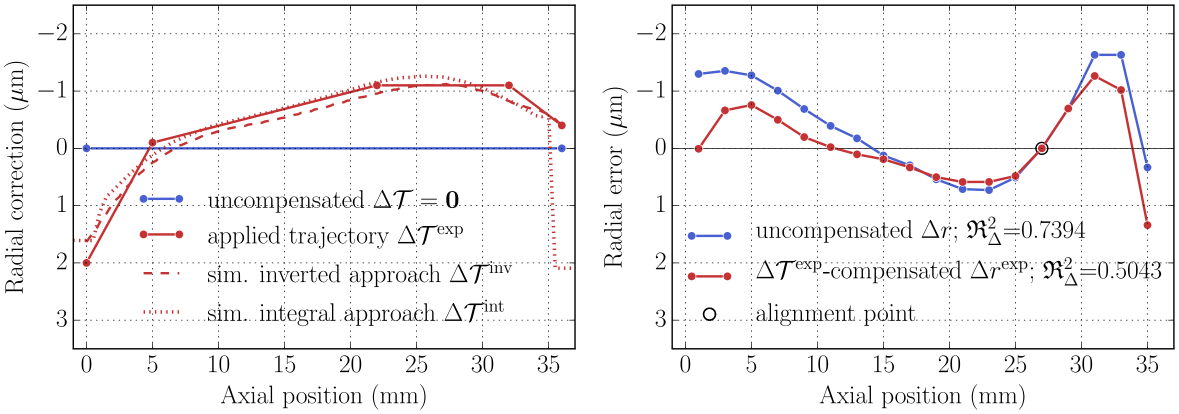

Figure 6.43: Experimental results after applying the simulation-based compensation approach. Measurement data by courtesy of ISF.

sponding resulting radial errors $\Delta x^{\bullet}$ are displayed in the right hand side part of the same figure. To enable a comprehensive interpretation of the data, the resulting measurements were normalised to the radius values corresponding to the horizontal section of the compensation trajectory $\Delta\mathcal{T}^{\text{exp}}$, cf. the alignment point depicted in Fig. 6.43.

It can be stated that the error reduction in the experimental data is generally visible, however by far not as strong as in the simulative prognosis. Though, along the entire engagement range $0 \leq z \leq 36\,\text{mm}$, a decrease of the radial error can be observed: The deviation at the local extremum at $z = 21\,\text{mm}$ diminishes from approximately $0.75\,\mu\text{m}$ to $0.5\,\mu\text{m}$, while the deviation for the entire range before the extreme value $z \leq 21\,\text{mm}$ is decreased on average by approximately $0.5\,\mu\text{m}$. The overall residual is lessened by around one third from 0.7394 to 0.5043.

In conclusion, the developed compensation strategies fundamentally work very well, although up to this point, not every machine characteristic, such as the spindle compliance, has been considered in the simulation.

Let us now extend the above discussion to the inclusion of transient clamping conditions and springback effects. In general, the compensation strategies developed in Sec. 6.4.1 are applicable to any ITG simulations, this can straightforwardly be executed here, too—only the shape of the compensation trajectories will differ due to the more transient response of the workpiece model.

Figure 6.44 displays the resulting trajectories along with the remaining radial errors when applying the compensation techniques to the corresponding boundary value problems. Similar to the above investigation, the non-compensated process simulation is compared to the compensated variations invoking on the one hand the inverted approach $\mathcal{T}^{\text{inv}}$, and on the other hand the integral approach $\mathcal{T}^{\text{int}}$ to compute the compensation trajectory. Moreover, the cooling of the workpiece after grinding was carried out in two different ways: Once, the workpiece clamping faces $\partial\mathcal{B}^{\boldsymbol{u}}_{\bullet}$ are linearly driven back to their

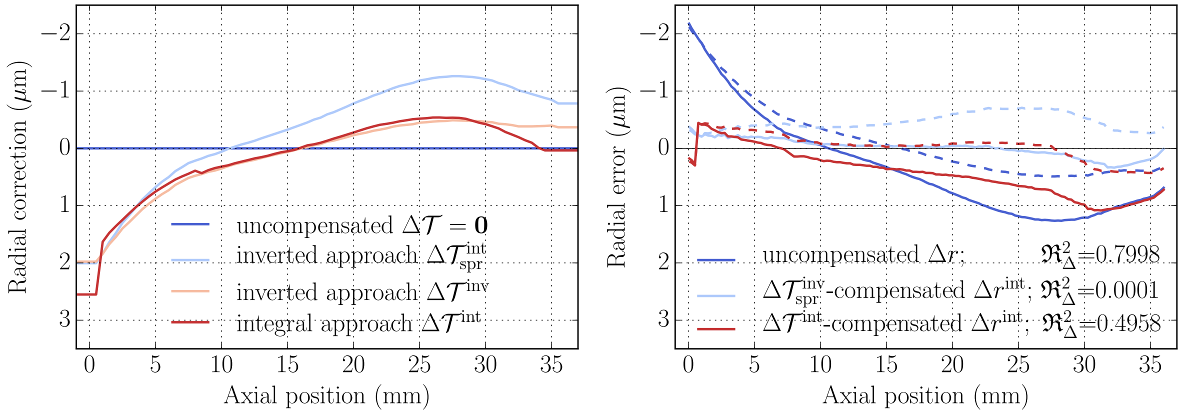

Figure 6.44: Results of the simulated compensation when applying transient Dirichlet boundary conditions representing the clamping. The left hand side depicts the compensation trajectories applied, whereas the right hand side shows the resulting radial errors. The dashed lines represent the resulting inner radial errors when *not* considering the springback effect.

initial positions during cooling, which is depicted as the dashed line representation of $\Delta r^{\bullet}$ in Fig. 6.44. In contrast,

$$\mathcal{D} = \emptyset \,|_{\partial \mathcal{B}^{\boldsymbol{u}}_{\mathrm{ex}}} \tag{6.61}$$

is applied, i.e. the boundary condition at the workpiece exit face is removed entirely during cooling to minimise the residual stress resulting from the transient loading and cooling of the workpiece. The resulting workpiece deflection that is based on the strain equivalent to the residual stress is depicted as the solid lines referring to $\Delta r^{\bullet}$ in the right hand side of Fig. 6.44. Since the latter effect is commonly referred to as springback, cf. e.g. [82] and Fig. 6.38, we will use this term here as well. Apart from these alterations, the simulation conditions are equal to the setup presented in Sec. 6.3.5.

Considering at first the resulting error Δr for the uncompensated case—which has already been briefly discussed in Sec. 6.3.5—an increase of the radial error is observable when taking the springback effect into account. This is emphasised by the comparably high resulting error norm of $\mathfrak{R}^{\mathrm{spr}}_{\Delta} = 0.7998$. So obviously, the residual stress induced into the workpiece during the process simulation fundamentally causes a widening of the ring-type part after cooling. When considering the dashed blue line in the same graph that represents a fixed clamping during cooling, a significantly lower radial error is observable, which can be quantified with $\mathfrak{R}^{\mathrm{fix}}_{\Delta} = 0.4975$. With these two curves at hand, we can now derive two different compensation trajectories invoking the inverted approach, namely $\Delta\mathcal{T}^{\mathrm{inv}}_{\mathrm{spr}}$ and $\Delta\mathcal{T}^{\mathrm{inv}}$, which are based on the solid blue line including springback and the dashed blue line, respectively. The corresponding trajectories are depicted in the left graph of Fig. 6.44 as light blue and light red line, correspondingly. In addition, the integral approach was used to derive the corrected tool trajectory $\Delta\mathcal{T}^{\mathrm{int}}$, which is displayed as solid red line in the same graph. Here, it is important to keep in mind that the integral compensation approach is by nature not able to take any springback or residual stress effects into account, since it calculates the tool position correction exclusively during the abrasive phase of the material removal simulation.

With this knowledge at hand, it is now very easy to explain why the resulting compensation trajectories $\Delta\mathcal{T}^{\mathrm{inv}}$ and $\Delta\mathcal{T}^{\mathrm{int}}$ are very similar, which is apparent in the trajectory graph. For this reason, only for $\Delta\mathcal{T}^{\mathrm{int}}$, the corresponding radial error of the compensated simulation will be examined in the following. Considering at first the radial error Δr^{int} resulting from the integral compensation approach, we have to admit that the result is quite unsatisfactory when springback is included—the solid red line representing Δr^{int} in the right hand side graph of Fig. 6.44 clearly depicts this, along with a residual of $\mathfrak{R}^2_\Delta = 0.4958$. When neglecting the springback, however, the integral compensation strategy delivers a very accurately reduced radial error with a residual norm of only $\mathfrak{R}^2_\Delta = 0.0005$, compare the dashed red line. This result is in very good accordance with the above-mentioned findings on the widening of the annular workpiece due to the springback effect. Examining finally the radial error Δr^{inv} resulting from the inverted trajectory $\Delta\mathcal{T}^{\mathrm{inv}}_{\mathrm{spr}}$ including springback, which is depicted as the light blue line in the error graph of Fig. 6.44, the latter strategy yields the best compensation results. In this case, the radial error neglecting the springback results in globally too small radii, as can be concluded from the dashed light blue line. When now enabling springback during cooling, the resulting widening of the workpiece causes the final inner workpiece surface to match the nominal values very well, which is reflected by the solid light blue line and the lowest residual observed, i.e. $\mathfrak{R}^2_\Delta = 0.0001$. During the first and last 7 mm after tool entry and exit, an average radial error of approximately only one third of a micrometer is observable, for $7\,\mathrm{mm} \leq z \leq 29\,\mathrm{mm}$, this error drops far below 0.1 µm, which represents an excellent result of the underlying compensation strategy.

Therefore, we can conclude that—against the hypothesis formulated in Sec. 6.3.5—the inverted compensation approach outperforms the integral version when applying the most realistic clamping boundary conditions. The latter essentially includes time-dependent axial clamping and foremost, the springback effect when removing the simulated clamping during the cooling phase of the process simulation. Invoking the recently gathered knowledge on the thermo-mechanic process response, it is now perfectly comprehensible why the inverted approach delivers more accurate results. Consequently, it constitutes the only method that directly includes the springback effect, which is only recoverable during the cooling phase of the process. The development of an integral method that would for example cool down the workpiece after each material removal step, could again boost the performance of the integral compensation approach, but will be consigned to future research.

7 Concluding remarks

This thesis deals with the modelling and simulation of high-performance grinding processes using electroplated grinding wheels, such as Internal Traverse Grinding (ITG). A hybrid simulation framework is presented, which ranges from parametric meso-scale single-grain finite element models to a macro-scale process model. The latter is capable of realistically predicting the thermo-mechanically induced geometric workpiece errors occurring during the abrasive process and is used to derive two different compensation approaches to minimise the workpiece inner radius deviation.

In **Chapter 2**, a topography analysis scheme that works on measured grinding wheel surface data is developed to automatically determine characteristic quantities that are necessary to describe the stochastic grinding wheel properties, such as grain protrusion height distribution, the cutting edge rake angle distribution or the grain density. These parameters can, in turn, be used to perform wheel quality checks, to examine the wear behaviour, or to serve as input parameters for a subsequent kinematic simulation as presented in **Chapter 3**. In this kinematic simulation, which constitutes a central component of the grinding simulation framework presented, the transient geometric interaction between workpiece and abrasive grit during grinding is computed in high detail. Therein, the grinding wheel is modelled based on the assumption of ideal cBN crystal growth and the previously determined stochastic topography properties. The kinematic simulation results consist of a transient engagement condition distribution that gives detailed insight into the meso-scale process kinematics and constitutes a valuable component for bridging the thermo-mechanical loads on the meso-scale to the macro-scale.

To determine these meso-scale workpiece loads, an h-adaptive finite-element-analysis which captures the thermo-mechanical loads on the workpiece in the proximity of a single abrasive grain is presented in **Chapter 4**. In this context, force and heat induction evolutions for a certain engagement condition parameter set are computed in high detail, based on a thermo-mechanically coupled, elasto-plastic constitutive material model that invokes work and strain rate hardening along with thermal softening and ductile damage. To enable the automatic incorporation of this component in the grinding simulation framework, a complete parametric formulation of the meso-scale finite element model is implemented and successfully applied. To even improve the accuracy of the underlying simulation framework, the incorporation of a three-dimensional single grain model is assigned to future research.

In **Chapter 5**, an approach for the estimation of a macroscopic heat source term based on a meso-scale finite-element model and a macro-scale kinematic simulation is presented, thereby contributing to a framework to model and simulate Internal Traverse Grinding. Starting from an engagement condition distribution that results from the kinematic simulation, a certain number of meso-scale thermo-mechanical simulations are carried out to calculate a defined heat source term that reflects the amount of thermal energy induced into the workpiece per unit volume of the workpiece material machined during the abrasive progress. With the use of a weighted least-square minimisation, this heat source term is approximated by an exponential regression function that can then be evaluated in the context of the kinematic simulation to finally retrieve a transient heat induction on a macro-scale.

The comparison of this estimated heat induction with experimental investigations shows a very good agreement and, thus, enables the application of the presenting bridging approach in the context of the ITG simulation framework currently under development. Furthermore, the presented approach can also be used for other quantities such as the process forces in different spatial directions of the model. This gives way to the development of a more flexible regression scheme, that can automatically determine e.g. the covariance in terms of the correlation of the quantities to be bridged from the meso- to the macro-scale. To improve the quality of the bridging scheme presented, a more detailed rake angle approximation in the context of the kinematic simulation along with a three-dimensional formulation of the meso-scale model is to be mentioned. This, in turn, necessitates a more sophisticated parametrisation of the single grain model and the respective scale-bridging algorithm to enable a robust automatic regression, which constitutes a highly challenging modelling task.

In **Chapter 6**, a process simulation is presented with the motivation to capture the general thermo-mechanical process response on a macroscopic workpiece scale and to develop compensation strategies to minimise the dimensional error of the resulting workpiece inner cylindrical shape after grinding. Compensation strategies are developed and implemented proving that, from a simulation point of view, the workpiece deviation could be minimised drastically. The application of these methods is proven to work for the experimental ITG process as well, although the magnitude of the compensation effect has been found to be distinctively lower than calculated in the simulations. The reason for this result is considered to be caused by yet not implemented characteristics of the entire machine—especially the elasticity of the spindles is to be mentioned here. To account for these effects, the simulation framework will be extended to include a distributed mechanical load along with the moving heat source to model the tool in the process in higher detail. Furthermore, the effect of the spindle stiffness will be included by an extension to a three-dimensional model of the workpiece in combination with elastic boundary conditions applied, thereby capturing this obviously non-negligible effect.

7.1 Outlook

As mentioned above, the three-dimensional extension of some simulation framework components constitute a valuable increase of the overall modelling accuracy. Therefore, various investigations have been carried out during the progress of this thesis, which shall briefly be outlined in the following.

7.1.1 Three-dimensional single grain meso-scale model

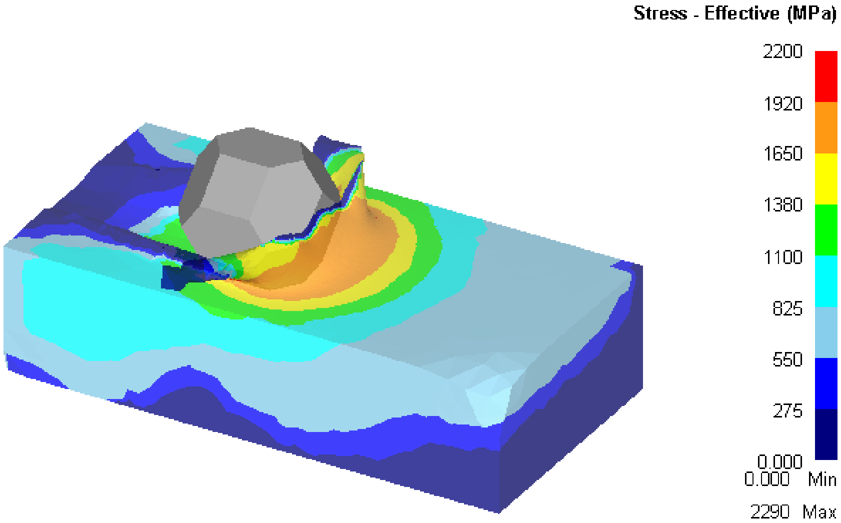

Figure 7.1: Results of the three-dimensional meso-scale model in terms of von Mises equivalent stress. The workpiece material model equals the one presented in Sec. 4.2; the grain is modelled as rigid body and is penetrating the workpiece from the left hand side with a constant velocity magnitude of 100 m/s.

A three-dimensional single grain model provides a more detailed insight into the meso-scale thermo-mechanic response of the workpiece during grinding. Especially material removal effects such as chip splitting cannot be captured by the current plane strain model. Some investigations using the commercial software package SFTC Deform have therefore been carried out with some basic grain geometry, cf. Fig. 7.1. As can be observed, the chip at some point tends to split along the vertical direction, causing the chip material to move sideways around the grain depicted in grey. This effect will cause the tangential cutting force component to decrease in comparison to the plane strain approach implemented so far.

In this context, the parametrisation scheme for the bridging quantities such as the heat source term r and the grinding force components $F_\bullet$ will have to be extended accordingly, since applying the same grain geometry in an altered orientation of the grain will result in a completely different workpiece response. Rasim et al. [74] investigate the influence of the meso-scale grain orientation on resulting chip formation, which basically constitutes a very valuable contribution to the scale-bridging scheme presented in Chapter 5 when extending the latter to three-dimensional single grain finite element models.

7.1.2 Three-dimensional process model

During the development of the process model, investigations of a three-dimensional thermal load model—neglecting the material removal at a first stage—have been carried out to model an elastic behaviour of the workpiece spindle. The respective results are depicted in Fig. 7.2. As can be observed, the temperature distribution in a cross-section of the workpiece equals the results presented in Chap. 6, which proves the assumptions made therein. However, the computation time—even with the comparatively coarse workpiece mesh invoked—does at the present stage not allow further development regarding the material removal targeted. The reason for this drawback is the comparatively high velocity of the moving heat compound substituting the tool. To enable a proper approximation of the heat induced, the time increments needed to discretise the process time span have to be very small and therefore cause a very high computational cost to solve the boundary value problem.

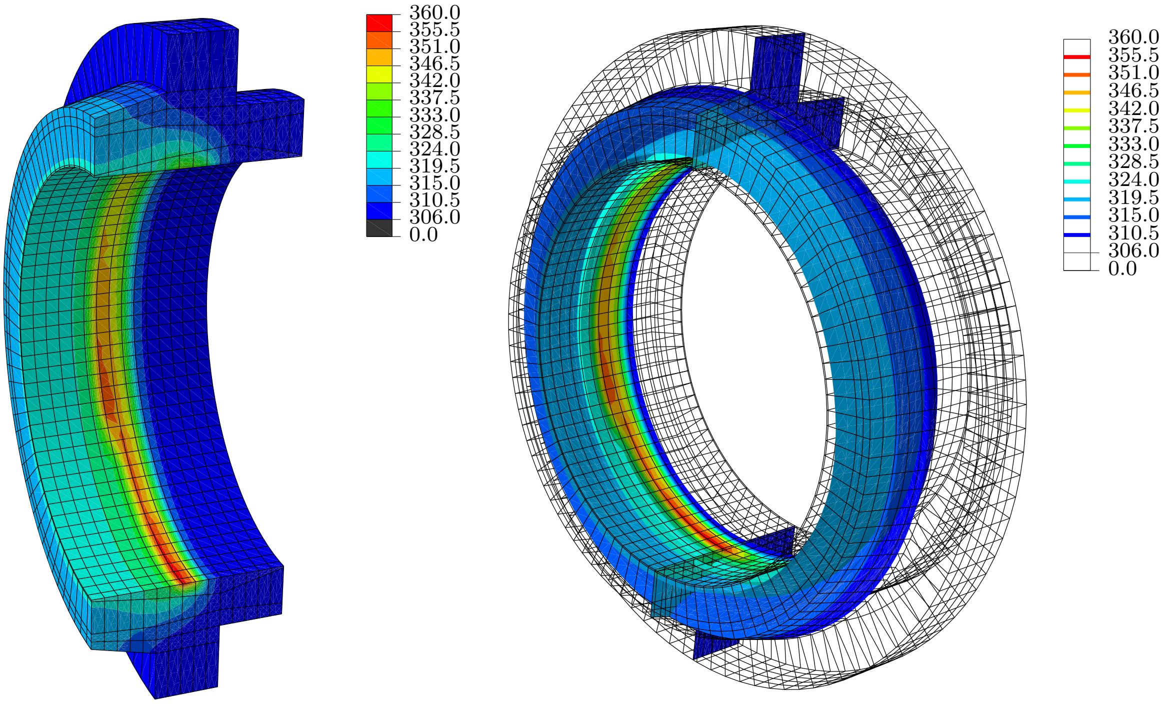

Figure 7.2: Thermal response (in K) of the three-dimensional process model. Cross-section of the workpiece (left) and isosurface plot of the complete surface (right). The moving load compound, which is not depicted here, is situated at the lower cross-section surface.

Bibliography

[1] S. Agarwal and P. V. Rao. Predictive modeling of force and power based on a new analytical undeformed chip thickness model in ceramic grinding. *International Journal of Machine Tools and Manufacture*, 65:68–78, 2013. ISSN 0890-6955. doi:10.1016/j.ijmachtools.2012.10.006.

[2] E. Ahearne and G. Byrne. Simulation of the local kinematics in rotational grinding. *CIRP Annals - Manufacturing Technology*, 57(1):333–336, 2008. ISSN 0007-8506. doi:10.1016/j.cirp.2008.03.080.

[3] M. Akbari, S. Buhl, C. Leinenbach, and K. Wegener. A new value for Johnson Cook damage limit criterion in machining with large negative rake angle as basis for understanding of grinding. *Journal of Materials Processing Technology*, 234: 58–71, 2016. ISSN 0924-0136. doi:10.1016/j.jmatprotec.2016.03.009.

[4] H. Altenbach. *Kontinuumsmechanik*. Springer Berlin Heidelberg, 2 edition, 2012. ISBN 978-3-642-24119-2. doi:10.1007/978-3-642-24119-2.

[5] Y. Altintas, P. Kersting, D. Biermann, E. Budak, B. Denkena, and I. Lazoglu. Virtual process systems for part machining operations. *CIRP Annals - Manufacturing Technology*, 63(2):585–605, 2014. ISSN 0007-8506. doi:10.1016/j.cirp.2014.05.007.

[6] P. Arrazola, T. Özel, D. Umbrello, M. Davies, and I. Jawahir. Recent advances in modelling of metal machining processes. *CIRP Annals - Manufacturing Technology*, 62(2):695–718, 2013. ISSN 0007-8506. doi:10.1016/j.cirp.2013.05.006.

[7] F. Aurenhammer. Voronoi diagrams – a survey of a fundamental geometric data structure. *ACM Comput. Surv.*, 23(3):345–405, September 1991. ISSN 0360-0300. doi:10.1145/116873.116880.

[8] F. Aurenhammer, R. Klein, D.-T. Lee, and R. Klein. *Voronoi Diagrams and Delaunay Triangulations*. World Scientific, 2013.

[9] J. Aurich and B. Kirsch. Kinematic simulation of high-performance grinding for analysis of chip parameters of single grains. *CIRP Journal of Manufacturing Science and Technology*, 5(3):164–174, 2012. ISSN 1755-5817. doi:10.1016/j.cirpj.2012.07.004.

[10] M. Bailey and L. Hedges. Die Kristallmorphologie von Diamant und ABN. *Industrie-Diamanten-Rundschau*, 3(29):126–129, 1995.

[11] E. Bain. The nature of martensite. *Transactions of the AIME*, 70:25–46, 1924.

[12] K. Bathe. *Finite Element Procedures.* Prentice Hall, 2006. ISBN 9780979004902.

[13] R. Berthelsen, H. Wilbuer, R. Holtermann, and A. Menzel. Computational modelling of wear – application to structured surfaces of elastoplastic tools. *GAMM-Mitteilungen*, 39(2):210–228, 2016. ISSN 1522-2608. doi:10.1002/gamm.201610013. URL `http://dx.doi.org/10.1002/gamm.201610013`.

[14] H. Bhadeshia. Steels for bearings. *Progress in Materials Science*, 57(2):268–435, 2012. ISSN 0079-6425. doi:10.1016/j.pmatsci.2011.06.002.

[15] D. Biermann, A. Menzel, T. Bartel, F. Höhne, R. Holtermann, R. Ostwald, B. Sieben, M. Tiffe, and A. Zabel. Experimental and computational investigation of machining processes for functionally graded materials. *Procedia Engineering*, 19:22–27, 2011. ISSN 1877-7058. doi:10.1016/j.proeng.2011.11.074. 1st CIRP Conference on Surface Integrity (CSI).

[16] D. Biermann, R. Holtermann, A. Menzel, and S. Schumann. Modelling and simulation of thermal effects in internal traverse grinding of hardened bearing steel. *CIRP Annals - Manufacturing Technology*, 65(1):321–324, 2016. doi:10.1016/j.cirp.2016.04.005.

[17] T. Bobach, G. Farin, D. Hansford, and G. Umlauf. Natural neighbor extrapolation using ghost points. *Computer-Aided Design*, 41(5):350–365, 2009. ISSN 0010-4485. doi:10.1016/j.cad.2008.08.007. Voronoi Diagrams and their Applications.

[18] J. Bonet. *Nonlinear Continuum Mechanics for Finite Element Analysis.* Cambridge Univ. Press, 2nd edition, 2008. ISBN 978-0-521-83870-2.

[19] E. Brinksmeier, J. Aurich, E. Govekar, C. Heinzel, H. Hoffmeister, F. Klocke, J. Peters, R. Rentsch, D. Stephenson, E. Uhlmann, K. Weinert, and M. Wittmann. Advances in modeling and simulation of grinding processes. *CIRP Annals - Manufacturing Technology*, 55(2):667–696, 2006. ISSN 0007-8506. doi:10.1016/j.cirp.2006.10.003.

[20] E. Brinksmeier and R. Rentsch. Tribology aspects in state of the art md cutting simulations. *8th. CIRP Int. Workshop on Modeling of Machining Operations*, page 401–408, May 2005.

[21] E. Brinksmeier, F. Klocke, D. A. Lucca, J. Sölter, and D. Meyer. Process signatures – a new approach to solve the inverse surface integrity problem in machining processes. *Procedia CIRP*, 13:429–434, 2014. ISSN 2212-8271. doi:10.1016/j.procir.2014.04.073. 2nd CIRP Conference on Surface Integrity (CSI).

[22] W. Böhm, G. Farin, and J. Kahmann. A survey of curve and surface methods in cagd. *Computer Aided Geometric Design*, 1(1):1–60, 1984. ISSN 0167-8396. doi:10.1016/0167-8396(84)90003-7.

[23] S. Chakrabarti and S. Paul. Numerical modelling of surface topography in superabrasive grinding. *The International Journal of Advanced Manufacturing Technology*, 39(1-2):29–38, 2008. ISSN 0268-3768. doi:10.1007/s00170-007-1201-y.

[24] R. W. Clough and J. L. Tocher. Finite element stiffness matrices for analysis of plates in bending. In *Proceedings of conference on matrix methods in structural analysis*, volume 1, page 515–545, 1965.

[25] K. de Payrebrune. *Analyse und Modellierung der Prozess-Strukturwechselwirkungen beim Werkzeugschleifen.* Dissertation, Institut für Maschinenelemente, Konstruktion und Fertigung, TU Bergakademie Freiberg University, 2013.

[26] B. Denkena, L. de Leon, A. Turger, and L. Behrens. Prediction of contact conditions and theoretical roughness in manufacturing of complex implants by toric grinding tools. *International Journal of Machine Tools and Manufacture*, 50(7): 630–636, 2010. ISSN 0890-6955. doi:10.1016/j.ijmachtools.2010.03.008.

[27] H. Ding, J. Tang, and J. Zhong. Accurate nonlinear modeling and computing of grinding machine settings modification considering spatial geometric errors for hypoid gears. *Mechanism and Machine Theory*, 99:155–175, 2016. ISSN 0094-114X. doi:10.1016/j.mechmachtheory.2016.01.008.

[28] D. Doman, A. Warkentin, and R. Bauer. Finite element modeling approaches in grinding. *International Journal of Machine Tools and Manufacture*, 49(2):109–116, 2009. ISSN 0890-6955. doi:10.1016/j.ijmachtools.2008.10.002.

[29] M. Feldhoff. *Modellgestützte Werkzeug- und Prozessentwicklung des Bohrschleifens faserverstärkter Duromere.* PhD thesis, Institut für Spanende Fertigung, TU Dortmund, 2012.

[30] J. Foley, S. Feiner, H. J.F., and P. R.L. *Introduction to computer graphics.* Addison-Wesley Longman Publishing Co., Boston (United States of America), 1994.

[31] K.-H. Grote and J. Feldhusen, editors. *DUBBEL – Taschenbuch für den Maschinenbau.* Springer, Berlin, 22. edition, 2007. ISBN 978-3-540-49714-1. doi:10.1007/978-3-540-68191-5.

[32] R. Hecker and S. Liang. Predictive modeling of surface roughness in grinding. *International Journal of Machine Tools & Manufacture*, 43:755–761, 2003.

[33] C. Heinzel. *Methoden zur Untersuchung und Optimierung der Kühlschmierung beim Schleifen.* PhD thesis, Universität Bremen, 1999.

[34] P. Herzenstiel and J. C. Aurich. cBN-grinding wheel with a defined grain pattern - extensive numerical and experimental studies. *Machining Science and Technology*, 14(3):301–322, 2010. doi:10.1080/10910344.2010.511574.

[35] R. Holtermann, D. Schumann, A. Menzel, and D. Biermann. A hybrid approach to the modelling and simulation of grinding processes. In *Proceedings of the 11th World Congress Computational Mechanics (WCCM XI)*, page 1932–1937, 2014.

[36] R. Holtermann, S. Schumann, A. Menzel, and D. Biermann. Ansätze zur Modellierung und Simulation des Innenrundschälschleifens. *Diamond Business*, 40:

30–41, 2012.

[37] R. Holtermann, S. Schumann, A. Menzel, and D. Biermann. Modelling, simulation and experimental investigation of chip formation in internal traverse grinding. *Production Engineering*, 7(2-3):251–263, 2013. ISSN 0944-6524. doi:10.1007/s11740-013-0449-3.

[38] R. Holtermann, A. Menzel, S. Schumann, D. Biermann, T. Siebrecht, and P. Kersting. Modelling and simulation of internal traverse grinding: bridging meso- and macro-scale simulations. *Production Engineering*, 9(4):451–463, 2015. ISSN 0944-6524. doi:10.1007/s11740-015-0613-z.

[39] R. Holtermann, S. Schumann, A. Zabel, D. Biermann, and A. Menzel. Numerical determination of process values influencing the surface integrity in grinding. *Procedia CIRP*, 45:39–42, 2016. doi:10.1016/j.procir.2016.02.072.

[40] C. Hortig. *Local and non-local thermomechanical modeling and finite-element simulation of high-speed cutting.* PhD thesis, TU Dortmund, Institute of Mechanics, 2011.

[41] C. Hortig and B. Svendsen. Simulation of chip formation during high-speed cutting. *Journal of Materials Processing Technology*, 186(1-3):66–76, 2007. ISSN 0924-0136. doi:10.1016/j.jmatprotec.2006.12.018.

[42] J. J. H.S. Carslaw. *Conduction of Heat in Solids.* Oxford University Press, London (England), 1959.

[43] Y. Huang and S. Y. Liang. Force modelling in shallow cuts with large negative rake angle and large nose radius tools application to hard turning. *International Journal of Advanced Manufacturing Technology*, 22(9-10):626–632, November 2003. ISSN 0268-3768. doi:10.1007/s00170-003-1550-0.

[44] T. W. Hwang, C. J. Evans, and S. Malkin. High speed grinding of silicon nitride with electroplated diamond wheels, part 2: Wheel topography and grinding mechanisms. *Journal of Manufacturing Science and Engineering*, 122(1):42–50, 2000. doi:10.1115/1.538909.

[45] T. Hwang, C. Evans, and S. Malkin. An investigation of high speed grinding with electroplated diamond wheels. *CIRP Annals - Manufacturing Technology*, 49(1): 245–248, 2000. ISSN 0007-8506. doi:10.1016/S0007-8506(07)62938-2.

[46] A. Irretier. Schlussbericht SFB570 - Teilprojekt C1 ”Stoffwertebestimmung”. Technical report, Universität Bremen, 2009. URL `http://www.sfb570.uni-bremen.de/?q=en/node/189`.

[47] M. J. Jackson and J. P. Davim. *Machining with Abrasives.* Springer-Verlag, Berlin Heidelberg (Germany), 2011.

[48] G. Johnson and W. Cook. A constitutive model and data for metals subjected to large strains, high strain rates and high temperatures. *Proc. 7th Int. Symposium*

on Ballistics, 1:541–547, 1983.

[49] R. Joliet and M. Kansteiner. A high resolution surface model for the simulation of honing processes. *Advanced Materials Research*, 769:69–76, 2013. doi:10.4028/www.scientific.net/AMR.769.69.

[50] O. Kienzle. Die Bestimmung von Kräften und Leistungen an spanenden Werkzeugen und Werkzeugmaschinen. *VDI-Z*, 94(11/12):299–305, 1952.

[51] B. Kirsch and J. Aurich. Influence of the macro-topography of grinding wheels on the cooling efficiency and the surface integrity. *Procedia CIRP*, 13:8–12, 2014. ISSN 2212-8271. doi:10.1016/j.procir.2014.04.002. 2nd {CIRP} Conference on Surface Integrity (CSI).

[52] F. Klocke. *Manufacturing Processes 2 – Grinding, Honing, Lapping*. Springer, 2009.

[53] F. Klocke, E. Brinksmeier, and K. Weinert. Capability profile of hard cutting and grinding processes. *CIRP Annals - Manufacturing Technology*, 54(2):22–45, 2005. ISSN 0007-8506. doi:10.1016/S0007-8506(07)60018-3.

[54] F. Klocke, M. Brumm, and J. Reimann. Modeling of Surface Zone Influences in Generating Gear Grinding. *Procedia CIRP*, 8:21–26, 2013. ISSN 2212-8271. doi:10.1016/j.procir.2013.06.059. 14th CIRP Conference on Modeling of Machining Operations (CIRP CMMO).

[55] P. Koshy, A. Iwasald, and M. Elbestawl. Surface generation with engineered diamond grinding wheels: Insights from simulation. *CIRP Annals - Manufacturing Technology*, 52(1):271–274, 2003. ISSN 0007-8506. doi:10.1016/S0007-8506(07)60582-4.

[56] S. Kumar and S. Paul. Numerical modelling of ground surface topography: effect of traverse and helical superabrasive grinding with touch dressing. *Production Engineering*, 6(2):199–204, 2012. ISSN 0944-6524. doi:10.1007/s11740-012-0370-1.

[57] H. P. Langtangen. *Python Scripting for Computational Science*. Springer Berlin Heidelberg, 3rd edition, 2009. ISBN 9783540739159.

[58] B. Lauwers, F. Klocke, A. Klink, A. E. Tekkaya, R. Neugebauer, and D. Mcintosh. Hybrid processes in manufacturing. *CIRP Annals - Manufacturing Technology*, 63 (2):561–583, 2014. ISSN 0007-8506. doi:10.1016/j.cirp.2014.05.003.

[59] I. Liu. *Continuum Mechanics*. Advanced Texts in Physics. Springer Berlin Heidelberg, 2002. ISBN 9783540430193.

[60] Y. Liu, A. Warkentin, R. Bauer, and Y. Gong. Investigation of different grain shapes and dressing to predict surface roughness in grinding using kinematic simulations. *Precision Engineering*, 37(3):758–764, 2013. ISSN 0141-6359. doi:10.1016/j.precisioneng.2013.02.009.

[61] G. Ljustina, R. Larsson, and M. Fagerström. A FE based machining simulation methodology accounting for cast iron microstructure. *Finite Elements in Analysis and Design*, 80(0):1–10, 2014. ISSN 0168-874X. doi:10.1016/j.finel.2013.10.006.

[62] S. Malkin. Thermal aspects of grinding - 2. surface temperatures and workpiece burn. *J. Eng. Ind. Trans. ASME*, 96 Series B(4):1184–1191, 1974.

[63] S. Malkin and R. Anderson. Thermal aspects of grinding – 1. energy partition. *J. Eng. Ind. Trans. ASME*, 96 Series B(4):1177–1183, 1974.

[64] K. Marschalkowski and D. Biermann. Hochleistungs-Innenrundschleifen mit galvanisch gebundenen cBN-Schleifscheiben. *Diamond Business*, 01-2009:48–55, 2009.

[65] K. Marschalkowski. *Beitrag zur Prozessentwicklung für das Hochleistungsinnenrund-Schälschleifen mit galvanisch gebundenen CBN-Schleifscheiben.* PhD thesis, Institut für Spanende Fertigung, TU Dortmund, 2010.

[66] K. Marschalkowski, D. Biermann, and K. Weinert. On the characteristics of high-performance internal traverse grinding using electroplated cbn wheels. In T. A. Y. and Takeuchi, editors, *Proceedings of the 4th CIRP International Conference on High Performance Cutting (CIRP HPC 2010)*, volume 1, page 393–398, 2010.

[67] W. M. Mohammed, E. Ng, and M. Elbestawi. Modeling the effect of the microstructure of compacted graphite iron on chip formation. *International Journal of Machine Tools and Manufacture*, 51(10–11):753–765, 2011. ISSN 0890-6955. doi:10.1016/j.ijmachtools.2011.06.005.

[68] H.-C. Möhring, O. Gümmer, and R. Fischer. Active error compensation in contour-controlled grinding. *CIRP Annals - Manufacturing Technology*, 60(1):429–432, 2011. ISSN 0007-8506. doi:10.1016/j.cirp.2011.03.033.

[69] G. M. Nielson. A method for interpolating scattered data based upon a minimum norm network. *Mathematics of Computation*, 40:253–271, 1983. doi:10.1090/S0025-5718-1983-0679444-7.

[70] H. Parisch. *Festkörper-Kontinuumsmechanik: Von den Grundgleichungen zur Lösung mit Finiten Elementen.* Vieweg+Teubner Verlag, 1 edition, 2003. ISBN 978-3-519-00434-9,978-3-322-80052-7.

[71] G. Poulachon and A. Moisan. Performance evaluation on hardened steel-(PCBN) tool pair in high speed turning. In H. Schulz, editor, *Scientific Fundamentals of HSC*, page 161–171. Carl Hanser Verlag, 2001.

[72] G. Poulachon and A. Moisan. A study of chip formation mechanisms in high speed cutting of hardened steel. In H. Schulz, editor, *Scientific Fundamentals of HSC*, page 11–21. Carl Hanser Verlag, 2001.

[73] A. Ramesh and S. N. Melkote. Modeling of white layer formation under thermally dominant conditions in orthogonal machining of hardened aisi 52100 steel. *Inter-*

national Journal of Machine Tools and Manufacture, 48(3-4):402–414, 2008. ISSN 0890-6955. doi:10.1016/j.ijmachtools.2007.09.007.

[74] M. Rasim, P. Mattfeld, and F. Klocke. Analysis of the grain shape influence on the chip formation in grinding. *Journal of Materials Processing Technology*, 226: 60–68, 2015. ISSN 0924-0136. doi:10.1016/j.jmatprotec.2015.06.041.

[75] S. Rausch, S. Odendahl, P. Kersting, D. Biermann, and A. Zabel. Simulation-based prediction of process forces for grinding free-formed surfaces on machining centers. *Procedia CIRP*, 4:161–165, 2012. ISSN 2212-8271. doi:10.1016/j.procir.2012.10.029.

[76] S. Rausch, T. Siebrecht, P. Kersting, and D. Biermann. Analysis and simulation of surface topographies in grinding of thermally sprayed coatings. *Advanced Materials Research*, 1018:91–98, 2014. doi:10.4028/www.scientific.net/AMR.1018.91.

[77] R. Renka and A. Cline. A triangle-based c^1 interpolation method. *Rocky Mountain J. Math.*, 14(1):223–238, 03 1984. doi:10.1216/RMJ-1984-14-1-223.

[78] N. Rüttimann, M. Roethlin, S. Buhl, and K. Wegener. Simulation of hexa-octahedral diamond grain cutting tests using the SPH method. *Procedia CIRP*, 8:322–327, 2013. ISSN 2212-8271. doi:10.1016/j.procir.2013.06.110. 14th CIRP Conference on Modeling of Machining Operations (CIRP CMMO).

[79] E. Salisbury, K. Domala, K. Moon, M. Miller, and J. Sutherland. A three-dimensional model for the surface texture in surface grinding, part 1: Surface generation model. *Journal of Manufacturing Science and Engineering, Transactions of the ASME*, 123(4):576–581, 2001. doi:10.1115/1.1391427.

[80] E. Salisbury, K. Domala, K. Moon, M. Miller, and J. Sutherland. A three-dimensional model for the surface texture in surface grinding, part 2: Grinding wheel surface texture model. *Journal of Manufacturing Science and Engineering, Transactions of the ASME*, 123(4):582–590, 2001. doi:10.1115/1.1391428.

[81] H. Sallem and H. Hamdi. Analysis of measured and predicted residual stresses induced by finish cylindrical grinding of high speed steel with CBN wheel. *Procedia CIRP*, 31:381–386, 2015. ISSN 2212-8271. doi:10.1016/j.procir.2015.03.080. 15th CIRP Conference on Modelling of Machining Operations).

[82] N. Schaal, F. Kuster, and K. Wegener. Springback in Metal Cutting with High Cutting Speeds. *Procedia CIRP*, 31:24–28, 2015. ISSN 2212-8271. doi:10.1016/j.procir.2015.03.065. 15th CIRP Conference on Modelling of Machining Operations (15th CMMO).

[83] V. Schulze, E. Uhlmann, R. Mahnken, A. Menzel, D. Biermann, A. Zabel, P. Bollig, I. Ivanov, C. Cheng, R. Holtermann, and T. Bartel. Evaluation of different approaches for modeling phase transformations in machining simulation. *Production Engineering*, 9(4):437–449, 2015. ISSN 0944-6524. doi:10.1007/s11740-015-0618-7.

[84] S. Schumann, R. Holtermann, D. Biermann, and A. Menzel. Hochleistungs-Innenrundschälschleifen – Thermomechanische Betrachtung in Abhängigkeit vom radialen Gesamtaufmaß. *diamond business*, 11(2):36–43, 2013.

[85] S. Schumann, T. Siebrecht, P. Kersting, D. Biermann, R. Holtermann, and A. Menzel. Determination of the thermal load distribution in internal traverse grinding using a geometric-kinematic simulation. *Procedia CIRP*, 31:322–327, 2015. ISSN 2212-8271. doi:10.1016/j.procir.2015.03.020. 15th CIRP Conference on Modelling of Machining Operations (15th CMMO).

[86] S. Schumann, R. Holtermann, D. Biermann, and A. Menzel. Lokale Betrachtung des Innenrundschälschleifens – Modellhafte Ermittlung der thermomechanischen Belastung in Abhängigkeit des Schruppzonenwinkels. *wt - Werkstattstechnik online*, 103(1):493–498, 2013.

[87] S. Schumann, E. Würz, D. Biermann, R. Holtermann, and A. Menzel. Wärmeeintrag beim Hochleistungs-Innenrundschälschleifen beherrschen – Ermittlung der thermischen Werkstückbelastungen mittels FEM. *VDI-Z Integrierte Produktion*, 154(I-2012):31–33, 2012. ISSN 1436-4913.

[88] S. Shimada, N. Ikawa, H. Tanaka, and J. Uchikoshi. Structure of Micromachined Surface Simulated by Molecular Dynamics Analysis. *CIRP Annals - Manufacturing Technology*, 43(1):51–54, 1994. ISSN 0007-8506. doi:10.1016/S0007-8506(07)62162-3.

[89] T. Siebrecht, D. Biermann, H. Ludwig, S. Rausch, P. Kersting, H. Blum, and A. Rademacher. Simulation of grinding processes using finite element analysis and geometric simulation of individual grains. *Production Engineering*, 8(3):345–353, 2014. ISSN 1863-7353. doi:10.1007/s11740-013-0524-9.

[90] T. Siebrecht, S. Rausch, P. Kersting, and D. Biermann. Grinding process simulation of free-formed WC-co hard material coated surfaces on machining centers using poisson-disk sampled dexel representations. *CIRP Journal of Manufacturing Science and Technology*, 7(2):168–175, 2014. ISSN 1755-5817. doi:10.1016/j.cirpj.2014.01.001.

[91] P. Stepień. A probabilistic model of the grinding process. *Applied Mathematical Modelling*, 33(10):3863–3884, 2009. ISSN 0307-904X. doi:10.1016/j.apm.2009.01.005.

[92] D. Sun, M. Sealy, Z. Liu, C. Fu, Y. Guo, F. Fang, and B. Zhang. Finite element analysis of machining damage in single-grit grinding of ceramic knee implants. *Procedia Manufacturing*, 1:644–654, 2015. ISSN 2351-9789. doi:10.1016/j.promfg.2015.09.058. 43rd North American Manufacturing Research Conference, 8-12 June 2015, UNC Charlotte, North Carolina, United States.

[93] D. Systèmes. *Abaqus documentation.* Dassault Systèmes, version 6.14 edition, 2014.

[94] T. Tawakoli, R. Schmid, A. Vesali, and A. Padilla-Ley. Rekonstruktion der Schleifscheibentopographie mit Hilfe der Bildverarbeitungsmethoden. *Diamant Hochleistungswerkzeuge. dihw Magazin*, 4(3):32–39, 2011.

[95] C. Treffert. *Hochgeschwindigkeitsschleifen mit galvanisch gebundenen CBN-Schleifscheiben*. PhD thesis, RWTH Aachen, 1994.

[96] C. Truesdell. *A First Course in Rational Continuum Mechanics*. Academic Press, New York, 1977. ISBN 9780127013015.

[97] C. Truesdell and W. Noll. *The Non-Linear Field Theories of Mechanics / Die Nicht-Linearen Feldtheorien der Mechanik*, page 1–541. Springer Berlin Heidelberg, Berlin, Heidelberg, 1965. ISBN 978-3-642-46015-9. doi:10.1007/978-3-642-46015-9_1.

[98] S. Turteltaub and A. S. J. Suiker. Transformation-induced plasticity in ferrous alloys. *J. Mech. Phys. Sol.*, 53:1747–1788, 2005.

[99] H. Tönshoff, J. Peters, I. Inasaki, and T. Paul. Modelling and simulation of grinding processes. *CIRP Annals - Manufacturing Technology*, 41(2):677–688, 1992. ISSN 0007-8506. doi:10.1016/S0007-8506(07)63254-5.

[100] E. Uhlmann, R. Gerstenberger, and J. Kuhnert. Cutting simulation with the meshfree finite pointset method. *Procedia CIRP*, 8(0):391–396, 2013. ISSN 2212-8271. doi:10.1016/j.procir.2013.06.122.

[101] T. Waffenschmidt, C. Polindara, A. Menzel, and S. Blanco. A gradient-enhanced large-deformation continuum damage model for fibre-reinforced materials. *Computer Methods in Applied Mechanics and Engineering*, 268:801–842, 2014. ISSN 0045-7825. doi:10.1016/j.cma.2013.10.013.

[102] T. Waffenschmidt, C. Polindara, and A. Menzel. A gradient-enhanced continuum damage model for residually stressed fibre-reinforced materials at finite strains. In T. Lenarz and P. Wriggers, editors, *Biomedical Technology*, page 19–40. Springer International Publishing, 2015. ISBN 978-3-319-10981-7. doi:10.1007/978-3-319-10981-7_2.

[103] Z. Wang and I. Al-Zkeri. Determination of flow stress data for AISI 52100 using machining tests. Technical Report Report No. ERC-NSM-07-R-08, Engineering Rearch Center for Net Shape Manufacturing, The Ohio State University 1971 Neil Avenue Columbus, Ohio 43201, 2007.

[104] G. Warnecke and U. Zitt. Kinematic simulation for analyzing and predicting High-Performance grinding processes. *CIRP Annals - Manufacturing Technology*, 47(1): 265–270, 1998. ISSN 0007-8506. doi:10.1016/S0007-8506(07)62831-5.

[105] P. Wriggers. *Nonlinear Finite Element Methods*. Springer Berlin Heidelberg, 2008. ISBN 9783540710004.

[106] R. Zaera, J. Rodríguez-Martínez, and D. Rittel. On the Taylor–Quinney coefficient in dynamically phase transforming materials. Application to 304 stainless steel. *International Journal of Plasticity*, 40:185–201, 2013. ISSN 0749-6419. doi:10.1016/j.ijplas.2012.08.003.

[107] O. C. Zienkiewicz and J. Z. Zhu. The superconvergent patch recovery and a posteriori error estimates. part 1: The recovery technique. *International Journal for Numerical Methods in Engineering*, 33(7):1331–1364, 1992. ISSN 1097-0207. doi:10.1002/nme.1620330702.

[108] O. C. Zienkiewicz and J. Z. Zhu. The superconvergent patch recovery and a posteriori error estimates. part 2: Error estimates and adaptivity. *International Journal for Numerical Methods in Engineering*, 33(7):1365–1382, 1992. ISSN 1097-0207. doi:10.1002/nme.1620330703.

Curriculum Vitæ

Personal Data

Name	Raphael Holtermann
Date of Birth	December 17, 1982
Place of Birth	Castrop-Rauxel, Germany
Nationality	German

Professional Occupation

10/2010 – 12/2016	Scientific Assistant, Institute of Mechanics, TU Dortmund University
10/2008 – 09/2009	Software Engineer, MAN Turbo AG, Oberhausen

University Education

10/2009	Academic Degree: Diploma (Dipl.-Ing.)
02/2009 – 09/2009	Diploma thesis: ”A program development on aerodynamic optimisation of radial compressors at design point using evolutionary algorithms”. German title: ”Entwicklung eines Programms zur aerodynamischen Optimierung des Auslegungspunkts von Radialverdichtern mittels evolutionärer Algorithmen”
06/2005 – 10/2008	Founding and active member of the GETracing formula student team, TU Dortmund University
08/2004 – 04/2008	Student assistant, Institute of Mechanics, TU Dortmund University
10/2003 – 10/2009	Studies of Mechanical Engineering, TU Dortmund University

Alternative Civilian Service (in lieu of military service)

09/2002 – 06/2003	Bundesanstalt für Arbeitsschutz und Arbeitsmedizin, Dortmund

School Education

08/1993 – 06/2002	Secondary School, Heinrich-Heine-Gymnasium, Dortmund

Institute of Mechanics – series of publications

Published to date:

2010/01	Palnau, V.: Implementierung eines netzfreien Diskretisierungsverfahrens und seine Anwendung auf die Scherbandanalyse. ISBN 978-3-921823-51-4
2010/02	Klusemann, B.: Application of homogenization methods and crystal plasticity to the modeling of heterogeneous materials of technological interest. ISBN 978-3-921823-53-8
2011/01	Hortig, C.: Local and non-local thermomechanical modeling and finite-element simulation of high-speed cutting. ISBN 978-3-921823-54-5
2011/02	Parvizian, F.: Modeling of microstructure evolution in aluminum alloys during hot extrusion. ISBN 978-3-921823-56-9
2011/03	Noman, M.: Characterization and model identification for the simulation of the forming behavior of ferritic steels. ISBN: 978-3-921823-55-2
2011/04	Kayser, T.: Characterization of microstructure in aluminum alloys based on electron backscatter diffraction. ISBN: 978-3-921823-57-6
2011/05	Bargmann, S.: Computational modeling of material behavior on different scales based on continuum mechanics. ISBN: 978-3-921823-58-3
2013/01	Waffenschmidt, T.: Modelling and simulation of adaptation and degradation in anisotropic biological tissues. ISBN: 978-3-921823-61-3
2015/01	Ostwald, R.: Modelling and simulation of phase-transformations in elasto-plastic polycrystals. ISBN: 978-3-921823-66-8
2016/01	Subramanian, M.: Phenomenological modelling and simulation of ferroelectric ceramics. ISBN 978-3-921823-74-3
2016/02	Clausmeyer, T.: Evolution of plastic anisotropy in metals: Material models, experiments and applications. ISBN 978-3-921823-76-7
2016/01	Holtermann, R.: Computational multiscale modelling of grinding processes. ISBN 978-3-921823-86-6